



QUENCH - LOCA - REPORTS Nr. 4

Results of the LOCA bundle test QUENCH-L3 with optimised ZIRLO™ claddings (SR-7737)

J. Stuckert, M. Große, C. Rössger, M. Steinbrück, M. Walter

Karlsruher Institut für Technologie

in der Helmholtz-Gemeinschaft

Wissenschaftliche Berichte

QUENCH – LOCA – REPORTS Nr. 4

Results of the LOCA bundle test QUENCH-L3
with optimised ZIRLO™ claddings (SR-7737)

J. Stuckert*, M. Große*, C. Rössger*, M. Steinbrück*, M. Walter**

Institut für Angewandte Materialien:

* Angewandte Werkstoffphysik (IAM-AWP)

** Werkstoff- und Biomechanik (IAM-WBM)

Programm Nukleare Entsorgung und Sicherheit

Karlsruher Institut für Technologie

Mai 2018

Impressum

Karlsruher Institut für Technologie (KIT)

Institut für Angewandte Materialien

Angewandte Werkstoffphysik IAM-AWP-KOR

Nukleare Sicherheitsforschung

Hermann-von-Helmholtz-Platz 1

76344 Eggenstein-Leopoldshafen

www.iam.kit.edu/awp/666.php

DOI: 10.5445/IR/1000083087

Zusammenfassung

Ergebnisse des unter Bedingungen eines LOCA-Störfalls ausgeführten Versuches QUENCH-LOCA-3 mit opt. ZIRLO™-Hüllrohren

Der QUENCH-L3-Bündelversuch wurde im Rahmen der QUENCH-LOCA-Testserie durchgeführt. Das Ziel der Testreihe ist die Untersuchung von Dehnung, Bersten, Oxidation und sekundärer Hydrierung der Hüllrohre unter repräsentativen Auslegungsstörfallbedingungen sowie der Einfluss dieser Parameter auf die mechanischen Eigenschaften dieser Rohre. Mit den Versuchen dieser Serie wird das Verhalten von verschiedenen Hüllrohrmaterialien mit und ohne Vorhydrierung untersucht. Für den QUENCH-L3-Versuch wurden frische opt. ZIRLO™-Hüllrohre (Außendurchmesser: 10,75 mm) verwendet. Die Bündelkonfiguration und das Testprotokoll waren ähnlich dem Referenztest QUENCH-L1, der mit frischen Zircaloy-4-Hüllrohren durchgeführt wurde. Spezifisches Ziel des QUENCH-L3-Tests war die Untersuchung des Verhaltens der ZIRLO-Hüllrohre, mit speziellem Fokus auf die Auswirkungen des Berstens dieser Rohre auf deren sekundäre Hydrierung. Der Test wurde am Karlsruher Institut für Technologie (KIT) am 17. März 2015 erfolgreich durchgeführt.

Zu Beginn des Experiments wurde zunächst die Teststrecke stabilisiert. Hierzu wurde das Bündel erwärmt mit einer elektrischen Leistung von 3,6 kW, einer Gasströmung von 6 g/s Argon sowie 2 g/s überhitzten Dampfes bis eine maximale Hüllrohrtemperatur von etwa 845 K erreicht war. Während dieser Stabilisierungsphase (mit einer Dauer von 1700 s) wurden die Stäbe bis auf 55 bar mit Krypton beaufschlagt. In der sich anschließenden 75,8 s dauernden Aufheizphase wurde die elektrische Leistung auf 60 kW erhöht. Während dieser Zeit stiegen die Temperaturen von ihren Anfangswerten (d.h. denen am Ende der Stabilisierungsphase) bis zu einem Maximum von 1325 K. Die durchschnittliche Aufheizgeschwindigkeit betrug 6,3 K/s. Die erhöhte Duktilität der erwärmten Hüllrohre führte zu deren fortschreitender Dehnung und anschließendem Bersten aller Rohre. Die Bersttemperatur betrug 1117 ± 30 K. Das Experiment wurde mit einer Leistungsreduzierung auf 3,5 kW (Modellierung der Zerfallswärme) und Einführung von Dampf bei einem Nennwert von 20 g/s fortgesetzt (Abkühlphase). In dieser Phase fand zuerst eine Aufwärmung auf 1346 K und danach eine Abkühlung auf etwa 920 K (an der Bündelebene 850 mm) und 950 K (950 mm) statt. Die darauf folgende Abschreckphase erfolgte vom Bündelboden aus mit einer Wassereinspeisung von bis zu 100 g/s (entspr. 3,3 g/s/Effektivstab). Das vollständige Abschrecken wurde nach 295 s erreicht.

Aufnahmen nach dem Versuch mit einem Videoskop vom Bündelinneren zeigen Ballooning-Bereiche typischerweise in den heißesten Bündelebenen zwischen 800 und 1000 mm. Das Bündel wurde demontiert und die geometrischen Parameter aller Stäbe wurden mit einem Laserscanner bestimmt; die gemessenen Hüllrohr-Umfangsdehnungen im Berstbereich lagen zwischen 20% und 35%. Mit Ultraschallmessungen wurde die Verminderung der Hüllrohrwandstärke in der Nähe von Berstöffnungen bestimmt. Die axiale und radiale Verteilung sowie die Stärke von Oxidschichten an den Hüllrohren wurden durch Wirbelstromverfahren ermittelt; die maximale Dicke von ZrO_2 - in Kombination mit α -Zr(O)-Schichten - betrug etwa 25 μ m für innere und 16 μ m für äußere Stäbe. Die Bestimmung der Konzentration und Verteilung von absorbiertem Wasserstoff wurde mit Hilfe der Neutronentomographie durchgeführt; über den Umfang gemittelte Wasserstoffkonzentrationen zwischen 200 und 500 wppm wurden oberhalb der Berstöffnungen (sekundäre Hydrierung) der inneren Stäben gemessen. Die Messung der mechanischen Eigenschaften und die Bestimmung der Restduktilität wurden durch Zugversuche mit Hüllrohrsegmenten bewerkstelligt; bei den äußeren Stäben zeigten sich Sprödbrüche bei Spannungen von etwa 500 MPa hauptsächlich aufgrund der Spannungskonzentration an den Spitzen von Berstöffnungen. Die Mehrheit der inneren Stäbe versagte durch

Einschnürung in weitem Abstand von der Berstöffnung; nur eines davon brach aufgrund Spannungskonzentration in den Spitzen der Berstöffnung.

Abstract

The QUENCH-L3 experiment was performed in the framework of the QUENCH-LOCA test series. The overall objective of this bundle test series is the investigation of ballooning, burst, degree of oxidation and secondary hydrogen uptake of the cladding under representative design-basis accident conditions and their influence on the mechanical properties. The various experiments of the series examine the behavior of different cladding materials and the effect of pre-hydriding. For the QUENCH-L3 test, as-received ZIRLO™ cladding tubes with an outside diameter of 10.75 mm have been used. Like in all experiments of the QUENCH-LOCA series, all 21 fuel rod simulators were separately pressurized with krypton to 55 bar. Bundle configuration and test protocol were similar to the reference test QUENCH-L1 with Zry-4 claddings. A difference with respect to the reference QUENCH-L1 experiment was the use of tungsten for the electrical heater elements with 4.6 mm diameter instead of tantalum heaters with 6.0 mm diameter. Specific objectives of QUENCH-L3 were to provide information about the response of ZIRLO alloy to a best-estimate large-break LOCA sequence, with special focus on the impact of burst parameters on secondary hydrogenation of the cladding. The experiment was successfully conducted at the Karlsruhe Institute of Technology (KIT) on March 17, 2015.

Prior to the experiment the rods were filled with krypton to 30 bar at 800 K. The experiment started with stabilizing the bundle conditions applying electrical bundle power of 3.6 kW in 6 g/s argon plus 2 g/s superheated steam resulting in maximum bundle temperatures of approximately 845 K. During this stabilization phase (duration 1700 s) the rod internal pressure was increased to 55 bar. The transient was initiated by increasing the electrical power to 60 kW and lasted 75.8 s. During this period the temperatures increased from their initial values to 1325 K. The average heatup rate at the maximum temperature location was 6.3 K/s. Both the increasing ductility and decreasing creep strength of the heated cladding resulted in a progressive ballooning and consequent burst of all of the rods. The burst temperature was 1117 ± 30 K. The experiment continued with a power decrease to 3.5 kW to simulate decay heat and injection of steam at a nominal of 20 g/s. The cladding temperatures increased to a maximum of 1346 K, followed by steady cooling to about 920 K (at elevation 850 mm) and 950 K (elevation 950 mm). The cooling phase was terminated by quenching with up to 100 g/s water injection from bundle bottom. Complete quench was achieved at 295 s.

Post-test videoscope inspection showed typical ballooning pictures at elevations between about 800 and 1000 mm. The bundle was dismantled and the following geometric characterization of all rods by laser scanning revealed formation of multiple ballooning regions; the range of circumferential strains measured was between 20% and 35%. Ultrasound measurements were used to determine the degree of thinning of cladding wall in vicinity of burst openings. Axial and radial distribution of oxidation rate was measured by eddy current methods; maximal combined thickness of ZrO_2 and $\alpha-Zr(O)$ layers was about 25 μm for inner rods and 16 μm for outer rods. Determination of concentration and distribution of absorbed hydrogen was performed by neutron imaging methods; a circumferentially averaged maximal hydrogen concentration between about 200 and 500 wppm was measured above the burst openings (secondary hydrogenation) of inner bundle rods. Measurement of mechanical properties and determination of residual ductility were carried out by tensile tests with cladding tube segments and showed fracture of claddings at engineering stress of about 500 MPa mostly due to stress concentration at burst opening tips for the outer bundle rods. The majority of the inner rods was fractured due to necking far away from the burst for the inner rods; only one cladding was fractured due to stress concentration at the opening middle.

Contents

Zusammenfassung	i
Abstract	iii
List of Tables	vi
List of Figures	vii
Introduction	xiii
1 Description of the Test Facility	3
1.1 The test bundle	3
1.2 Bundle surroundings	4
1.3 Rod pressurization	5
2 Test Bundle Instrumentation	5
2.1 Thermocouples	5
2.2 Gas Measurement System	5
3 Data Acquisition and Process Control	6
4 Test Performance and Results of Online Measurements	7
5 Posttest Examinations	8
5.1 Optical Observation of Cladding Surfaces	8
5.2 Profilometry of Claddings with Laser Scanner	9
5.2.1 Linear Laser Scanning	9
5.2.2 Main Characteristics of the Measuring Device and Procedures	9
5.2.3 Results of the Scans	10
5.3 Nondestructive Eddy Current and Ultrasound Measurements	10
5.4 Results of Neutron Radiography and Tomography; Analysis of Absorbed Hydrogen.	11
5.4.1 Basic Principles	11
5.4.2 Technique	12
5.4.3 Results of Radiography	12
5.4.4 Results of Tomography: Hydrogen Content	12
5.5 XRD investigations	13
5.6 Mechanical Tests	13
5.6.1 Tensile Test Set-up	13
5.6.2 Results of the Tensile Tests	14
6 Summary and Conclusions	14
7 Acknowledgments	15
8 References	15
Tables and Figures	18

List of Tables

Table 1	QUENCH Test Matrix 1997 – 2015	19
Table 2	Design characteristics of the QUENCH-L3 test bundle	22
Table 3	Properties of opt. ZIRLO cladding tubes	23
Table 4	Main characteristics of the ZrO ₂ pellet material, yttria-stabilized (type FZY).....	24
Table 5	QUENCH-L3; Electrical resistances of rods [mΩ] at 20°C.....	25
Table 6	Properties of zirconia fiber insulating boards.....	26
Table 7	List of instrumentation for the QUENCH-L3 test	27
Table 8	QUENCH-L3; Rod thermocouple positions.....	33
Table 9	QUENCH-L3; Sequence of events.....	34
Table 10	QUENCH-L3; Wetting of TFS thermocouples	35
Table 11	QUENCH-L3; Burst parameters	36
Table 12	QUENCH-L3; Strain parameters	37
Table 13	QUENCH-L3; Content of hydrogen absorbed by secondary hydrogenation (n ⁰ -tomography): axial maximum averaged for cross section and axial absolute local maximum	38
Table 14	Table 14: QUENCH-L3: average hydrogen content in hydrogen bands according to hot extraction (LECO TCH600 device, cladding segments with h=11 mm, d=5 mm).....	38
Table 15	QUENCH-L3; Results of tensile tests	39

List of Figures

Figure 1	QUENCH Facility - Main components.	40
Figure 2	Flow diagram of the QUENCH test facility.	41
Figure 3	QUENCH Facility; Containment and test section.	42
Figure 4	QUENCH-L3; Test section with flow lines.	43
Figure 5	QUENCH-L2; Fuel rod simulator bundle (cross section, top view) including rod type indications corresponding to table “List of Instrumentation”.	44
Figure 6	Heated fuel rod simulator.	45
Figure 7	QUENCH-L3; Rod pressure control and measurement panel.	46
Figure 8	QUENCH-L3; Rod pressurization.	47
Figure 9	QUENCH-L3; Rod pressurization process at $T_{pct}=850$ K.	48
Figure 10	QUENCH-L3; Concept for TC fastening at the test rod.	49
Figure 11	Axial temperature measurement locations in the QUENCH-L3 test section.	50
Figure 12	QUENCH-L3; Test bundle; TC instrumentation and rod designation (top view).	51
Figure 14	QUENCH Facility; H ₂ measurement with the GAM 300 mass spectrometer.	52
Figure 15	Mass spectrometer sampling position at the off-gas pipe of the QUENCH test facility.	52
Figure 16	QUENCH-L3; test progress.	53
Figure 17	QUENCH-L3; voltage and current of two DC-generators.	53
Figure 18	QUENCH-L3; System pressure measured at test section inlet P 511, at outlet P 512, and in the off-gas pipe P 601.	54
Figure 19	QUENCH-L3; Argon pressure between shroud and cooling jacket P 406 demonstrates tightness of the shroud.	54
Figure 20	QUENCH-L3; Quench measurement of collapsed water level (L 501), top, water mass flow rate (Fm 104), center, condensed water (L 701), bottom.	55
Figure 21	QUENCH-L3; Steam rate and integral mass (top), hydrogen rate and integral mass (middle), krypton concentration (bottom) measured by mass spectrometry.	56
Figure 22	QUENCH-L3; Temperatures measured by gas inlet thermocouple (T 511) at -412 mm and rod cladding (TFS 7/1) thermocouple at -250 mm elevation.	57
Figure 23	QUENCH-L3; Temperatures measured by rod cladding (TFS 7/2) thermocouple at -150 mm elevation.	57
Figure 24	QUENCH-L3; Temperatures measured by rod cladding (TFS 7/3) and shroud (TSH 3/0) thermocouples at -50 mm elevation.	58
Figure 25	QUENCH-L3; Temperatures measured by rod cladding (TFS 7/4) and shroud (TSH 4/90) thermocouples at 50 mm elevation.	58
Figure 26	QUENCH-L3; Temperatures measured by rod cladding (TFS 7/5) and shroud (TSH 5/180) thermocouples at 150 mm elevation.	59
Figure 27	QUENCH-L3; Temperatures measured by rod cladding (TFS) and shroud (TSH 6/270) thermocouples at 250 mm elevation.	59

Figure 28	QUENCH-L3; Temperatures measured by rod cladding (TFS) and shroud (TSH 7/0) thermocouples at 350 mm elevation.....	60
Figure 29	QUENCH-L3; Temperatures measured by rod cladding (TFS) and shroud (TSH 8/90) thermocouples at 450 mm elevation.....	60
Figure 30	QUENCH-L3; Temperatures measured by rod cladding (TFS) and shroud (TSH 9/180) thermocouples at 550 mm elevation.....	61
Figure 31	QUENCH-L3; Temperatures measured by rod cladding (TFS) and shroud (TSH 10/270) thermocouples at 650 mm elevation.....	61
Figure 32	QUENCH-L3; Temperatures measured by rod cladding (TFS) and shroud (TSH 11/0), and corner rod internal (TIT D/11) thermocouples at 750 mm elevation.	62
Figure 33	QUENCH-L3; Temperatures measured by rod cladding (TFS) and shroud (TSH 12/90), and corner rod internal (TIT C/12) thermocouples at 850 mm elevation.	62
Figure 34	QUENCH-L3; Temperatures measured by rod cladding (TFS) and shroud (TSH 13/180), and corner rod internal (TIT A/13) thermocouples at 950 mm elevation.	63
Figure 35	QUENCH-L3; Temperatures measured by rod cladding (TFS) and shroud (TSH 14/270) thermocouples at 1050 mm elevation.....	63
Figure 36	QUENCH-L3; Temperatures measured by rod cladding (TFS) and shroud (TSH 15/0) thermocouples at 1150 mm elevation.....	64
Figure 37	QUENCH-L3; Temperatures measured by rod cladding (TFS) thermocouples at 1250 mm elevation.....	64
Figure 38	QUENCH-L3; Temperatures measured by rod cladding (TFS 7/17) thermocouple at 1350 mm elevation and gas temperature (T 512) thermocouple between shroud and rod #20; T 511 depicts the gas temperature at the bundle inlet.	65
Figure 39	QUENCH-L3; Overview of the TCI (inner cooling jacket).	65
Figure 40	QUENCH-L3; Axial temperature profile TFS internal and external rod group together with TSH, left, and axial temperature profile of all TFS, right, at 47,8 s (first cladding burst).....	66
Figure 41	QUENCH-L3; Axial temperature profile TFS internal and external rod group together with TSH, left, and axial temperature profile of all TFS, right, at 68 s (last cladding burst).	67
Figure 42	QUENCH-L3; Axial temperature profile TFS internal and external rod group together with TSH, left, and axial temperature profile of all TFS, right, at 76,8 s (end of transient).	68
Figure 43	QUENCH-L3; Axial temperature profile TFS internal and external rod group together with TSH, left, and axial temperature profile of all TFS, right, at 81,8 s (max temperature).	69
Figure 44	QUENCH-L3; comparison of thermocouple readings at elevations 950 mm (upper dia-gram) and 850 mm (lower diagram) of QUENCH-L3 bundle with corresponding data of QUENCH-L1 reference test. More stable and homogeneous conditions for the QUENCH-L3 due to less bending of rods.	70
Figure 45	QUENCH-L3; circumferential temperature difference for rod #7 at elevations 850 and 950 mm.	71
Figure 46	QUENCH-L3: temperatures and cladding ballooning of rod #4; possibility of ballooning propagation from about 950 mm to lower and upper elevations.....	72
Figure 47	QUENCH-L3: temperatures and cladding ballooning of rod #7.	72
Figure 48	QUENCH-L3: temperatures and cladding ballooning of rod #11; possibility of ballooning propagation from about 950 mm to lower elevations.	73

Figure 49	QUENCH-L3: temperatures and cladding ballooning of rod #19; possibility of ballooning propagation from about 900 mm to lower elevations.	73
Figure 50	QUENCH-L3; Pressure changing during heating phase; ballooning and burst.	74
Figure 51	QUENCH-L3; videoscope observations with camera inserted from the bundle bottom at position of corner rod A.	75
Figure 52	QUENCH-L3; videoscope observations with camera inserted from the bundle bottom at position of corner rod B.	76
Figure 53	QUENCH-L3; videoscope observations with camera inserted from the bundle bottom at position of corner rod C.	77
Figure 54	QUENCH-L3; videoscope observations with camera inserted from the bundle bottom at position of corner rod D.	78
Figure 55	QUENCH-L3; Views of bundle at angle positions of 0° and 90°: negligible rod bending and intact thermocouples.	79
Figure 56	QUENCH-L3; Views of bundle at angle positions of 180° and 270°: negligible rod bending and intact thermocouples.	80
Figure 57	QUENCH-L3; overview of burst positions.	81
Figure 58	QUENCH-L3; burst opening orientations of QUENCH-L1 and QUENCH-L3 bundles.	82
Figure 59	Vertical positions of burst openings for QUENCH-L1 and QUENCH-L3 bundles.	83
Figure 60	QUENCH-L3; post-test overview of inner rods; burst front view (top): no bending, mat region around burst opening (surface cracks in oxide layer); burst side view (bottom): cladding bending about 2°, kink in burst region, burst opening always at concave side.	84
Figure 61	QUENCH-L3; post-test overview of outer rods; burst front view (top): no bending, mat region around burst opening (surface cracks in oxide layer); burst side view (bottom): cladding bending about 2°, kink in burst region, burst opening always at concave side.	85
Figure 62	QUENCH-L3; Overview of burst structures of rods #1 - #6.	86
Figure 63	QUENCH-L3; Overview of burst structures of rods #7 - #12.	87
Figure 64	QUENCH-L3; Overview of burst structures of rods #13 - #18.	88
Figure 65	QUENCH-L3; Overview of burst structures of rods #19 - #21.	89
Figure 66	QUENCH-L3; cladding surface structure ("tree bark") around burst opening of rod #1: formation of longitudinal cracks in outer oxide layer during ballooning.	90
Figure 67	QUENCH-L3; cladding surface structure ("tree bark") near to burst opening of rod #1: formation of longitudinal cracks in outer oxide layer during ballooning at all circumferential positions.	91
Figure 68	QUENCH-L3; Rod #5: surface cracks ("tree bark") formed during ballooning about 5 mm below the burst opening (angle 184°) and penetrated ZrO ₂ and α-Zr(O) layers in the region of intensively thinned cladding (with density of ≈20 cracks/mm). Outside of opening circumferential position only cracks inside oxide layer were formed (with density of ≈40 cracks/mm).	92
Figure 69	QUENCH-L3, Rod #1; longitudinal changing of circumferential strain (top); azimuthal diameter downwards from burst (bottom).	93
Figure 70	QUENCH-L3, Rod #2; longitudinal changing of circumferential strain (top); azimuthal diameter downwards from burst (bottom).	94

Figure 71	QUENCH-L3, Rod #3; longitudinal changing of circumferential strain (top); azimuthal diameter downwards from burst (bottom).	95
Figure 72	QUENCH-L3, Rod #4; longitudinal changing of circumferential strain (top); azimuthal diameter downwards from burst (bottom). Spikes: thermocouple.	96
Figure 73	QUENCH-L3 , Rod #5; longitudinal changing of circumferential strain (top); azimuthal diameter downwards from burst (bottom).	97
Figure 74	QUENCH-L3, Rod #6; longitudinal changing of circumferential strain (top); azimuthal diameter downwards from burst (bottom).	98
Figure 75	QUENCH-L3, Rod #7; longitudinal changing of circumferential strain (top); azimuthal diameter downwards from burst (bottom).Spikes: thermocouples.....	99
Figure 76	QUENCH-L3, Rod #8; longitudinal changing of circumferential strain (top); azimuthal diameter downwards from burst (bottom).	100
Figure 77	QUENCH-L3, Rod #9; longitudinal changing of circumferential strain (top); azimuthal diameter downwards from burst (bottom).	101
Figure 78	QUENCH-L3, Rod #10; longitudinal changing of circumferential strain (top); azimuthal diameter downwards from burst (bottom).	102
Figure 79	QUENCH-L3, Rod #11; longitudinal changing of circumferential strain (top); azimuthal diameter downwards from burst (bottom). Spikes: thermocouple.	103
Figure 80	QUENCH-L3, Rod #12; longitudinal changing of circumferential strain (top); azimuthal diameter downwards from burst (bottom).	104
Figure 81	QUENCH-L3, Rod #13; longitudinal changing of circumferential strain (top); azimuthal diameter downwards from burst (bottom).	105
Figure 82	QUENCH-L3, Rod #14; longitudinal changing of circumferential strain (top); azimuthal diameter downwards from burst (bottom).	106
Figure 83	QUENCH-L3, Rod #15; longitudinal changing of circumferential strain (top); azimuthal diameter downwards from burst (bottom). Spikes: thermocouple.	107
Figure 84	QUENCH-L3, Rod #16; longitudinal changing of circumferential strain (top); azimuthal diameter downwards from burst (bottom).	108
Figure 85	QUENCH-L3, Rod #17; longitudinal changing of circumferential strain (top); azimuthal diameter downwards from burst (bottom).	109
Figure 86	QUENCH-L3, Rod #18; longitudinal changing of circumferential strain (top); azimuthal diameter downwards from burst (bottom).	110
Figure 87	QUENCH-L3, Rod #19; longitudinal changing of circumferential strain (top); azimuthal diameter downwards from burst (bottom).Spikes: thermocouples.....	111
Figure 88	QUENCH-L3, Rod #20; longitudinal changing of circumferential strain (top); azimuthal diameter downwards from burst (bottom).	112
Figure 89	QUENCH-L3, Rod #21; longitudinal changing of circumferential strain (top); azimuthal diameter downwards from burst (bottom).	113
Figure 90	Axial distribution of coolant channel blockage for QUENCH-L1 and -L3 bundles.	114
Figure 91	QUENCH-L3: results of eddy-current measurements of axial layer thickness distribution for claddings of inner rods.....	115

Figure 92	QUENCH-L3: results of eddy-current measurements of axial layer thickness distribution for claddings of outer rods.	115
Figure 93	QUENCH-L3; ultrasound measurement of wall thickness for rod #6 with corresponding results of neutron radio- and tomography.	116
Figure 94	QUENCH-L3; Neutron radiographs of inner rods: hydrogen bands above burst openings and hydrogen spots below burst openings.....	117
Figure 95	QUENCH-L3; Neutron radiographs of outer rods	118
Figure 96	QUENCH-L3; tomography of rod #1: correspondence between long section (view from burst opening) and cross sections (bottom view); left - features of burst opening, right - areas with high hydrogen concentration (light segments).....	119
Figure 97	QUENCH-L3; tomography of rod #6: correspondence between long section (view from burst opening) and cross sections (bottom view); left - features of burst opening, right - areas with high hydrogen concentration (light segments).....	120
Figure 98	QUENCH-L3; tomography results for inner rods: hydrogen bands above burst opening and hydrogen spots below burst opening.	121
Figure 99	QUENCH-L3; outer rods: absence of hydrogen bands.....	122
Figure 100	QUENCH-L3; correspondence between videoscope observations and tomography for rods #4 and #5: hydrogen spot at the position of contact between pellet and cladding below burst opening.	123
Figure 101	QUENCH-L3; correspondence between videoscope observations and tomography for rod #6: hydrogen band at the position of slightly oxidised inner cladding surface.	124
Figure 102	QUENCH-L3; correspondence between reconstruction of tomography image and plots of mean and maximal hydrogen concentrations in rod #2, plots adjusted to edges of burst opening.	125
Figure 103	QUENCH-L3; correspondence between reconstruction of tomography image and plots of mean and maximal hydrogen concentrations in rod #3, plots adjusted to edges of burst opening.	126
Figure 104	QUENCH-L3; correspondence between reconstruction of tomography image and plots of mean and maximal hydrogen concentrations in rod #4, plots adjusted to edges of burst opening.	127
Figure 105	QUENCH-L3; correspondence between reconstruction of tomography image and plots of mean and maximal hydrogen concentrations (calculated for each cross section slice of 40 μm width) in rod #5, plots adjusted to edges of burst opening.	128
Figure 106	QUENCH-L3; correspondence between reconstruction of tomography image and plots of mean and maximal hydrogen concentrations in rod #6, plots adjusted to position of the grease spot at the burst opening edge.	129
Figure 107	QUENCH-L3; Comparison of two methods of hydrogen concentration measurement for rod #6: neutron tomography and hot extraction.....	130
Figure 108	QUENCH-L3; correspondence between reconstruction of tomography image and plots of mean and maximal hydrogen concentrations (calculated for each cross section slice of 40 μm width) in rod #7, plots adjusted to edges of burst opening.	131

Figure 109	QUENCH-L3; correspondence between reconstruction of tomography image and plots of mean and maximal hydrogen concentrations (calculated for each cross section slice of 40 μm width) in rod #8, plots adjusted to edges of burst opening.	132
Figure 110	QUENCH-L3; correspondence between reconstruction of tomography image and plots of mean and maximal hydrogen concentrations (calculated for each cross section slice of 40 μm width) in rod #9, plots adjusted to edges of burst opening.	133
Figure 111	QUENCH-L3; correspondence between reconstruction of tomography image and plots of mean and maximal hydrogen concentrations (calculated for each cross section slice of 40 μm width) in rod #10, plots adjusted to edges of burst opening.	134
Figure 112	QUENCH-L3; positions of 4 cladding segments of rod #6 for hot extraction.....	135
Figure 113	QUENCH-L3; positions of 4 cladding segments of rod #5 for XRD analysis (2 segments at the line of the burst opening and 2 segments at the opposite side).	136
Figure 114	QUENCH-L3; XRD analysis of rod #5 at the elevations of hydrogen band: ϵ -, and γ -hydrides and β -Zr (due to Nb) inside the band at opening front and at opposite side of opening. ..	137
Figure 115	QUENCH-L3; XRD analysis of rod #5 at the elevations of hydrogen spot: ϵ -, δ -, and γ -hydrides and β -Zr (due to Nb) inside the spot and at the cladding side opposite to spot. .	138
Figure 116	QUENCH-L3; results of tensile tests with claddings of the inner rod group.	139
Figure 117	QUENCH-L3; results of tensile tests with claddings of the outer rod group.	140

Introduction

Under the licensing procedures for pressurized water reactors (PWR) evidence must be given that the impacts of all pipe ruptures, hypothetically occurring in the primary loop and implying a loss of coolant, can be controlled when the other cooling lines are not available. The double-ended break of the main coolant line between the main coolant pump and the reactor pressure vessel is considered to constitute the design basis for the emergency core cooling system (ECCS) in a loss-of-coolant accident (LOCA). The break of a coolant line leads to the loss of coolant in the primary circuit of a PWR and the decrease in system pressure from 15.5 MPa to eventually around 0.32 MPa (boiling point, corresponding to 135 °C). Consequently, the remaining coolant in the core as well as the emergency cooling water fed into the reactor core evaporate, the temperature of the fuel elements rises and the fuel rods start to balloon since they contain pressurized filling gas and fission gas products. At temperatures above 700 °C, the load within the metallic wall of cladding reaches a critical value and the most ballooned section finally bursts.

Upon rupture of the reactor coolant line the reactor is shut down. However, as the production of decay heat will be continued, reliable sustainment of the reactor core rod geometry and long-term emergency cooling of the core are required. To retain the core rod geometry the cladding embrittlement increasing during oxidation in steam has to be limited to an acceptable value. The current LOCA criteria and their safety goals are applied worldwide with minor modifications since the NRC release in 1973 [1, 2]. The criteria are given as limits on peak cladding temperature ($T_{PCT} \leq 1200$ °C) and on oxidation level ECR (equivalent cladding reacted) calculated as a percentage of cladding oxidized ($ECR \leq 17\%$ using the Baker-Just oxidation correlation). These two items constitute the criterion of cladding embrittlement due to oxygen uptake and, according to the RSK (Reactor Safety Commission) Guidelines, are included in the current German LOCA criteria, too [3].

The results elaborated worldwide in the 1980's on the Zircaloy-4 (Zry-4) cladding tubes behavior (oxidation, deformation and bundle coolability) under LOCA conditions constitute a reliable data base and an important input for the safety assessment of LWRs. With respect to the LOCA conditions for German LWRs, different out-of-pile with more prototypical internal heating [4, 8] and outer heating [5, 6], the FR2 in-pile [7] single rod as well as the REBEKA out-of-pile bundle tests [9, 10] were performed. It was concluded that the ECC-criteria established by licensing authorities are conservative and that the coolability of an LWR and the public safety can be maintained in a LOCA [11]. In-pile test data (with burn-up up to 35 MWd/kgU) were consistent with the out-of-pile data and did not indicate an influence of the nuclear environment on cladding deformation.

Due to major advantages in fuel-cycle costs, optimised reactor operation, and waste management, the current trend in the nuclear industry is to increase fuel burn-up. At high burn-up, fuel rods fabricated from conventional Zry-4 often exhibit significant oxidation, hydriding, and oxide spallation. Thus, fuel vendors have developed and proposed the use of new cladding alloys, such as Duplex DX-D4, M5[®], ZIRLO™ and other. Therefore, it is important to verify the safety margins for high burn-up fuel and fuel claddings with advanced alloys. In recognition of this, LOCA-related behaviour of new types of cladding is being actively investigated in several countries [12, 13]. Due to the long cladding hydriding period for the high fuel burn-up, post-quench ductility is not only influenced by oxidation, but also significantly depending on the hydrogen concentration. Consequently, the 17% ECR limit is inadequate to ensure post-quench ductility at hydrogen concentrations higher than ≈ 500 wppm [14]. Due to so-called secondary hydriding (during oxidation of inner cladding surface after burst), which was firstly observed by JAERI [15], the hydrogen content can reach 4000 wppm in Zircaloy cladding regions around the burst [16].

Particularly to investigate the influence of the secondary hydriding phenomena on the applicability of the embrittlement criteria for the German nuclear reactors, it was decided to perform the QUENCH-LOCA bundle test series in the QUENCH facility of KIT, supported by the association of the German utilities (VGB). Additionally, the QUENCH-LOCA bundle tests could support experiments performed in-pile and in-cell, respectively, e.g. single-rod tests as those planned in the OECD SCIP-2 project [17]. Compared to single-rod

experiments, bundle tests have the advantage to study the mutual interference of rod ballooning among fuel rod simulators as well as to take into account the local coolant channel blockages in this more realistic arrangement.

The first test QUENCH-L0 was performed with Zry-4 cladding tubes not pre-oxidised on July 22, 2010 as commissioning test and terminated with reflood immediately after the transient phase [18, 19]. The QUENCH-L1 test was performed on February 02, 2012 as reference test, using a similar bundle compared to the QUENCH-L0 test but including a cool-down phase between transient and reflood [20, 21]. The present report describes the results of the experiment QUENCH-L3 with as-received optimised ZIRLO™ claddings; the experiment was conducted at KIT on March 17, 2015.

1 Description of the Test Facility

The QUENCH facility was constructed 1997 at KIT for the investigation of the hydrogen source term during reflood, i.e. of the measurement of hydrogen release during the reflood of an overheated reactor core. Since then 17 bundle tests were performed under severe accident conditions ([Table 1](#)). The main components of the QUENCH test facility are presented in [Fig. 1](#). The test section is enclosed by a safety containment with a wall thickness of 5.6 mm and an inner diameter of 801.8 mm. The facility can be operated in two modes: a forced-convection mode depicted in the flow diagram of [Fig. 2](#) and a boil-off mode. In the forced-convection mode (relevant for QUENCH-L3) superheated steam from the steam generator and superheater together with argon as a carrier gas enter the test bundle at the bottom ([Figs. 3 and 4](#)). The system pressure in the test section for the QUENCH-LOCA tests is about 0.3 MPa. The argon, steam and hydrogen produced in the zirconium-steam reaction flow upward inside the bundle and from the outlet at the top through a water-cooled off-gas pipe to the condenser where the remaining steam is separated from the non-condensable gases argon and hydrogen. The water cooling circuits for bundle head and off-gas pipe are temperature-controlled to guarantee that the steam/gas temperature is high enough so that condensation at the test section outlet and inside the off-gas pipe can be avoided. The temperature of the cooling water in the bundle head is kept at 348 K, and the water flow rate is 250 g/s.

The off-gas pipe consists of water-cooled pipes with a counter-current flow (flow rate of 370 g/s) and inner pipe. The inlet temperature of cooling water is controlled at 393 K. Between the off-gas pipe and inner pipe there is stagnant off-gas. The main dimensions of the tubes that make up the off-gas pipe are:

- Inner pipe: outer diameter 139.7 mm, wall thickness 4.5 mm; total length 3256 mm, material: stainless steel;
- Inner cooling pipe: outer diameter 154 mm, wall thickness 2 mm, material: stainless steel;
- Outer cooling pipe: outer diameter 168.3 mm, wall thickness 5 mm, material: stainless steel.

The quenching water is injected into the bundle through a separate line marked “bottom quenching” in [Fig. 4](#).

1.1 The test bundle

The design characteristics of the test bundle are given in [Table 2](#). The test bundle is made up of 21 fuel rod simulators, each with a length of approximately 2.5 m, and of four corner rods (see cross section in [Fig. 5](#)). Insertion of four corner rods avoids an atypically large flow cross section at the outer positions and hence helps to obtain a rather uniform radial temperature profile. The fuel rod simulators ([Fig. 6](#)) are held in their positions by five grid spacers made of ZIRLO. This bundle design is applied with a pitch of 14.3 mm. All test rods are heated electrically over a length of 1900 mm (thereof 1024 mm in the middle with W heater and residual length with Mo heaters at rod ends).

1.1.1 Claddings

Unlike the QUENCH-L0 and -L1 experiment with fresh Zry-4 claddings, the QUENCH-L3 test was performed with fresh optimised ZIRLO claddings. The properties of this cladding are listed in [Table 3](#).

1.1.2 Heaters and electrodes

Tungsten (chemically clean tungsten) heating elements of 4.6 mm diameter are installed in the center of rods. W heaters with this small diameter were used for the first time in the QUENCH-L2 experiment. Their higher electrical resistance in comparison to tungsten heaters of 6 mm diameter (used for commissioning test QUENCH-L0) results in higher maximum heating rates, especially during the first transient phase and hence to

a more prototypical test conduct. The tungsten heaters with a diameter of 4.6 mm produce a similar heat amount as the tantalum heaters with a diameter of 6 mm (used for the QUENCH-L1 test), but they are more rigid at high temperatures. These heaters are surrounded by annular yttria-stabilized ZrO₂ pellets. The physical properties of the ZrO₂ pellets are described in [Table 4](#).

The tungsten heaters are connected to molybdenum heaters (chemically clean molybdenum) and copper electrodes (material 2.1293 with Cr 0.8, Zr 0.08 and balance Cu) at each end of the W heater. The molybdenum heaters and copper electrodes are joined by high-frequency/high-temperature brazing under vacuum (2×10^{-3} mbar) using an AuNi 18 powder (particle size $< 105 \mu\text{m}$). For electrical insulation the surfaces of both joint parts are plasma-coated with 0.2 mm ZrO₂ layer. They are water-cooled (lower and upper cooling chambers filled with demineralized water) to protect the copper electrodes and the O-ring-sealed wall penetrations against excessive heat.

The copper electrodes are connected to the DC electric power supply by means of special sliding NiBe (Au coated) contacts at the top and bottom. The total heating power is limited by a maximal current of 7200 A and voltage of 9 V. Two DC-generators were used for two groups of rods connected in parallel: 1) 10 internal rods: #1...#9 and rod #15; 2) 11 external rods: #10...#14 and #16...#21. The electrical resistance of the rod heating system, combined of W and Mo heaters as well as Cu alloy electrodes, was measured before (at the end of bundle assembling) and after the test ([Table 5](#)). The electric resistance of a single heater (W+Mo+Cu sections) measured at room temperature was about 5 mΩ before and after the test. The additional resistance of the external electric circuit between the axial end of the single heater and the connection to the generator (sliding contacts, cables, and bolts) is 3.75 mΩ for the inner rod group and 4.05 mΩ for the outer rod group. These values can be taken as constant because the external electric circuit remains at ambient temperature throughout the experiment.

1.2 Bundle surroundings

The bundle is surrounded by a 3.17 mm thick shroud (79.66 mm ID) made of the Zr702 alloy. This part has two functions: 1) The shroud acts as steam and gas guide tube; 2) It simulates an adiabatic surrounding of the reactor core. The consideration of heated rod claddings, corner rods and shroud, manufactured from similar zirconium alloys, results in the surface of 30.6 effective rod simulators. The shroud is surrounded by a 36 mm thick ZrO₂ fibre insulation (physical properties are given in [Table 6](#)) and an annular cooling jacket made of Inconel 600 (inner tube) and stainless steel (outer tube; see [Fig. 5](#)). The annulus between shroud and cooling jacket was filled (after several cycles of degasing) with stagnant argon of about 0.3 MPa ([Fig. 19](#)) and was connected to a flow-controlled argon feeding system in order to prevent steam access to the annulus after possible shroud failure. The 6.7 mm annulus of the cooling jacket is cooled by an argon flow. Above the heated zone, i.e. above the 1024 mm elevation there is no ZrO₂ fibre insulation to allow for higher radial heat losses. This region of the cooling jacket is cooled by a water flow ([Figs. 3 and 4](#)). Both, the lack of ZrO₂ insulation above the W heaters and the water cooling, force the axial temperature maximum downward.

The lower boundary for the lower cooling chamber is a sealing plate made of stainless steel with plastic inlays for electrical insulation, sealed toward the system by O-shaped rings. The upper boundary of the lower cooling chamber is a sealing plate of stainless steel. An insulation plate made of plastic (PEEK) forms the top of the upper cooling chamber, and a sealing plate of Al₂O₃, functioning as a heat-protection shield, is the lower boundary of the upper cooling chamber (see [Fig. 6](#)).

In the region below the upper Al₂O₃ plate the copper electrode is connected firmly to the cladding. This is done by rotary swaging the cladding onto the electrode. In the swaging region a sleeve of boron nitride is put between electrode and cladding for electrical insulation. The axial position of the fuel rod simulator in the test bundle is fixed by a groove and a locking ring in the top Cu electrodes. Referred to the test bundle the fixing point of the fuel rod simulators is located directly above the upper edge of the upper insulation plate. So, during operation the fuel rod simulators are allowed to expand downwards. Clearance for expansion of the

test rods is provided in the region of the lower sealing plate. Also in this region, relative movement between cladding and internal heater/electrode can take place.

1.3 Rod pressurization

All fuel rod simulators were separately pressurized. The gas supply system (Fig. 7) for individual pressurization of rods consists of pressure controller, 21 valves, 21 pressure transducers, and 21 justified compensation volumes for simulation of prototypic plenum volumes of 31.5 cm³. The gas supply is connected with capillary tubes (with inner diameter 1 mm, length ca. 1.2 m) to each rod at its lower end via drill axial holes in the copper electrodes (Fig. 8). The gas gap between the cladding and the Cu/Mo parts and the W heater/ZrO₂-pellets is 0.15 mm and 0.075 mm, respectively.

Before gas filling, the rods and the gas supply system were evacuated. At the beginning of experiment, the fuel rod simulators were backfilled with Kr gas to 30 bar. Then, before the transient, they were separately pressurized to the target pressure of 55 bar as shown in Fig. 9.

2 Test Bundle Instrumentation

A list of all instruments for the experiment QUENCH-L3, which were installed in the test section and at the test loop is given in Table 7. The distribution of the thermocouples along the bundle is shown in Table 8. No failed thermocouples were detected during the test.

2.1 Thermocouples

The test bundle was instrumented with sheathed thermocouples (TC) attached to the rod claddings (Fig. 10) at 17 different elevations between -250 mm and 1350 mm and at different orientations according to Figs. 11 and 12. The NiCr/Ni thermocouples (1 mm diameter, stainless steel sheath 1.4541 (X6CrNiTi18-10), MgO insulation) are used for temperature measurement at rod cladding and shroud outer surfaces. The TC tip is held in place by a Zr ferrule welded to the surface. The cables of the rod-thermocouples from the -250 mm to the 850 mm level leave the test section at the bottom whereas those of the TCs above 850 mm are routed out on the top of the test section to prevent TC cables passing the hot zone. On the same account the cables of the shroud-thermocouples in this region are routed outside the isolation. The thermocouples are designated as following:

- “TFS” for the thermocouples attached to the outer surface of the rod claddings;
- “TSH” for the shroud thermocouples mounted at the outer surface between -250 mm and 1250 mm;
- “TIT” for the thermocouples installed inside the Zry-4 instrumentation rods at the three corner positions of the bundle (positions A, C and D) (see Fig. 13);
- “TCI” for the thermocouples at the cooling jacket are installed inside the wall of the inner cooling tube (from 550 mm to 1150 mm, designation).

2.2 Gas Measurement System

The flow rates of noble gases (Ar, Kr) are regulated with the BRONKHORST flow controllers. Steam and water flows are controlled with the SIEMENS flow controllers. Numerous pressure transmitters from WIKA measure absolute and differential pressures along the gas supply system, at inlet and outlet of the test section.

The outlet steam and released hydrogen are analyzed by a Balzers mass spectrometer (MS) "GAM 300" (Fig. 14). Due to its location at the off-gas pipe in the facility the mass spectrometer responds almost immediately (less than 10 s). The "BALZERS GAM 300" is a completely computer-controlled quadrupole MS with an 8 mm rod system which allows reliable quantitative measurement of gas concentrations down to about 10 ppm. For the MS measurement a sampling tube is inserted in the off-gas pipe located approx. 2.7 m downstream from the test section outlet (see Fig 2 and 4). It has several holes at different elevations to guarantee that the sampling of the gas to be analyzed is representative (see Fig. 15). To avoid steam condensation in the gas pipes between the sampling position and the MS the temperature of the gas at the MS inlet is controlled by heating tapes to about 150 °C (the upper operating temperature of the MS inlet valves). This allows the MS to analyze the steam production rate. Besides, the concentrations of the following species were continuously measured by the mass spectrometer during all test phases: argon, hydrogen, steam, nitrogen, oxygen, and krypton. The fuel rod simulators are filled with krypton which can be used as an indicator for cladding failure. Additionally, the MS is used to control the atmosphere in the facility, e.g., to monitor the gas composition at the beginning of the test.

The temperature and pressure of the analyzed gas are measured near to the inlet valve of the MS. The MS is calibrated for hydrogen with well-defined argon/gas mixtures and for steam with mixtures of argon and steam supplied by a BRONKHORST controlled evaporator mixing (CEM) device. The MS off-gas is released into the atmosphere because the amount of sampling gas taken out of the system is negligible. A heated measuring gas pump was used to ensure a continuous flow of the steam-gas mixture from the off-gas pipe to the mass spectrometer.

By the MS the mass flow rate of each gas species is calculated by referring the measured gas concentration to the known argon mass flow rate according to equation:

$$\dot{m}_G = \frac{M_G}{M_{Ar}} \cdot \frac{C_G}{C_{Ar}} \cdot \dot{m}_{Ar} \quad (1)$$

with M representing the molecular masses, C the concentrations in vol% and \dot{m} the mass flow rates of the corresponding gases.

3 Data Acquisition and Process Control

A LabView-based control and data acquisition system is used in the QUENCH facility. Data acquisition, data storage, online visualization as well as process control, control engineering and system protection are accomplished by three computer systems that are linked in a network.

During the QUENCH-L3 test the data acquisition system recorded all measurement channels at a frequency of 5 Hz per channel. The experimental data and the date and time of the data acquisition are stored as raw data in binary format. After the experiment the raw data are converted into SI units and stored as ASCII data.

For process control, a system flow chart with the most important actual measurement values is displayed on the computer screen. Furthermore, the operating mode of the active components (pumps, steam generator, superheater, DC power system, valves) is indicated. Blocking systems and limit switches ensure safe plant operation. Operating test phases, e.g. heating or quenching phases, are pre-programmed and can be started on demand during the experiment. The parameter settings of the control circuits and devices can be modified online.

Online visualization allows to observe and to document the current values of selected measurement positions in the form of tables or line graphs. Eight diagrams with six curves each can be displayed as graphs. This means

that altogether 48 measurement channels can be selected and displayed online during the course of the experiment.

The data of the main data acquisition system and of the mass spectrometers are stored on different computers. Both computers are synchronized. The data of the mass spectrometer data are recorded at a frequency of approx. 0.8 Hz during the entire test.

4 Test Performance and Results of Online Measurements

The test procedure was based on pre-test calculations for the QUENCH-LOCA series performed by the Paul Scherrer Institute (PSI, Villigen). According to the planned LOCA scenario, the transient phase should be performed with 8 K/s followed by slow cool-down phase and quenching.

The sequence of the test events is represented in [Table 9](#). The experiment started by stabilizing the bundle conditions with an application of electrical bundle power of 3.6 kW (corresponding to a linear heat rate of approx. 1 W/cm) in 6 g/s (specific rate 0.2 g/s/(effective rod)) argon plus 2 g/s (specific rate 0.07 g/s/(effective rod)) superheated steam resulting in maximum bundle temperatures of approximately 845 K ([Fig. 16](#)). During this stabilization phase the rod internal pressure was increased to 55 bar. The bundle was kept at this peak cladding temperature and pressure for 355 s before the start of the transient. The current and voltage progression during the test are depicted in [Fig. 17](#).

The transient was initiated (at $t = 0$ s) by rapidly increasing the electrical power to 41 kW (linear heat rate ≈ 9 W/cm) reached after 3.6 s and followed by steady increase to 60 kW (linear heat rate ≈ 13 W/cm) within the next 42 s, and stayed at that level for the rest of the transient (until 75.8 s after transient start). During this period the peak cladding temperature increased from their initial values to 1300 K. Due to limitation of the maximal electrical current of the DC generators the average heatup rate at the maximum temperature location was 6.3 K/s. The experiment continued with a power decrease to 3.5 kW at 75.8 s to simulate decay heat and injection of steam at a nominal of 20 g/s. The cladding temperatures increased to a maximum of 1346 K at 81.8 s, followed by steady cooling to about 920 K (at elevation 850 mm) and 950 K (elevation 950 mm). The cooling phase was terminated at 217 s by quenching with up to 100 g/s water injection. There was a period of about 40 s while the lower volume was being filled during which time the temperatures increased somewhat in the absence of significant flow. The first quench occurred at the bottom of the bundle at 235 s. Quenching progressed readily toward the top, and the first quench in the ballooned region occurred at 278 s ([Table 10](#)). Complete quench was achieved at 295 s.

Oscillation of the gas pressures during the whole test are presented in [Figs. 18, 19](#). [Fig. 20](#) shows the water flow characteristics. Mass spectrometer data on steam registration (during steam supply and evaporation phases), hydrogen production (due to oxidation of bundle and shroud) and krypton release (due to failure of claddings) are presented in [Fig. 21](#).

The readings of thermocouples at each bundle elevation are shown in [Figs. 22 – 38](#). The temperatures of cooling jacket were practically not changed during the whole test ([Fig. 39](#)). The axial temperature profile in the bundle has a pronounced maximum between 850 and 1050 mm ([Figs. 40 – 43](#)). For each bundle elevation there is also a radial temperature gradient due to two reasons: 1) radial heat flux to the shroud, 2) electrical power supplied to the internal rod group was higher than the power for the external group because both DC generators reached their current limit (≈ 3600 A) but the electrical resistance of the 11 external rods connected in parallel is lower than for the 10 internal rods. The temperature homogeneity inside one rod group (internal and external rods) depends on bundle geometry. [Fig. 44](#) compares the QUENCH-L3 thermocouple readings at the hottest elevations with corresponding readings during the reference test

QUENCH-L1. The temperature scatter inside certain elevation is noticeable lower for QUENCH-L3 due to less bending of rods (increased bending for QUENCH-L1 occurred mostly due to limited possibility for the axial elongation).

Two additional (in comparison to the reference test QUENCH-L1) thermocouples TFS 7/12i and TFS 7/13i installed at the cladding surface of rod #7 at the azimuthal position adjacent to the central rod #1 (i.e. opposite to thermocouples TFS 7/12 and TFS 7/13) allowed the registration of radial temperature gradients at the hottest elevations (Fig. 45). According to the REBEKA burst criterion [9], the azimuthal temperature difference has the dominant influence on the circumferential burst strain. Significant azimuthal temperature difference can be developed during the transient not only due to global radial temperature gradient across the bundle (heat loss through the shroud), but also due to non-coaxial positioning of pellets and cladding [4]. The highest temperature was achieved at the contact between pellet and cladding (absence of gas gap with relatively low heat conductivity). The temperature difference between this contact position and opposite cladding side increased during ballooning process, which occurred in such manner that the gas gap at the cold side increased whereas no gas gap formed at the hot side before burst. This effect was detected by in-situ X-ray observation [4, 11] and confirmed by QUENCH-L3 post-test neutron tomography.

Both the increasing ductility and decreasing creep strength of the heated cladding resulted in a progressive ballooning and consequent burst of all of the rods (Table 11). During the ballooning development at the hottest elevation, the ballooning can be developed before the cladding burst also at higher and lower bundle positions due to achievement of temperature threshold for ballooning onset (Figs. 46 - 49). The first burst occurred 47.8 s after transient initiation for inner rod #01 at about 1103 K, according to the thermocouple reading at the adjacent rod #07. All rods failed within the next 20 s (Fig. 50). The time frame of rod failures as indicated by internal pressure readings correlated with the time frame of the krypton signal measured in the off-gas by mass spectrometer (Fig. 21).

There was a small amount of oxidation during the experiment, resulting in approximately 0.6 g hydrogen released during the high temperature period, including the period of rod burst and shortly after (Fig. 21). Some of the hydrogen produced is expected to have been taken up by inner surface of the cladding after burst.

5 Posttest Examinations

Posttest Examinations (PTE) included nondestructive methods (optical bundle observations, laser profilometry of all claddings, ultrasound cladding wall thickness measurements, eddy current measurements of outer layers of claddings, neutron radio- and tomography) as well as destructive investigations (tensile tests, metallography, fractography, XRD).

5.1 Optical Observation of Cladding Surfaces

First observations of burst positions were performed immediately after the test by means of an OLYMPUS videoscope. The camera of the videoscope (diameter 6 mm, total cable length 9 m) was introduced through the bundle bottom at positions of withdrawn corner rods (Figs. 51 - 54). For the peripheral rods no contacts between adjacent claddings due to ballooning or rod bending were observed. All observed thermocouples remained intact after the test.

The bundle was withdrawn from the shroud for further investigations. No noticeable changes of bundle geometry were indicated (Figs. 55 and 56). Grid spacers were removed for the separation of the single rods. The surface of the claddings is mostly shining black, only the regions around the burst openings are matte black (Figs. 60 and 61) due to surface micro cracks (Figs. 66-68) formed during ballooning. No rod bending was observed in the plane with overhead view to burst opening. For the plane with the side view of openings only

negligible rod bending was observed for the inner rods and some of the outer rods with values less than 3 mm deviation from original rod axis.

The shape of burst openings of all rods is quite similar, whereas their geometry varies widely (Fig. 57). The lengths of openings varied between 12 and 20 mm, the width between 2.6 and 6.2 mm, and the opening areas determined by image analyses are 17 - 67 mm² (Table 11). The tangential burst positions of all rods correspond to the hottest rod region and are directed mostly to the bundle centre (Fig. 58). All bursts are axially located between 890 and 970 mm (Fig. 59). No global blockage was formed due to relatively small cladding strengths and due to the variation of the axial ballooning positions.

Observations of the cladding surface were performed with a Keyence digital microscope equipped with a macroscopic objective. The shapes of burst openings are shown in Figs. 62 - 65. Figs. 66 - 68 illustrate the structure of oxidized cladding surfaces near to the opening of rod #1. It can be seen that the cladding surface is covered with a network of crossed longitudinal cracks developed during the ballooning process. A large-scale crack cells network is located near to the burst opening, whereas small-scale cells are typical for the cladding side opposite to burst. The cell sizes change not only circumferentially, but also longitudinally: they decrease with increasing distance to the burst location. The cell size strongly depends on strain: the higher the strain the larger are the cells.

The inner surface of three claddings was investigated by videoscope (Figs. 100 - 101). Typical traces of contact between pellet and cladding slightly below the burst opening were observed. Similar observations were made previously also for some claddings of the QUENCH-L2 bundle and confirmed the early suggestions [4] that relatively often the burst occurs at the position of contact between pellet and cladding. Due to absence of the gas gap, the heat transport from pellet to cladding is the highest at this circumferential position. Concerning the gas penetration to these contact spots, the corresponding surface areas were not oxidised because access of steam was not possible to this area. Because the metal in these areas is not covered by oxide layer, the hydrogen, which has a higher diffusivity than steam penetrating very narrow gaps, can be absorbed at these contacts between pellet and claddings.

5.2 Profilometry of Claddings with Laser Scanner

5.2.1 Linear Laser Scanning

The profilometry of the rods was performed with a Linear Laser Scanner made by ANT Antriebstechnik GmbH for quantifying the deformations produced on the rods as a result of the QUENCH-LOCA experiments. The ballooned parts of the bundle rods exposed to LOCA scenarios acquire a variety of shapes and sizes due to different temperature conditions. Therefore a precise method to detect the local variations in diameter along the rods was required.

5.2.2 Main Characteristics of the Measuring Device and Procedures

The measuring mechanism is based upon photocells which compare the amount of laser light blocked by the rod in relation to the portion of light that reaches the sensors. The equipment is mounted vertically and supported on a wall of the experimental hall in order to minimize the effects of shocks and vibrations propagated by the floor. The rod to be measured is placed vertically and linked to a step motor which ensures the precise turning of the rod according to a given number of measurements that should be made during a rotation of 360°. A resolution of 0.25° is provided. The laser scanner itself moves a predetermined length up or down the driving rails in order to cover a specific section of the examined rod. The smallest vertical step is 100 µm and the maximum length which the scanner can handle is 2000 mm.

Automatic settings allow the scanner to work for many hours without the need of supervision. For safety reasons and because of mechanical limitations, the data gathering is quite slow. A total of approximately 5700

points are measured each hour. This means that a scanning of a 1500 mm rod section takes roughly 4 days considering a measurement every 1 mm and 1°.

All data generated can be processed in various ways in order to determine different information. For instance, it allows the exact location and orientation of each burst, determination of radial strain, calculation of cross-section area reduction and thus blockage. Also, a digital 3D rendered image is generated as a record and for further analysis, since every rod is sooner or later damaged by mechanical testing or cut for metallographic examination.

5.2.3 Results of the Scans

The evaluation of the scans can be divided into azimuthal and longitudinal analysis.

The azimuthal plots ([Figs. 69 - 89, bottom](#)) clearly show the orientation of the bursts and also give an idea of the shape. It was revealed that the bursts were mostly oriented to the center of the bundle, mainly because of the radial thermal gradient which was established in the test section. The maximal cladding diameter was observed in the burst plane, the minimal diameter – in the perpendicular plane. It is also to be seen, that immediately below and above the burst opening the maximal diameter was measured in the plane perpendicular to the burst plane. All azimuthal plots illustrate this fact: the neighboring elevations lower the burst evident the maximal diameter in the plane perpendicular to the burst. I.e. during ballooning and immediately before burst, the cladding extends here more in the directions perpendicular to the burst plane.

The shape of the bursts vary widely, neither size nor symmetry have any apparent correlation to burst temperature.

Also based on these scans, the circumferential strains can be determined ([Table 12](#)), which are depicted on [Figs. 69 - 89, top](#). There is a clear correlation of the burst location (position with a largest strain) and the temperature distribution on the longitudinal axis. Maximum strain of 36.8% was observed on the inner rod #6, minimum strain of 20.0% was observed on the outer rod #18.

For all rods the deformation starts at elevations about 250 mm and ends at 1250 mm. The axial extension of cladding region with more than 5% strain is usually shorter than 185 mm. It is worth to notice that besides the main strain maximum some of the rods (#4, #6, #9, #10, #11, #15, #18 - #21) have a second (or sometimes even third) strain maximum located ≈100 mm (or ≈200 mm) below or above main maximum. I.e. the ballooning was initiated at many axial locations inside the hot zone. The second balloon regions were observed also for several rods of the QUENCH-L2 test. The intensity and extension of ballooning were comparable for both bundle tests.

The blockage is the quotient of total increase of the rod cross-sections divided by initial empty area inside the inner surface of the shroud. Since the burst locations are scattered between elevations 901 and 962 mm ([Table 11](#)), the blockage wasn't too significant. As shown in [Fig. 90](#), the maximum blockage occurs at about 922 mm and reaches 21% of area reduction. If, hypothetically, all burst were located at the same level, the blockage would be 38%.

5.3 Nondestructive Eddy Current and Ultrasound Measurements

Before cutting the cladding tubes for further investigations, some analyses had to take place. The oxidation degree of each cladding was measured by means of the eddy current measurement device ISOSCOPE FMP30 from Helmut Fischer GmbH. The device was calibrated with two plastic foils of 24.3 and 99.3 μm thicknesses, which were disposed at the surface of opt. ZIRLO prototype tube. At least 20 circumferential measurements at each axial position were used to achieve the averaged result. The axial step width was 20 mm. The device shows the distance between the gauge and the internal metallic layer; i.e. the measured values correspond to

the sum of the thicknesses of ZrO_2 and α -Zr(O) layers. The comparison of eddy current results with metallographic results confirms this assumption.

[Fig. 91](#) and [Fig. 92](#) show results of eddy current measurements for the inner and the outer groups of rods respectively. The most oxidized region is between 750 and 950 mm, what corresponds to the axial temperature profile. Irregular thickness changes were observed inside the axial zone with the pronounced ballooning due to deviations of the cladding thickness from the cladding thickness for the original calibration sample.

The thinning of the cladding wall along the line of the burst opening in the ballooned region of the rod #6 was proved by ultrasound measurements ([Fig. 93](#)) performed by the Echometer device from Karl Deutsch GmbH. The wall thickness increases from 400 μm in vicinity of the opening tip to the regular thickness of 725 μm at a distance of about 50 mm.

5.4 Results of Neutron Radiography and Tomography; Analysis of Absorbed Hydrogen.

5.4.1 Basic Principles

Neutron radiography is a powerful tool for the determination of hydrogen concentration and distribution in zirconium alloys [22-26]. Hydrogen can be quantitatively and non-destructively determined with a spatial resolution of up to 40 μm . The method was applied for the post-test hydrogen analysis of selected QUENCH-L3 cladding tubes.

Firstly, a short introduction into neutron radiography will be given. The sample is positioned into a parallel neutron beam. The intensity distribution behind the sample is measured for each pixel. From the intensity the transmission T can be calculated:

$$T(x, y) = \frac{I(x, y) - I_B(x, y)}{I_0(x, y) - I_B(x, y)} \quad (2)$$

where x and y are the coordinates of the pixel position. I , I_0 and I_B are the intensities behind and before the sample and the background intensity, respectively. From the neutron transmission the total macroscopic neutron cross section Σ_{total} can be calculated:

$$\Sigma_{\text{total}}(x, y) = \frac{-\ln(T(x, y))}{s(x, y)} \quad (3)$$

where s is the neutron path length through the material. The total macroscopic neutron cross section is the sum of the total microscopic cross section σ of the isotopes i multiplied with their number density N :

$$\Sigma_{\text{total}}(x, y) = \sum_i \sigma_i \cdot N_i = \underbrace{N_{Zry}(x, y) \overline{\sigma_{Zry}}}_{\Sigma_{\text{samples reserved}}} + N_O(x, y) \sigma_O + N_H(x, y) \sigma_H \quad (4)$$

In the case of steam oxidation of cladding materials it can be assumed that only the amount of oxygen and hydrogen is changed whereas the amount of zirconium and the alloying elements is not influenced significantly.

In order to reconstruct the specimen three-dimensionally, radiography projections have to be taken from different orientations. According to the sampling theorem, the number n of projections is connected with the

spatial resolution (pixel size) d and the radius R of the object circle that fully encompasses the object formed by the rotating of the sample:

$$n = \sqrt{2\pi} \frac{R}{d} \quad (5)$$

5.4.2 Technique

The neutron radiography measurements were performed at the BOA facility at the Swiss neutron source SINQ at Paul Scherrer Institute Villigen. The investigations were performed applying a medium-resolution setup (pixel size 39 μm). The field of view is 80 mm x 80 mm. The samples were scanned through the field of view with a step width of 25 mm. Exposure times of 420 s were applied. The specimens were measured horizontally.

The neutron tomography experiments were performed at Berlin research reactor at the Lise-Meitner-Campus of the Helmholtz Center HZB Berlin. Three samples were measured simultaneously. 400 projections were measured with a pixel size of 40 μm and an illumination time of 3x40 s per projection. A field of view of 102 mm (axial direction) x 102 mm (radial direction) was applied.

5.4.3 Results of Radiography

The investigations comprise measurements of several rods of the QUENCH-L3 test. Because of the uncertainties of the tube wall thickness caused by the plastic deformation as well as the contribution of front and back side of the tube, quantitative information cannot be extracted from one single radiograph alone. However, the radiographies give information about the occurrence of hydrogen enrichments and their positions. For the inner rods, not only the bended hydrogen enriched bands known from the former QUENCH-L0, -L1, -L2 and -L4 tests were found but also hydrogen spots corresponding to contacts between pellets and claddings ([Fig. 94](#)). In the peripheral rods no hydrogen enrichments are obvious ([Fig. 95](#)).

5.4.4 Results of Tomography: Hydrogen Content

In order to obtain quantitative information about the hydrogen concentrations in the claddings, neutron tomography investigations were performed. For the sample reconstruction the MuhRec3 software of PSI Villigen was used. The reconstructed data set was analyzed for each slice (axial cut) using the macro "Background correction" developed at KIT in the software package ImageJ. The different steps of the analysis are

- Sample identification by background correction (definition of threshold value at which it is assumed that the voxel is part of the sample, dilatation of the marked volume to close the sample area, shrinking of the marked volume by the same numbers)
- Additional shrinking of the sample to neglect sample surface positions with increased cross section as an artefact or surface effects like total reflection and refraction.
- Determination of minimum, mean and maximum values in the marked sample volume.

For the experimental setup applied the following correlation was determined:

$$\Sigma_{total} = 0.204 \text{ cm}^{-1} + 2.327 \text{ cm}^{-1} \frac{H}{Zr} \quad (6)$$

This procedure was applied for the reconstructions of QUENCH-L3 rods. All nine inner rods and several outer rods were investigated before the tensile tests. [Figs. 96 and 97](#) show results of tomographical 3D and cross-section reconstructions for the inner rods #1 and #6 correspondingly. [Fig. 98](#) and [Fig. 99](#) illustrate the

tomography results for inner and outer rods correspondingly. The concentration of absorbed hydrogen for relatively cold outer rods was noticeably low (if any) in comparison to inner rods. Fig. 100 illustrates the correspondence between positions of contacts between pellet/cladding and hydrogen spots below burst opening for rods #4 and #5. The videoscope observations above burst opening of the rod #6 showed slightly oxidized cladding inner surface at the location of the hydrogen band (Fig. 101).

The statistical analysis of the tomography data allows determining the axial distribution of hydrogen concentration in the vicinity of burst openings. The resolution of this distribution is very high due to small pixel size (40 μm). Figs. 102 - 106 and 108 - 111 depict distribution of mean and maximal concentrations calculated for each cross section (width of cross section is 40 μm). It can be seen that the mean hydrogen concentration within the burst opening region is about 130 wppm. This value was observed for whole measured section of the outer rod #10, whereas inner rods show an increase of hydrogen content above (hydrogen band) and below (spot) the burst opening. A comparison between inner and peripheral rods indicates that profiled hydrogen enrichments are formed if the temperature exceeds 1273 K. The axial profiles of maximal concentrations are similar to profiles of mean values and shifted by 800 - 900 wppm in comparison to mean curves. The maxima of both curves for each measured rod are represented in Table 13.

The average hydrogen content inside the enriched cladding segments (bands and spots) were measured by *hot extraction* for the rod #6. Fig. 112 depicts the positions of corresponding samples. Similar segments were taken also from claddings opposite to the enriched regions. The corresponding measurement results of hot extraction are collected in Table 14. Comparison of average values determined by hot extraction with integral hydrogen content calculated on the basis of tomography measurements for the corresponding tube segment (Fig. 107) shows very good coincidence between the two measurement methods. However, the advantage of neutron tomography is very fine spatial resolution, whereas the hot extraction method gives only average integral results for relative large tube segments.

5.5 XRD investigations

The rod #5 was investigated by XRD in the region of the hydrogen band (Figs. 113 - 115). The peak positions corresponding to γ - and ϵ -hydrides were indicated. The other interesting observation was the indication of β -Zr, probably stabilized by Nb.

5.6 Mechanical Tests

Tensile tests on relevant cladding sections were performed at room temperature (RT) to determine the residual strength and ductility of QUENCH-LOCA tested claddings, particularly to identify the embrittlement in dependence of the different quench test conditions.

5.6.1 Tensile Test Set-up

The tensile tests were carried out using a universal testing machine from INSTRON (type 4505, 50 kN load cell), equipped with specially developed grip holders. The experiments were performed displacement-controlled with a displacement rate of 2 mm/min at RT. Exact fitting end plugs were mounted to clamp the tubes without deforming their end sections. Since a cladding tested in a QUENCH experiment usually shows an inhomogeneous $\text{ZrO}_2/\alpha\text{-Zr(O)}$ layer thickness along the main tube axis, the specimens were optically subdivided with paint markers to determine both the global and the local axial elongation during a test by using a CCD-camera measurement system. Three cameras were used for the tests to increase the resolution of the optical measurement device. Generally, the initial gauge length l_0 of a specimen was 800 mm and a sample was prepared in that way, that the ballooning section was positioned in the axial center. After the tests, the strain was calculated from the captured pictures by using the Digital Image Correlation and Tracing program

provided by MATLAB [28] and the stress was calculated by using average values of the measured initial inner and outer diameters from the ends of a tube.

5.6.2 Results of the Tensile Tests

One inner rod failed at the positions of thermocouple, the failure of another rod was due to stress concentration at opening middle, whereas others failed after necking. During the tensile tests with outer rods also typical fracture after necking with fracture surfaces perpendicular to the load direction was observed for several rods. However, mostly was observed fracture from (pre)crack tip to (pre)crack tip at which the final crack propagates around a sample. This fracture mode doesn't occur abruptly. In fact one can observe that the onset of failure is driven by strong local deformations, starting at the (pre)crack tips. It is interesting to note, that only claddings from the outer area of the bundle failed in this mode, in parts with remarkable elongations at fracture up to more than 5%.

In general, the elongation at fracture of all QUENCH-L3 tested claddings varies between 4.7 and 15.7%, and the strength at fractures was on average 385 for necking and 496 MPa for stress concentration at opening tips. An overview of all determined mechanical properties is given in [Table 15](#). [Fig. 116](#) and [Fig. 117](#) depict the stress-strain curves of all inner and outer specimens, respectively.

6 Summary and Conclusions

The QUENCH-LOCA-3 (QUENCH-L3) test with as-received opt. ZIRLO™ claddings was performed according to a temperature/time-scenario typical for a LBLOCA in a German PWR with similar test parameters as the QUENCH-LOCA-1 test with fresh Zry-4 claddings: maximal heat-up rate 8 K/s, cooling phase lasted 120 s and terminated with 3.3 g/s/rod water flooding.

Similar to the reference test QUENCH-L1, the maximum temperature of 1350 K was reached at the end of the heat-up phase at elevation 950 mm. The circumferential temperature gradient across a rod was up to 70 K at burst onset. The maximum thickness of oxide and alpha layers at outer cladding surface was between 17 and 25 µm for inner rods and between 9 and 16 µm for outer rods. Integral hydrogen release at the end of the test was about 0.6 g.

Some rods have up to three ballooning regions. The reason is the successive onset of ductile temperature threshold at different elevations. The maximum blockage ratio of the cooling channel due to ballooning (21% at 918 mm) was slightly lower in comparison to QUENCH-L1 (25% at 946 mm). Due to moderate blockage good bundle coolability was kept for both bundles.

Cladding wall thinning from 725 µm to 450 µm due to ballooning was observed at the burst side along 50 mm below and above burst opening (ultrasound measurement). The cladding burst occurred at temperatures between 1064 and 1188 K (QUENCH-L1: 1074 and 1169 K). Average burst temperatures were 1126 K (853 °C) for QUENCH-L1 and 1117 K (844 °C) for QUENCH-L3. The average burst opening parameters were: width 3.9 ± 0.9 mm; length 14.4 ± 2.2 mm (slightly smaller in comparison to QUENCH-L1). I.e. the sizes of openings are relatively small and only small fragments of fuel pellets in the reactor case could be released from the claddings.

The inner rod pressure relieved to system pressure during about 30 s (similar to QUENCH-L2). After pressure relief the steam penetrated through the burst opening and propagated between pellets and cladding. The hydrogen, produced by oxidation of the inner cladding surface around the burst opening, could be absorbed by metal with formation of hydrogen enrichments around the oxidized area (secondary hydrogenation). Such enrichments were observed for inner rods having seen peak cladding temperatures of more than 1200 K. No hydrogen bands were observed for all outer rods - the peak cladding temperature measured for these rods

was less than 1200 K. Neutron tomography analyses showed the maximal values of hydrogen concentration (averaged through cladding cross section) between 180 and 505 wppm and maximum values between 1070 and 1455 wppm. XRD analysis detected hydrides inside hydrogen bands.

During quenching, following the high-temperature test stages, no fragmentation of claddings was observed indicating that the residual strengths and ductility was sufficient.

Tensile tests at RT revealed the following: no claddings failed at hydrogen bands; seven claddings failed due to stress concentration at edges of burst opening (similar to all QL1 clads with less than 1500 wppm hydrogen); thirteen clads failed after necking far away from burst opening. This indicates that the hydrogen enrichments formed at used LOCA scenario had only minor effect on the mechanical cladding failure behaviour.

7 Acknowledgments

The QUENCH-LOCA experiments are supported and partly sponsored by the association of the German utilities (VGB).

The broad support needed for preparation, execution, and evaluation of the QUENCH-L3 experiment is gratefully acknowledged. In particular, the authors would like to thank Mr. J. Moch for the assembly including instrumentation as well as disassembly of the test bundle, Dr. H. Leiste for the X-ray diffractometry measurements, Mrs. U. Peters for the metallographic examinations and the photographic documentation.

The determination of the test protocol was based on numerous calculations with SCDAP/RELAP5 and SCDAPSIM performed by Dr. J. Birchley and Dr. L. Fernandez-Moguel, Paul Scherrer Institute (PSI), Switzerland.

8 References

- [1] Atomic Energy Commission Rule-Making Hearing, Opinion of the Commission, Docket RM-50-1, 28 December, 1973.
- [2] G. Hache and H. M. Chung, "The History of LOCA Embrittlement Criteria," NUREG/CP-0172, May 2001, pp. 205-237.
- [3] RSK-Leitlinien für Druckwasserreaktoren. Ursprungsfassung (3. Ausgabe vom 14. Oktober 1981) mit Änderungen vom 15.11.1996. <http://www.rskonline.de/downloads/8110dwr.pdf>
- [4] K. Wiehr, He. Schmidt, Out-of-pile-Versuche zum Aufblähvorgang von Zirkaloy-Hüllen. Ergebnisse aus Vorversuchen mit verkürzten Brennstabsimulatoren. Wissenschaftliche Berichte, KFK-2345. Karlsruhe, 1977. <http://bibliothek.fzk.de/zb/kfk-berichte/KFK2345.pdf>
- [5] P. Hofmann, S. Raff. Verformungsverhalten von Zirkaloy-4-Hüllrohren unter Schutzgas im Temperaturbereich zwischen 600 und 1200°C. Wissenschaftliche Berichte, KFK-3973, Karlsruhe, 1981. <http://bibliothek.fzk.de/zb/kfk-berichte/KFK3168.pdf>
- [6] L. Schmidt, H. Lehning, D. Piel. Berstversuche an Zirkaloy-Huellrohren unter kombinierter mechanisch-chemischer Beanspruchung (FABIOLA). In: Projekt Nukleare Sicherheit. Jahresbericht 1982. KFK-3350 (Juli 83) S.4200/69-4200/70. http://quench.forschung.kit.edu/img/fabiola_kfk_1980_1983_schmidt.pdf

- [7] E. H. Karb, M. Prüßmann, L. Sepold, P. Hofmann, G. Schanz. LWR Fuel Rod Behavior in the FR2 In-pile Tests Simulating the Heatup Phase of a LOCA. Final Report. Wissenschaftliche Berichte, KFK-3346, Karlsruhe, 1983. <http://bibliothek.fzk.de/zb/kfk-berichte/KFK3346.pdf>
- [8] M. E. Markiewicz, F. J. Erbacher. Experiments on Ballooning in Pressurized and Transiently Heated Zircaloy-4 Tubes. Wissenschaftliche Berichte, KFK-4343, Karlsruhe, 1988. <http://bibliothek.fzk.de/zb/kfk-berichte/KFK4343.pdf>
- [9] K. Wiehr. REBEKA-Bündelversuche Untersuchungen zur Wechselwirkung zwischen aufblähenden Zircaloyhüllen und einsetzender Kernnotkühlung. Abschlußbericht. Wissenschaftliche Berichte, KFK-4407, Karlsruhe, 1988. <http://bibliothek.fzk.de/zb/kfk-berichte/KFK4407.pdf>
- [10] F. J. Erbacher, H. J. Neitzel, K. Wiehr. Cladding Deformation and Emergency Core Cooling of a Pressurized Water Reactor in a LOCA. Summary Description of the REBEKA Program. Wissenschaftliche Berichte, KFK-4781, Karlsruhe, 1990. <http://bibliothek.fzk.de/zb/kfk-berichte/KFK4781.pdf>
- [11] F. J. Erbacher, S. Leistikow. A Review of Zircaloy Fuel Cladding Behavior in a Loss-of-Coolant Accident. Wissenschaftliche Berichte, KFK-3973, Karlsruhe, 1985. <http://bibliothek.fzk.de/zb/kfk-berichte/KFK3973.pdf>
- [12] J.-C. Brachet, V. Vandenberghe-Maillot, L. Portier, D. Gilbon, A. Lesbros, N. Waeckel, and J.-P. Mardon, Hydrogen Content, Preoxidation, and Cooling Scenario Effects on Post-Quench Microstructure and Mechanical Properties of Zircaloy-4 and M5[®] Alloys in LOCA Conditions. J. ASTM Intl., Vol. 5, No. 5 (2008). Available online as JAI101116 at www.astm.org.
- [13] T. Chuto, F. Nagase and T. Fuketa. High Temperature Oxidation of Nb-containing Zr Alloy Cladding in LOCA Conditions. Nuclear Engineering and Technology, Vol.41, No.2, March 2009.
- [14] Hee M. Chung. Fuel Behavior under Loss-of-Coolant Accident Situations. Nuclear Engineering and Technology, Vol.37 No.4, August 2005.
- [15] H. Uetsuka, T. Furuta and S. Kawasaki. Zircaloy-4 Cladding Embrittlement due to Inner Surface Oxidation under Simulated Loss-of-Coolant Condition. Journal of Nuclear Science and Technology, 18[9], pp. 705~717 (September 1981).
- [16] M. Billone, Y. Yan, T. Burtseva, R. Daum. Cladding Embrittlement During Postulated Loss-of-Coolant Accidents, NUREG/CR-6967, July 2008.
- [17] OECD SCIP-2 Project: <http://www.oecd-nea.org/jointproj/scip-2.html>
- [18] J. Stuckert, M. Große, C. Rössger, M. Steinbrück, M. Walter. Results of the commissioning bundle test QUENCH-L0 performed under LOCA conditions. KIT Scientific Reports, KIT-SR 7571 (March 2013).
- [19] J. Stuckert, M. Große, C. Rössger, M. Klimenkov, M. Steinbrück, M. Walter. QUENCH-LOCA program at KIT on secondary hydriding and results of the commissioning bundle test QUENCH-L0. Nuclear Engineering and Design, 255(2013), pp. 185-201. DOI:10.1016/j.nucengdes.2012.10.024.
- [20] J. Stuckert, M. Große, C. Rössger, M. Steinbrück, M. Walter. Results of the LOCA reference bundle test QUENCH-L1 with Zircaloy-4 claddings. KIT Scientific Reports, KIT-SR 7651 (2013).
- [21] J. Stuckert, M. Große, C. Rössger, M. Steinbrück, M. Walter. Influence of the temperature history on secondary Hydriding and mechanical properties of zircaloy-4 claddings - An analysis of the QUENCH-LOCA bundle tests. Proceedings of 22nd International Conference on Nuclear Engineering (ICONE 2014); Vol. 3, Paper 30792; July 7-11, 2014, Prague. DOI: 10.1115/ICONE22-30792.

<http://proceedings.asmedigitalcollection.asme.org/proceeding.aspx?articleid=1937123>, Presentation:
<http://bibliothek.fzk.de/zb/veroeff/96364.pdf>.

- [22] M. Grosse, E. Lehmann, P. Vontobel, M. Steinbrueck: "Quantitative determination of absorbed hydrogen in oxidised Zircaloy by means of neutron radiography", Nucl. Instr. & Methods in Phys. Res. A 566 (2006), 739.
- [23] M. Große, G. Kühne, M. Steinbrück, E. Lehmann, P. Vontobel, J. Stuckert. Determination of the hydrogen uptake of steam-oxidised zirconium alloys by means of quantitative analysis of neutron radiographs. J. Phys.: Condens. Matter 20 (2008), 104263.
- [24] M. Grosse, E. Lehmann, M. Steinbrueck, G. Kühne, J. Stuckert. Influence of oxide layer morphology on hydrogen concentration in tin and niobium containing zirconium alloys after high temperature steam oxidation. J. Nucl. Mater. 385 (2009), 339.
- [25] J. Stuckert, J. Birchley, M. Grosse, B. Jaeckel, M. Steinbrück. Experimental and calculation results of the integral reflood test QUENCH-14 with M5 cladding tubes. Annals of Nuclear Energy, 37(2010) S.1036-47, DOI:10.1016/j.anucene.2010.04.015.
- [26] M. Grosse, M. Van den Berg, C. Goulet, E. Lehmann, B. Schillinger. In-situ neutron radiography investigations of hydrogen diffusion and absorption in zirconium alloys. Nuclear Instruments and Methods in Physics Research Section A: Accelerators, Spectrometers, Detectors and Associated Equipment, Volume 651, Issue 1, 21 September 2011, Pages 253–257.
- [27] J. Stuckert, M. Große, M. Walter. Mechanical properties of pre-hydrogenated (600 – 5000 wppm) cladding segments. 16th International QUENCH-Workshop, Karlsruhe, November 2010, ISBN 978-3-923704-74-3.
- [28] C. Eberl, D.S. Gianola, K. J. Hemker. Mechanical Characterization of Coatings Using Microbeam Bending and Digital Image Correlation Techniques. Experimental Mechanics, January 2010, Volume 50, Issue 1, pp 85-97.

Tables and Figures

Table 1 QUENCH Test Matrix 1997 – 2015

Test	Quench medium and injection rate	Temp. at onset of flooding or cool-down ¹⁾	Max. ZrO ₂ before transient ²⁾	Max. ZrO ₂ (X s) before flooding ²⁾	Posttest average ZrO ₂ thickness ³⁾	H ₂ production before / during cooldown, g	Remarks, objectives
QUENCH-00 October 9 - 16, 97	Water 80 g/s	≈ 1800 K			completely oxidized		Commissioning tests.
QUENCH-01 February 26, 98	Water 52 g/s	≈ 1830 K	312 μm		500 μm at 913 mm	36 / 3	COBE Project; partial fragmentation of pre-oxidized cladding.
QUENCH-02 July 7, 98	Water 47 g/s	≈ 2400 K			completely oxidized	20 / 140	COBE Project; no additional pre-oxidation; quenching from high temperatures.
QUENCH-03 January 20, 99	Water 40 g/s	≈ 2350 K			completely oxidized	18 / 120	No additional pre-oxidation, quenching from high temperatures.
QUENCH-04 June 30, 99	Steam 50 g/s	≈ 2160 K	82 μm		280 μm	10 / 2	Cool-down behavior of slightly pre-oxidized cladding by cold steam injection.
QUENCH-05 March 29, 2000	Steam 48 g/s	≈ 2020 K	160 μm		420 μm	25 / 2	Cool-down behavior of pre-oxidized cladding by cold steam injection.
QUENCH-06 December 13, 2000	Water 42 g/s	≈ 2060 K	207 μm ⁵⁾	300 μm, (60 s), SVECHA modeling	670 μm ⁴⁾ (60% metal converted to outer ZrO ₂)	32 / 4	OECD-ISP 45; prediction of H ₂ source term by different code systems.
QUENCH-07 July 25, 2001	Steam 15 g/s	≈ 2100 K	230 μm		completely oxidized	66 / 120	COLOSS Project; impact of B ₄ C absorber rod failure on H ₂ , CO, CO ₂ , and CH ₄ generation.

Test	Quench medium and injection rate	Temp. at onset of flooding or cool-down ¹⁾	Max. ZrO ₂ before transient ²⁾	Max. ZrO ₂ (X s) before flooding ²⁾	Posttest average ZrO ₂ thickness ³⁾	H ₂ production before / during cooldown, g	Remarks, objectives
QUENCH-09 July 3, 2002	Steam 49 g/s	≈ 2100 K			completely oxidized	60 / 400	As QUENCH-07, steam-starved conditions prior to cooldown.
QUENCH-08 July 24, 2003	Steam 15 g/s	≈ 2090 K	274 μm		completely oxidized	46 / 38	As QUENCH-07, no absorber rod.
QUENCH-10 July 21, 2004	Water 50 g/s	≈ 2200 K	514 μm	613 μm (at 850 mm)	completely oxidized	48 / 5	LACOMERA Project; Air ingress.
QUENCH-11 Dec. 08, 2005	Water 18 g/s	≈ 2040 K		170 μm	completely oxidized	9 / 132	LACOMERA Project; Boil-off.
QUENCH-12 Sept. 27, 2006	Water 48 g/s	≈ 2100 K	160 μm, breakaway	300 μm, (110 s) breakaway	completely oxidized	34 / 24	ISTC Project No. 1648.2; VVER bundle with E110 claddings.
QUENCH-13 November 7, 2007	Water 52 g/s	≈ 1820 K		400 μm, after AgInCd rod failure	750 μm	42 / 1	SARNET; impact of AgInCd absorber rod failure on aerosol generation.
QUENCH-14 July 2, 2008	Water 41 g/s	≈ 2100 K	170 μm ⁶⁾	470 μm ⁶⁾ , (30 s)	840 μm ⁴⁾ (74% metal converted to outer ZrO ₂)	34 / 6	ACM series: M5 [®] cladding.
QUENCH-15 May 27, 2009	Water 48 g/s	≈ 2100 K	145 μm ⁶⁾	380 μm ⁶⁾ , (30 s)	630 μm ⁴⁾ (70% metal converted to outer ZrO ₂)	41 / 7	ACM series: ZIRLO [™] cladding.
QUENCH-LO July 22, 2010	Water, 100 g/s	1330 K	1 μm	≈ 18 μm	20 μm (central rod)	0.748/0.3	VGB Project; Commissioning test with Zry-4.

Test	Quench medium and injection rate	Temp. at onset of flooding or cool-down ¹⁾	Max. ZrO ₂ before transient ²⁾	Max. ZrO ₂ (X s) before flooding ²⁾	Posttest average ZrO ₂ thickness ³⁾	H ₂ production before / during cooldown, g	Remarks, objectives
QUENCH-16 July 27, 2011	Water 53 g/s	≈ 1870 K	135 μm	130 μm at 450-950 mm, breakaway	1075 μm at 550-650 mm	16 / 128	LACOME Project; Air ingress.
QUENCH-L1 Feb. 02, 2012	Water, 100 g/s	1373 K	1 μm	≈ 19 μm	22 μm (central rod)	0.718/0.01	VGB Project; Reference test.
QUENCH-17 January 31, 2013	Water 10 g/s	≈ 1800 K		completely oxidized	completely oxidized	110 / 1	SARNET-2; Debris formation and coolability.
QUENCH-L2 July 30, 2013	Water, 100 g/s	1373 K	1 μm	n.a.	13 μm (central rod)	0.4 total	VGB Project; M5 ⁶⁾ test.
QUENCH-L3HT March 21, 2014	Water, 100 g/s	1623 K	1 μm	n.a.	70 μm (central rod)	1 total	VGB Project; Opt. ZIRLO test.
QUENCH-L4 July 30, 2014	Water, 100 g/s	1385 K	1 μm	n.a.	13 μm (central rod)	0.8 total	VGB Project; M5 ⁶⁾ test.
QUENCH-L3 March 17, 2015	Water, 100 g/s	1346 K	1 μm	n.a.	14 μm (central rod)	0.6 total	VGB Project; Opt. ZIRLO test.

¹⁾ Maximum measured bundle temperature at 950 mm elevation.

³⁾ Measured posttest at the bundle elevation of maximum temperature.

⁵⁾ Oxide thickness during transient phase.

²⁾ Measured (or calculated for LOCA tests) at the withdrawn corner rod at 950 mm elevation.

⁴⁾ Some claddings were completely oxidized at 950 mm elevation.

⁶⁾ Zircaloy-4 corner rods.

Revised: July 2016

Table 2

Design characteristics of the QUENCH-L3 test bundle

Bundle type		PWR
Bundle size		21 heated rods
Effective number of rods	(considering surface of heated rods, shroud and corner rods)	30.6 rods (21 + 7.4 from shroud + 2.2 from corner rods)
Pitch		14.3 mm
Coolant channel area		29.65 cm ²
Hydraulic diameter		11.5 mm
Cladding material		Opt. ZIRLO
Cladding outside diameter		10.75 mm
Cladding thickness		0.725 mm
Cladding length	(position in the bundle)	2278 mm (between -593 and 1685 mm)
Rod length	(elevations)	2480 mm (-690 to 1790 mm)
Internal rod pressure (gas)		5.5 MPa abs. (Kr)
Material of middle heater	surface roughness	Tungsten (W) Ra=1.6 μm
Tungsten heater length		1024 mm
Tungsten heater diameter		4.6 mm
Annular pellet	material dimensions surface roughness	ZrO ₂ ;Y ₂ O ₃ -stabilized ∅ 9.15/4.75 mm; L=11 mm Ra=0.3 μm
Pellet stack		0 mm to ~1020 mm
Corner rod (4)	material instrumented (A, C, D) not instrumented (B)	Zircaloy-4 tube ∅ 6x0.9 (bottom: -1140 mm) rod ∅ 6 mm (top: +1300 mm) rod ∅ 6 mm (-1350 to +1155 mm)
Grid spacer (cutout of 16x16 spacer)	material length sheet thickness elevation of lower edge	low tin ZIRLO 59 mm 0.6 mm -100, 150, 550, 1050, 1410 mm
Shroud	material wall thickness outside diameter length (extension)	Zirconium 702 (flange: Zry-4) 3.17 mm 86.0 mm 1600 mm (-300 mm to 1300 mm)
Shroud insulation	material insulation thickness elevation	ZrO ₂ fiber ~ 36 mm -300 to ~1000 mm
Molybdenum heaters and copper electrodes	length of upper part length of lower part outer diameter: prior to coating after coating with ZrO ₂ coat. surface roughness borehole of Cu-electrodes	766 mm (576 Mo, 190 mm Cu) 690 mm (300 Mo, 390 mm Cu) 8.6 mm 9.0 mm Ra=6-12 μm diameter 2 mm, length 96 mm
Cooling jacket	Material: inner/outer tube inner tube outer tube	Inconel 600 (2.4816) / SS (1.4571) ∅ 158.3 / 168.3 mm ∅ 181.7 / 193.7 mm

Table 3 Properties of opt. ZIRLO cladding tubes

Table 3.1. Chemical composition of opt. ZIRLO in weight-%

Element	Symbol	Measured value
Tin	Sn	0.7
Niobium	Nb	1.1
Iron	Fe	0.11
Oxygen	O	0.12

Table 3.2. Mechanical properties of opt. ZIRLO at RT in tension

Element	Measured value
0.2 Yield strength Rp 0.2	520 MPa
Ultimate tensile stress Rm	700 MPa
Elongation at fracture A ₅₀ mm	25%

Table 3.3. Microstructure of opt. ZIRLO

Grain size: 4.5 µm	Nr. 13.0 according to ASTM E 112 (acceptable average grain size shall be < Nr. 10, i.e. < 13 µm)	
Surface Conditions:	Roughness (out- and inside):	Ra = 0.35 µm

Table 4 Main characteristics of the ZrO₂ pellet material, yttria-stabilized (type FZY)

Property		Data*
Density		5.5-5.8 g/cm ³
Open porosity		0
Mean grain size		50 μm
Hardness (Knoop, 100 g)		17000 N/mm ²
Yield strength under compression		2000 N/mm ²
Bending strength		350 N/mm ²
Elastic modulus		165 GPa
Specific heat at 20 °C		400 J/kg K
Thermal conductivity at 100 °C		2.5 W/m K
Linear expansion, 20-1000 °C		10.5 x 10 ⁻⁶ /K
Specific electric resistance	at 20 °C	10 ¹⁰ Ω cm
	at 500 °C	5000 Ω cm
	at 1000 °C	50 Ω cm

*According to FRIATEC, Mannheim

Table 5 QUENCH-L3; Electrical resistances of rods [mΩ] at 20°C

Table 5.1. Internal circuit with 9+1 rods

rod	1	2	3	4	5	6	7	8	9	15	Ave- rage	10 rods paralle l
pre- test	4.7	4.8	4.7	4.8	4.8	4.7	4.8	4.8	4.8	4.7	4.8	0.48
post- test	4.6	4.6	4.6	4.6	4.5	4.6	4.7	4.6	4.6	4.6	4.6	0.46

Note: Measured values include the resistance of slide contacts $R_s=0.75\text{ m}\Omega$

Table 5.2. External circuit with 11 rods

rod	10	11	12	13	14	16	17	18	19	20	21	Ave- rage	11 rods parallel
pre- test	4.7	4.9	4.7	4.7	4.7	4.7	4.7	4.7	5.2	4.8	4.7	4.8	0.43
post- test	4.6	16.0	4.6	4.6	4.6	4.6	4.6	4.6	9	4.6	4.6	6.0	0.47

Note: Measured values include the resistance of slide contacts $R_s=0.75\text{ m}\Omega$

Each circuit connected to the DC generator with 4 parallel bonded cables. The resistance of each cable is $R_c=1.2\text{ m}\Omega$. Therefore, the external (outside) resistance corresponding to each heated rod (indicated by SCDAP/RELAP as **fxwid**) is $R_{ie}=R_s+10*R_c/4=3.75\text{ m}\Omega$ for the inner rod group and $R_{oe}=R_s+11*R_c/4=4.05\text{ m}\Omega$ for the outer rod group.

Table 6 Properties of zirconia fiber insulating boards

Table 6.1. Chemical composition*

Oxide	ZrO ₂	Y ₂ O ₃	HfO ₂	TiO ₂	SiO ₂	CaO	MgO	Fe ₂ O ₃	Al ₂ O ₃	Na ₂ O
typical wt%	88	10	2	0.14	0.12	0.09	0.03	0.04	0.01	0.01

Table 6.2. Physical properties*

bulk density	porosity	shrinkage		thermal expansion coefficient @298-1453K	melting point	max. service temperature	flexural strength	Compressive strength @10% compression
		1 hour @1925 K	24 hours @1925 K					
g/cm ³	%	%		1/K	K	K	MPa	MPa
0.48	92	1.2	2.8	10.7*10 ⁻⁶	2866	2500	0.59	0.29

Table 6.3. Thermal conductivity*

temperature, K	673	1073	1373	1673	1923
conductivity, W/(m*K)	0.08	0.11	0.14	0.19	0.24

Table 6.4. Specific heat capacity*

temperature, K	366	2644
specific heat capacity, J/(kg*K)	544	754

*According to specifications of manufacturer ZIRCAR PRODUCTS on the ZYFB3 material

Table 7 List of instrumentation for the QUENCH-L3 test

Chan	Designation	Instrument, location	Unit
0	P rod 13	Internal pressure of rod #13	bar
1	P rod 14	Internal pressure of rod #14	bar
2	P rod 15	Internal pressure of rod #15	bar
3	P rod 12	Internal pressure of rod #12	bar
4	P rod 03	Internal pressure of rod #03	bar
5	P rod 04	Internal pressure of rod #04	bar
6	P rod 05	Internal pressure of rod #05	bar
7	P rod 16	Internal pressure of rod #16	bar
8	P rod 11	Internal pressure of rod #11	bar
9	P rod 02	Internal pressure of rod #02	bar
10	P rod 01	Internal pressure of rod #01	bar
11	P rod 06	Internal pressure of rod #06	bar
12	P rod 17	Internal pressure of rod #17	bar
13	P rod 10	Internal pressure of rod #10	bar
14	P rod 09	Internal pressure of rod #09	bar
15	P rod 08	Internal pressure of rod #08	bar
16	P rod 07	Internal pressure of rod #07	bar
17	P rod 18	Internal pressure of rod #18	bar
18	P rod 21	Internal pressure of rod #21	bar
19	P rod 19	Internal pressure of rod #19	bar
20	P rod 20	Internal pressure of rod #20	bar
21..31		20 mA, Reserve	
32..34		TC (W/Re), Reserve	
35	TSH 15/0	TC (NiCr/Ni), shroud outer surface, 1150 mm, 21°, feed cable outside of shroud insulation.	K
36	TSH 14/270	TC (NiCr/Ni), shroud outer surface, 1050 mm, 289°, feed cable outside of shroud insulation.	K
37		TC (W/Re), Reserve	K
38	TFS 15/13	TC (NiCr/Ni), surface of fuel rod simulator 15, group 5, 950 mm	K
39	TFS 19/12	TC (NiCr/Ni), surface of fuel rod simulator 19, group 5, 850 mm	K

Chan	Designation	Instrument, location	Unit
40..41		TC (W/Re), Reserve	
42	TFS 7/12	TC (NiCr/Ni), surface of fuel rod simulator 7, group 3, 850 mm	K
43	TFS 15/12	TC (NiCr/Ni), surface of fuel rod simulator 15, group 5, 850 mm	K
44	TFS 2/12	TC (NiCr/Ni), surface of fuel rod simulator 2, group 2, 850 mm	K
45	TFS 4/12	TC (NiCr/Ni), surface of fuel rod simulator 4, group 2, 850 mm	K
46	TFS 19/13	TC (NiCr/Ni), surface of fuel rod simulator 19, group 5, 950 mm	K
47..57		TC (W/Re), Reserve	K
58	TFS 7/10	TC (NiCr/Ni), surface of fuel rod simulator 7, group 3, 650 mm	K
59..60		TC (W/Re), Reserve	K
61	TFS 11/12	TC (NiCr/Ni), surface of fuel rod simulator 11, group 4, 850 mm	K
62	P 206	Reserve	
63	F 206	Reserve	
64	T 402 b	TC (NiCr/Ni), Ar super heater	K
65..67		TC (W/Re), Reserve	
68	T 512	TC (NiCr/Ni), gas temperature at 1360 mm (bundle outlet) between rod #20 and shroud	K
69..70		TC (W/Re), Reserve	K
71	<i>Ref. T01</i>	<i>Temperature of measuring crate 1 (reference temperature)</i>	K
72	TFS 11/13	TC (NiCr/Ni) surface of fuel rod simulator 11, group 4, 950 mm	K
73	TFS 7/13	TC (NiCr/Ni), surface of fuel rod simulator 7, group 3, 950 mm	K
74	TFS 2/13	TC (NiCr/Ni), surface of fuel rod simulator 2, group 2, 950 mm	K
75	TFS 4/13	TC (NiCr/Ni), surface of fuel rod simulator 4, group 2, 950 mm	K
76	TFS 15/11	TC (NiCr/Ni), surface of fuel rod simulator 15, group 5, 750 mm	K
77	TFS 19/11	TC (NiCr/Ni), surface of fuel rod simulator 19, group 5, 750 mm	K
78	TFS 11/11	TC (NiCr/Ni) surface of fuel rod simulator 11, group 4, 750 mm	K
79	TFS 7/11	TC (NiCr/Ni), surface of fuel rod simulator 7, group 3, 750 mm	K
80	TFS 2/11	TC (NiCr/Ni) surface of fuel rod simulator 2 group 2, 750 mm	K
81	TSH 12/90	TC (NiCr/Ni), shroud outer surface, 850 mm, 109°	K
82	TFS 2/10	TC (NiCr/Ni); surface of fuel rod simulator 2, group 2, 650 mm	K
83	TSH 10/270	TC (NiCr/Ni), shroud outer surface, 650 mm, 289°	K
84	TSH 9/180	TC (NiCr/Ni), shroud outer surface, 550 mm, 191°	K

Chan	Designation	Instrument, location	Unit
85	TSH 8/90	TC (NiCr/Ni), shroud outer surface, 450 mm, 109°	K
86	TSH 7/0	TC (NiCr/Ni), shroud outer surface, 350 mm, 11°	K
87	TSH 6/270	TC (NiCr/Ni) shroud outer surface, 250 mm, 281°	K
88	TSH 5/180	TC (NiCr/Ni), shroud outer surface, 150 mm, 191°	K
89	TSH 4/90	TC (NiCr/Ni), shroud outer surface, 50 mm, 109°	K
90	TSH 11/0	TC (NiCr/Ni), shroud outer surface, 750 mm, 11°	K
91	TCI 9/270	TC (NiCr/Ni), cooling jacket inner tube wall, 550 mm, 270°	K
92	TCI 10/270	TC (NiCr/Ni), cooling jacket inner tube wall, 650 mm, 270°	K
93	TCI 11/270	TC (NiCr/Ni), cooling jacket inner tube wall, 750 mm, 270°	K
94	TCI 13/270	TC (NiCr/Ni), cooling jacket inner tube wall, 950 mm, 270°	K
95	TFS 4/11	TC (NiCr/Ni), surface of fuel rod simulator 4, group 2, 750 mm	K
96	TFS 15/10	TC (NiCr/Ni), surface of fuel rod simulator 15, group 5, 650 mm	K
97	TFS 19/10	TC (NiCr/Ni), surface of fuel rod simulator 19, group 5, 650 mm	K
98	TFS 11/10	TC (NiCr/Ni), surface of fuel rod simulator 11, group 4, 650 mm	K
99	TSH 13/180	TC (NiCr/Ni), shroud outer surface, 950 mm, 191°, feed cable outside of shroud insulation.	K
100	TSH 3/0	TC (NiCr/Ni), shroud outer surface, -50 mm, 11°	K
101	TFS 4/10	TC (NiCr/Ni), surface of fuel rod simulator 4, group 2, 650 mm	K
102	TFS 15/14	TC (NiCr/Ni), surface of fuel rod simulator 15, group 5, 1050 mm	K
103	TFS 19/14	TC (NiCr/Ni), surface of fuel rod simulator 19, group 5, 1050 mm	K
104	TFS 11/14	TC (NiCr/Ni), surface of fuel rod simulator 11, group 4, 1050 mm	K
105	TFS 7/14	TC (NiCr/Ni), surface of fuel rod simulator 7, group 3, 1050 mm	K
106	TFS 2/14	TC (NiCr/Ni), surface of fuel rod simulator 2, group 2, 1050 mm	K
107	TFS 4/14	TC (NiCr/Ni), surface of fuel rod simulator 4, group 2, 1050 mm	K
108	TFS 15/9	TC (NiCr/Ni), surface of fuel rod simulator 15, group 5, 550 mm	K
109	TFS 11/9	TC (NiCr/Ni), surface of fuel rod simulator 11, group 4, 550 mm	K
110	TFS 7/9	TC (NiCr/Ni), surface of fuel rod simulator 7, group 3, 550 mm	K
111	TFS 4/9	TC (NiCr/Ni), surface of fuel rod simulator 4, group 2, 550 mm	K
112	TFS 15/15	TC (NiCr/Ni), surface of fuel rod simulator 15, group 5, 1150 mm	K
113	TFS 19/15	TC (NiCr/Ni), surface of fuel rod simulator 19, group 5, 1150 mm	K
114	TFS 11/15	TC (NiCr/Ni), surface of fuel rod simulator 11, group 4, 1150 mm	K

Chan	Designation	Instrument, location	Unit
115	TFS 7/15	TC (NiCr/Ni), surface of fuel rod simulator 7, group 3, 1150 mm	K
116	TFS 2/15	TC (NiCr/Ni), surface of fuel rod simulator 2, group 2, 1150 mm	K
117	TFS 4/15	TC (NiCr/Ni), surface of fuel rod simulator 4, group 2, 1150 mm	K
118	TFS 11/8	TC (NiCr/Ni), surface of fuel rod simulator 11, group 4, 450 mm	K
119	TFS 7/8	TC (NiCr/Ni), surface of fuel rod simulator 7, group 3, 450 mm	K
120	TFS 4/8	TC (NiCr/Ni), surface of fuel rod simulator 4 group 2, 450 mm	K
121	TFS 11/16	TC (NiCr/Ni), surface of fuel rod simulator 11, group 4, 1250 mm	K
122	TFS 7/16	TC (NiCr/Ni), surface of fuel rod simulator 7, group 3, 1250 mm	K
123	T 601	Temperature off-gas, 2660 mm from test section outlet (flange)	K
124	TFS 11/7	TC (NiCr/Ni), surface of fuel rod simulator 11, group 4, 350 mm	K
125	TFS 7/12i	TC (NiCr/Ni), surface of fuel rod simulator 7, group 3, 850 mm, near to rod #1	K
126	TFS 7/7	TC (NiCr/Ni), surface of fuel rod simulator 7, group 3, 350 mm	K
127	TFS 4/7	TC (NiCr/Ni), surface of fuel rod simulator 4, group 2, 350 mm	K
128	T 104	Temperature quench water	K
129	T 201	Temperature steam generator heating pipe	K
130	TIT C/12	TC (NiCr/Ni), center line of corner rod C, 850 mm	K
131	T 205	Temperature upstream steam flow instrument location 10 g/s	K
132	T 301A	Temperature downstream superheater	K
133	T 302	Temperature superheater heating pipe	K
134	T 303	Temperature upstream total flow instrument location	K
135	T 401	Temperature upstream Ar flow instrument (orifice) location	K
136	T 403	Temperature of Ar at inlet cooling jacket	K
137	T 404	Temperature of Ar at outlet cooling jacket	K
138	T 501	Temperature in containment (near from bundle head)	K
139	TFS 7/6	TC (NiCr/Ni), surface of fuel rod simulator 7, group 3, 250 mm	K
140	TFS 4/6	TC (NiCr/Ni), surface of fuel rod simulator 4, group 2, 250 mm	K
141	TFS 7/17	TC (NiCr/Ni), surface of fuel rod simulator 7, group 3, 1350 mm	K
142	TFS 7/5	TC (NiCr/Ni), surface of fuel rod simulator 7, group 3, 150 mm	K
143	TFS 7/4	TC (NiCr/Ni), surface of fuel rod simulator 7, group 3, 50 mm	K
144	TFS 7/3	TC (NiCr/Ni), surface of fuel rod simulator 7, group 3, -50 mm	K

Chan	Designation	Instrument, location	Unit
145	TFS 7/2	TC (NiCr/Ni), surface of fuel rod simulator 7, group 3, -150 mm	K
146	TFS 7/1	TC (NiCr/Ni), surface of fuel rod simulator 7, group 3, -250 mm	K
147	TFS 7/13i	TC (NiCr/Ni), surface of fuel rod simulator 7, group 3, 950 mm, near to rod #1	K
148	T 511	Gas temperature at bundle inlet	K
149	TIT D/11	TC (NiCr/Ni), center line of corner rod D, 750 mm	K
150	TIT A/13	TC (NiCr/Ni), center line of corner rod A, 950 mm	K
151	Ref. T02	Temperature of measuring crate 2 (reference temperature)	K
152	P 201	Pressure steam generator	bar
153	P 204	Pressure at steam flow instrument location 50 g/s	bar
154	P 205	Pressure at steam flow instrument location 10 g/s	bar
155	P 303	Pressure upstream total flow instrument (orifice) location	bar
156	P 401	Pressure upstream gas flow instrument location	bar
157	P 511	Pressure at bundle inlet, L501 low leg	bar
158	P 512	Pressure at bundle outlet	bar
159	P 601	Pressure upstream off-gas flow instrument (orifice) F 601	bar
160	P 901	Pressure at bundle inlet, L501 upper leg	bar
161	L 201	Liquid level steam generator	mm
162	L 501	Liquid level quench water	mm
163	L 701	Liquid level condensation vessel	mm
164	Fm 401	Argon (carrier gas) mass flow rate (Bronkhorst device)	g/s
165	P 411	Reserve (Pressure Kr supply for heated rods)	bar
166	P 403	Pressure Ar cooling of cooling jacket	bar
167	P 406	Pressure insulation shroud/cooling jacket	bar
168	Fm 104	Flow rate quench water	g/s
169	Fm 204	Flow rate steam (flow control up to 50 g/s)	g/s
170	Fm 205	Flow rate steam (flow control up to 10 g/s)	g/s
171	F 303	Flow rate at bundle inlet (steam + argon), orifice	mbar
172	F 401	Argon (carrier gas) volumetric flow rate	Nm ³ /h
173	Fm 403	Mass flow rate of cooling gas (Ar)	g/s

Chan	Designation	Instrument, location	Unit
174	F 601	Flow rate off-gas (orifice), 2000 mm from test section outlet (flange)	mbar
175	Fm 406	Flow rate argon into room between shroud and cooling jacket	g/s
176	E 201	Electric current steam generator	A
177	E 301	Electric current superheater	A
178	E 501	Electric current of left group of fuel rod simulators	A
179	E 502	Electric current of right group of fuel rod simulators	A
180	E 503	Electric voltage of left group of fuel rod simulators	V
181	E 504	Electric voltage of right group of fuel rod simulators	V
182	Hub_V302	Gas supply valve lift	%
183	<i>Ref. T03</i>	<i>Temperature of buffer amplifier (reference temperature)</i>	K
184..... 199		Binary inputs	
200..... 215		Analog outputs	
250	E 505	Electric power inner ring of fuel rod simulators	W
251	E 506	Electric power outer ring of fuel rod simulators	W
252	EP	Gross electrical power	kW

Groups of the rods for modeling:

central groups

- group 1: rod 1;
- group 2: rods 2, 4, 6, 8;
- group 3: rods 3, 5, 7, 9;

peripheral groups

- group 4: rods 11, 14, 17, 20;
- group 5: rods 10, 12, 13, 15, 16, 18, 19, 21.

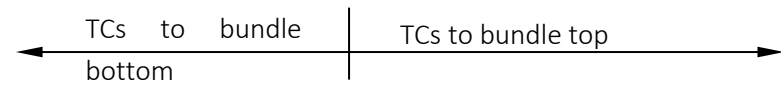
Indications:

- TFS - TC at the rod surface;
- TIT - TC at the inside of corner rods;
- TSH - TC at outer surface of shroud.

Table 8 QUENCH-L3; Rod thermocouple positions

Elevation, mm	-250	-150	-50	50	150	250	350	450	550	650	750	850	950	1050	1150	1250	1350
Rod/Elevation	1	2	3	4	5	6	7	8	9	10	11	12	13	14	15	16	17
1																	
2										X	X	X	X	X	X		
3																	
4						X	X	X	X	X	X	X	X	X	X		
5																	
6																	
7	X	X	X	X	X	X	X	X	X	X	X	X, Xi	X, Xi	X	X	X	X
8																	
9																	
10																	
11							X	X	X	X	X	X	X	X	X	X	
12																	
13																	
14																	
15									X	X	X	X	X	X	X		
16																	
17																	
18																	
19										X	X	X	X	X	X		
20																	
21																	

Number per elevation 1 1 1 1 1 2 3 3 4 6 6 6+1 6+1 6 6 2 1



TFS (rod surface, shroud direction), indicated as X in table above	56
TFS (rod surface, central rod direction), indicated as Xi in table above	2
TIT (inside corner rods)	3
TSH (outer shroud surface)	13

Table 9 QUENCH-L3; Sequence of events

Time [s]	Event
-1849 (10:33:52; 17.03.2015)	Start data recording, $T_{max} = TFS\ 7/13i = 849\ K$, el. power at 3.25 kW. L701 = 1048 mm. L 501 = -400 mm. System pressure 3 bar. Hot Ar 6 g/s (heated in superheater), superheated steam 2 g/s.
-1770... -350	Pressurization of rods from 30 to 55 bar.
0	Start of transient with max electrical power increase rate.
3.6; 22; 45	Electrical power 41.3; 55.3; 60 kW.
38...56	Sequential onset of ballooning from inner rod #8 to peripheral rod #11.
47.8...68	Sequential onset of burst for rods from inner rod #1 to peripheral rod #10. See burst table (Table 11).
75.8...76.2	Switch of the electrical power from max 59 kW to decay heat of 3.9 kW. Initiation of rapid steam supply line (20 g/s) additionally to carrier argon (6 g/s). Switch-off of slow steam supply (2 g/s). $T_{max} = TFS\ 7/13i = 1300\ K$.
81.8	Cladding surface temperature maximum reached. Maximal hydrogen production rate. $T_{max} = TFS\ 7/13i = 1346\ K$.
81.8...211	Cool-down of bundle in steam. Decrease of TFS 7/13i reading from 1346 K to 950 K.
211...221	Increase of maximal bundle temperatures to $\approx 1019\ K$ due to switch-off of the steam cooling (closing of gas inlet valve at 211 s).
217.2	Initiation of quench water supply. Switch of argon to bundle top supply.
239.6	Maximal quench rate (about 100 g/s) reached.
235.8...283	Wetting of cladding surface thermocouples (TFS) at elevations between -250 and 1350 mm at temperatures between 520 (TFS 7/1; -250 mm) and 772 K (TFS 2/13; 1050 mm). (Table 10).
257...308	Maximal water evaporation rate (about 25 g/s).
363	Bundle completely filled with water (L 501 = 1307 mm).
475.8	Electrical power switched off. $T_{max} = TFS\ 7/17 = 380\ K$.
892	End of data recording.

Table 10

QUENCH-L3; Wetting of TFS thermocouples

Bundle elevation, mm	Wetting time, s	<i>Collapsed water front (L501), mm</i>
-250 (TFS 7/1)	235.4	-403
-150 (TFS 7/2)	241	-225
-50 (TFS 7/3)	241.2	-177
50 (TFS 7/4)	247	-40
150 (TFS 7/5)	249	30
250 (TFS 4,7/6)	250.6	88
350 (TFS 11,7,4/7)	250.8..251.2	100..200
450 (TFS 11,7,4/8)	253.2..253.6	52..160
550 (TFS 7,4,11,15/9)	253.4..253.8	160..161
650 (TFS 11,7,15,19,4,7,2/10)	257.6..269	184..366
750 (TFS 4,7,19,15,2,11/11)	258..277.2	139..426
850 (TFS 15,4,11,7,2,19/12)	261.8..288	316..647
950 (TFS 4,7,15,11,2,19/13)	277.8..288.2	560..674
1050 (TFS 15,11,7,4,2,19/14)	258.8..280.4	91..484
1150 (TFS 7,2,15,11,4,19/15)	261.6..294.2	316..668
1250 (TFS 7,11/16)	269..283	366..600
1350 (TFS 7/17)	253.6*	154

*condensation of stagnant steam at the bundle head due to injection of cold argon

Table 11

QUENCH-L3; Burst parameters

rod	burst time, s	interpolated burst T, K	burst azimuth. position, °	burst middle elev., mm	max burst width, mm	burst length, mm	burst area, mm ²
1	47.8	1103	191	925	4.7	16	36
2	51.6	1140	77	962	3.2	11.5	21
3	53	1111	205	930	4.6	15	37
4	55	1108	112	914	3.9	12	26
5	52	1109	184	901	4.8	18	44
6	51.8	1112	186	917	6.2	20	67
7	53.6	1124	259	915	4.6	14	36
8	49.6	1107	18	941	2.9	12	20
9	53.2	1132	15	954	4.7	16	43
10	68	1188 (Max)	36	934	3.4	13	24
11	65.6	1126	122	947	4.1	14.5	33
12	65.8	1175	92	921	3.3	14	24
13	61.8	1138	143	921	2.7	12	18
14	59.4	1124	153	920	3.6	15	27
15	54.4	1105	232	915	3.3	13.5	24
16	62	1142	250	921	3.9	15	29
17	60	1094	260	915	3.6	14	28
18	63	1114	290	935	2.6	12.5	17
19	66.2	1073	352	939	2.8	12	18
20	64	1064 (Min)	352	937	4.5	15.5	39
21	67.2	1073	5	934	4.1	17.5	40
<i>average</i>		1117		929	3.9	14.4	31
<i>standard deviation</i>		±30		±15	±0.9	±2.2	±12

Table 12 QUENCH-L3; Strain parameters

rod group	rod #	elevation of burst <i>middle</i> , mm	max strain %	max D mm	<i>at azimuth</i> °	min D mm	<i>at azimuth</i> °
central group	1	925	26	14.57	170	12.60	90
	2	962	25	14.38	91	12.67	170
	3	930	31	15.21	5	13.04	110
	4	914	30	15.00	126	12.98	22
	5	901	27.8	14.97	29	12.71	104
	6	917	36.8	16.31	40	13.40	112
	7	915	28.6	15.06	98	12.69	174
	8	941	21	13.87	34	12.29	113
	9	954	30.2	15.28	41	12.88	116
peripheral group	10	934	23.2	14.21	230	12.36	130
	11	947	27.8	14.86	130	12.67	30
	12	921	22.7	14.23	110	12.35	7
	13	921	20.4	13.89	159	12.20	57
	14	920	23.9	14.39	170	12.40	250
	15	915	22.7	14.10	40	12.42	140
	16	921	23.7	14.32	232	12.36	55
	17	915	23.5	14.34	100	12.44	177
	18	935	20.0	13.79	127	12.21	26
	19	939	21.4	14.00	6	12.23	85
	20	937	22.1	14.87	152	12.64	79
	21	934	27.5	15.40	43	12.51	122
Average		929±15	25.5±4.2	14.6±0.6		12.6±0.3	

Table 13 QUENCH-L3; Content of hydrogen absorbed by secondary hydrogenation (n^0 -tomography): axial maximum averaged for cross section and axial absolute local maximum

rod #	C_H above burst opening (H-band), wppm		elevation, mm		C_H below burst opening (H-spot), wppm		elevation, mm	
	averaged	absolute	aver.	abs.	averaged	absolute	aver.	abs.
2	240±15	1070±60	985	980	317±10	1350±100	942	940
3	180±10	1106±70	955	951	115±15	1215±100	907	906
4	505±10	1455±70	935	933	280±15	1450±100	880	870
5	366±10	1312±70	928	920	216±15	1320±100	884	884
6	475±5	1455±70	952	938	278±15	1460±100	886	902
7	363±10	1202±70	953	929	210±15	1114±100	875	875
8	307±10	1191±70	964	958	280±15	1303±100	897	922
9	190±15	1196±70	988	990	239±15	1244±100	912	917
10	165±20	1060±120	970	970	165±20	990±120	915	895

Table 14 Table 14: QUENCH-L3: average hydrogen content in hydrogen bands according to hot extraction (LECO TCH600 device, cladding segments with h=11 mm, d=5 mm)

rod #	position of sample in cladding	hydrogen content, wppm	measurement deviation, wppm
6 H band	934-945 mm, 2 samples left and right from 186°	552	±50
6 oppositely to H band	934-945 mm, 2 samples left and right from 6°	70	±8
6 H spot	879-902 mm, 2 samples along 186°	641	±60
6 oppositely to H spot	879-902 mm, 2 samples along 6°	48	±6

Table 15 QUENCH-L3; Results of tensile tests

rod $l_0=800$ mm	ultimate tensile strength [MPa]	fracture stress [MPa]	elongation at fracture (graded) [%]	rupture based on
01	516	384	8.4	fracture after necking
02	526	373	9.0	fracture after necking
03	515	379	9.7	fracture after necking
04	532	379	7.9	fracture after necking
05	520	386	8.7	fracture after necking
06	531	529	5.8	<i>stress concentration at opening middle</i>
07	521	521	4.7	<i>welding of TC TFS 7/13 and 7/13i</i>
08	518	384	9.6	fracture after necking
09	520	372	9.1	fracture after necking
10	521	392	14.2	fracture after necking
11	524	387	15.7	fracture after necking
12	511	492	10.9	<i>stress concentration at opening tips</i>
13	520	517	12.2	<i>stress concentration at opening tips</i>
14	520	388	10.5	fracture after necking
15	514	393	11.9	fracture after necking
16	509	459	8.6	<i>stress concentration at opening tips</i>
17	501	498	7.5	<i>stress concentration at opening tips</i>
18	512	506	10.2	<i>stress concentration at opening tips</i>
19	523	391	13.7	fracture after necking
20	517	401	14.0	fracture after necking
21	517	503	9.1	<i>stress concentration at opening tips</i>
QL3aver.	520 ± 5	385 ± 11	11.0 ± 2.6	fracture after necking
QL3aver.	512 ± 7	496 ± 20	9.8 ± 1.7	<i>stress concentration at opening tips</i>

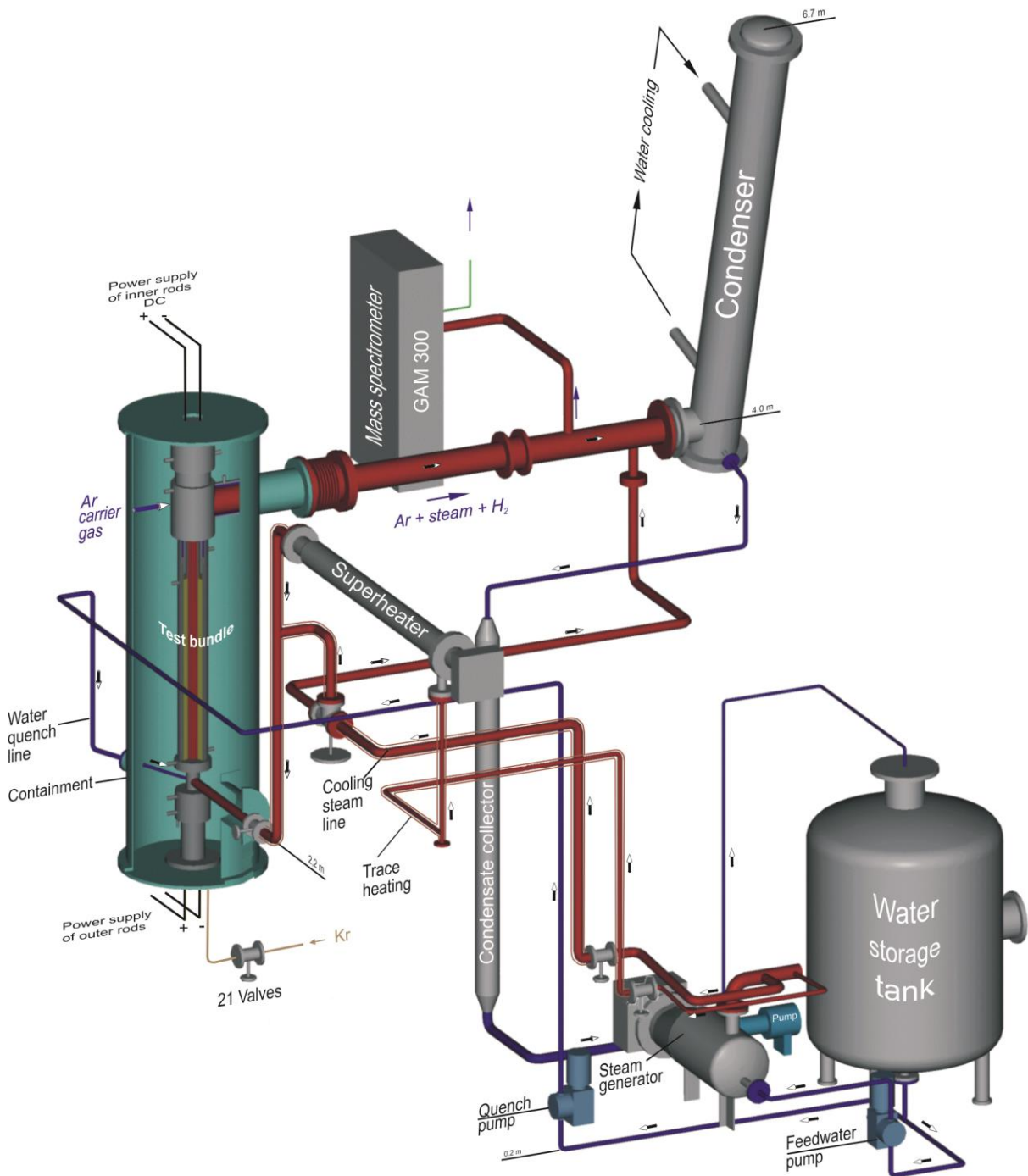


Figure 1 QUENCH Facility - Main components.

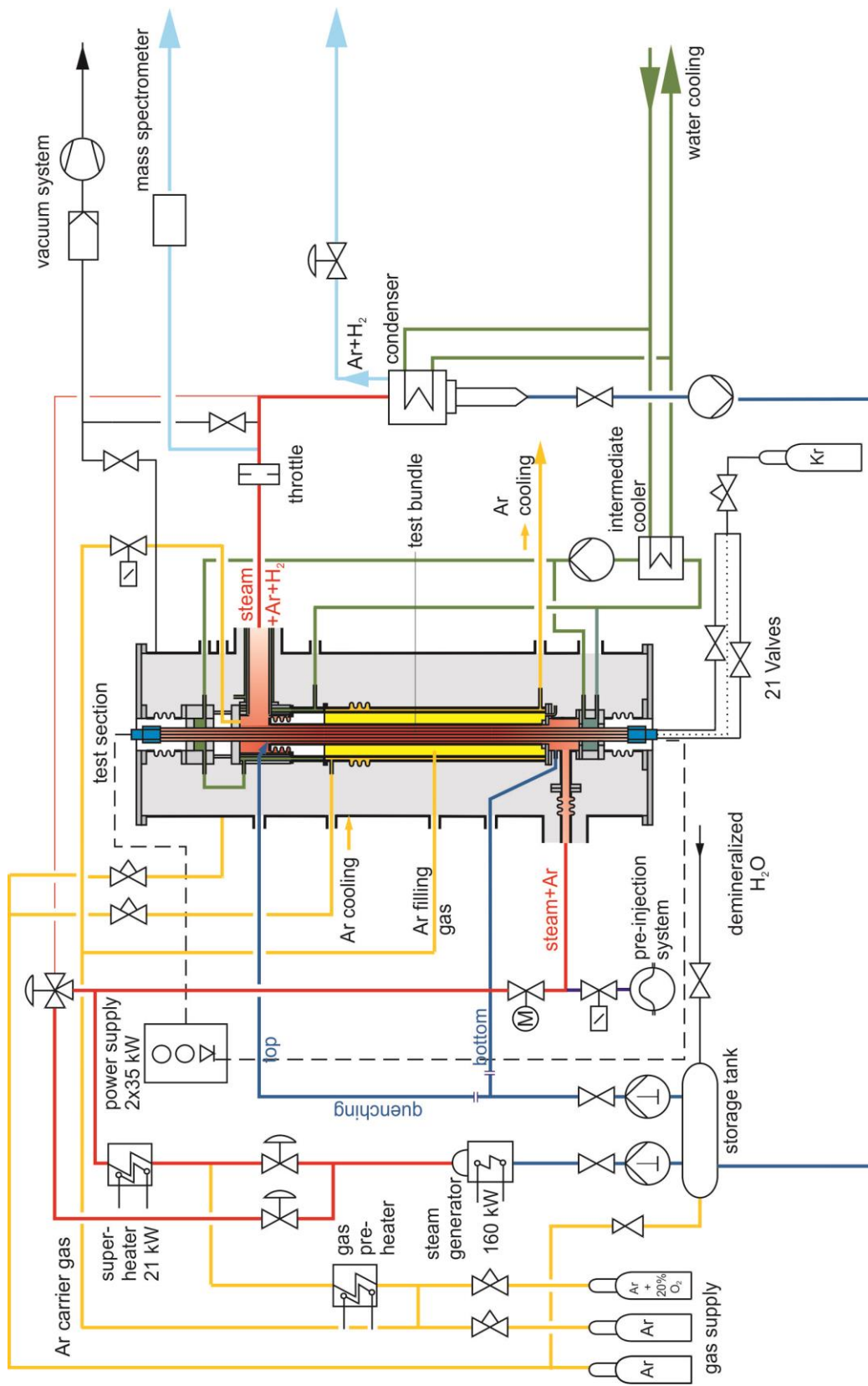


Figure 2 Flow diagram of the QUENCH test facility.

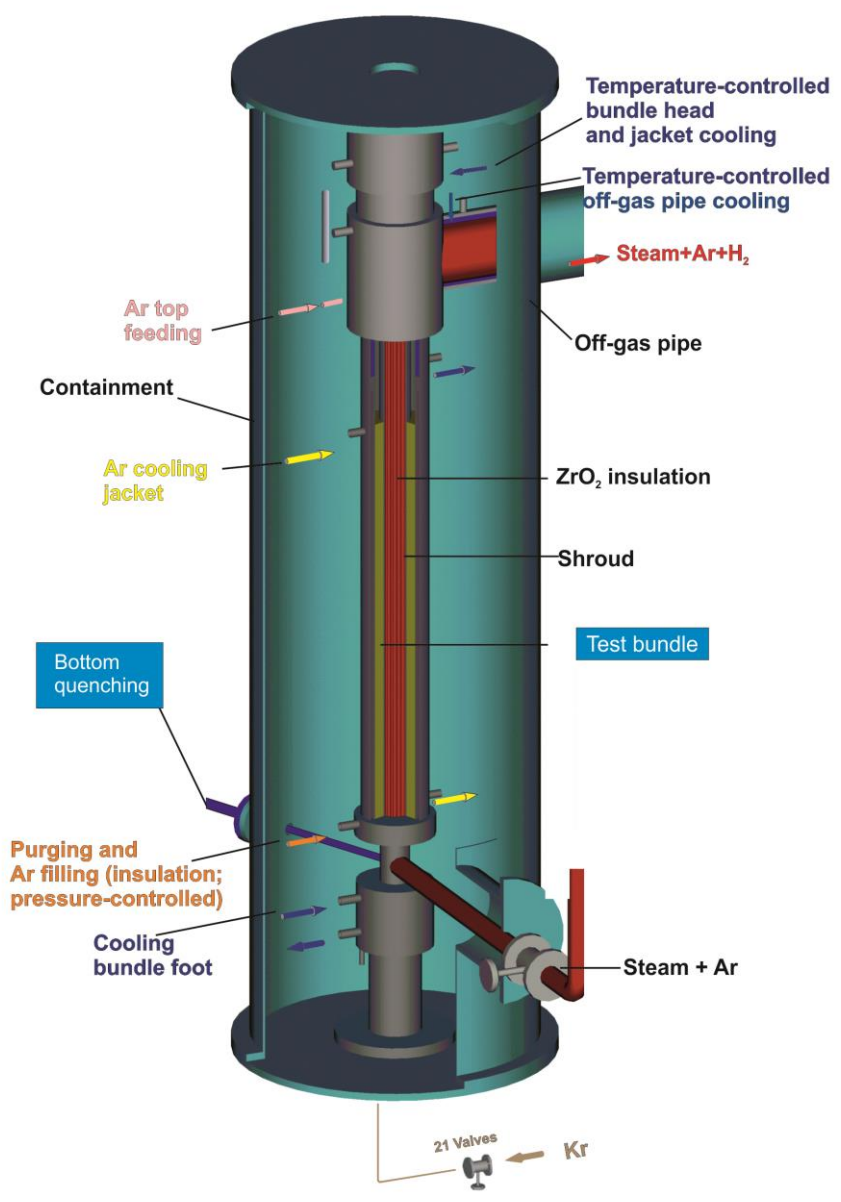


Figure 3 QUENCH Facility; Containment and test section.

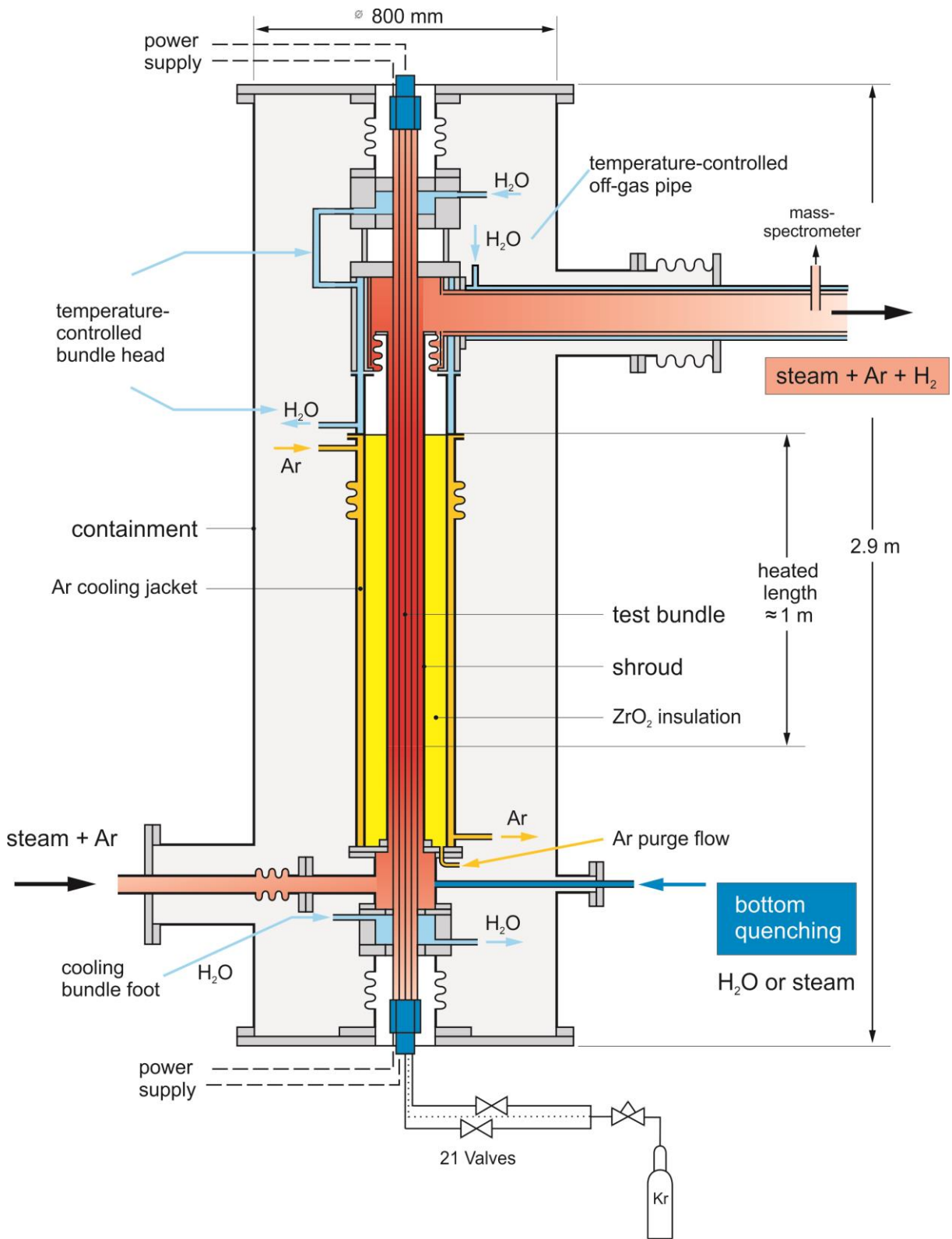


Figure 4 QUENCH-L3; Test section with flow lines.

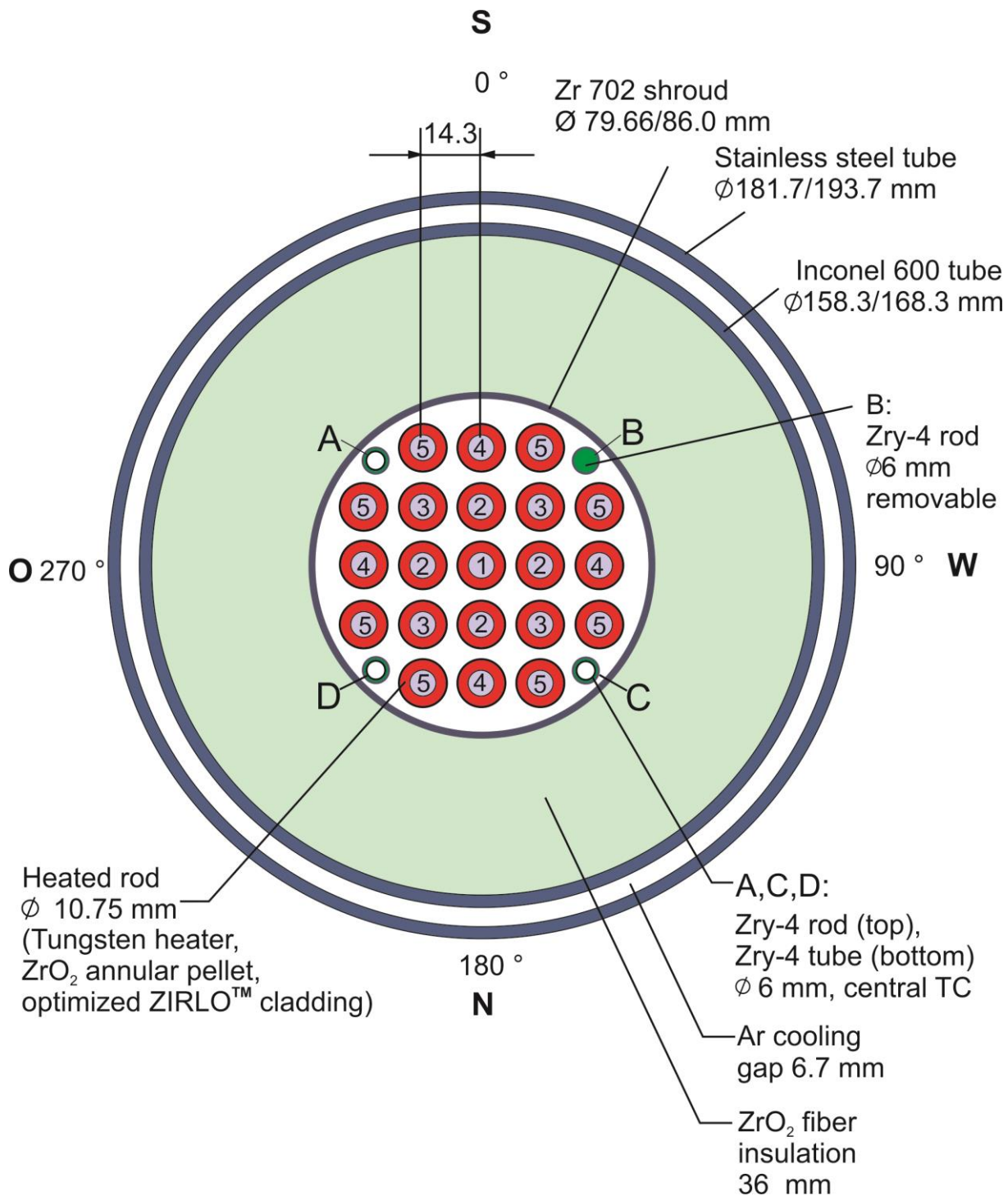


Figure 5 QUENCH-L2; Fuel rod simulator bundle (cross section, top view) including rod type indications corresponding to table “List of Instrumentation”.

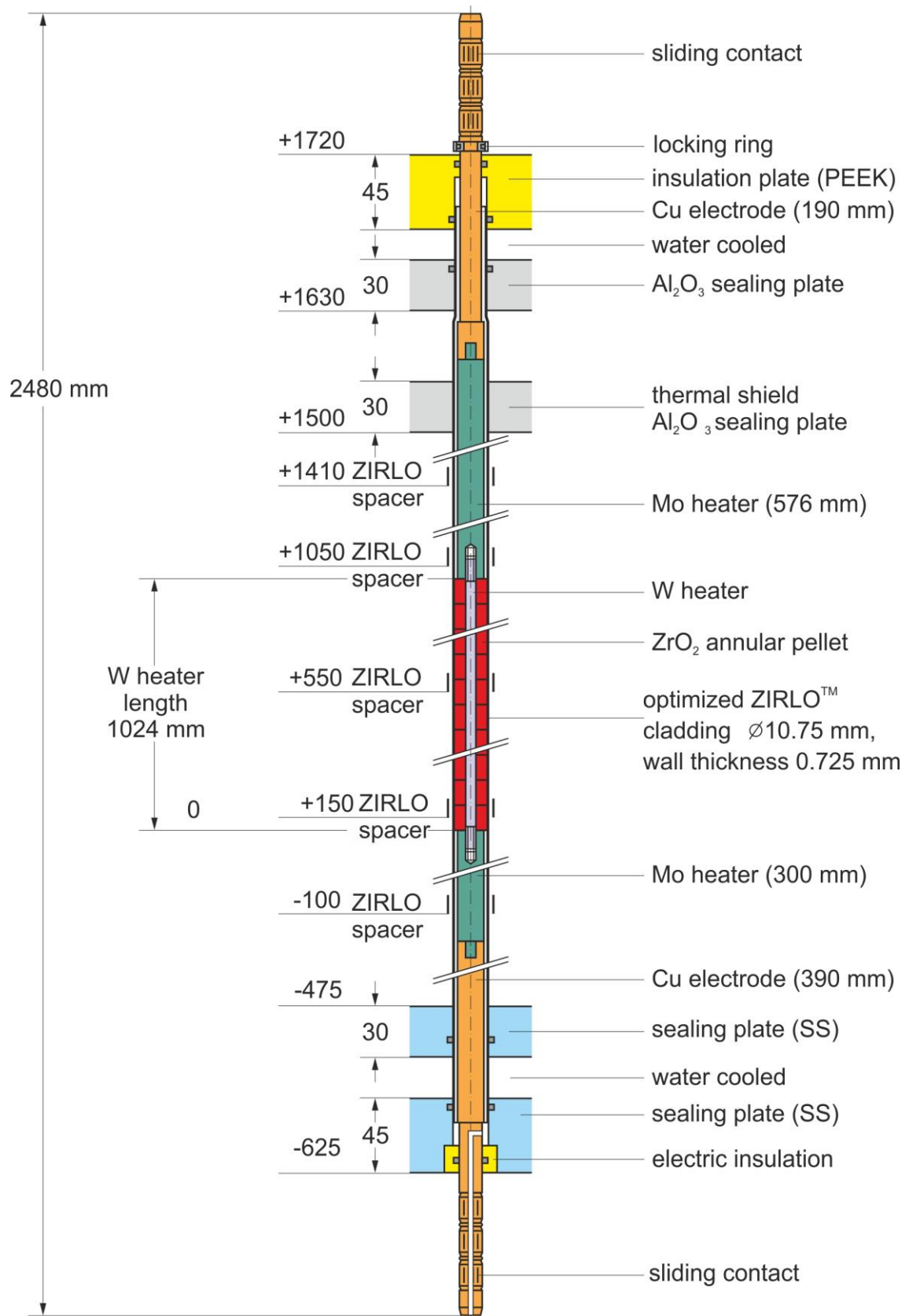
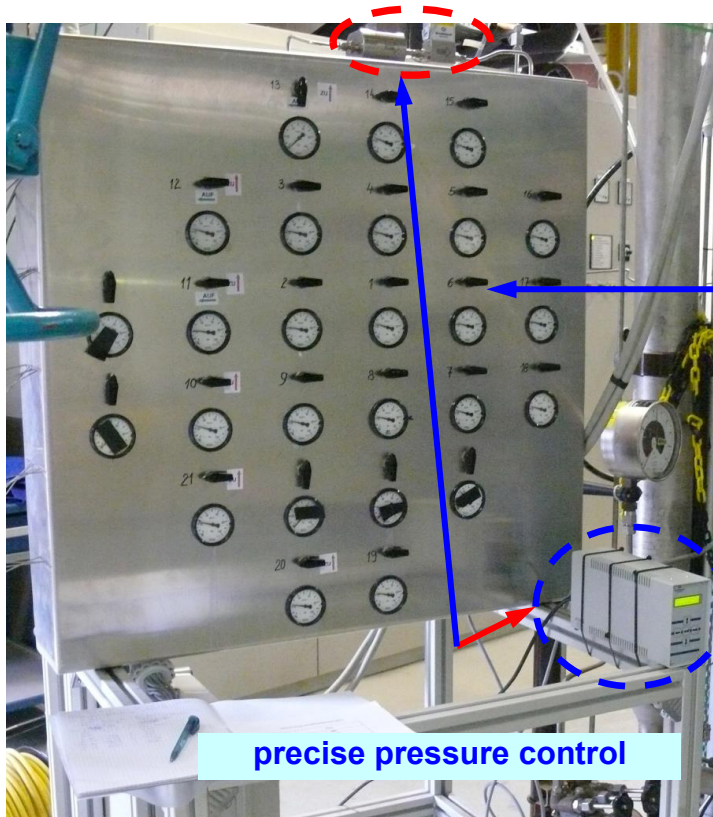
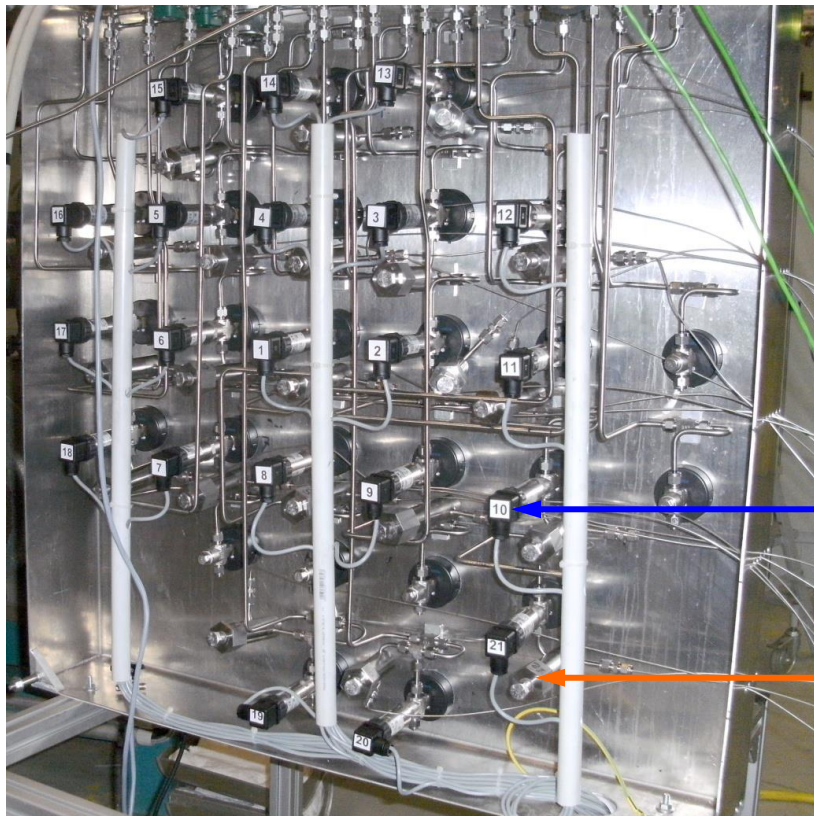


Figure 6 Heated fuel rod simulator.



Front side with:
21 pressure valves

precise pressure control



Rear side with :

21 capillary tubes
to test bundle

21 pressure
transducers

21 adjustable
compensation volumes
to setting of original
volume value
of 31.5 cm^3

Figure 7 QUENCH-L3; Rod pressure control and measurement panel.

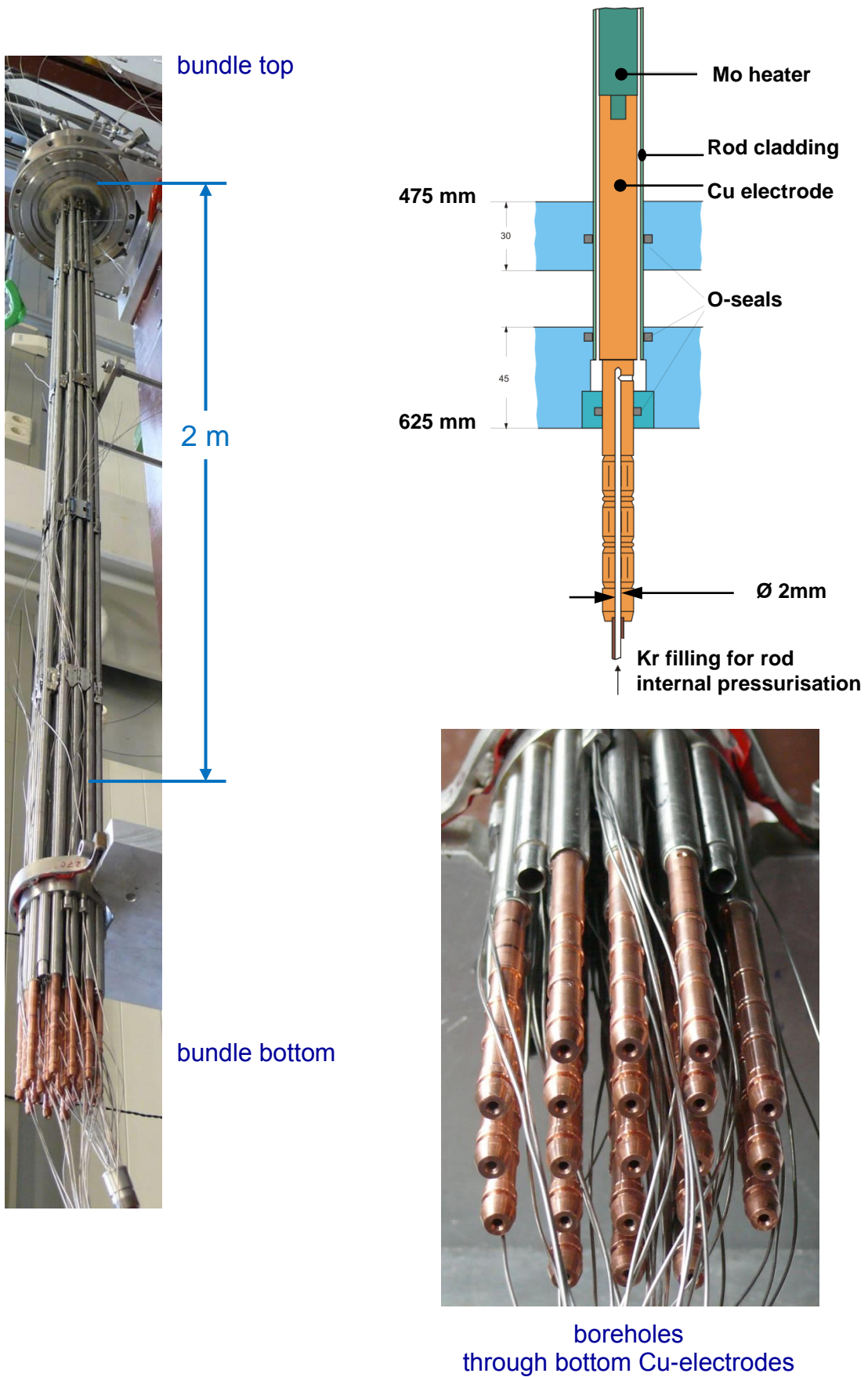


Figure 8 QUENCH-L3; Rod pressurization.

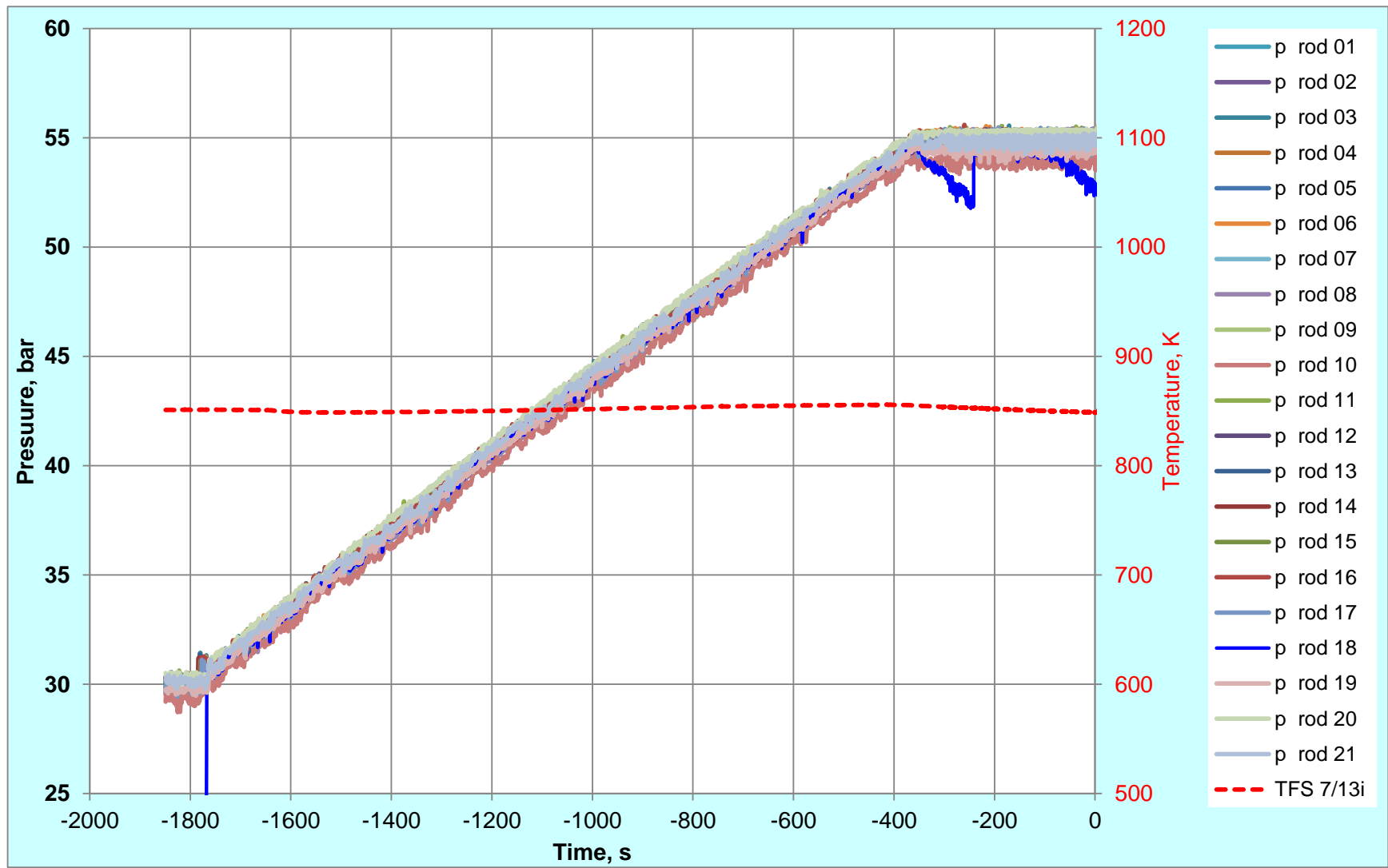


Figure 9 QUENCH-L3; Rod pressurization process at $T_{pct}=850$ K.

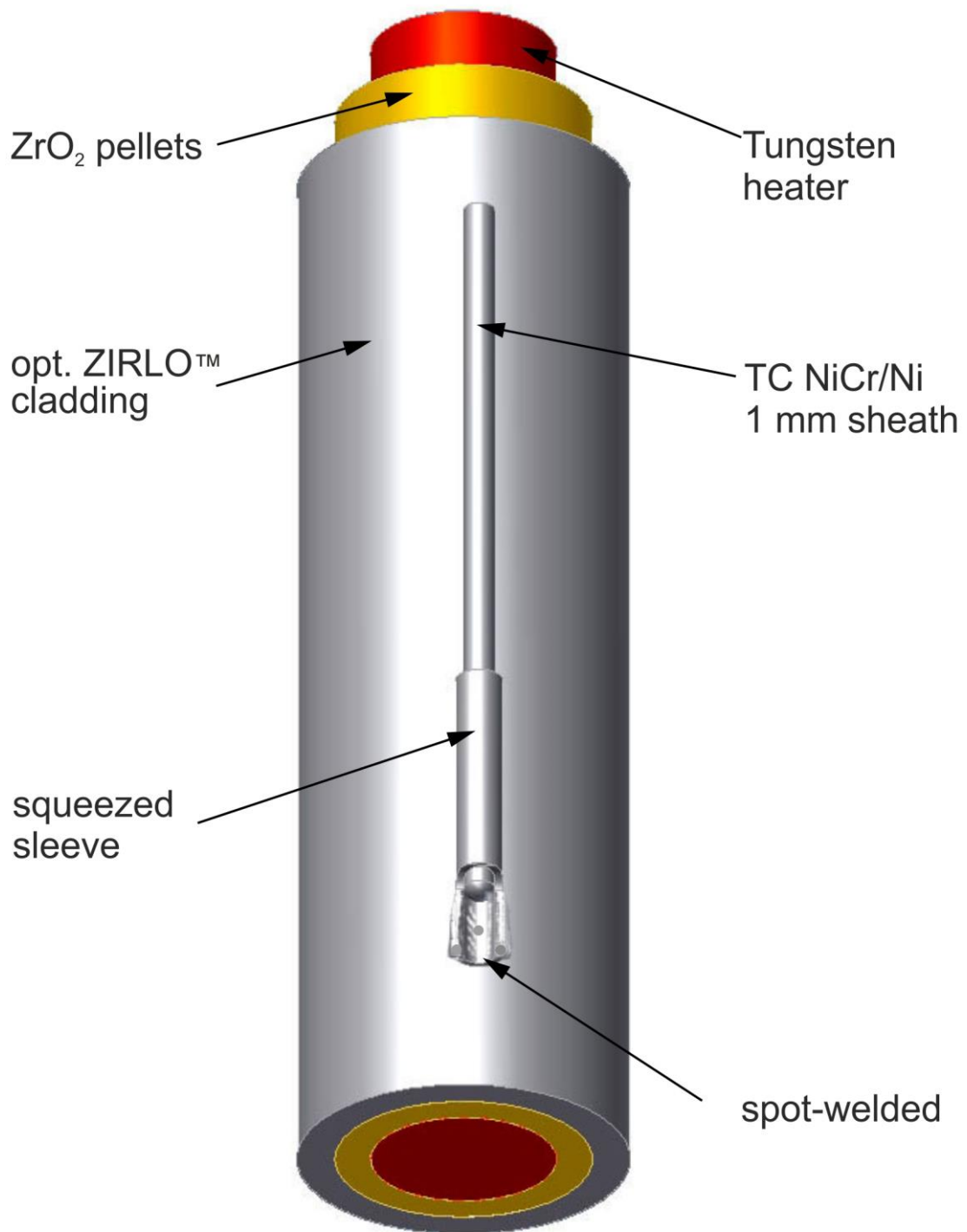


Figure 10 QUENCH-L3; Concept for TC fastening at the test rod.

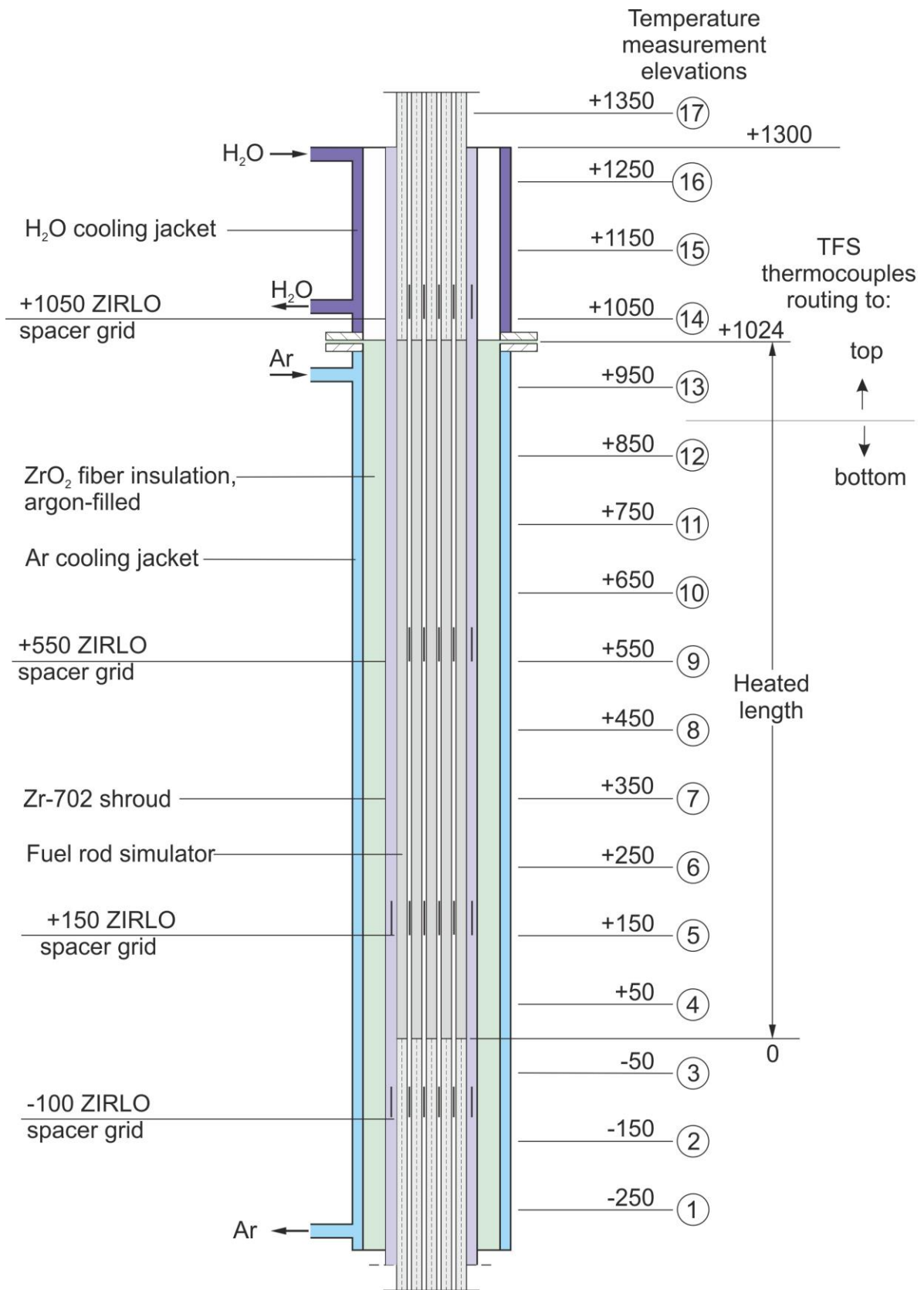


Figure 11 Axial temperature measurement locations in the QUENCH-L3 test section.

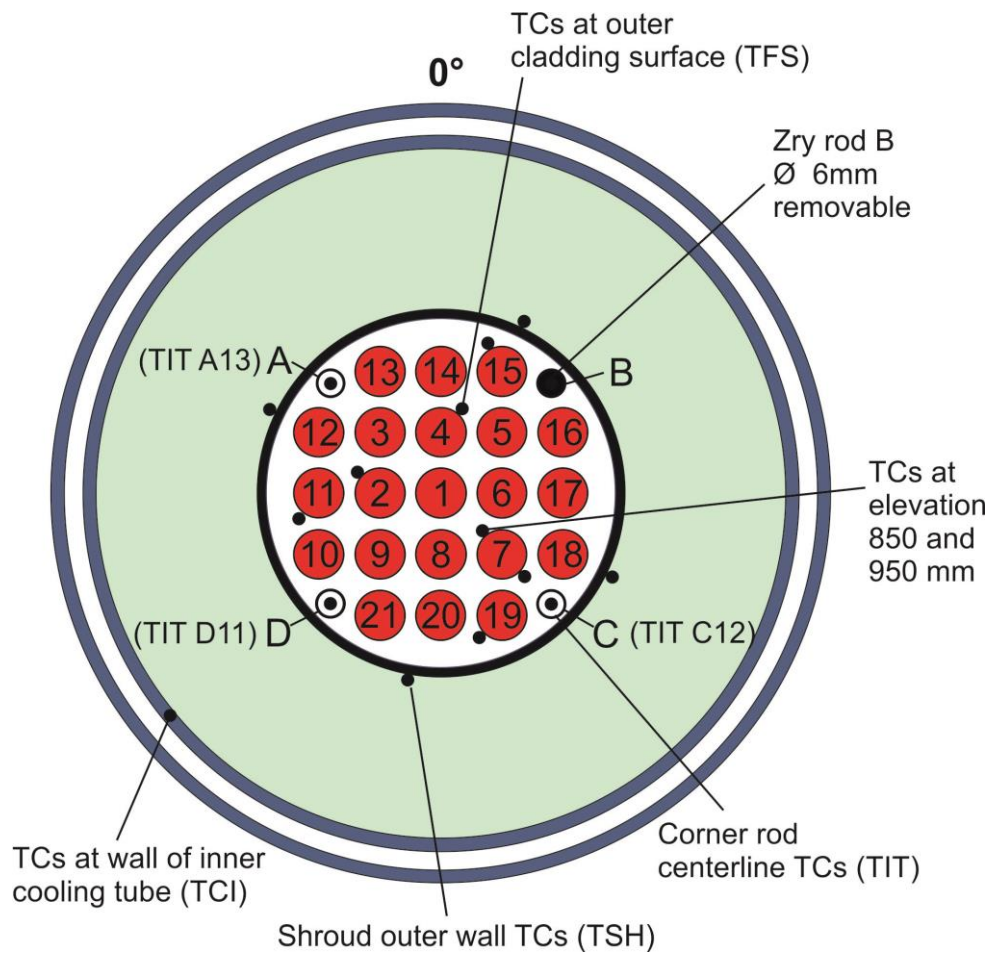
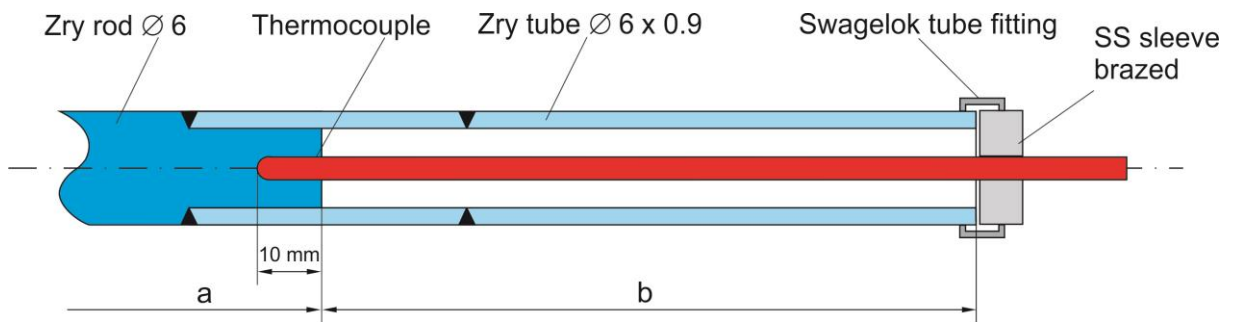


Figure 12 QUENCH-L3; Test bundle; TC instrumentation and rod designation (top view).



Rod A: TIT A13 (950 mm), a = 360 mm, b = 2080 mm
 Rod C: TIT C12 (850 mm), a = 460 mm, b = 1980 mm
 Rod D: TIT D11 (750 mm), a = 560 mm, b = 1880 mm

Figure 13 QUENCH-L3; Arrangement of the thermocouples inside the corner rods.

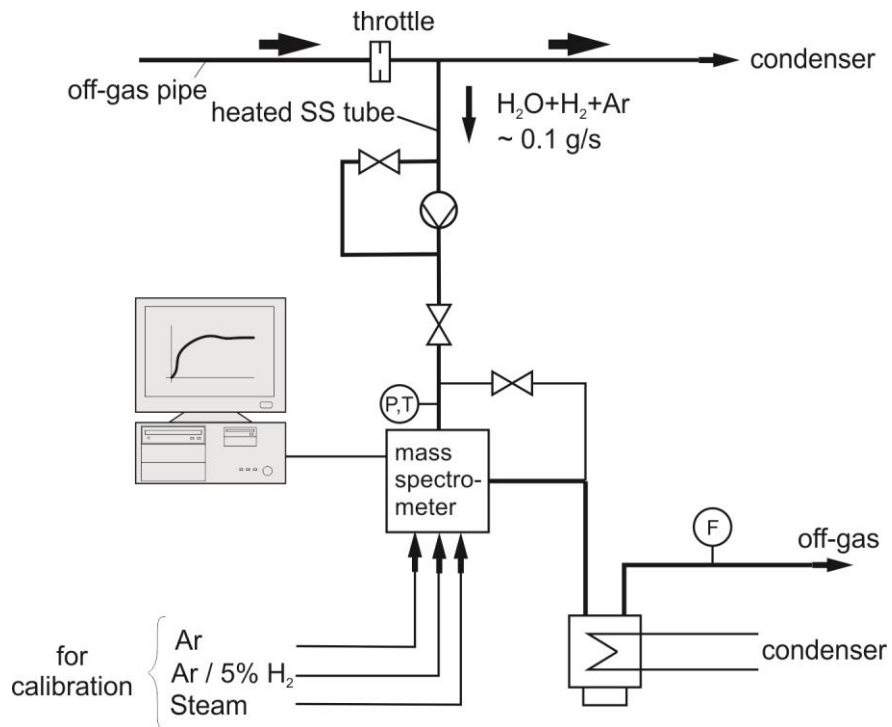


Figure 14 QUENCH Facility; H₂ measurement with the GAM 300 mass spectrometer.

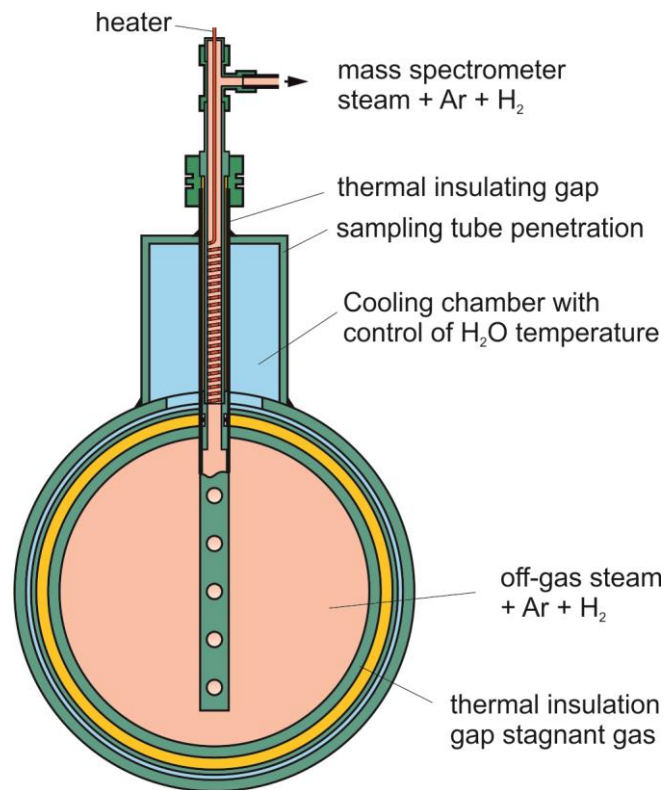


Figure 15 Mass spectrometer sampling position at the off-gas pipe of the QUENCH test facility.

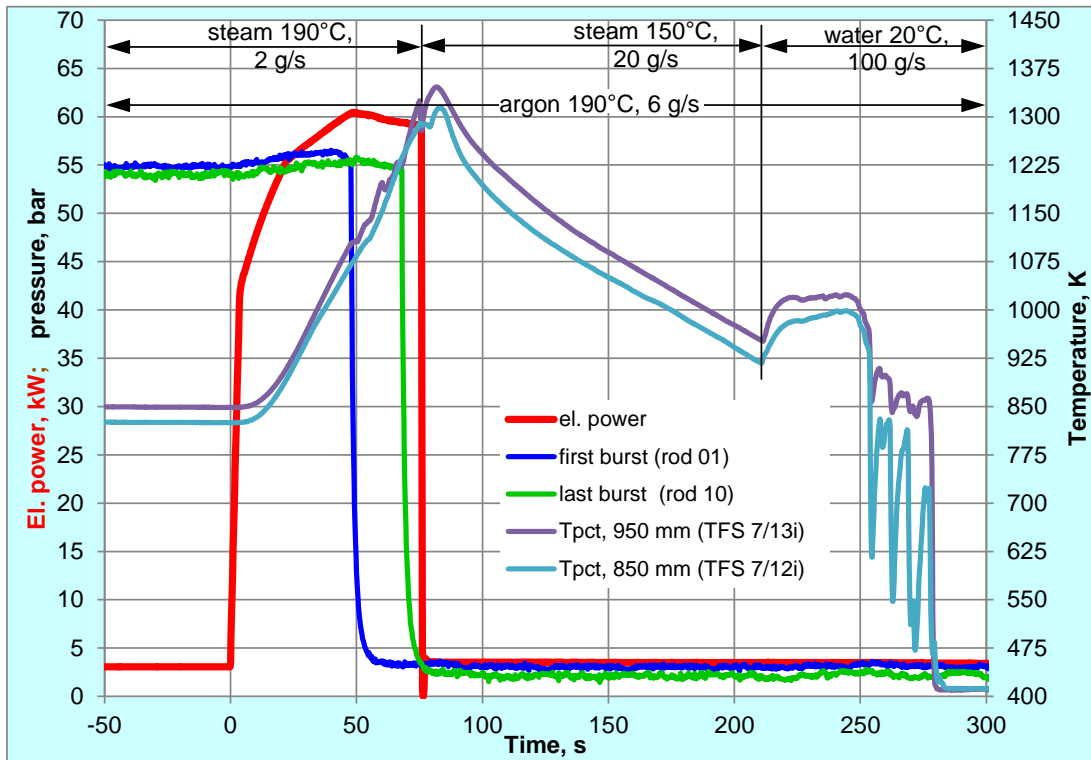


Figure 16 QUENCH-L3; test progress.

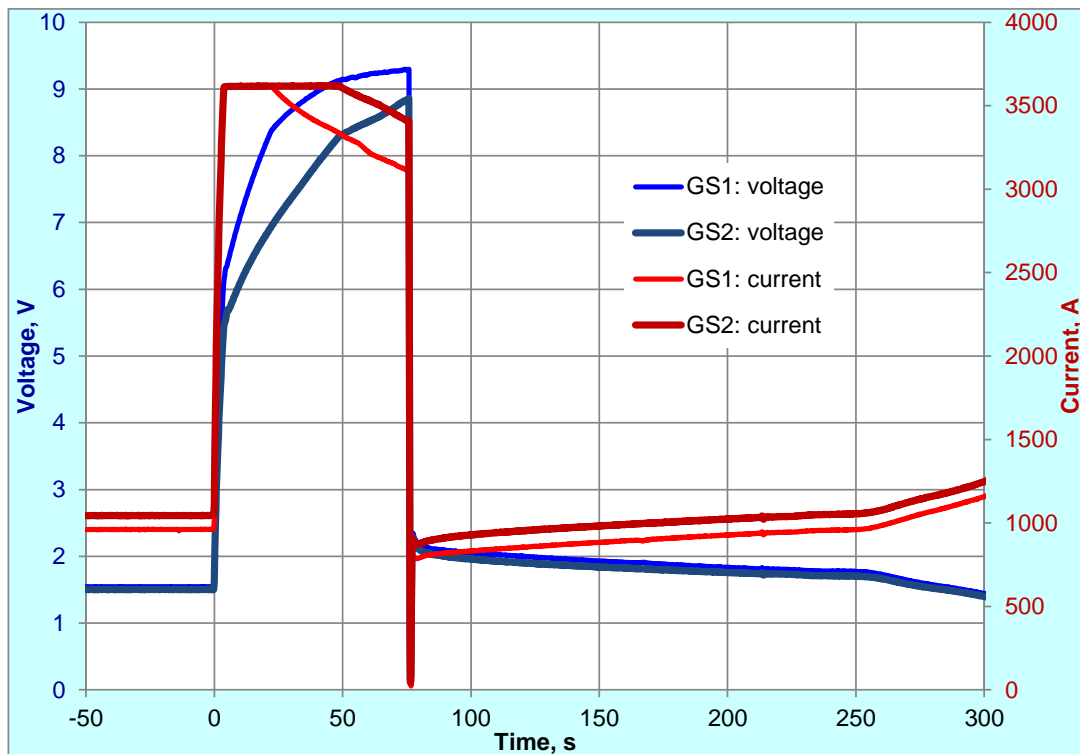


Figure 17 QUENCH-L3; voltage and current of two DC-generators.

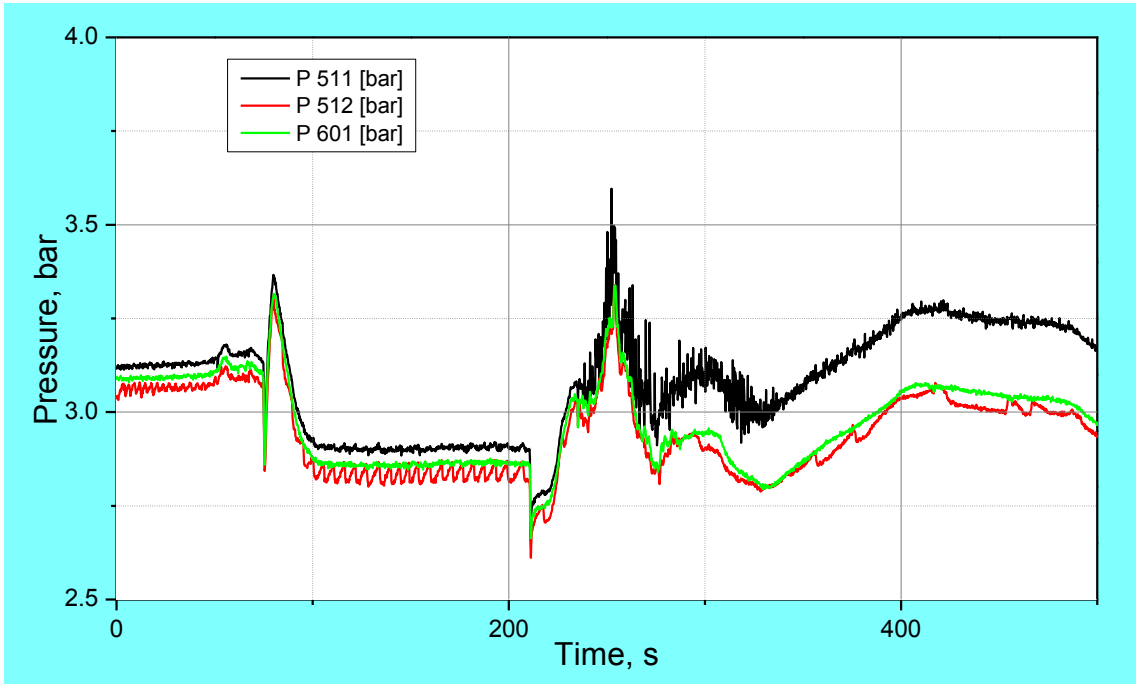


Figure 18 QUENCH-L3; System pressure measured at test section inlet P 511, at outlet P 512, and in the off-gas pipe P 601.

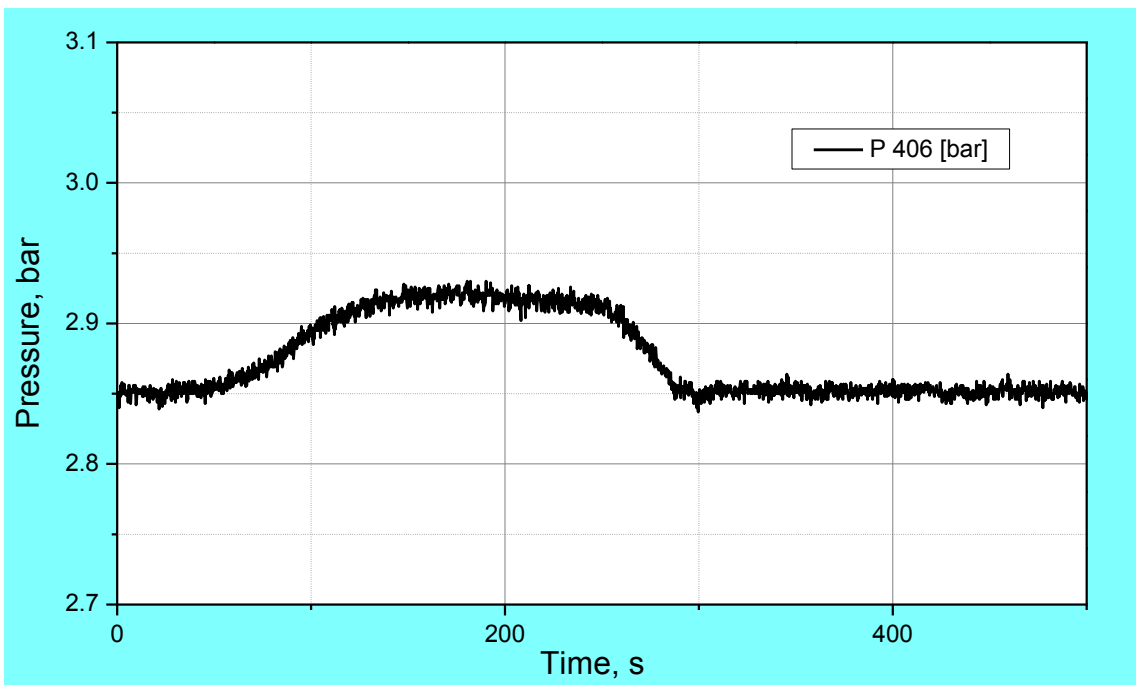


Figure 19 QUENCH-L3; Argon pressure between shroud and cooling jacket P 406 demonstrates tightness of the shroud.

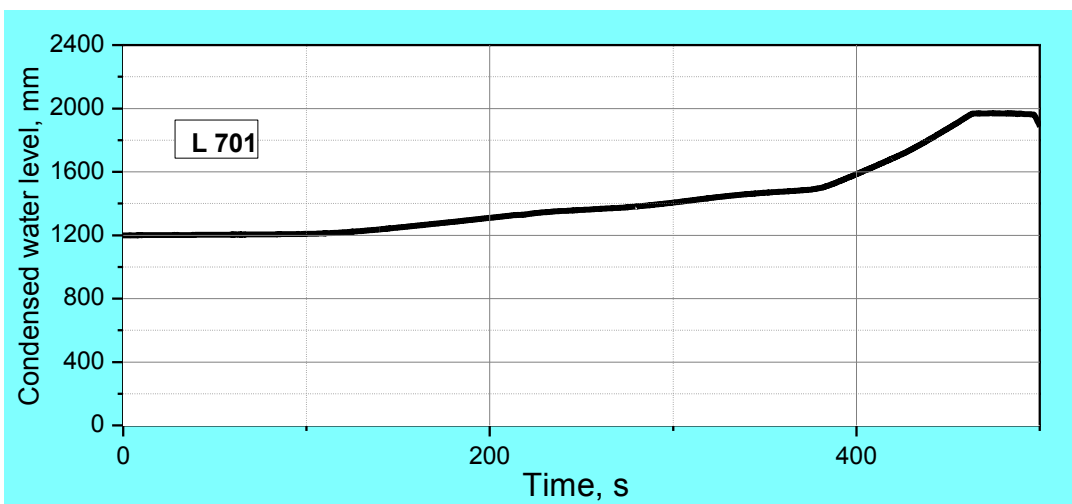
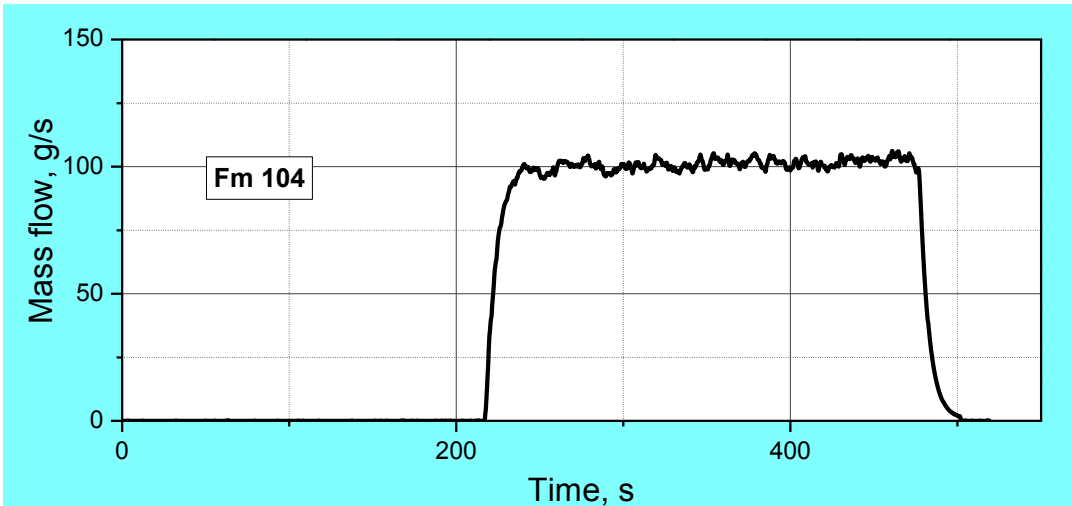
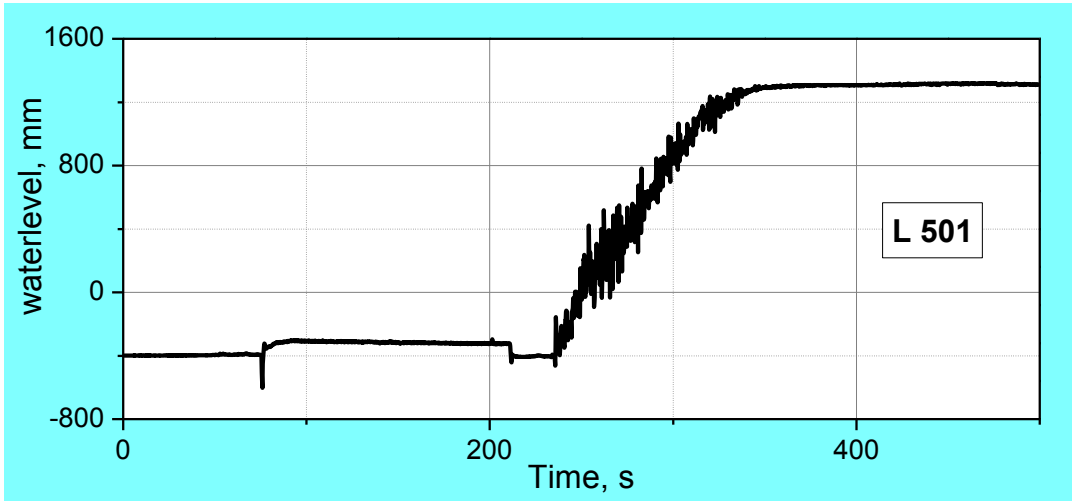


Figure 20 QUENCH-L3; Quench measurement of collapsed water level (L 501), top, water mass flow rate (Fm 104), center, condensed water (L 701), bottom.

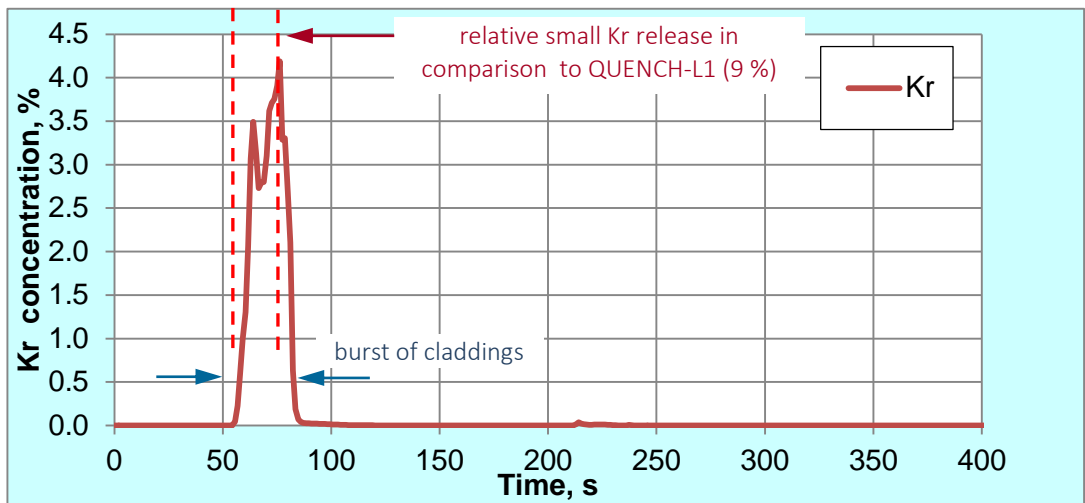
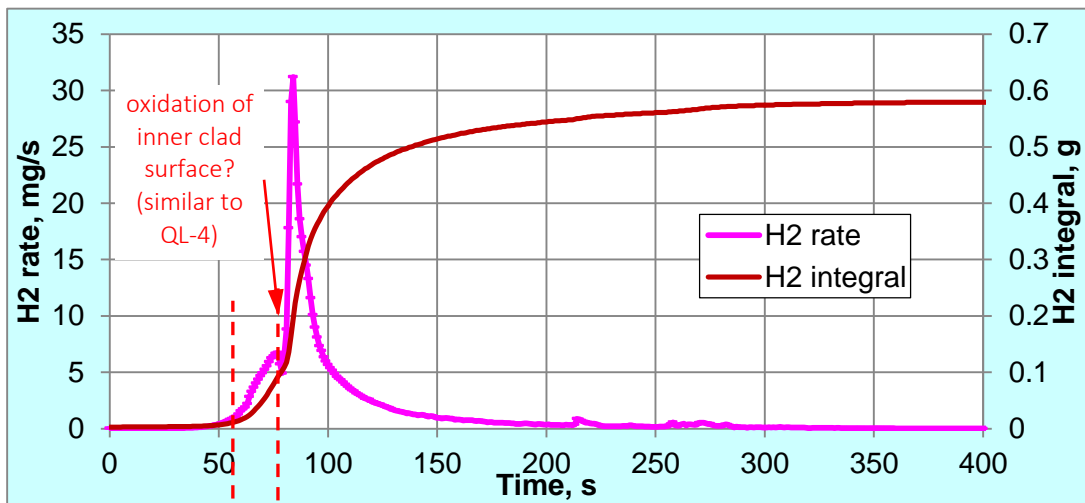
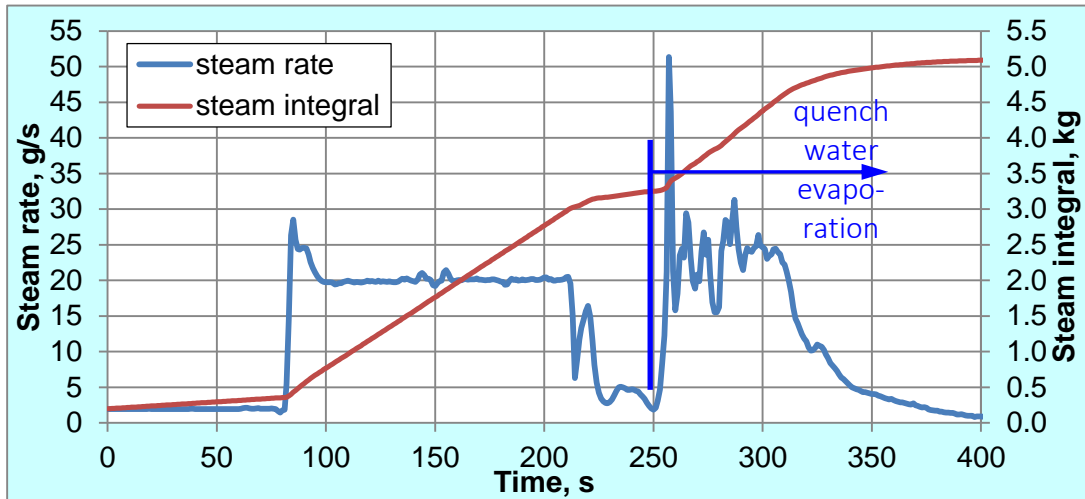


Figure 21 QUENCH-L3; Steam rate and integral mass (top), hydrogen rate and integral mass (middle), krypton concentration (bottom) measured by mass spectrometry.

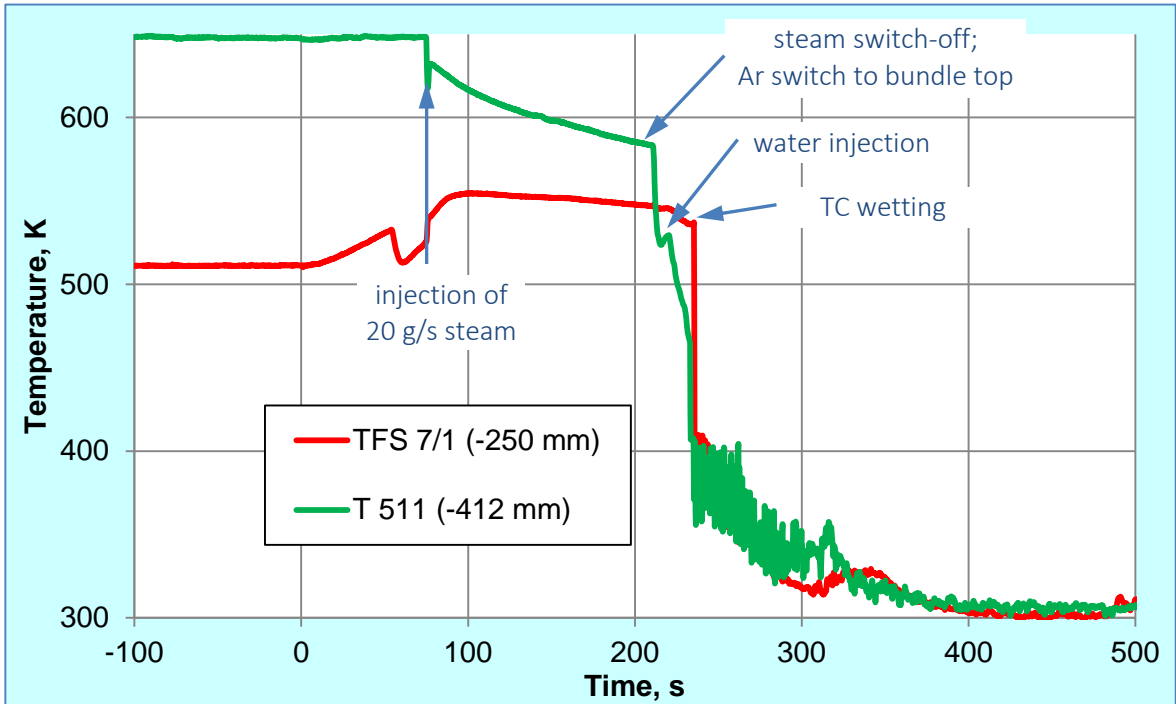


Figure 22 QUENCH-L3; Temperatures measured by gas inlet thermocouple (T 511) at -412 mm and rod cladding (TFS 7/1) thermocouple at -250 mm elevation.

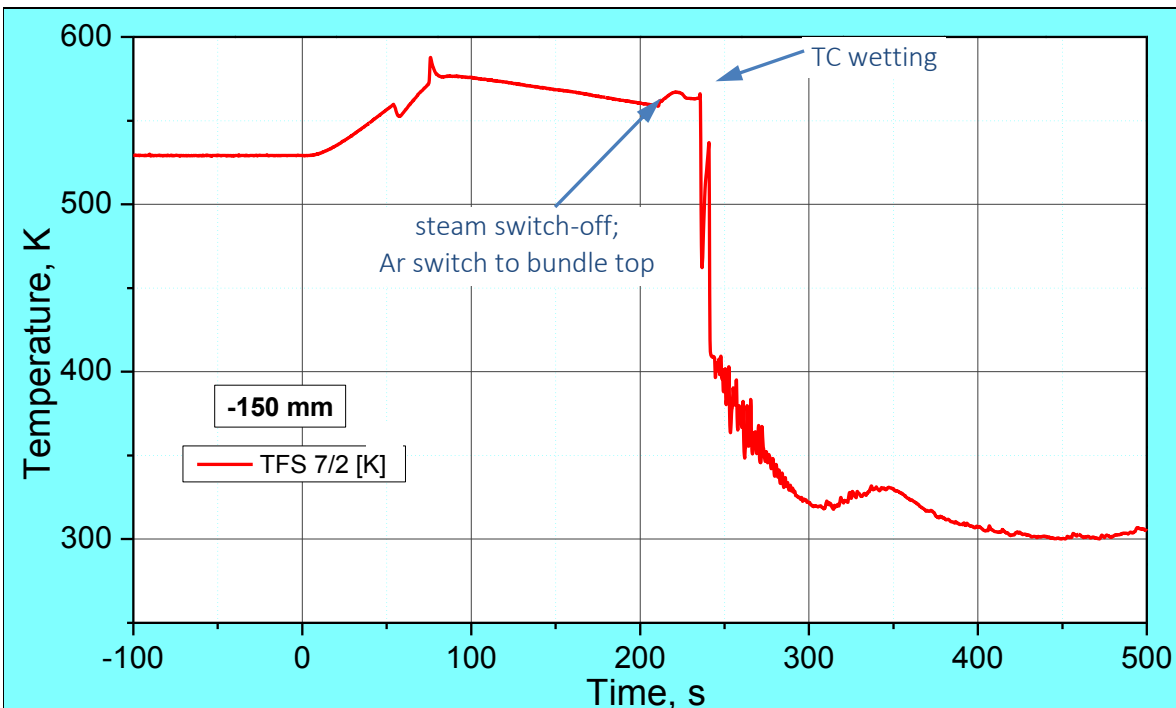


Figure 23 QUENCH-L3; Temperatures measured by rod cladding (TFS 7/2) thermocouple at -150 mm elevation.

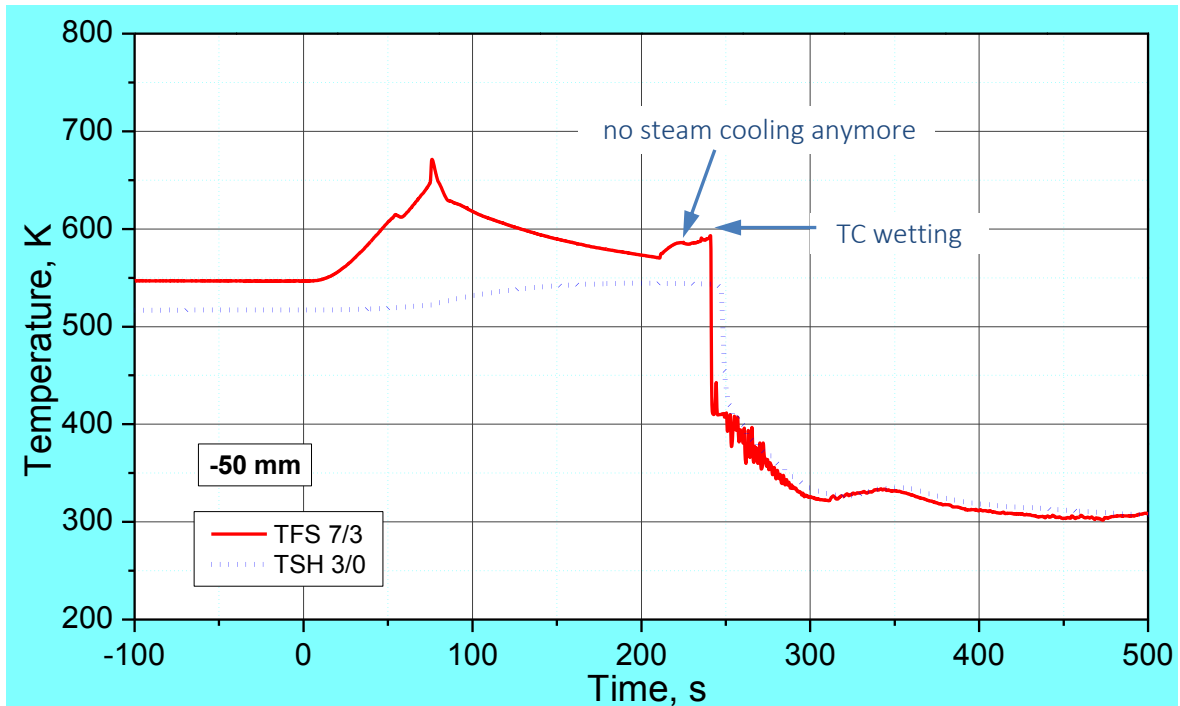


Figure 24 QUENCH-L3; Temperatures measured by rod cladding (TFS 7/3) and shroud (TSH 3/0) thermocouples at -50 mm elevation.

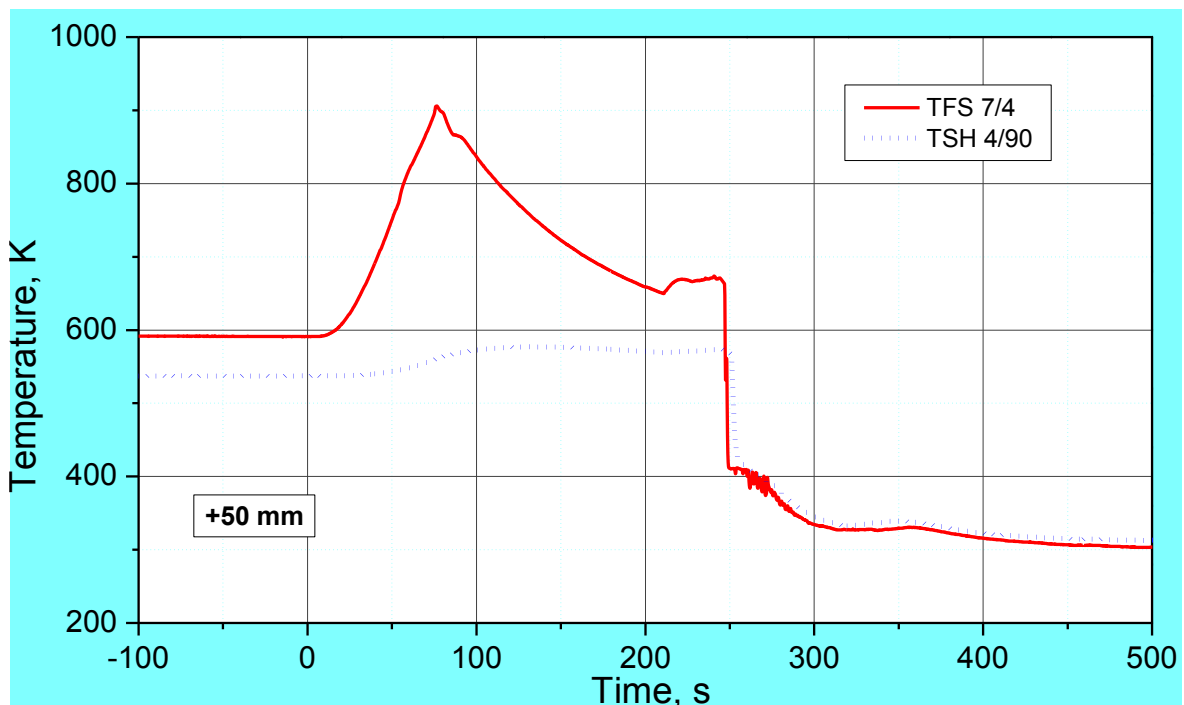


Figure 25 QUENCH-L3; Temperatures measured by rod cladding (TFS 7/4) and shroud (TSH 4/90) thermocouples at 50 mm elevation.

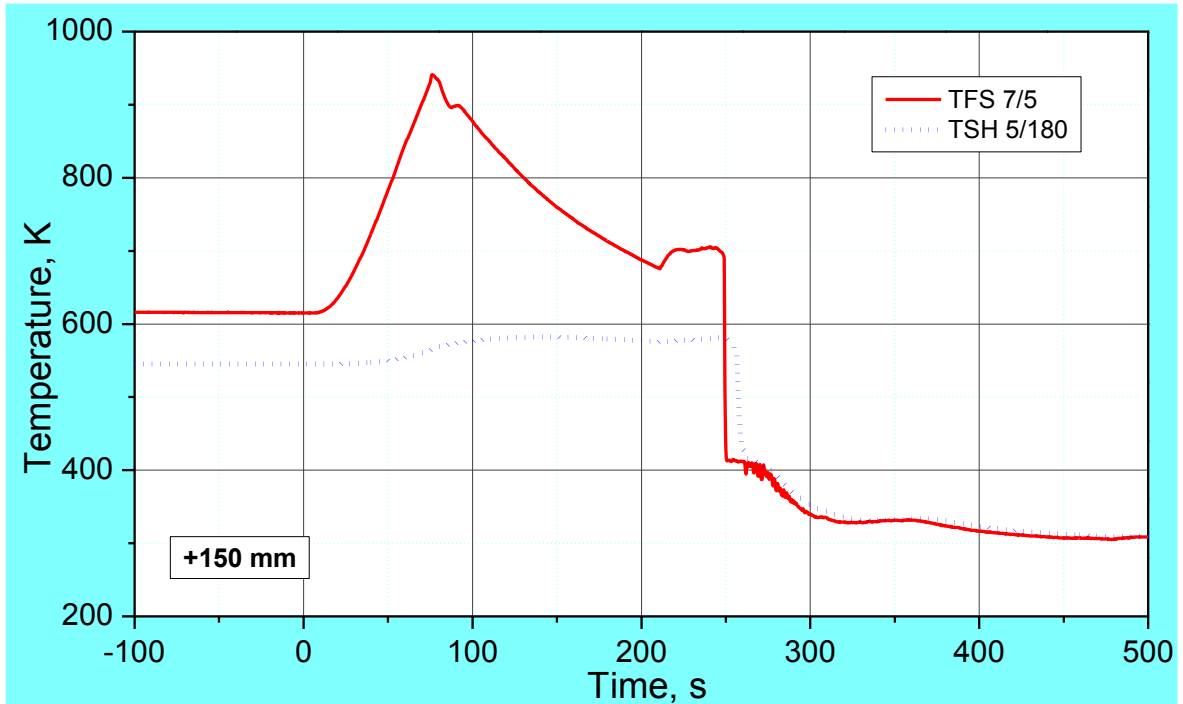


Figure 26 QUENCH-L3; Temperatures measured by rod cladding (TFS 7/5) and shroud (TSH 5/180) thermocouples at 150 mm elevation.

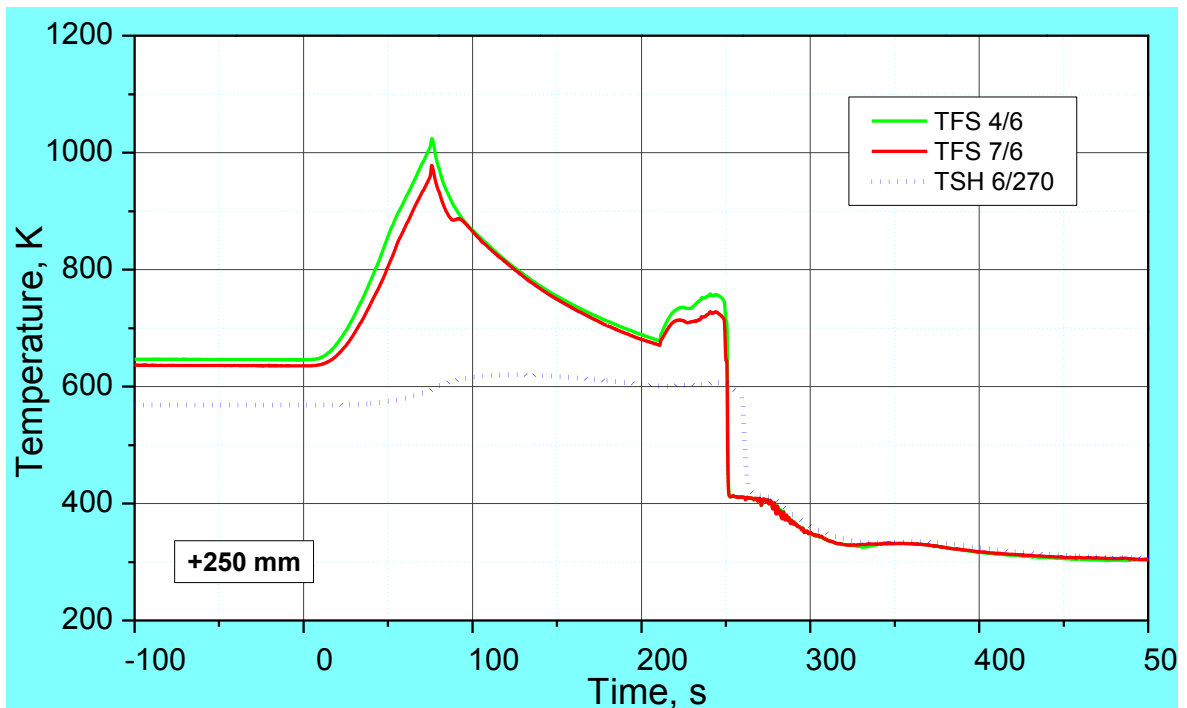


Figure 27 QUENCH-L3; Temperatures measured by rod cladding (TFS) and shroud (TSH 6/270) thermocouples at 250 mm elevation.

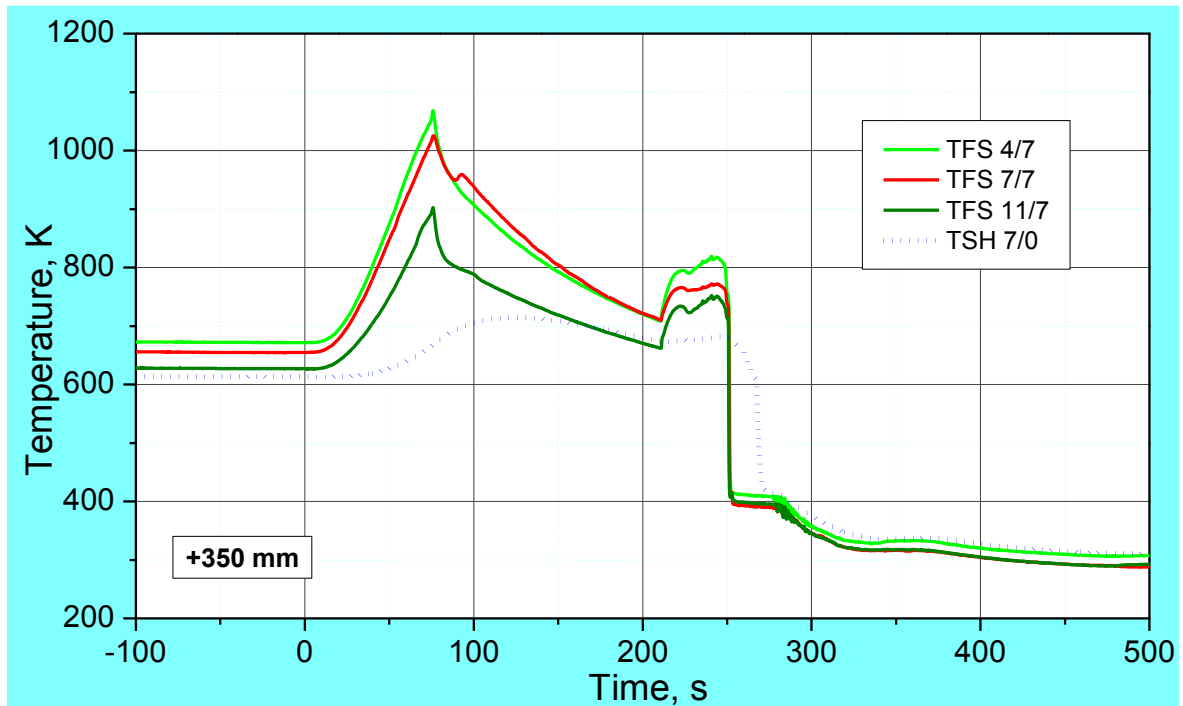


Figure 28 QUENCH-L3; Temperatures measured by rod cladding (TFS) and shroud (TSH 7/0) thermocouples at 350 mm elevation.

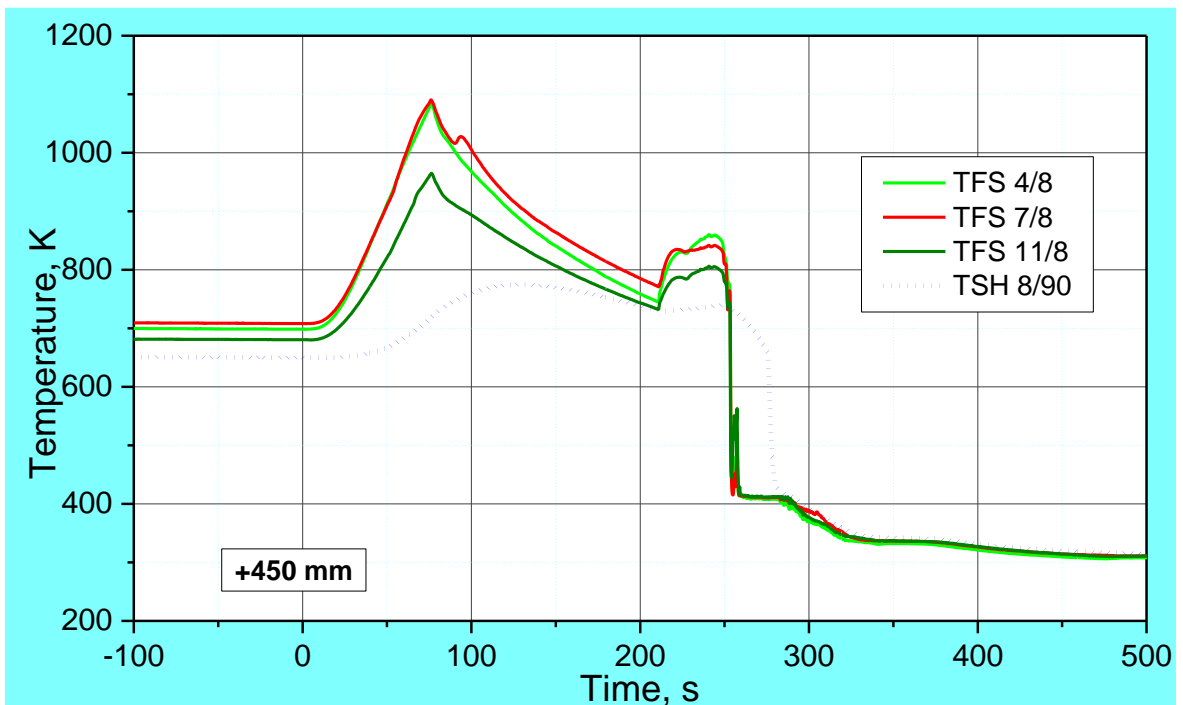


Figure 29 QUENCH-L3; Temperatures measured by rod cladding (TFS) and shroud (TSH 8/90) thermocouples at 450 mm elevation.

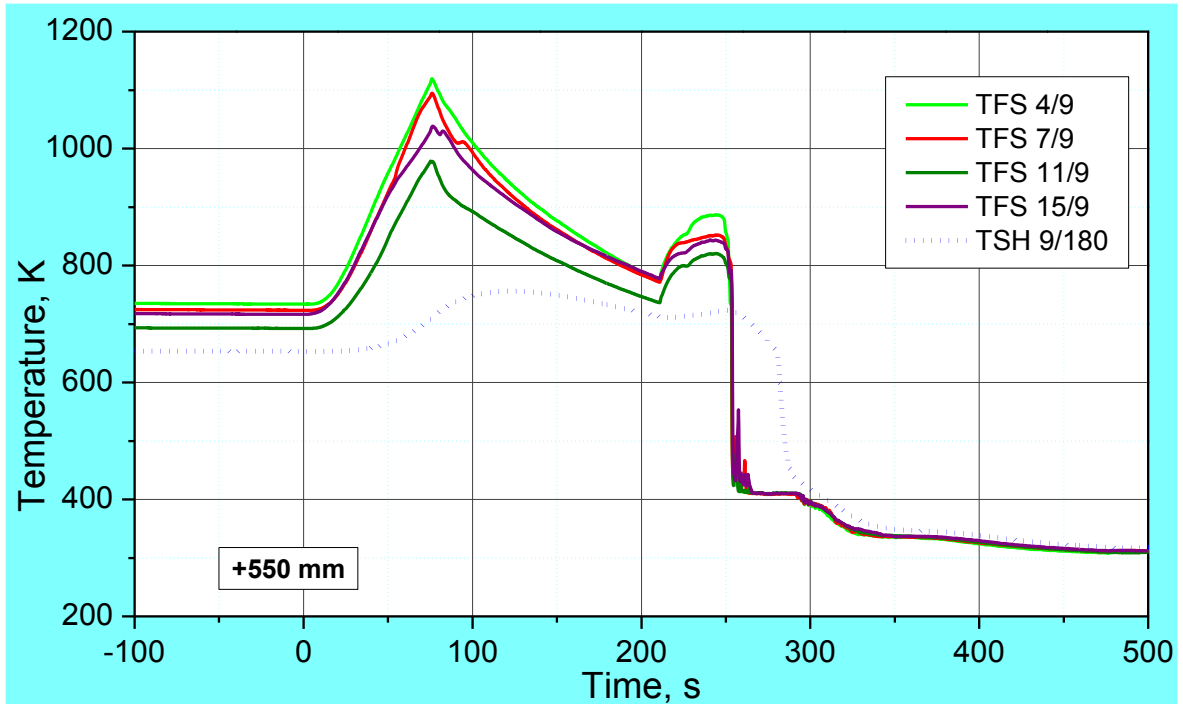


Figure 30 QUENCH-L3; Temperatures measured by rod cladding (TFS) and shroud (TSH 9/180) thermocouples at 550 mm elevation.

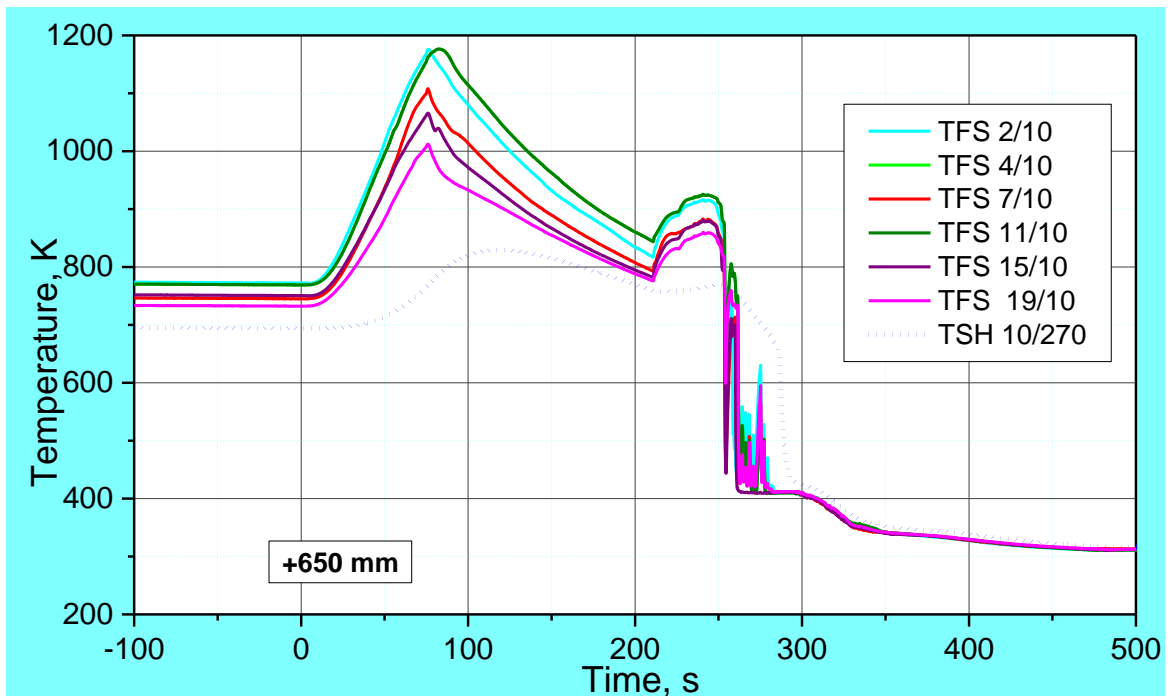


Figure 31 QUENCH-L3; Temperatures measured by rod cladding (TFS) and shroud (TSH 10/270) thermocouples at 650 mm elevation.

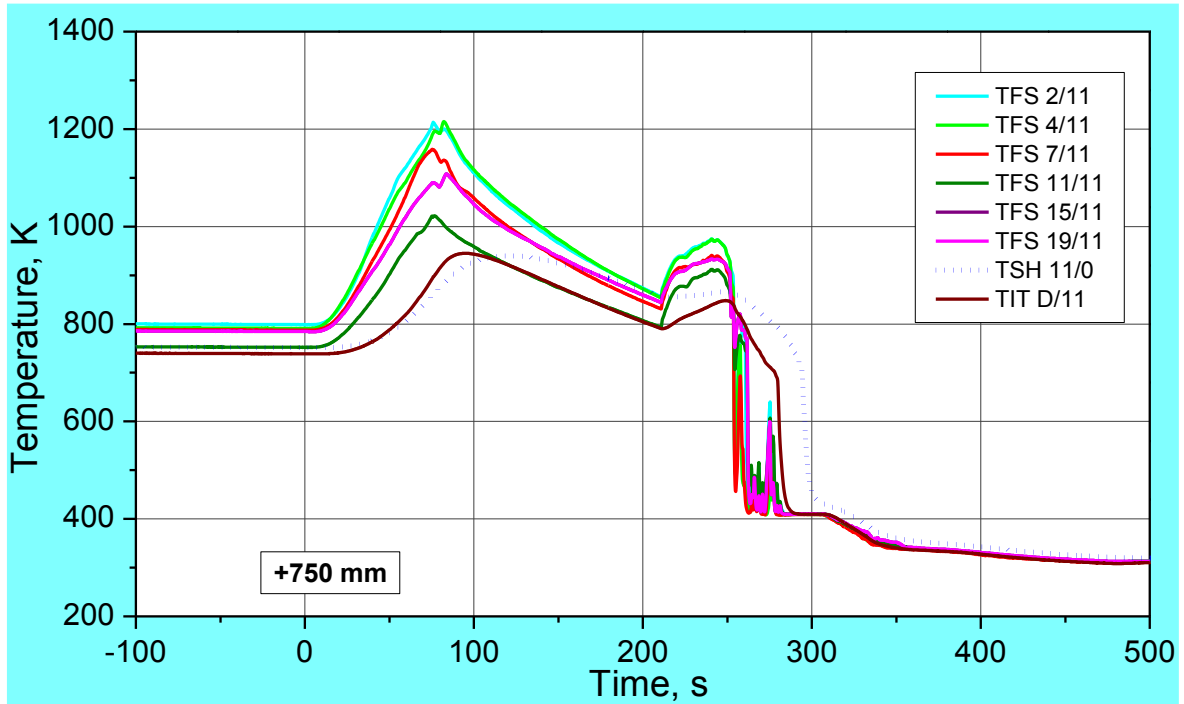


Figure 32 QUENCH-L3; Temperatures measured by rod cladding (TFS) and shroud (TSH 11/0), and corner rod internal (TIT D/11) thermocouples at 750 mm elevation.

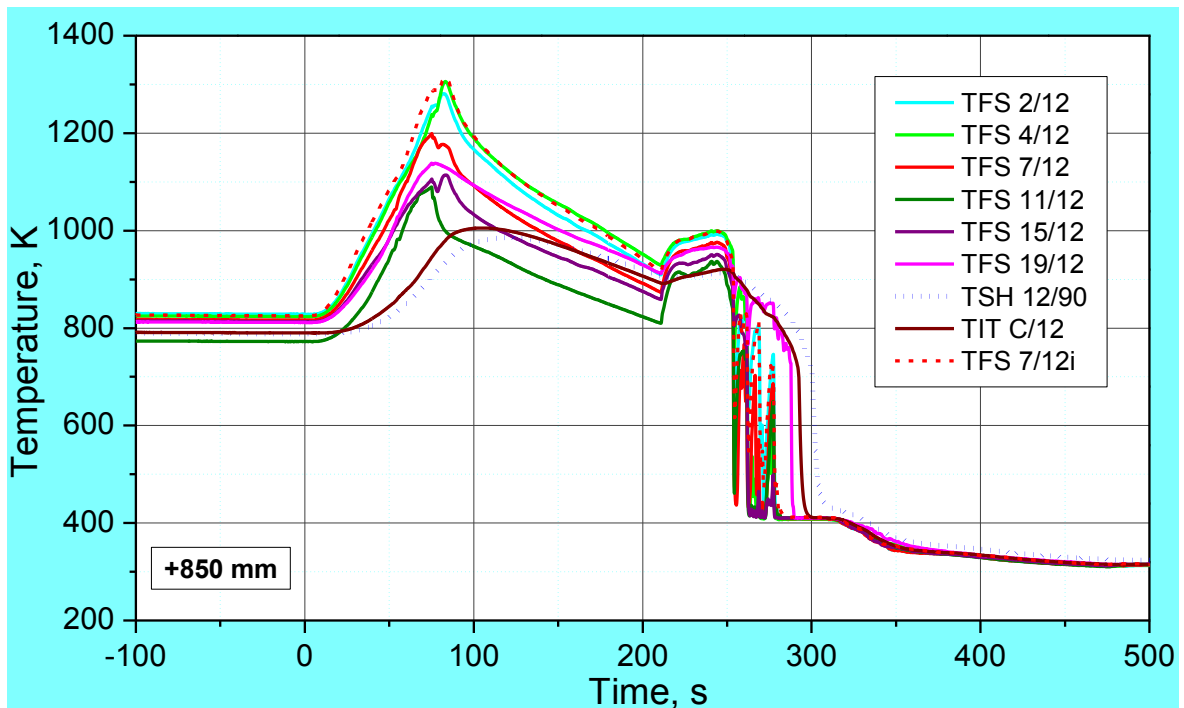


Figure 33 QUENCH-L3; Temperatures measured by rod cladding (TFS) and shroud (TSH 12/90), and corner rod internal (TIT C/12) thermocouples at 850 mm elevation.

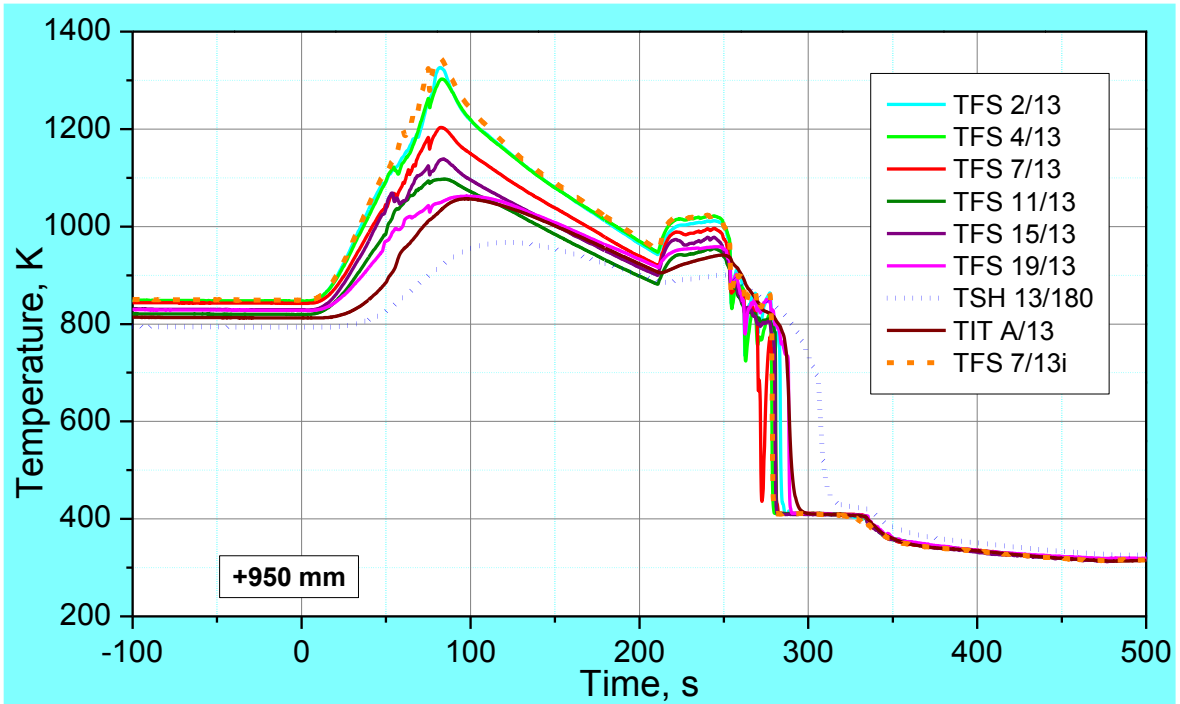


Figure 34 QUENCH-L3; Temperatures measured by rod cladding (TFS) and shroud (TSH 13/180), and corner rod internal (TIT A/13) thermocouples at 950 mm elevation.

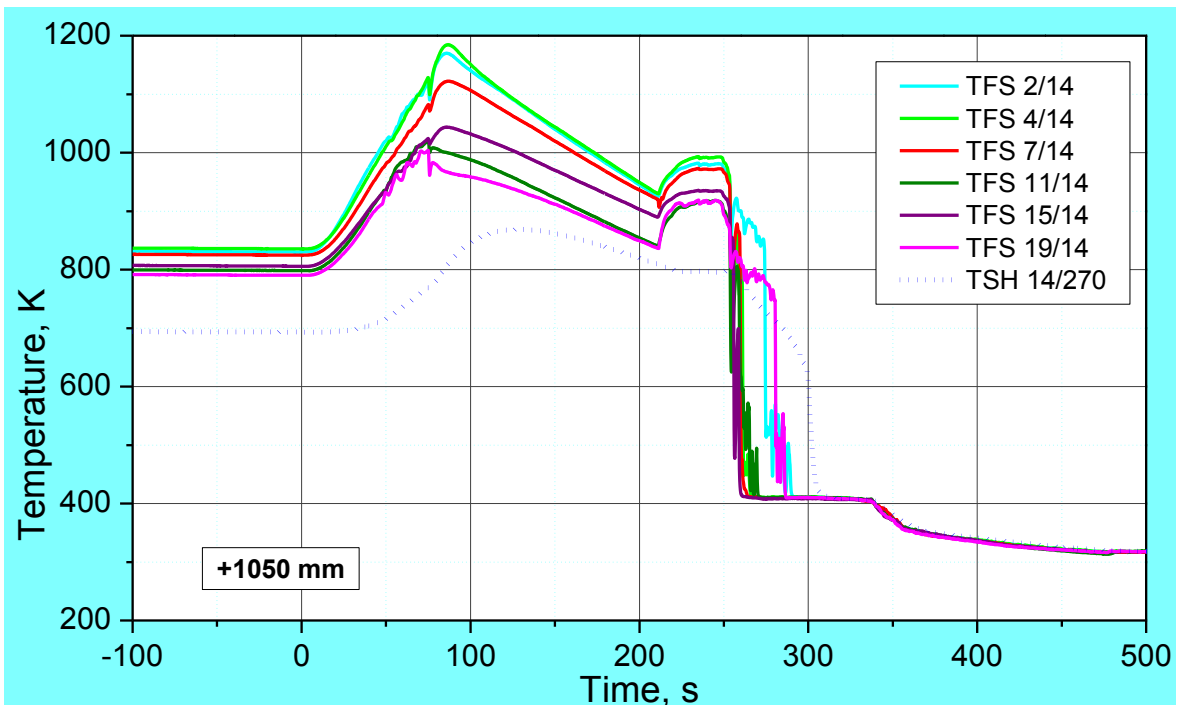


Figure 35 QUENCH-L3; Temperatures measured by rod cladding (TFS) and shroud (TSH 14/270) thermocouples at 1050 mm elevation.

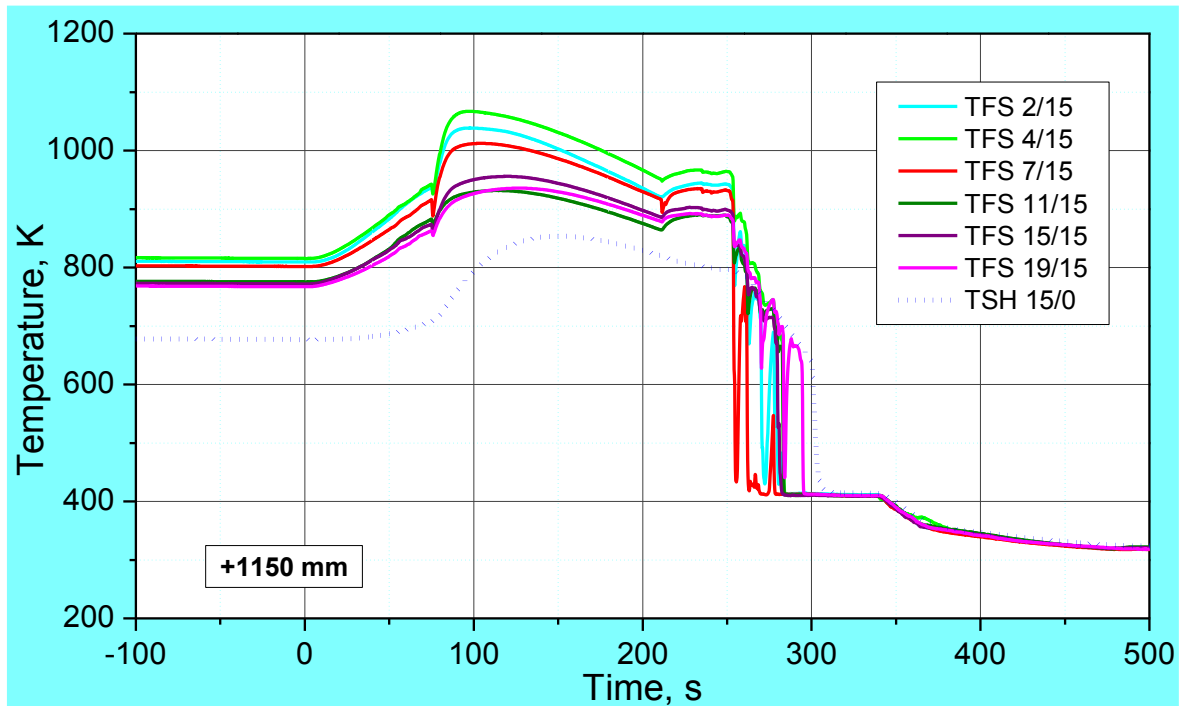


Figure 36 QUENCH-L3; Temperatures measured by rod cladding (TFS) and shroud (TSH 15/0) thermocouples at 1150 mm elevation.

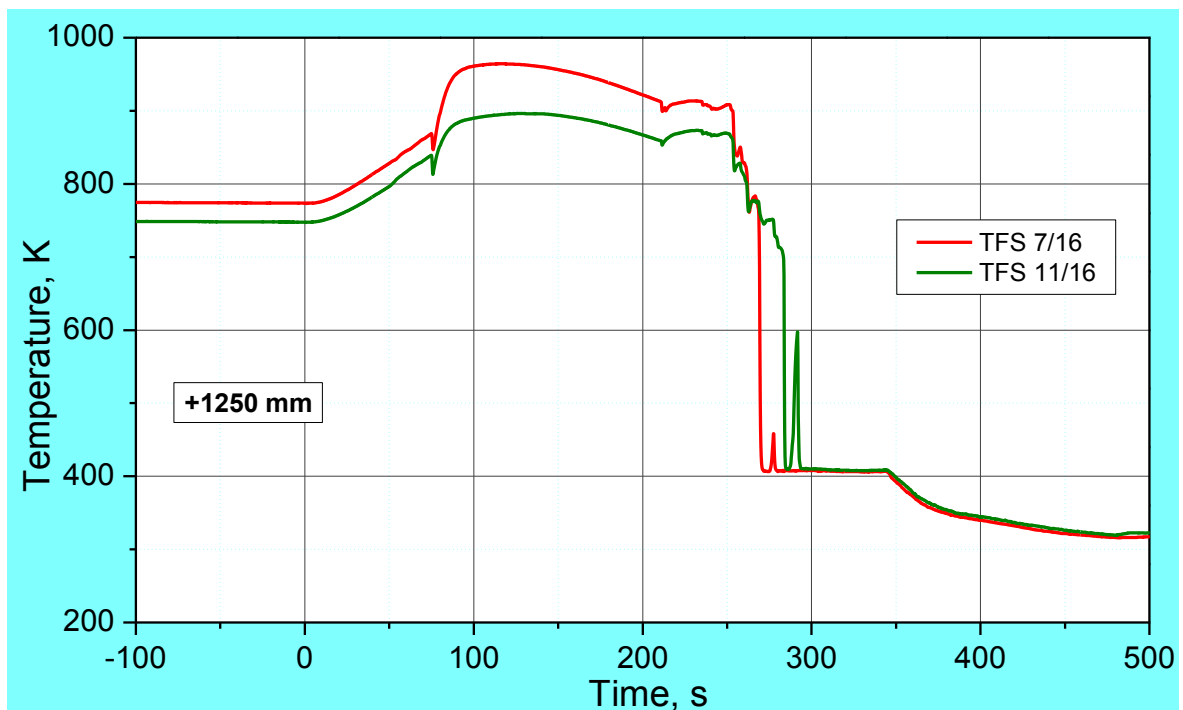


Figure 37 QUENCH-L3; Temperatures measured by rod cladding (TFS) thermocouples at 1250 mm elevation.

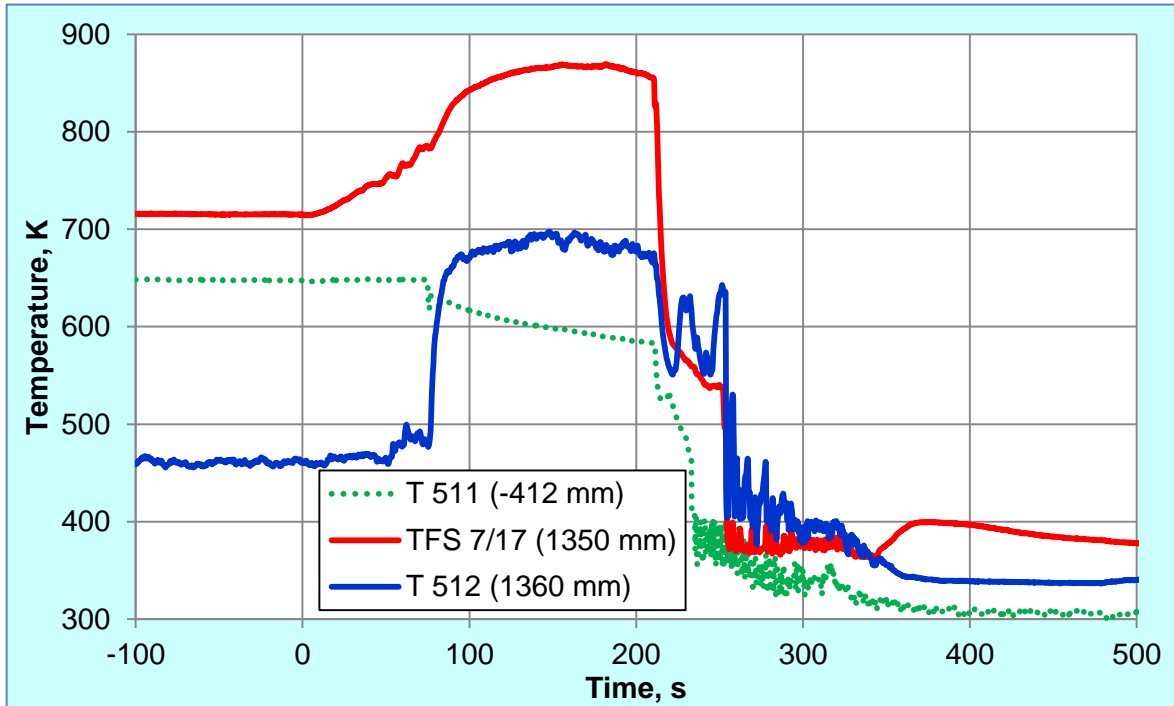


Figure 38 QUENCH-L3; Temperatures measured by rod cladding (TFS 7/17) thermocouple at 1350 mm elevation and gas temperature (T 512) thermocouple between shroud and rod #20; T 511 depicts the gas temperature at the bundle inlet.

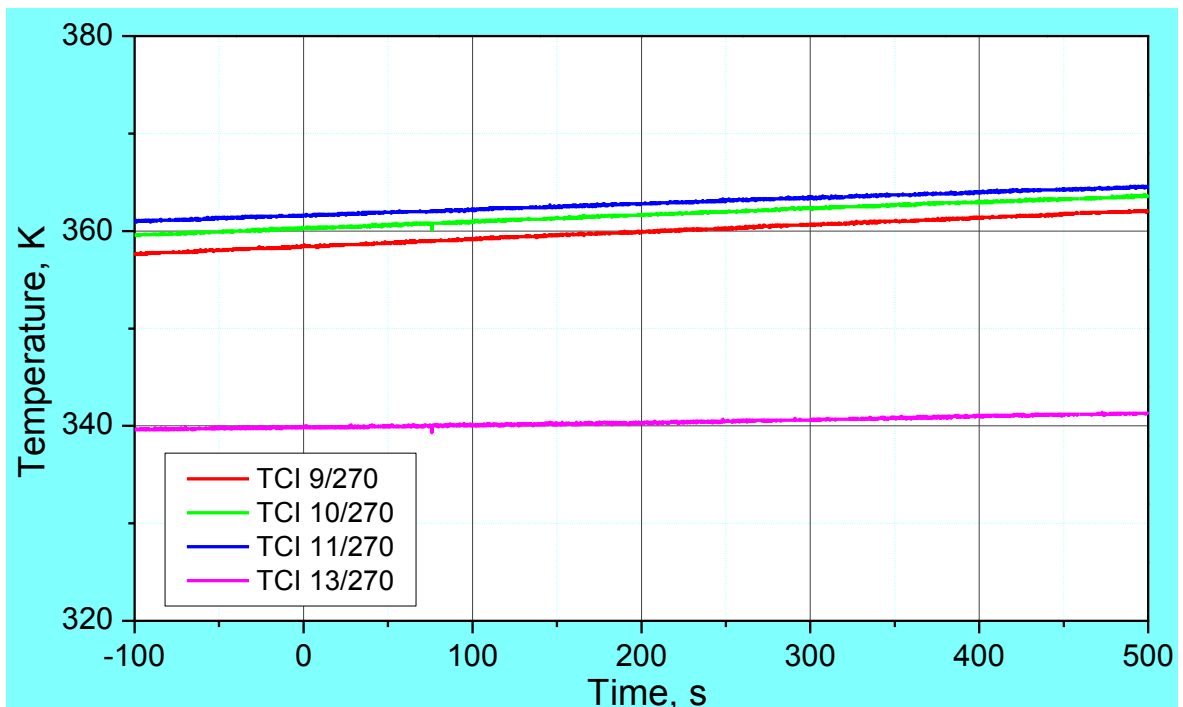


Figure 39 QUENCH-L3; Overview of the TCI (inner cooling jacket).

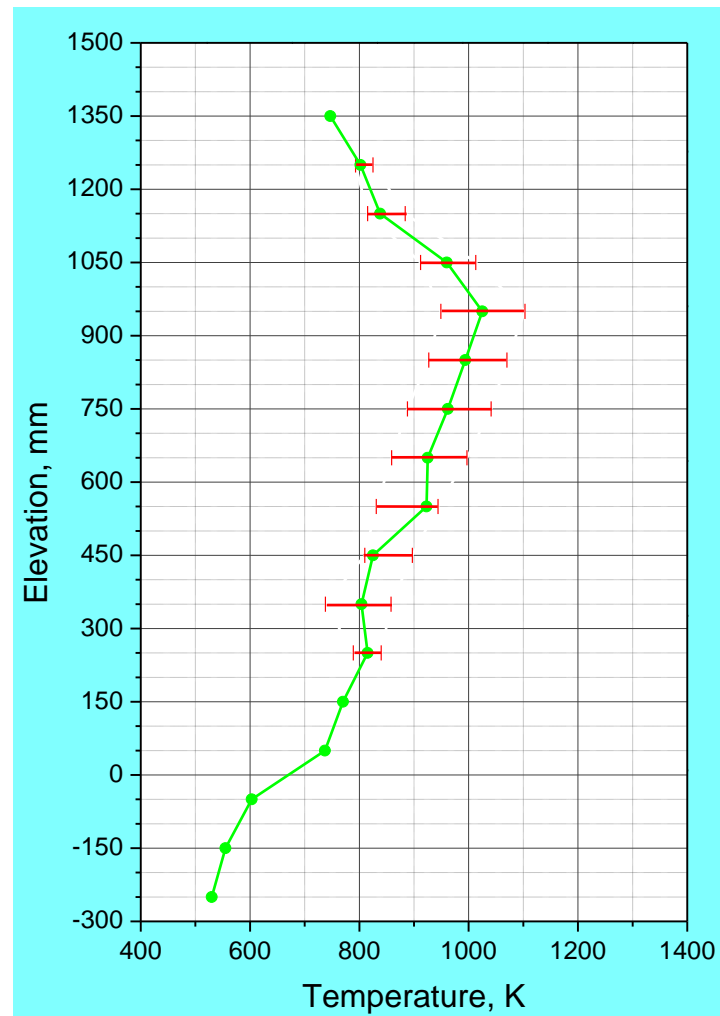
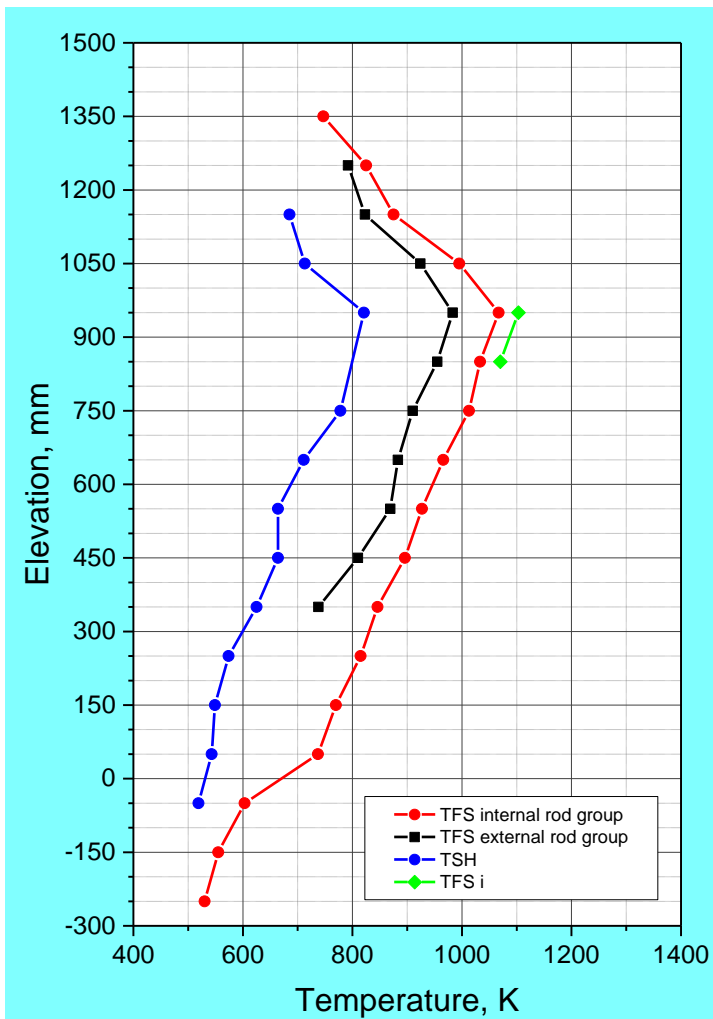


Figure 40 QUENCH-L3; Axial temperature profile TFS internal and external rod group together with TSH, left, and axial temperature profile of all TFS, right, at 47,8 s (first cladding burst).

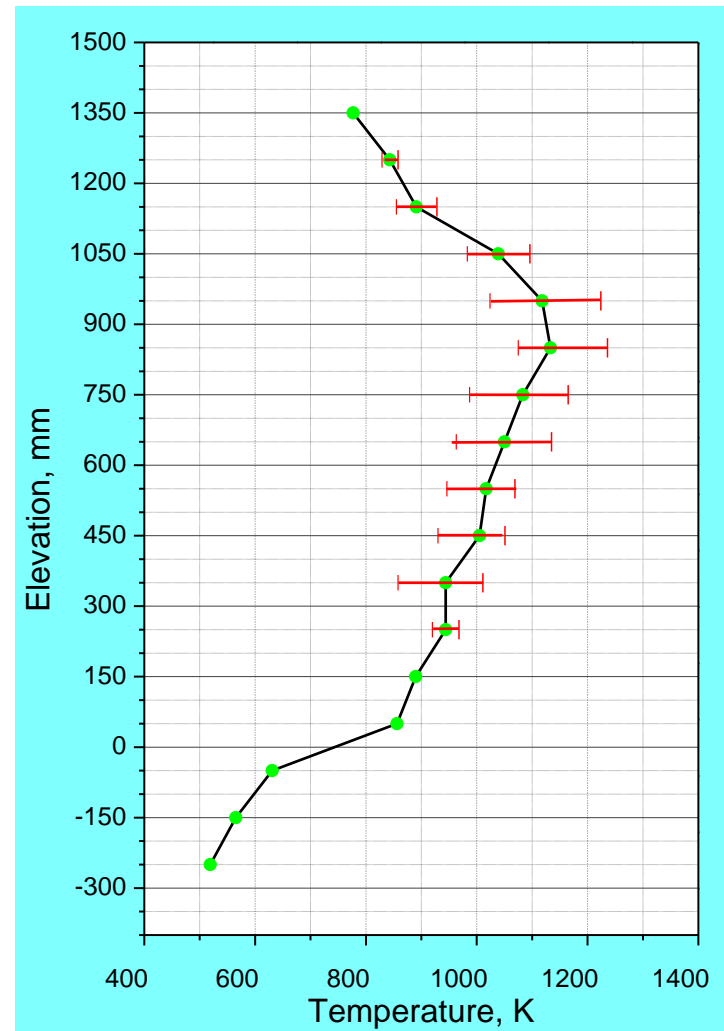
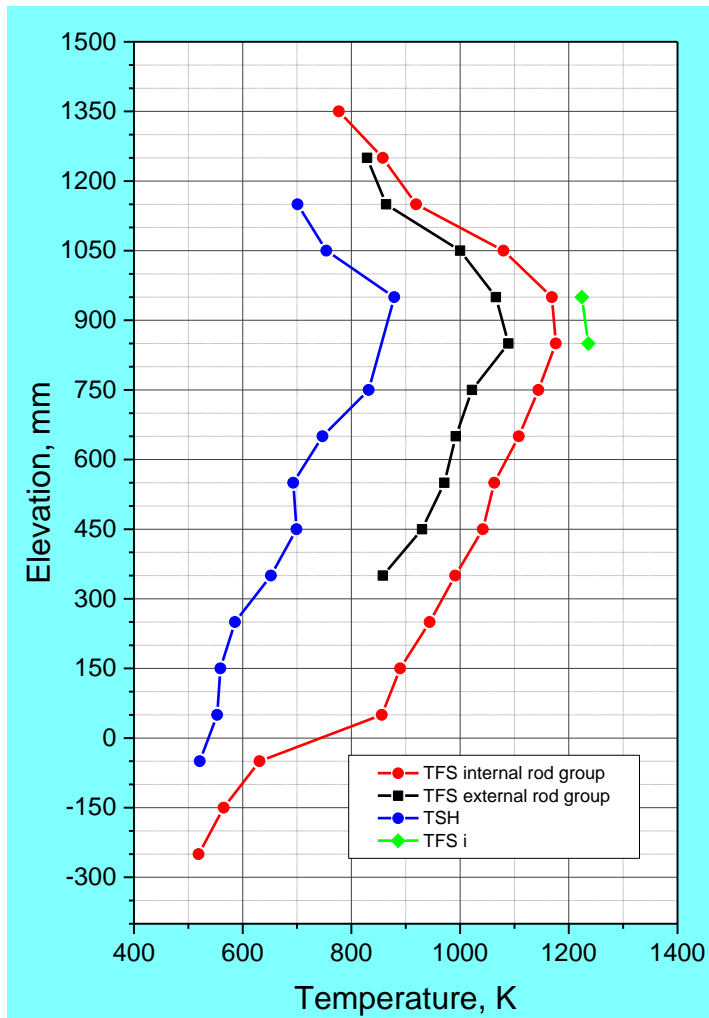


Figure 41 QUENCH-L3; Axial temperature profile TFS internal and external rod group together with TSH, left, and axial temperature profile of all TFS, right, at 68 s (last cladding burst).

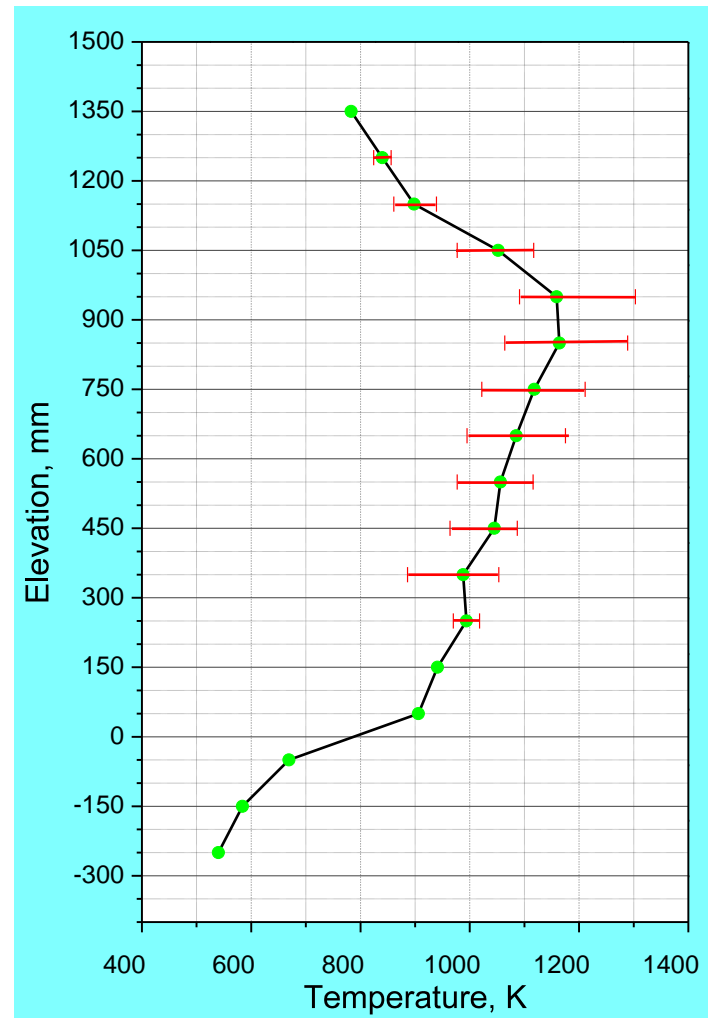
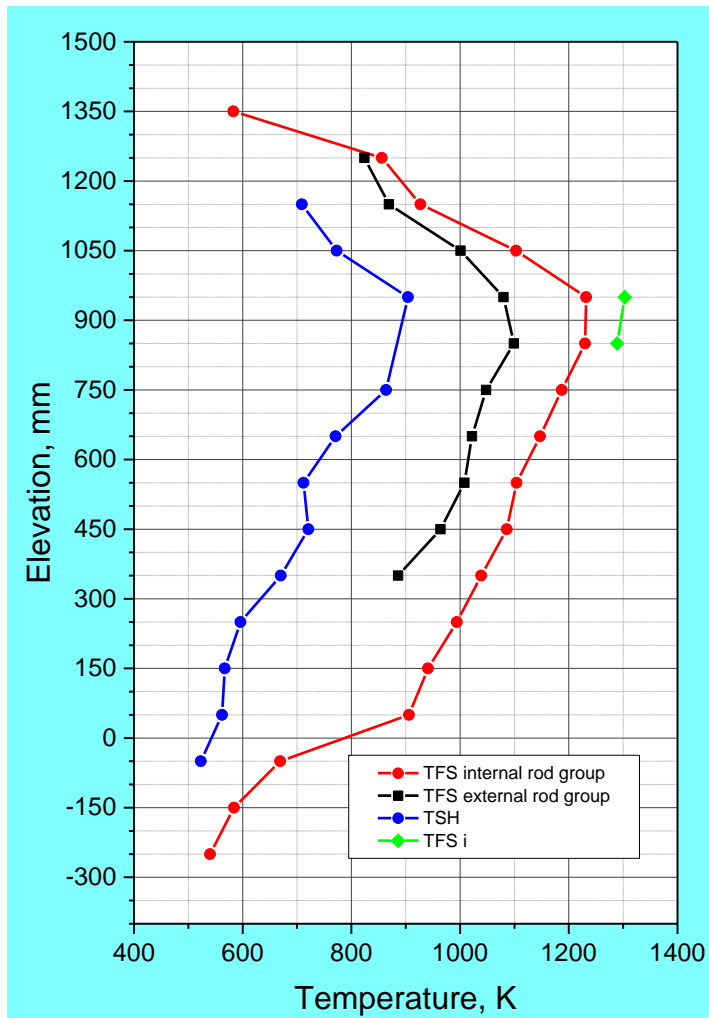


Figure 42 QUENCH-L3; Axial temperature profile TFS internal and external rod group together with TSH, left, and axial temperature profile of all TFS, right, at 76,8 s (end of transient).

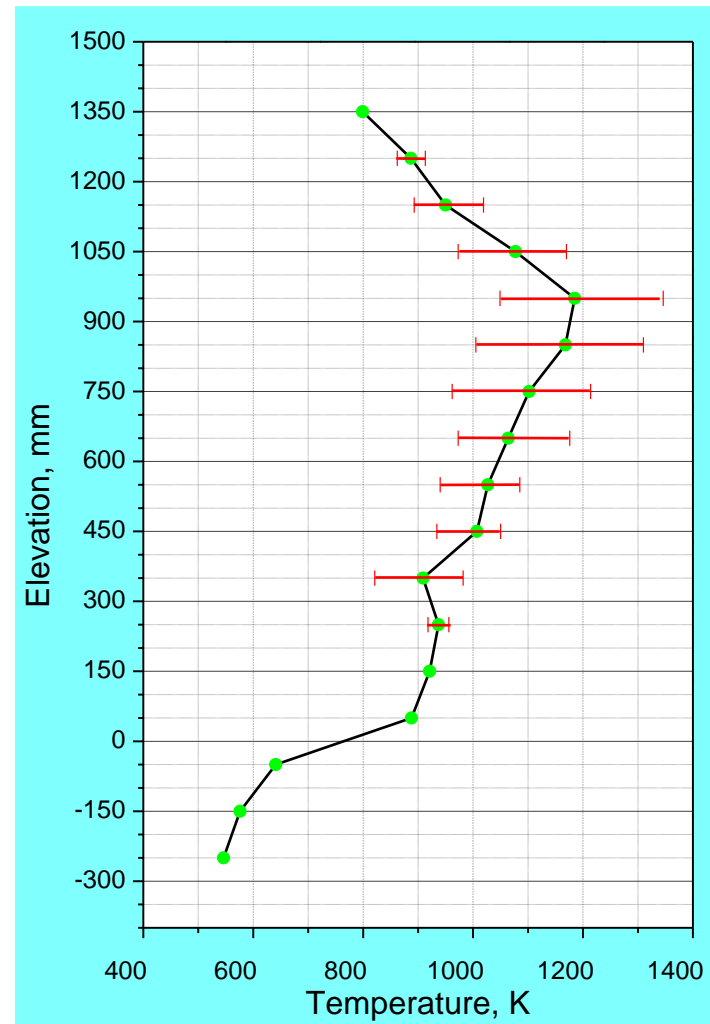
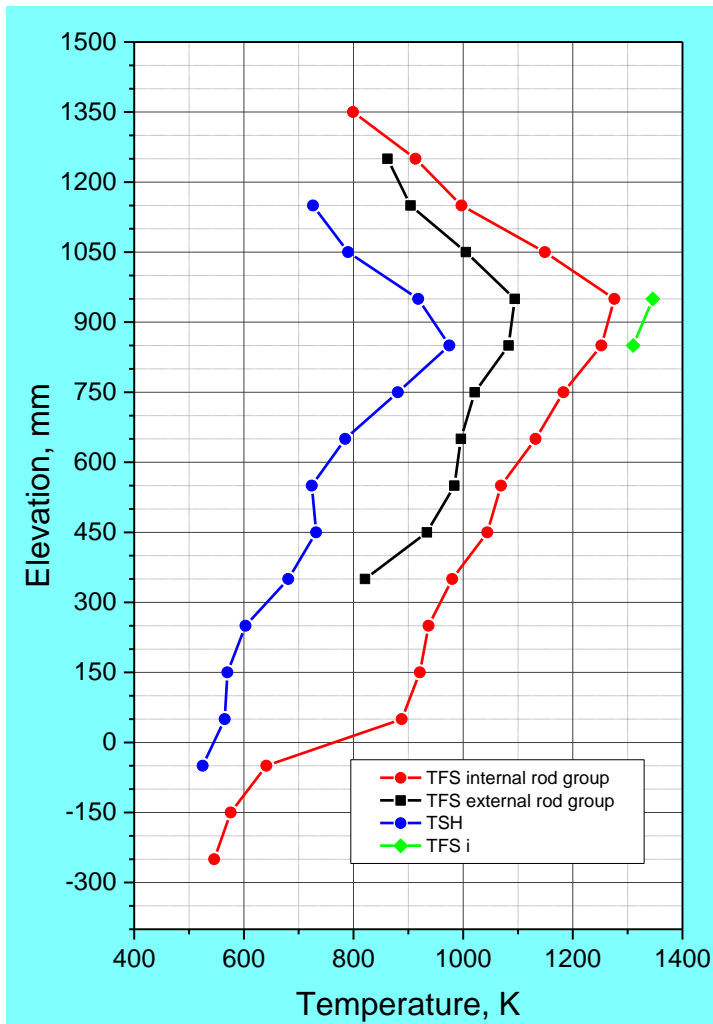


Figure 43 QUENCH-L3; Axial temperature profile TFS internal and external rod group together with TSH, left, and axial temperature profile of all TFS, right, at 81,8 s (max temperature).

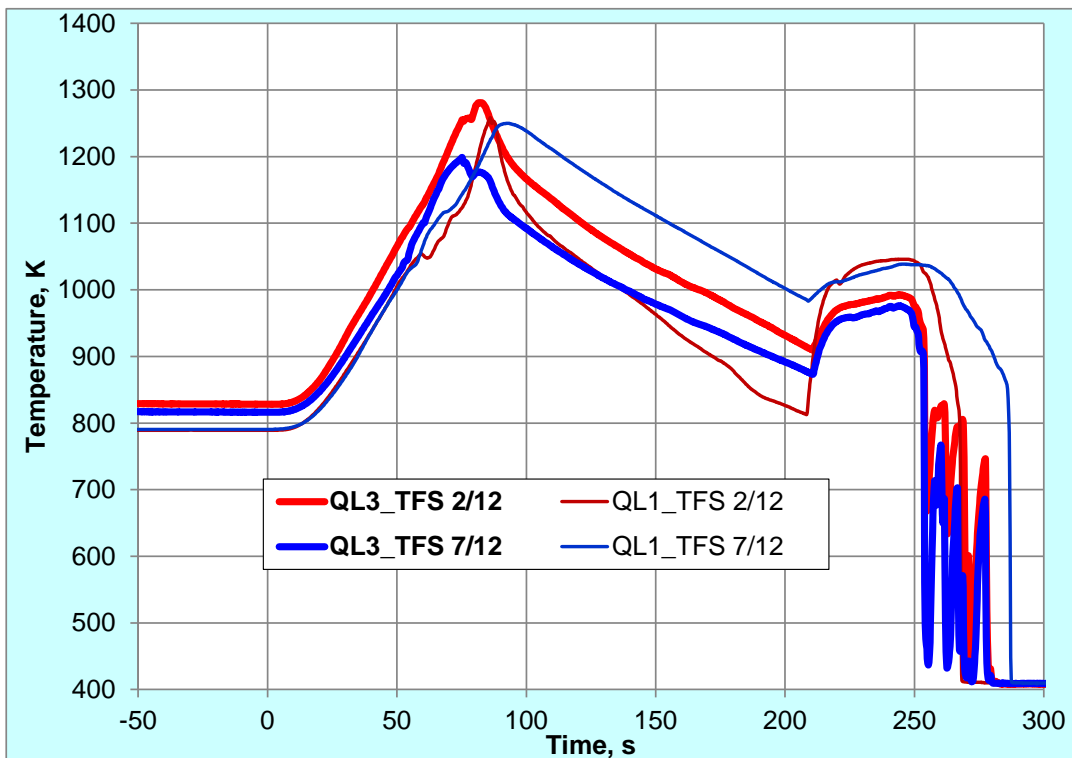
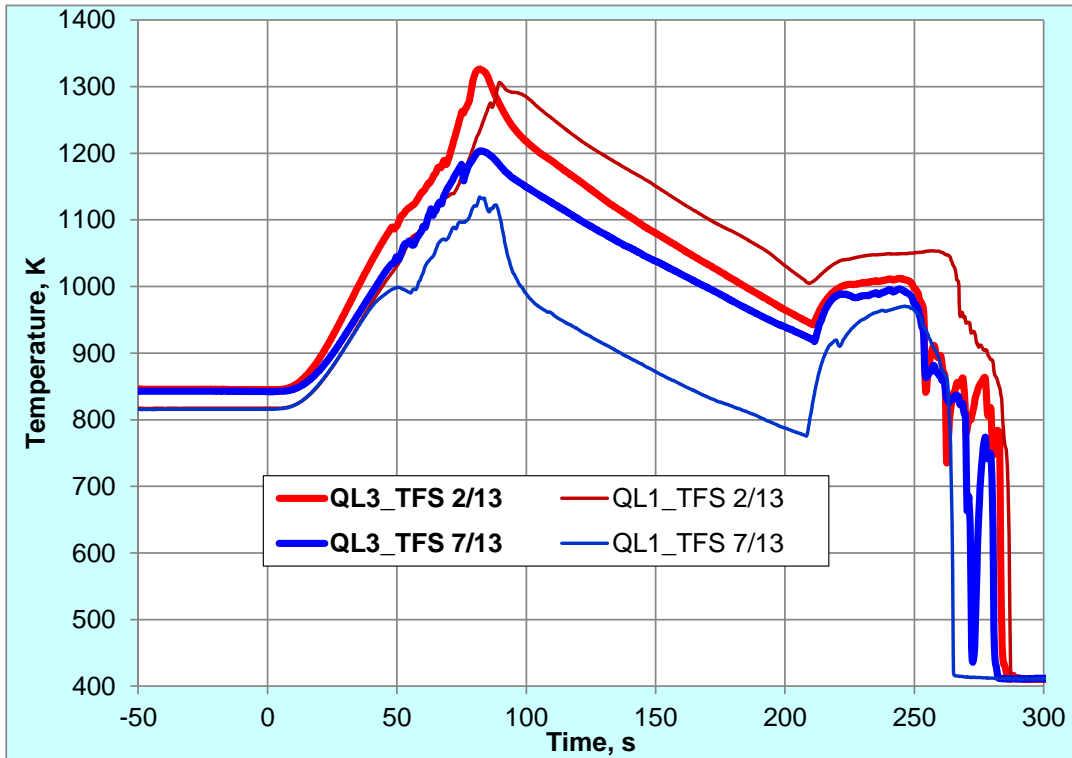


Figure 44 QUENCH-L3; comparison of thermocouple readings at elevations 950 mm (upper diagram) and 850 mm (lower diagram) of QUENCH-L3 bundle with corresponding data of QUENCH-L1 reference test. More stable and homogeneous conditions for the QUENCH-L3 due to less bending of rods.

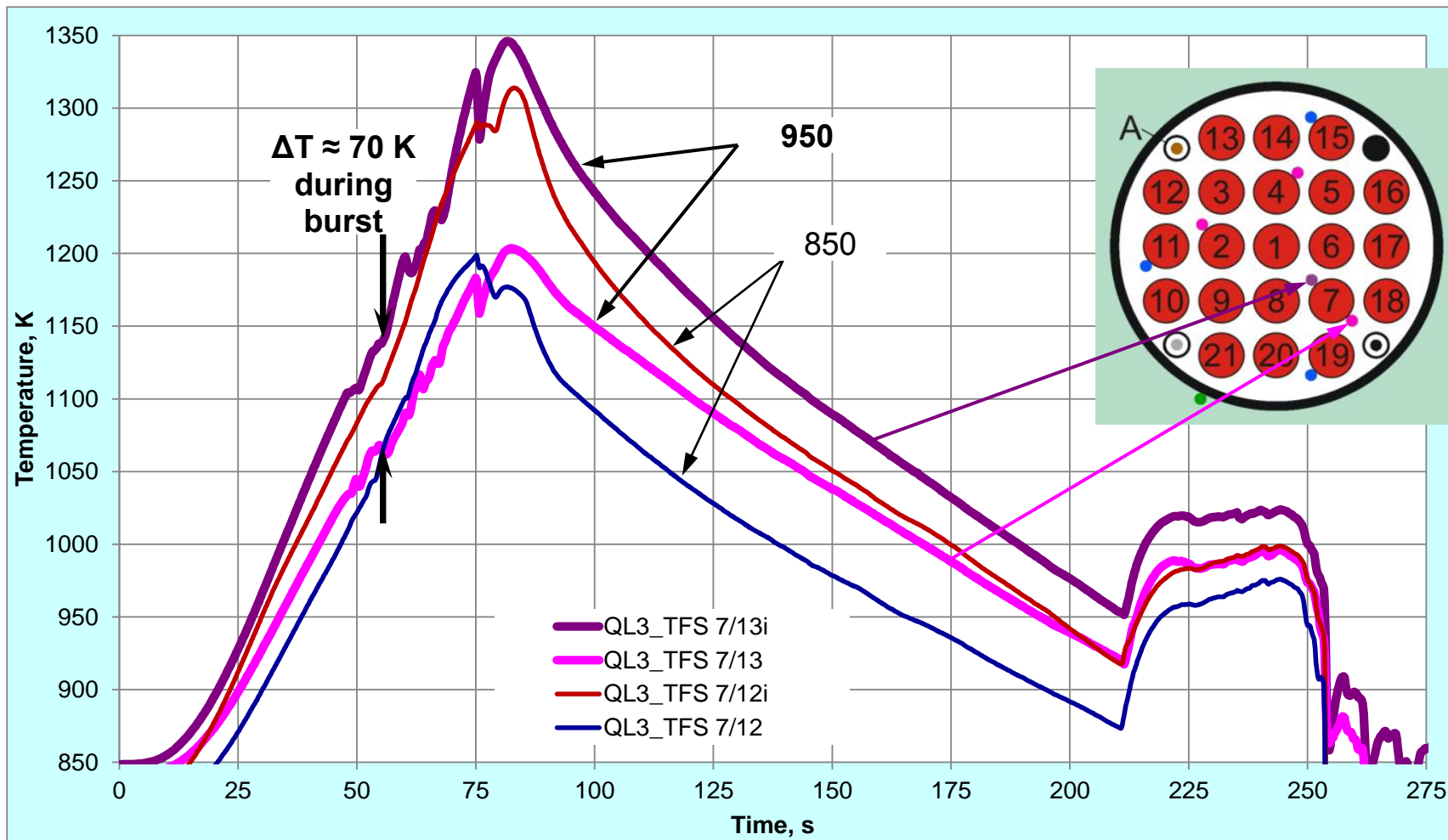


Figure 45 QUENCH-L3; circumferential temperature difference for rod #7 at elevations 850 and 950 mm.

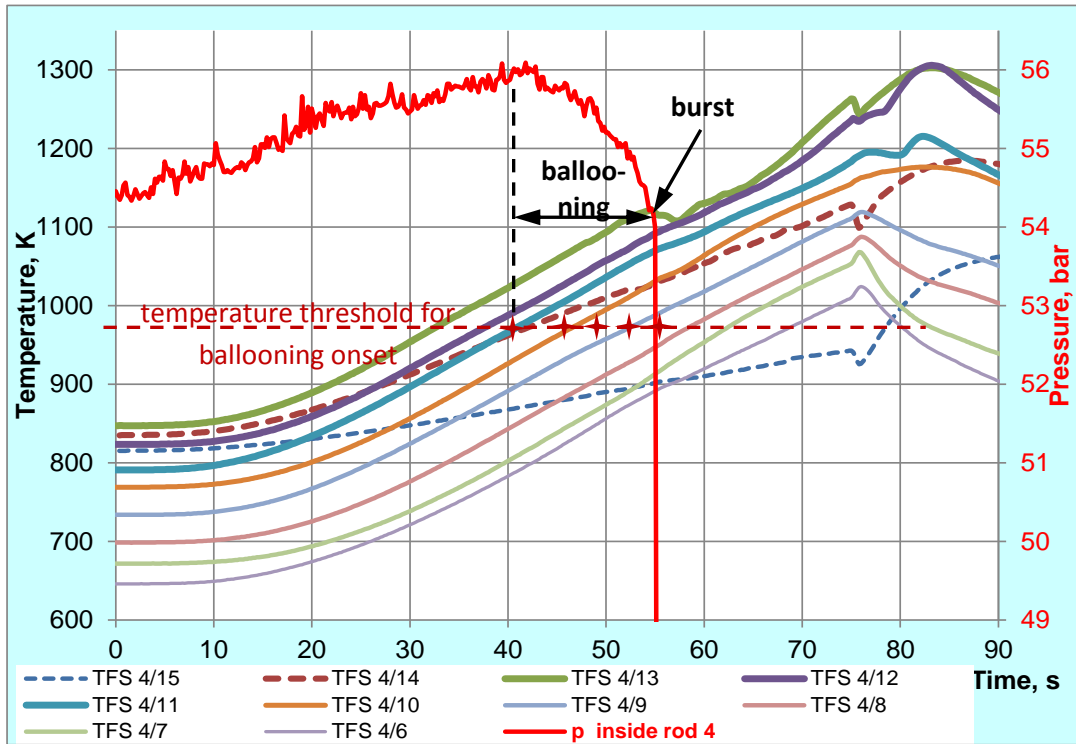


Figure 46 QUENCH-L3: temperatures and cladding ballooning of rod #4; possibility of ballooning propagation from about 950 mm to lower and upper elevations.

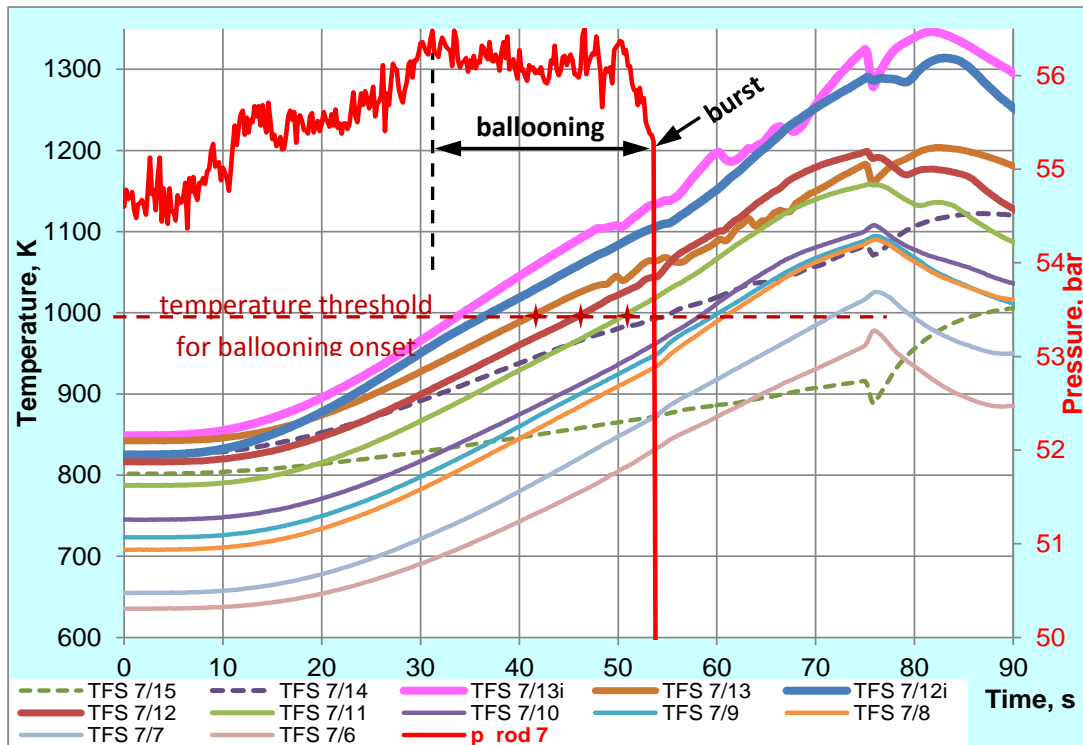


Figure 47 QUENCH-L3: temperatures and cladding ballooning of rod #7.

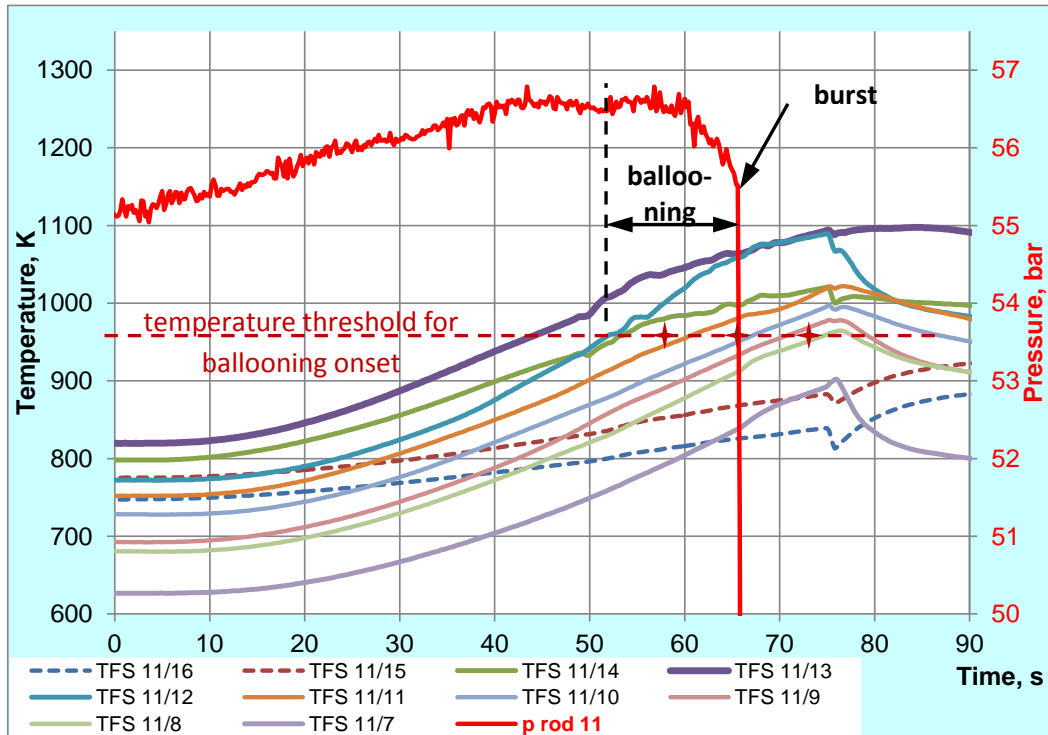


Figure 48 QUENCH-L3: temperatures and cladding ballooning of rod #11; possibility of ballooning propagation from about 950 mm to lower elevations.

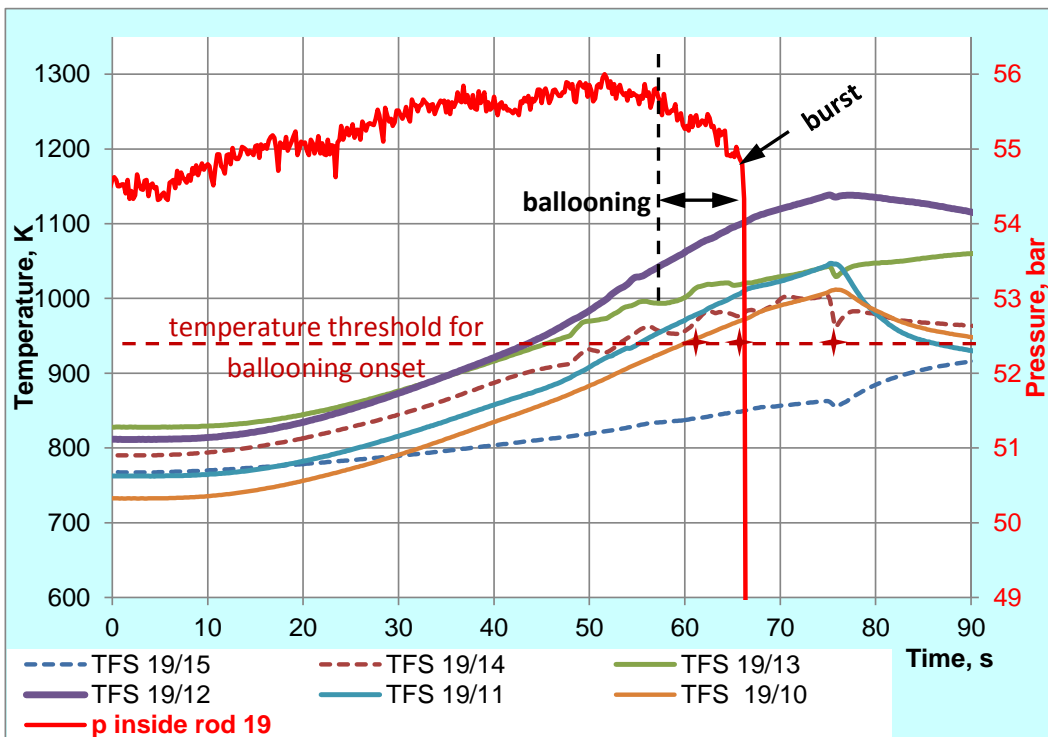


Figure 49 QUENCH-L3: temperatures and cladding ballooning of rod #19; possibility of ballooning propagation from about 900 mm to lower elevations.

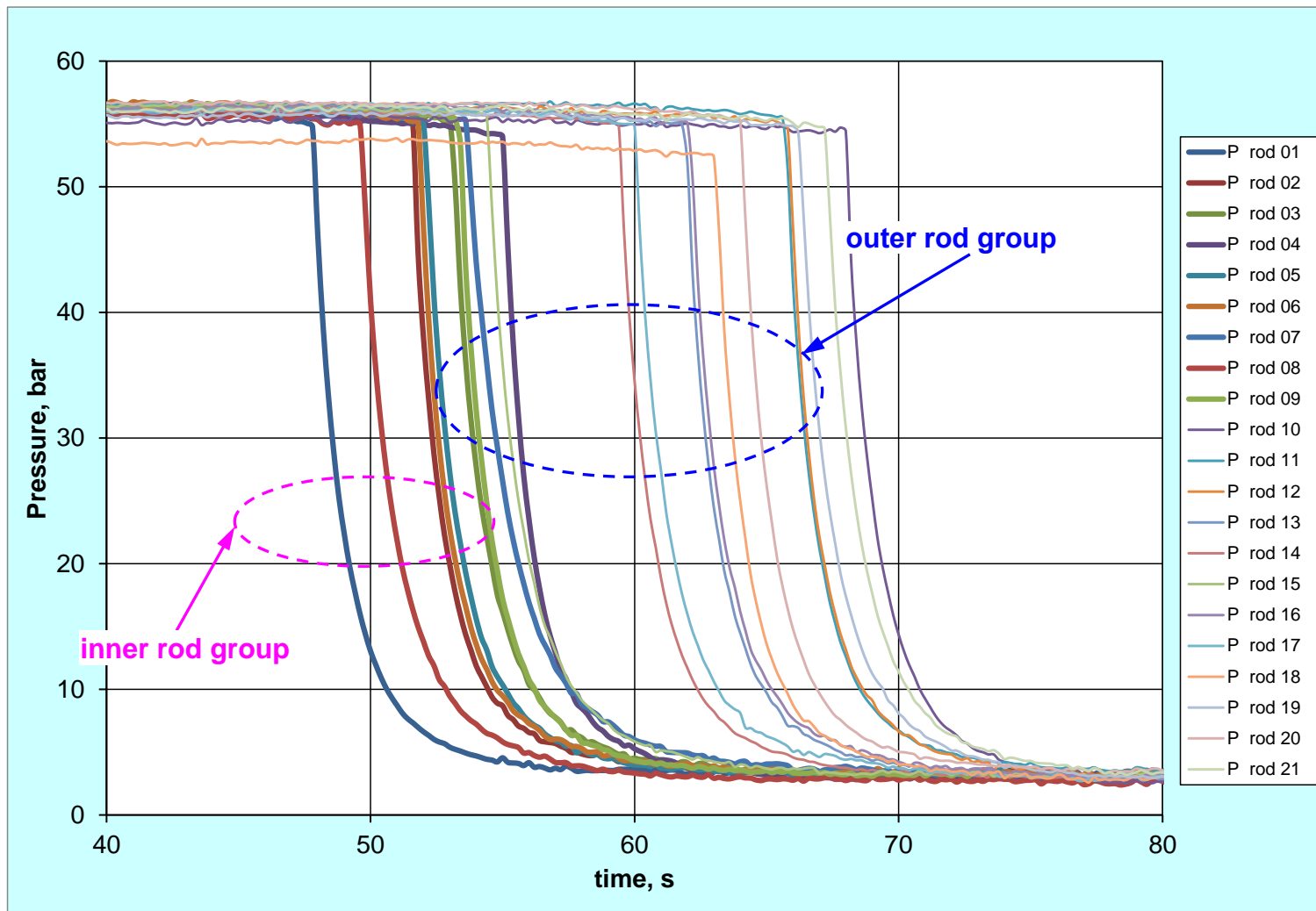


Figure 50 QUENCH-L3; Pressure changing during heating phase; ballooning and burst.

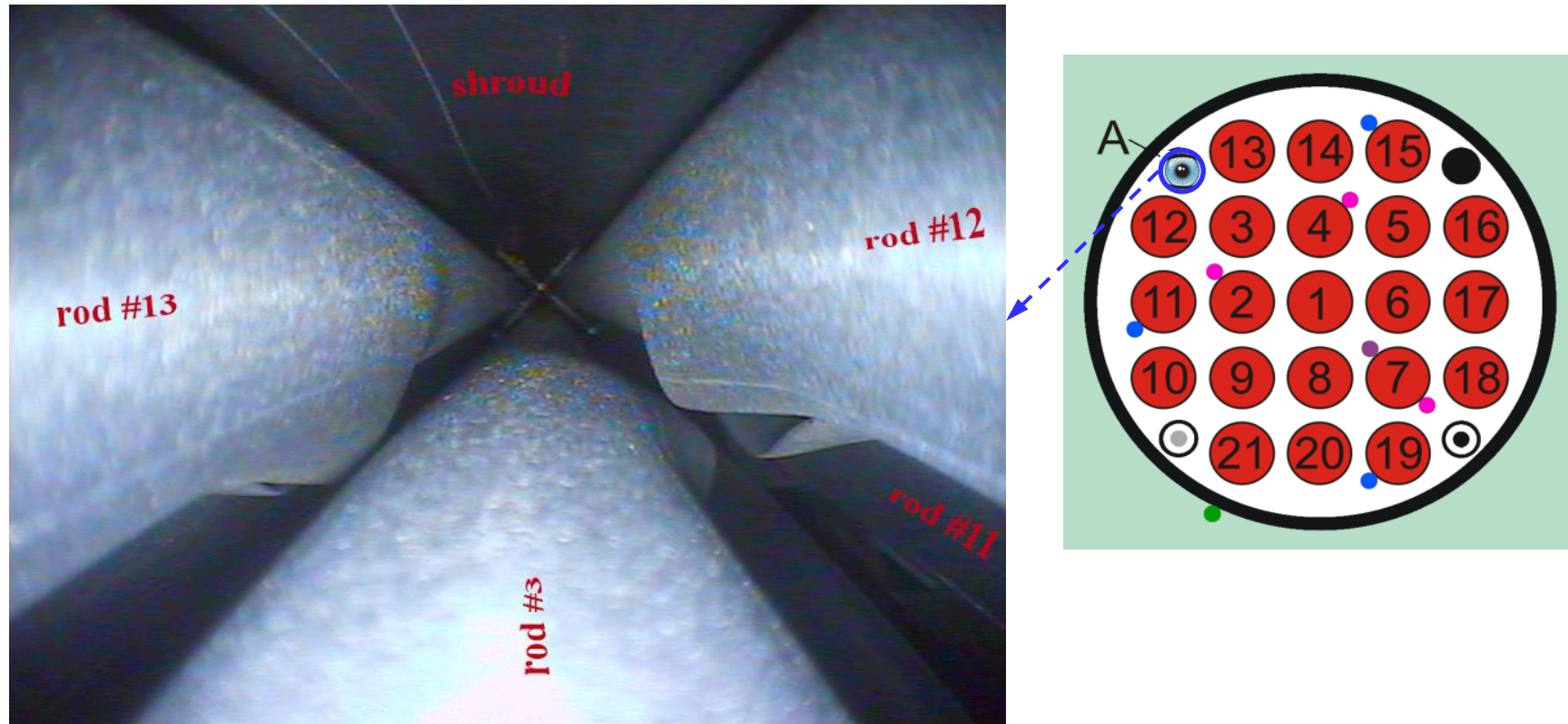


Figure 51 QUENCH-L3; videoscope observations with camera inserted from the bundle bottom at position of corner rod A.

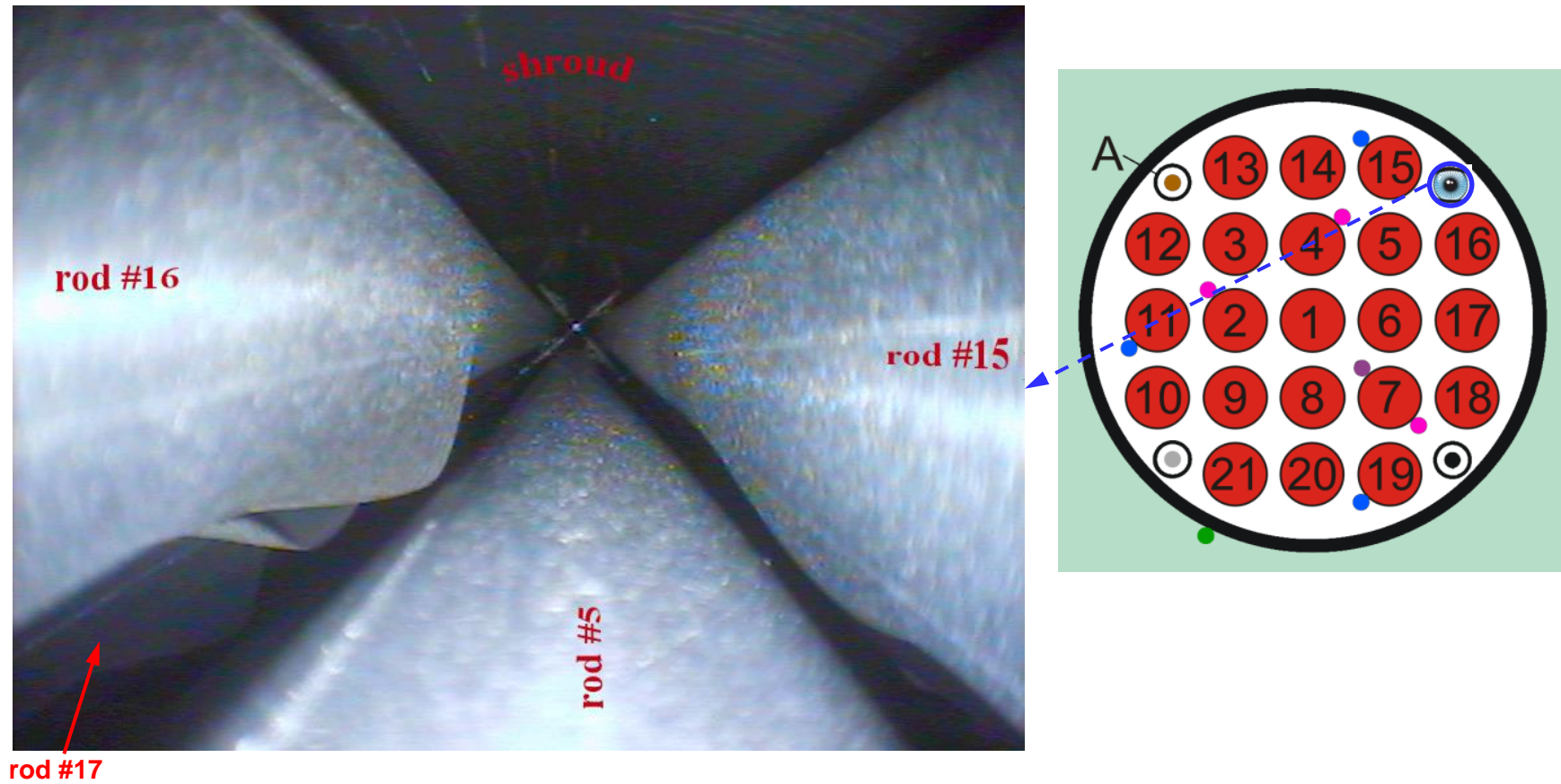


Figure 52 QUENCH-L3; videoscope observations with camera inserted from the bundle bottom at position of corner rod B.

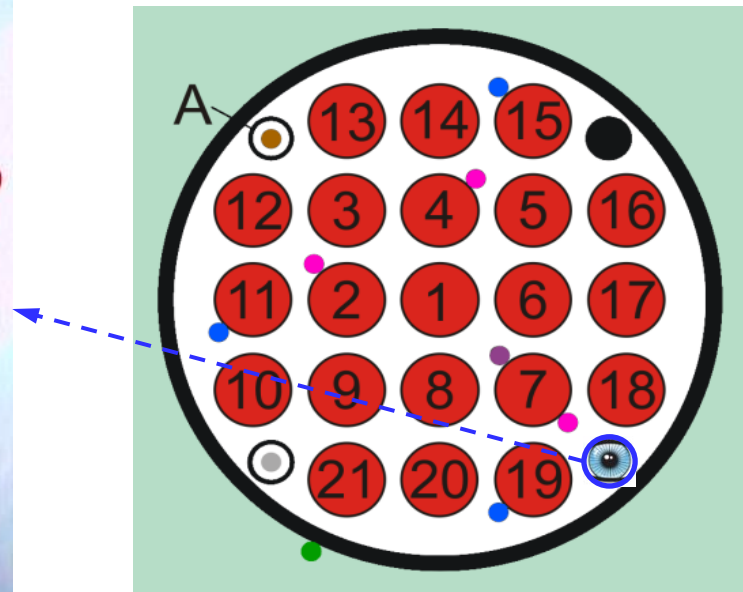


Figure 53 QUENCH-L3; videoscope observations with camera inserted from the bundle bottom at position of corner rod C.

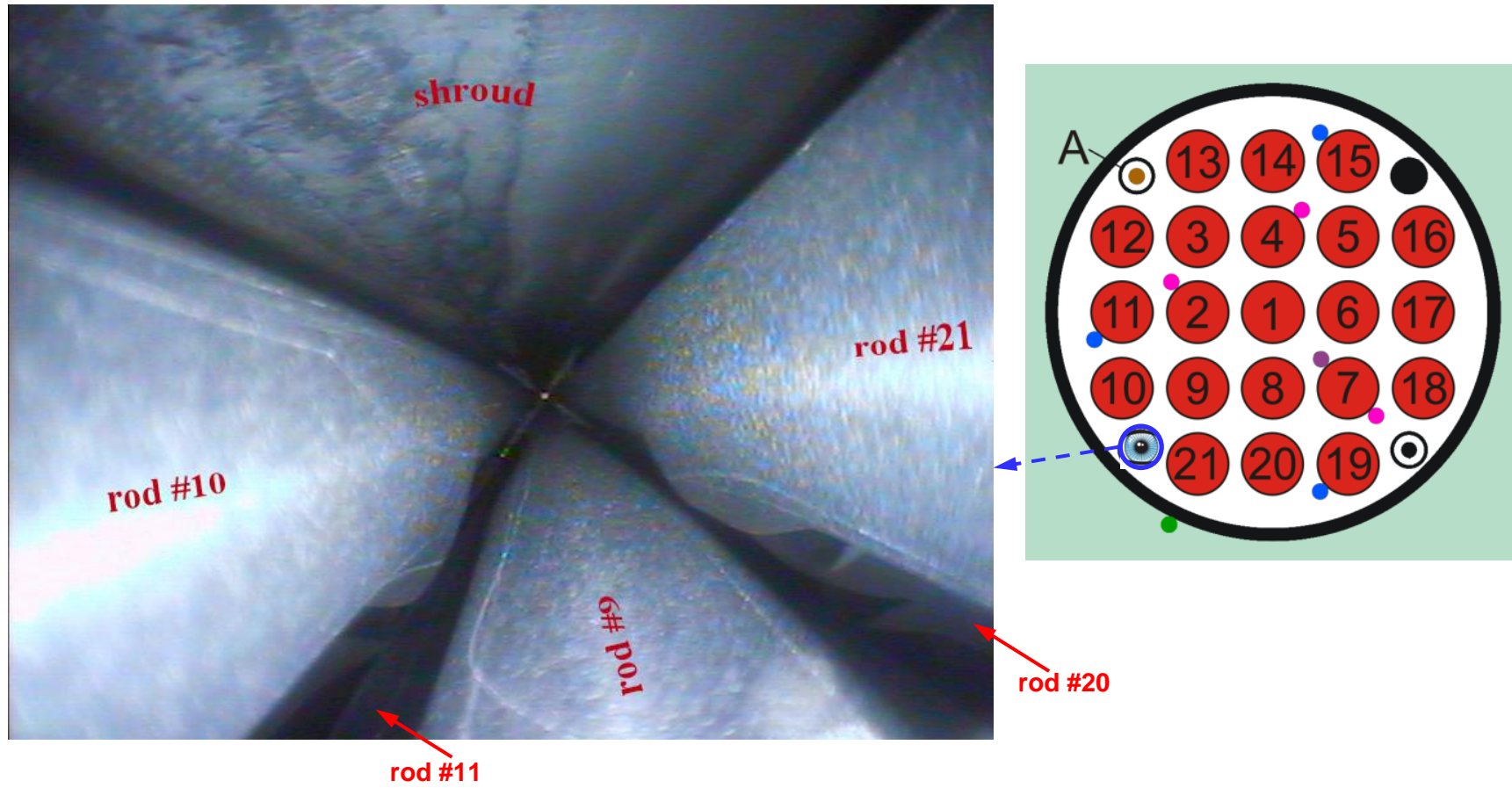


Figure 54 QUENCH-L3; videoscope observations with camera inserted from the bundle bottom at position of corner rod D.

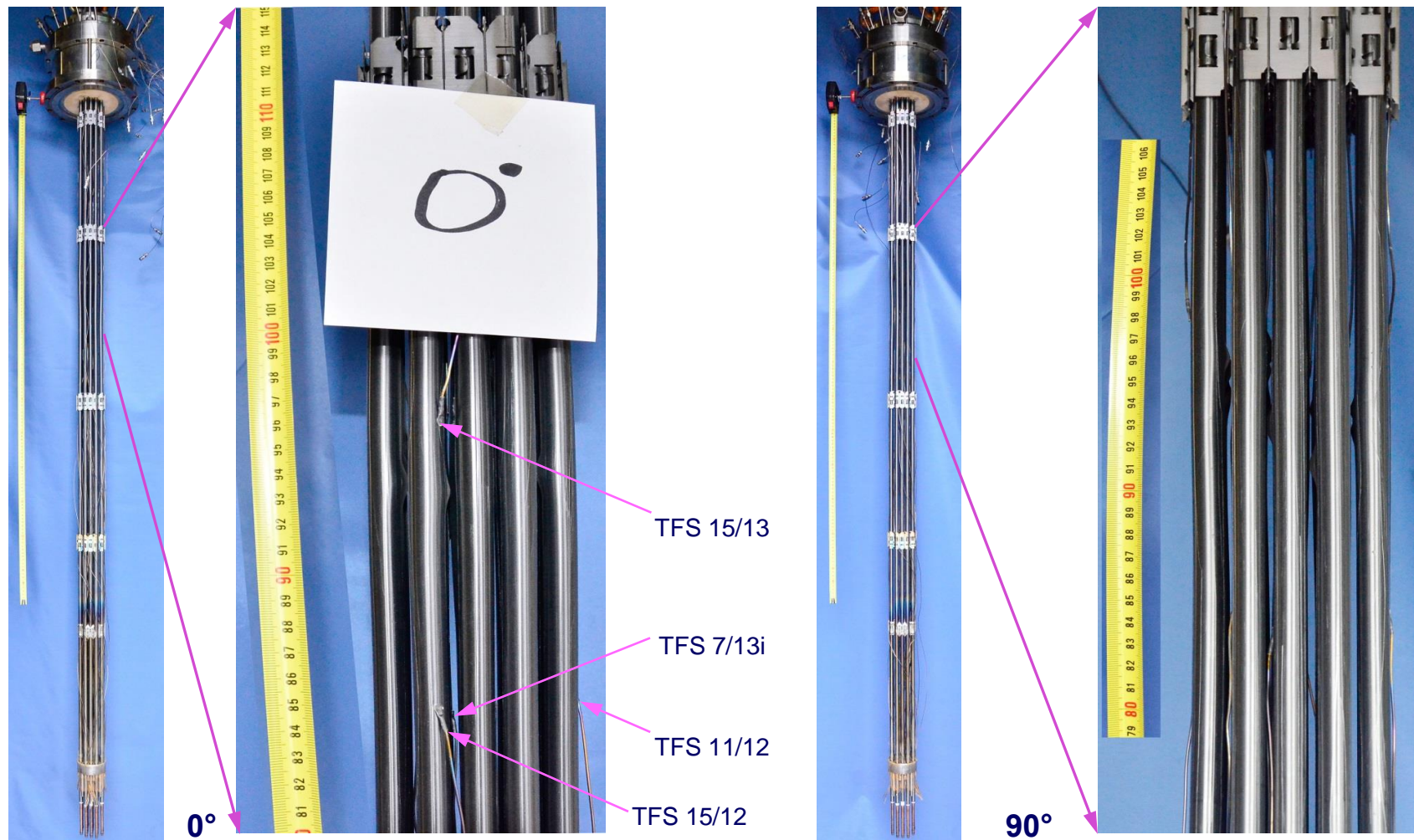


Figure 55 QUENCH-L3; Views of bundle at angle positions of 0° and 90°: negligible rod bending and intact thermocouples.

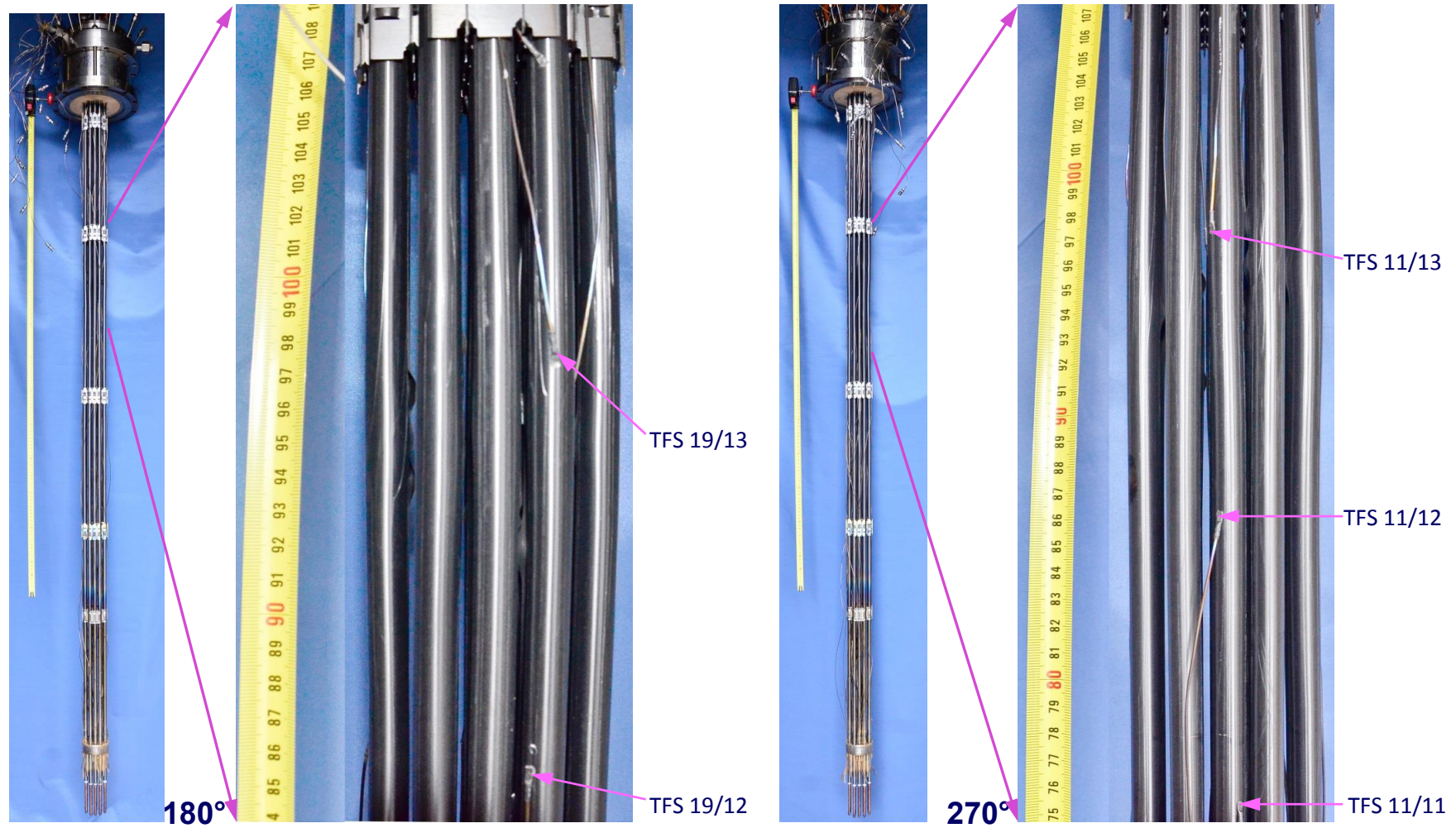


Figure 56 QUENCH-L3; Views of bundle at angle positions of 180° and 270°: negligible rod bending and intact thermocouples.

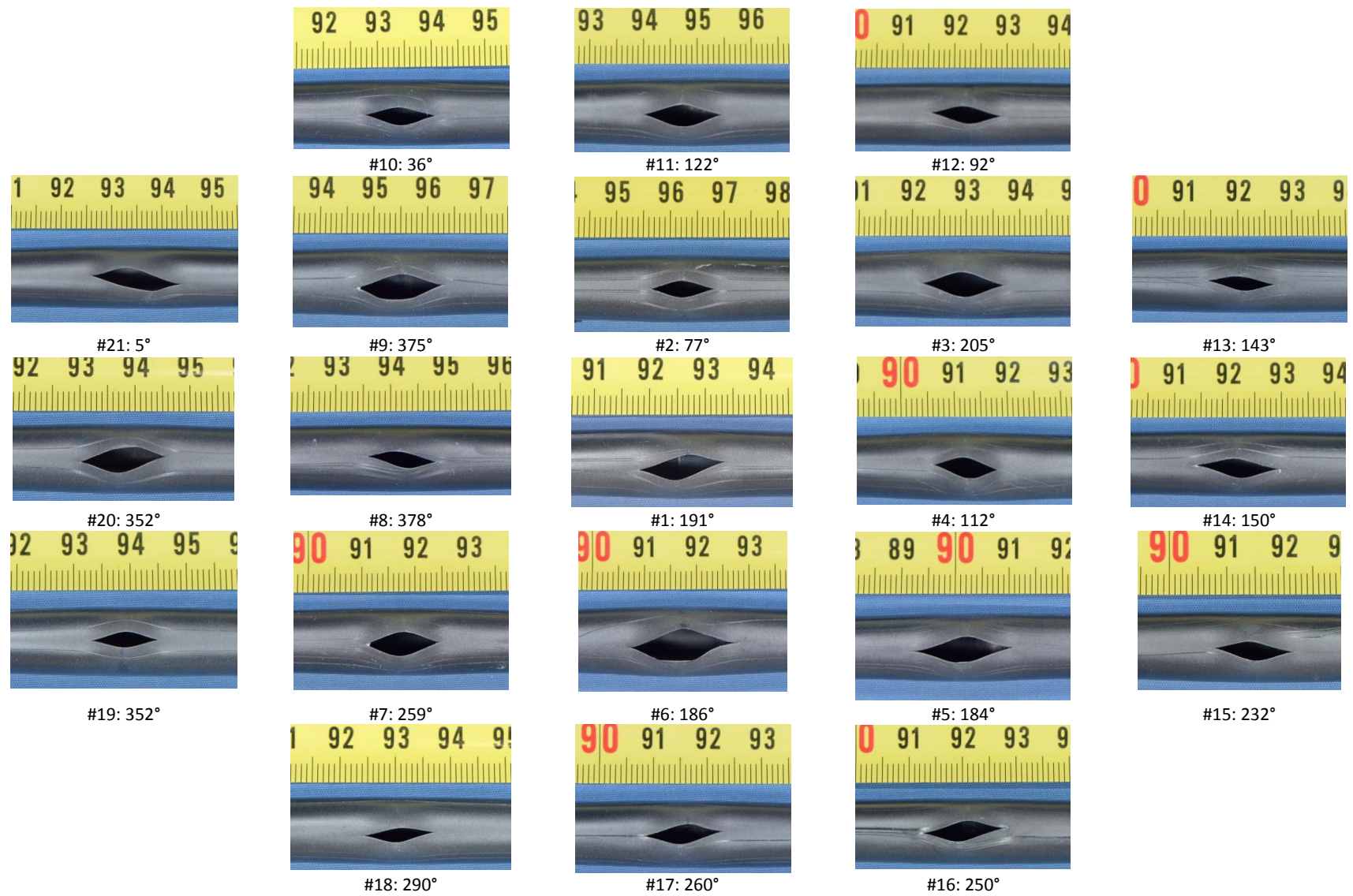
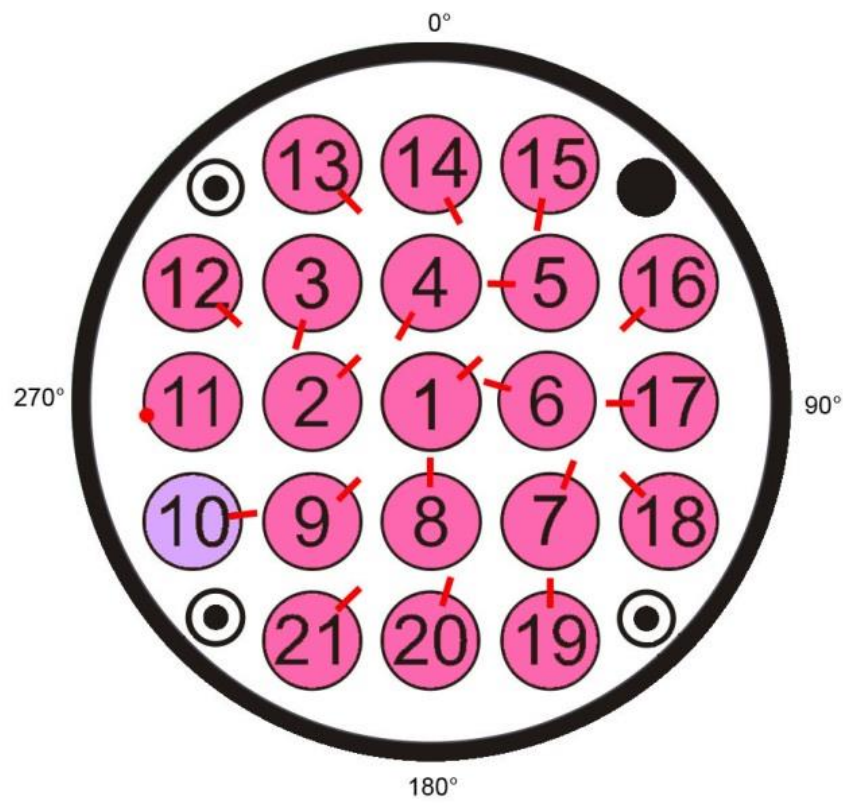
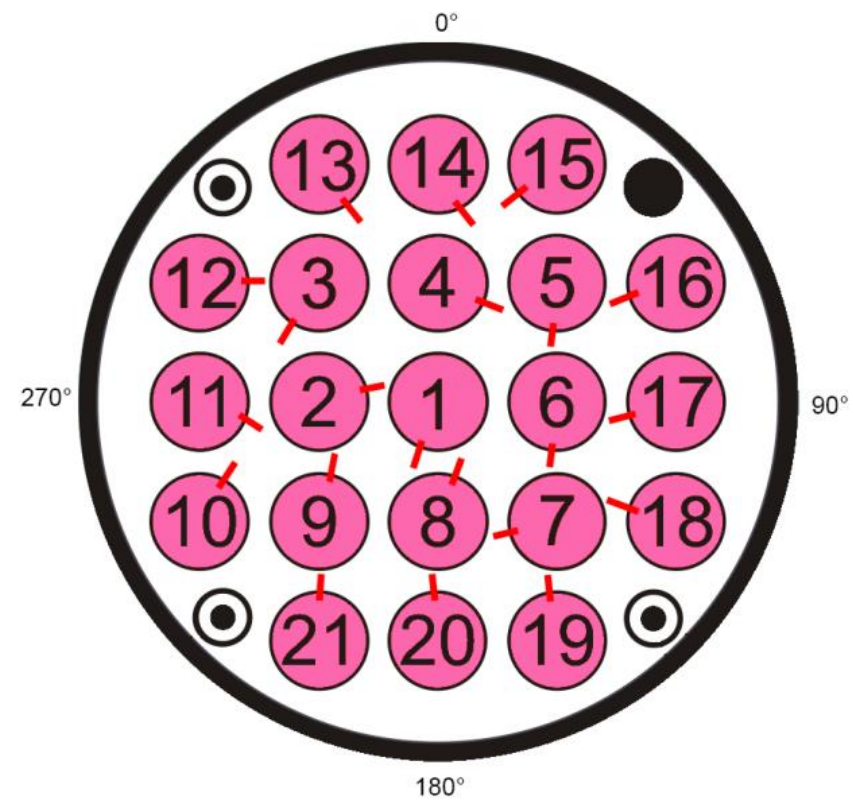


Figure 57 QUENCH-L3; overview of burst positions.



LOCA-1 (reference test with Zry-4)



LOCA-3

Figure 58 QUENCH-L3; burst opening orientations of QUENCH-L1 and QUENCH-L3 bundles.

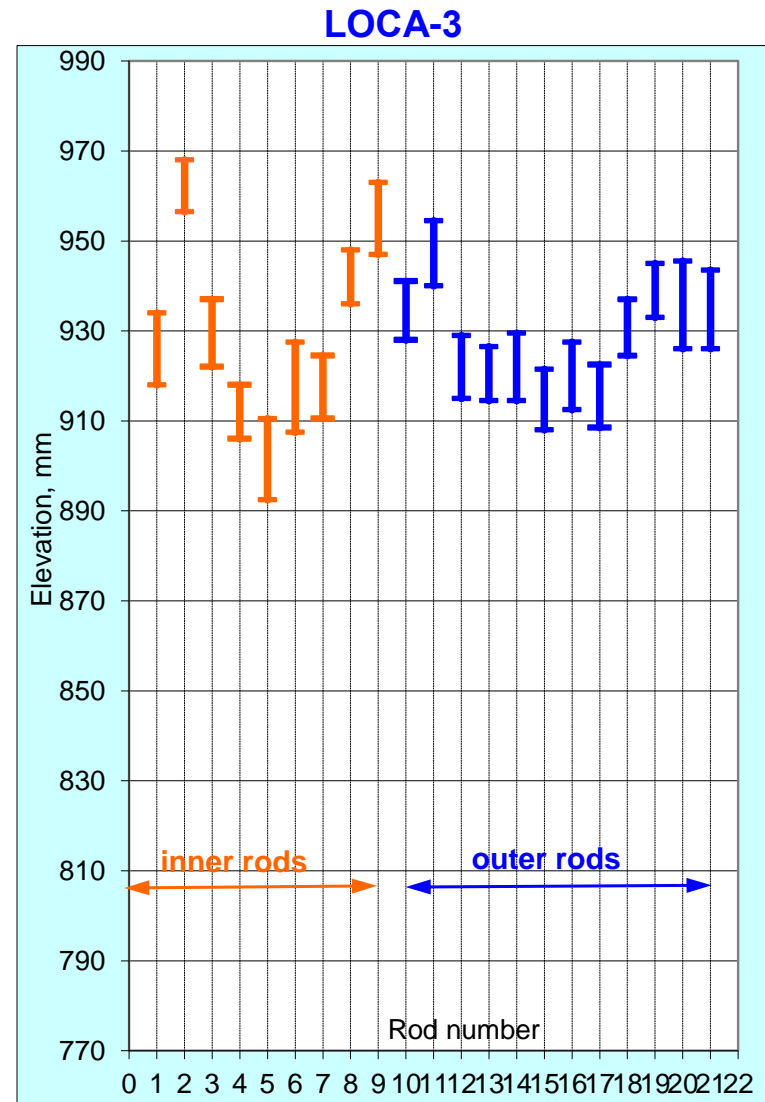
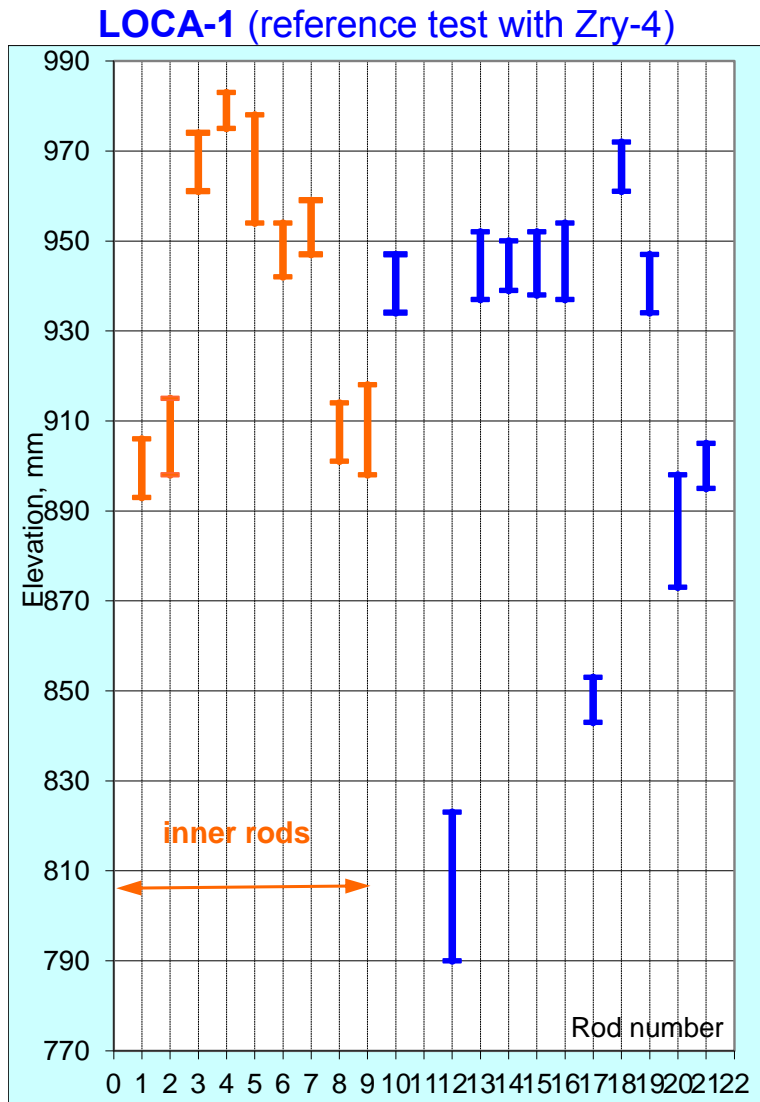


Figure 59 Vertical positions of burst openings for QUENCH-L1 and QUENCH-L3 bundles.

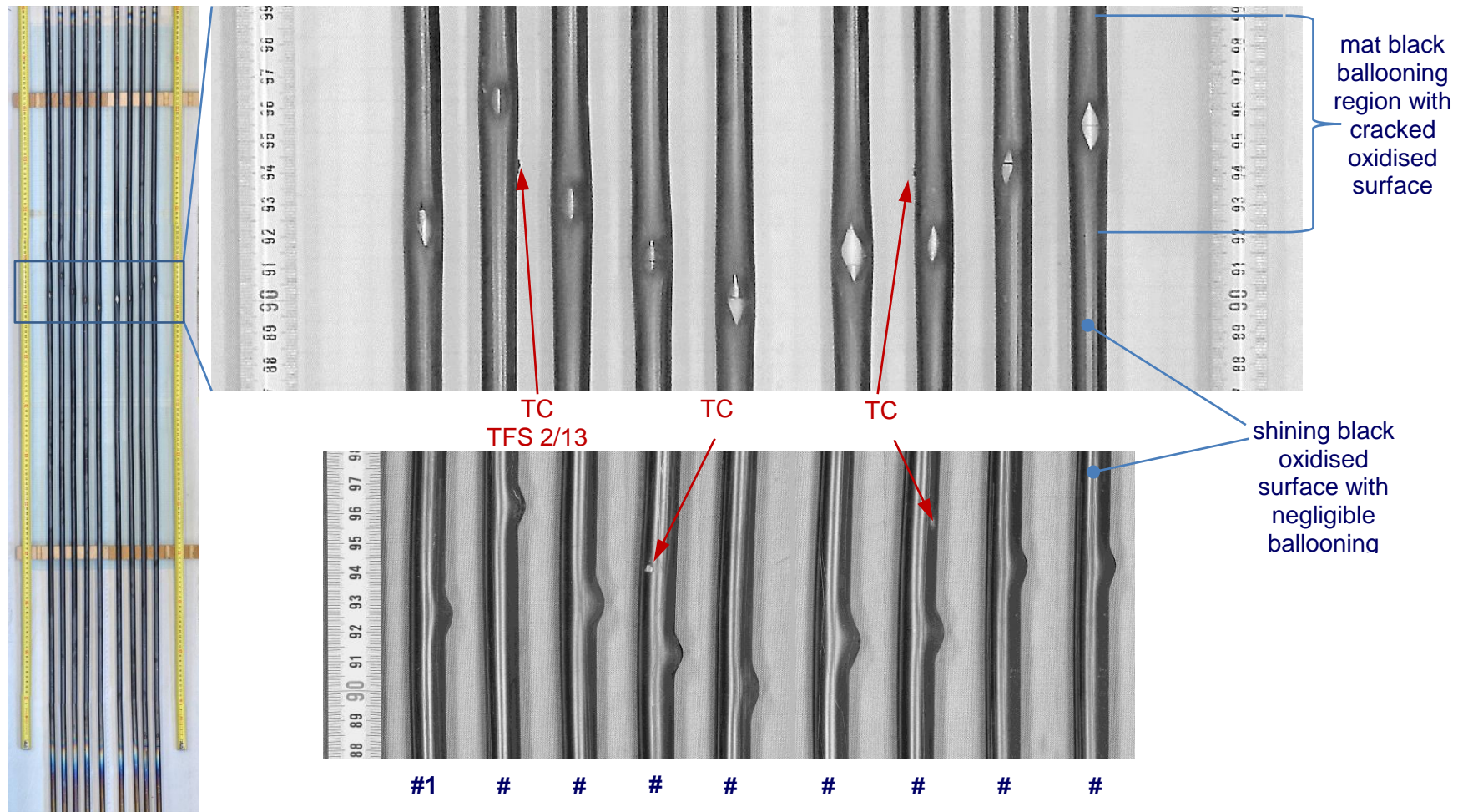


Figure 60 QUENCH-L3; post-test overview of inner rods; burst front view (top): no bending, mat region around burst opening (surface cracks in oxide layer); burst side view (bottom): cladding bending about 2°, kink in burst region, burst opening always at concave side.

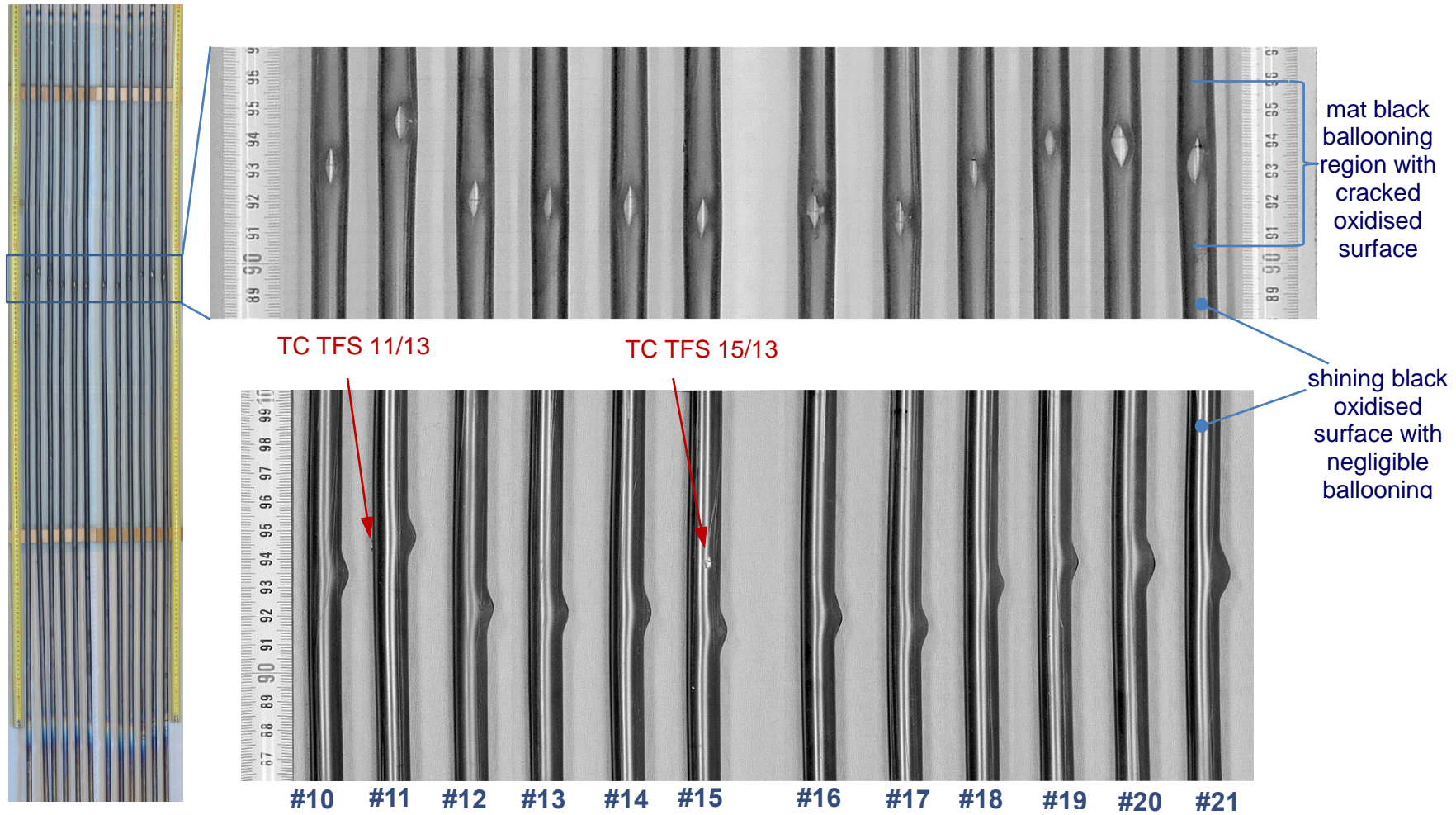


Figure 61 QUENCH-L3; post-test overview of outer rods; burst front view (top): no bending, mat region around burst opening (surface cracks in oxide layer); burst side view (bottom): cladding bending about 2° , kink in burst region, burst opening always at concave side.



#1 at 191°, $A_{burst} = 36 \text{ mm}^2$, $w = 4.7 \text{ mm}$, $h = 16 \text{ mm}$



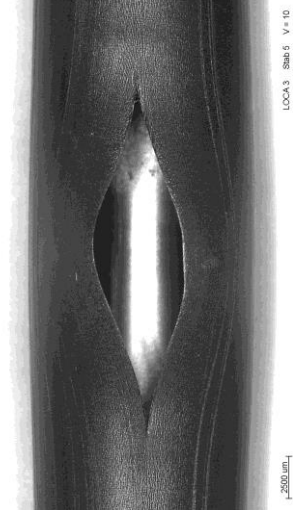
#2 at 77°, $A_{burst} = 21 \text{ mm}^2$, $w = 3.2 \text{ mm}$, $h = 11.5 \text{ mm}$



#3 at 205°, $A_{burst} = 37 \text{ mm}^2$, $w = 4.6 \text{ mm}$, $h = 15 \text{ mm}$



#4 at 112°, $A_{burst} = 26 \text{ mm}^2$, $w = 2.9 \text{ mm}$, $h = 12 \text{ mm}$

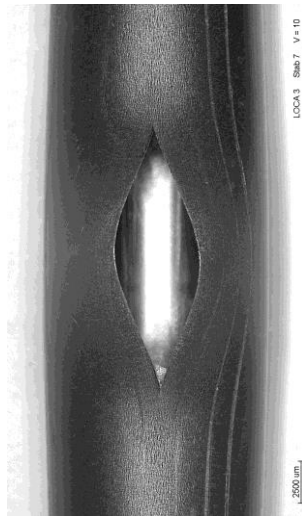


#5 at 184°, $A_{burst} = 44 \text{ mm}^2$, $w = 3.0 \text{ mm}$, $h = 18 \text{ mm}$

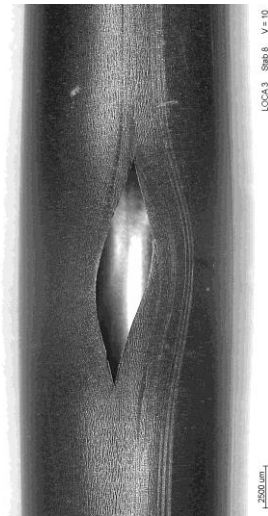


#6 at 186°, $A_{burst} = 67 \text{ mm}^2$, $w = 6.2 \text{ mm}$; $h = 20 \text{ mm}$

Figure 62 QUENCH-L3; Overview of burst structures of rods #1 - #6.



#7 at 259°, $A_{burst} = 36 \text{ mm}^2$, $w = 4.6 \text{ mm}$, $h = 14 \text{ mm}$



#8 at 18°, $A_{burst} = 20 \text{ mm}^2$, $w = 2.9 \text{ mm}$, $h = 12 \text{ mm}$



#9 at 15°, $A_{burst} = 43 \text{ mm}^2$, $w = 4.7 \text{ mm}$, $h = 16 \text{ mm}$



#10 at 36°, $A_{burst} = 24 \text{ mm}^2$, $w = 3.4 \text{ mm}$, $h = 13 \text{ mm}$

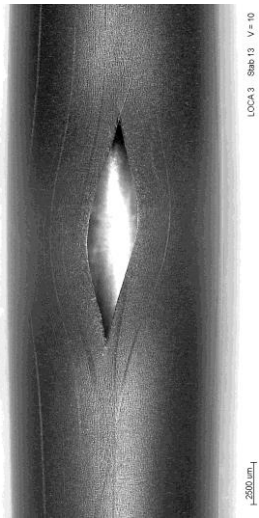


#11 at 122°, $A_{burst} = 33 \text{ mm}^2$, $w = 4.1 \text{ mm}$, $h = 14.5 \text{ mm}$

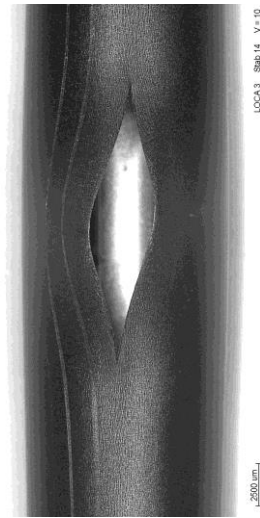


#12 at 92°, $A_{burst} = 24 \text{ mm}^2$, $w = 3.3 \text{ mm}$; $h = 14 \text{ mm}$

Figure 63 QUENCH-L3; Overview of burst structures of rods #7 - #12.



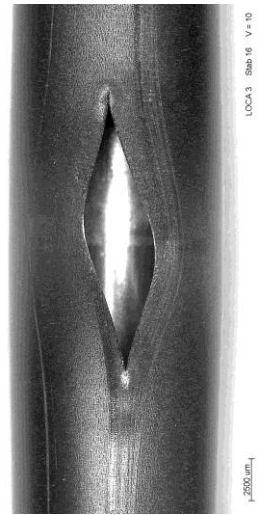
#13 at 143°, $A_{burst} = 18 \text{ mm}^2$, $w = 2.7 \text{ mm}$, $h = 12 \text{ mm}$



#14 at 150°, $A_{burst} = 27 \text{ mm}^2$, $w = 3.6 \text{ mm}$, $h = 15 \text{ mm}$



#15 at 232°, $A_{burst} = 24 \text{ mm}^2$, $w = 3.3 \text{ mm}$, $h = 13.5 \text{ mm}$



#16 at 250°, $A_{burst} = 29 \text{ mm}^2$, $w = 3.9 \text{ mm}$, $h = 15 \text{ mm}$

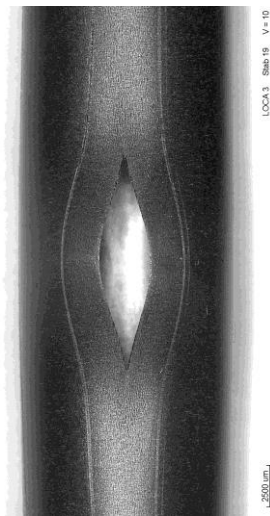


#17 at 260°, $A_{burst} = 28 \text{ mm}^2$, $w = 3.6 \text{ mm}$, $h = 14 \text{ mm}$

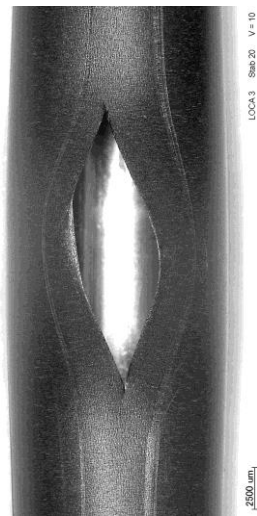


#18 at 290°, $A_{burst} = 17 \text{ mm}^2$, $w = 2.6 \text{ mm}$; $h = 12.5 \text{ mm}$

Figure 64 QUENCH-L3; Overview of burst structures of rods #13 - #18.



#19 at 352°, $A_{burst} = 18 \text{ mm}^2$, $w = 2.8 \text{ mm}$, $h = 12 \text{ mm}$



#20 at 352°, $A_{burst} = 39 \text{ mm}^2$, $w = 4.5 \text{ mm}$, $h = 15.5 \text{ mm}$



#21 at 5°, $A_{burst} = 40 \text{ mm}^2$, $w = 4.1 \text{ mm}$; $h = 17.5 \text{ mm}$

Figure 65 QUENCH-L3; Overview of burst structures of rods #19 - #21.

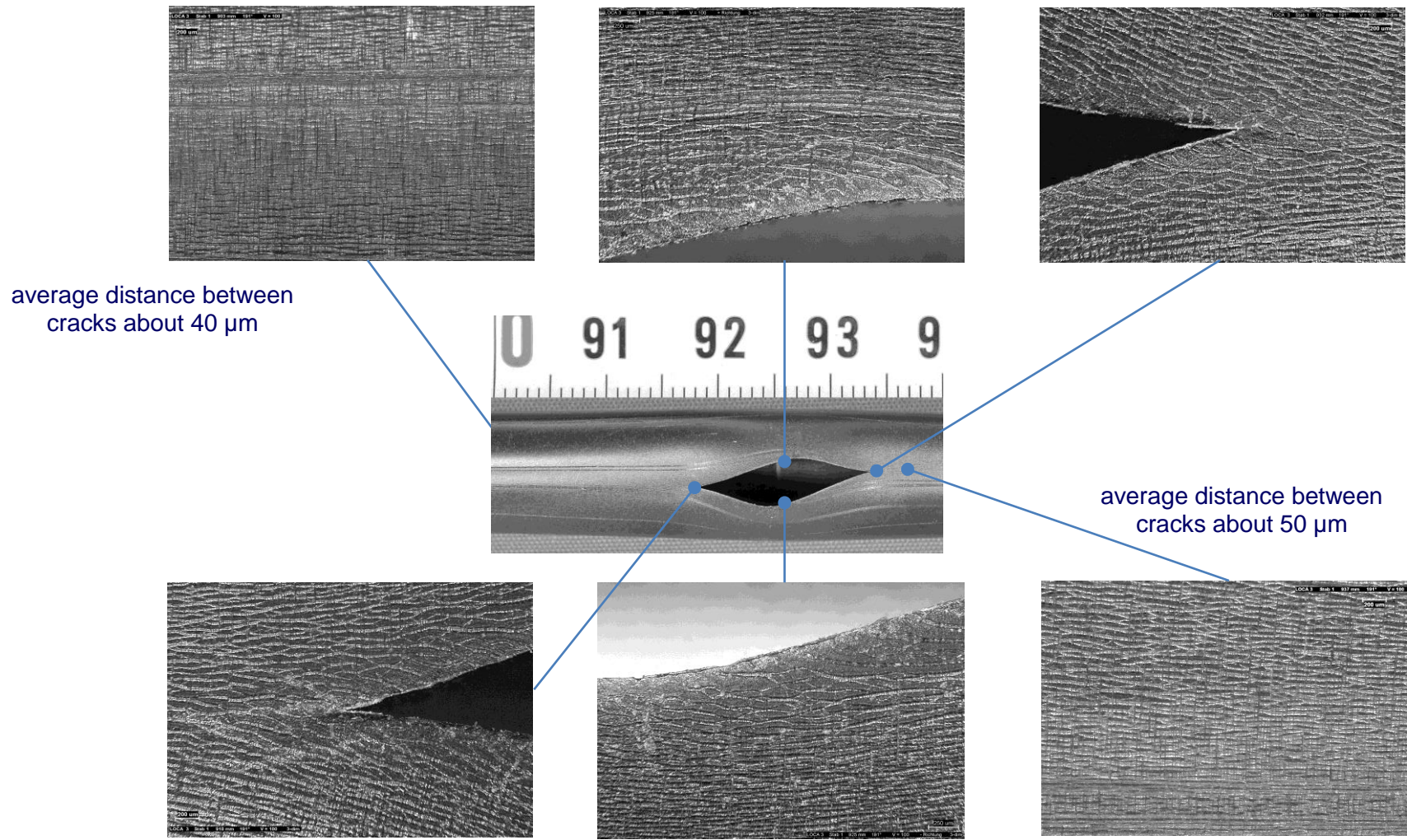


Figure 66 QUENCH-L3; cladding surface structure (“tree bark”) around burst opening of rod #1: formation of longitudinal cracks in outer oxide layer during ballooning.

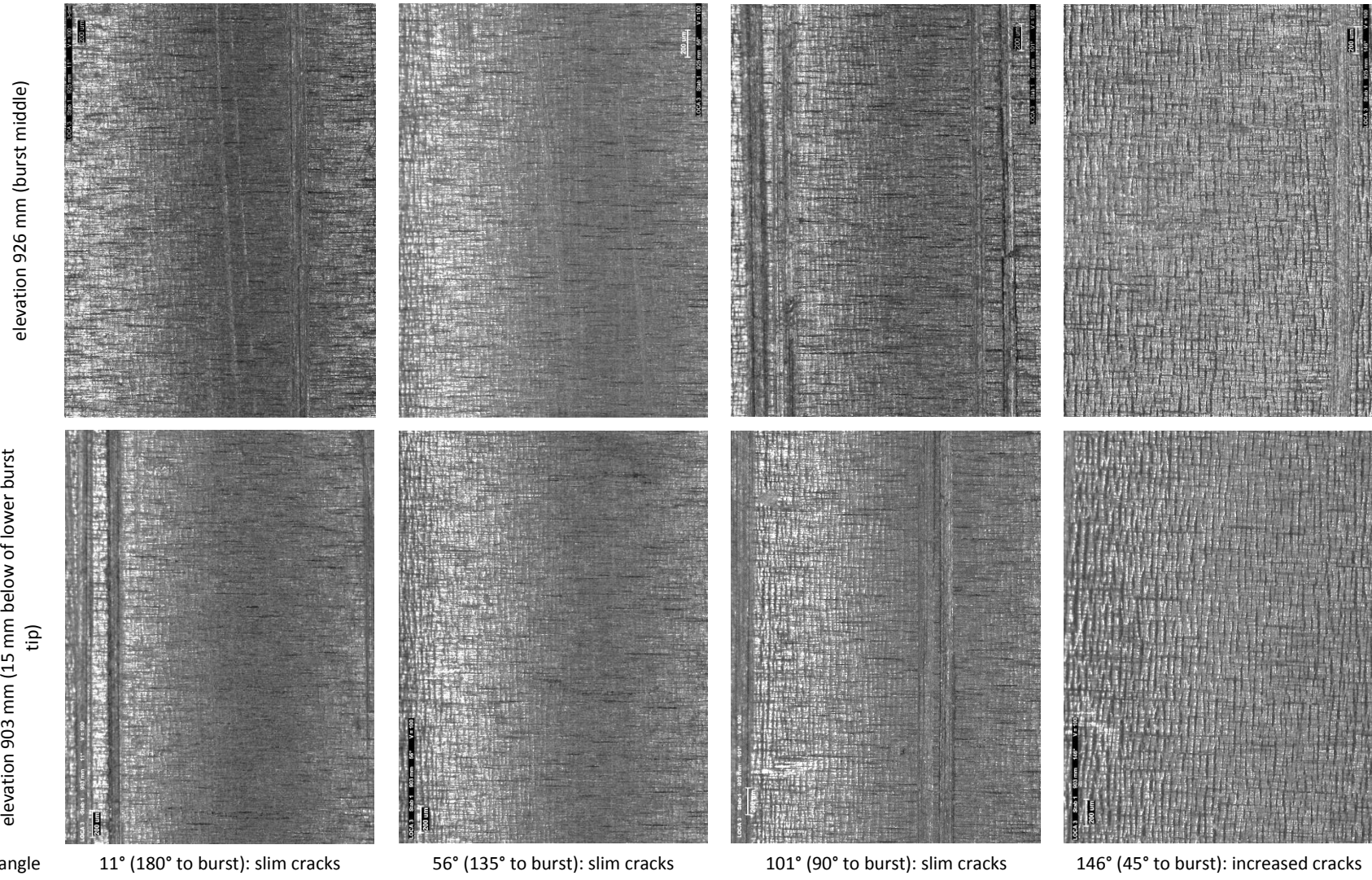


Figure 67 QUENCH-L3; cladding surface structure (“tree bark”) near to burst opening of rod #1: formation of longitudinal cracks in outer oxide layer during ballooning at all circumferential positions.

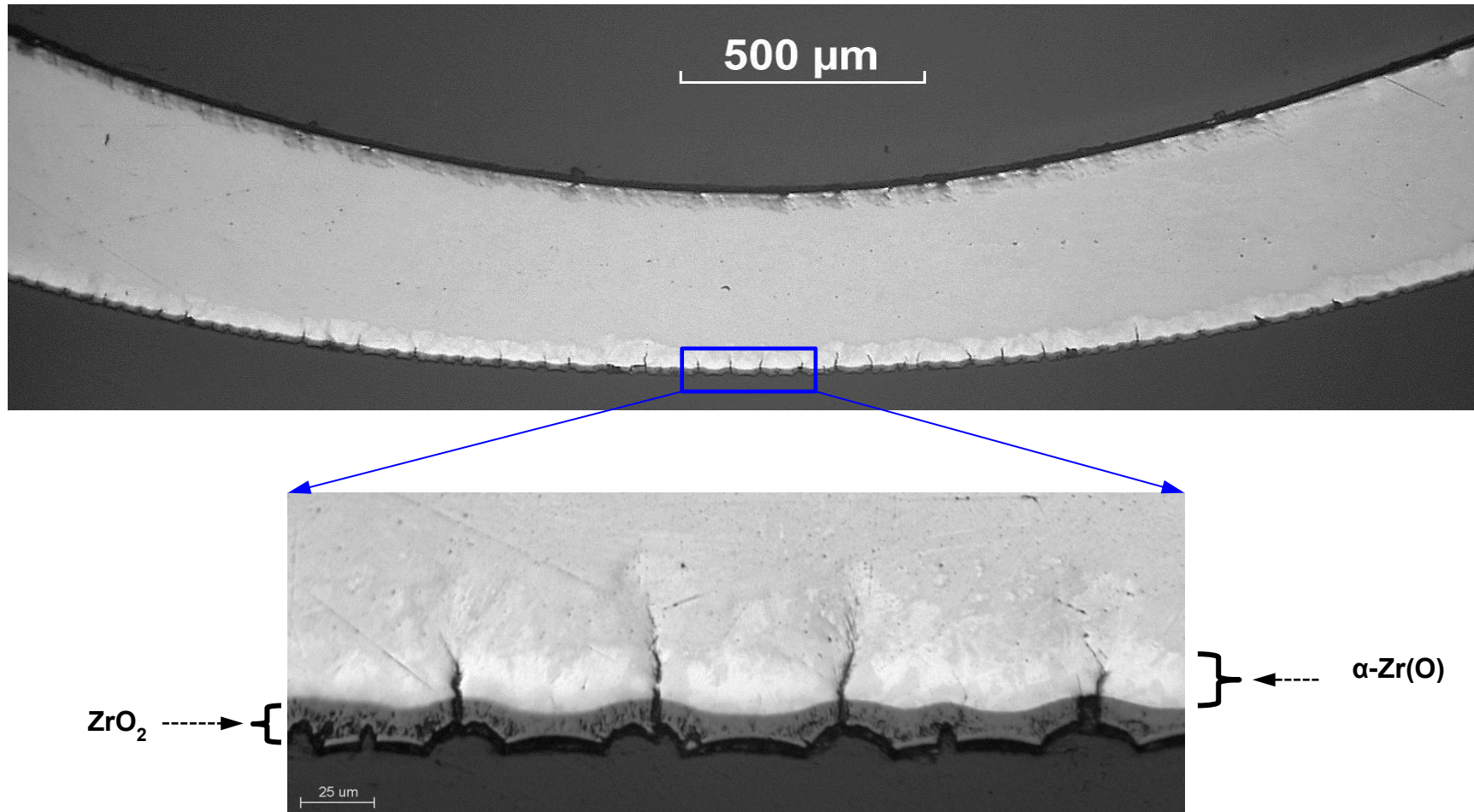


Figure 68 QUENCH-L3; Rod #5: surface cracks (“tree bark”) formed during ballooning about 5 mm below the burst opening (angle 184°) and penetrated ZrO_2 and $\alpha-Zr(O)$ layers in the region of intensively thinned cladding (with density of ≈ 20 cracks/mm). Outside of opening circumferential position only cracks inside oxide layer were formed (with density of ≈ 40 cracks/mm).

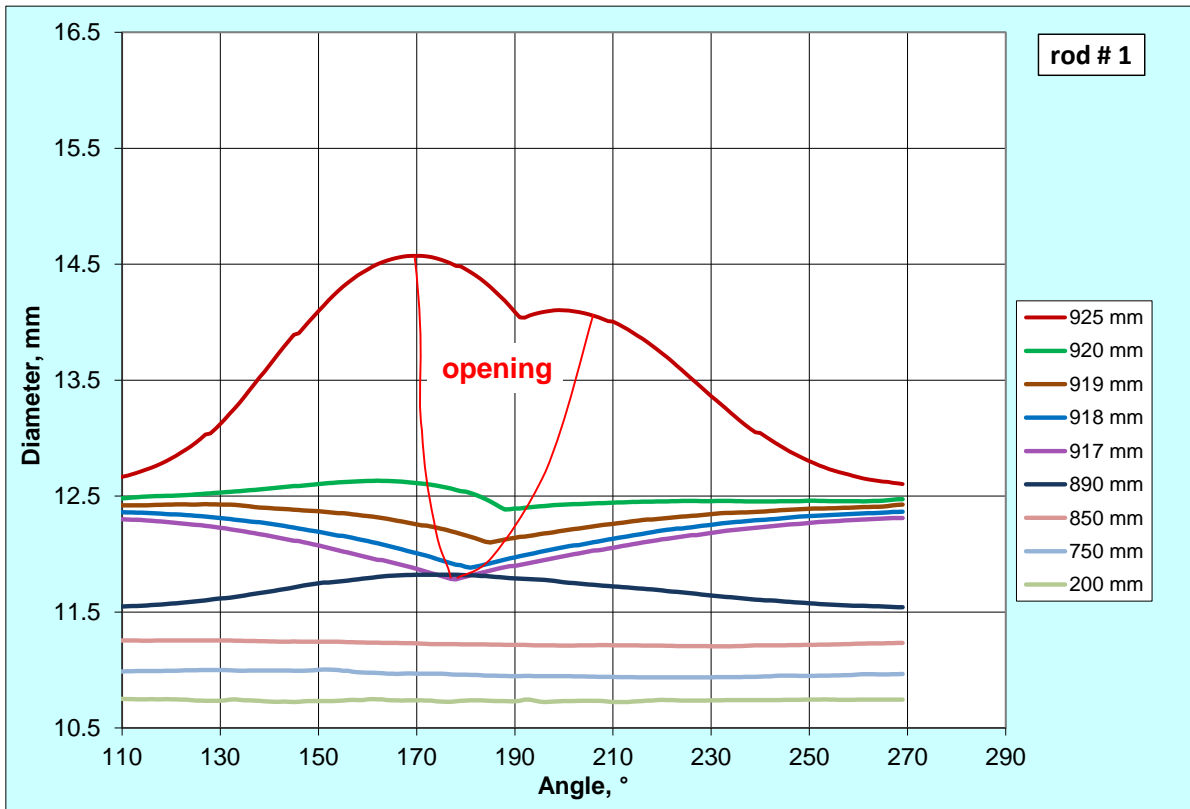
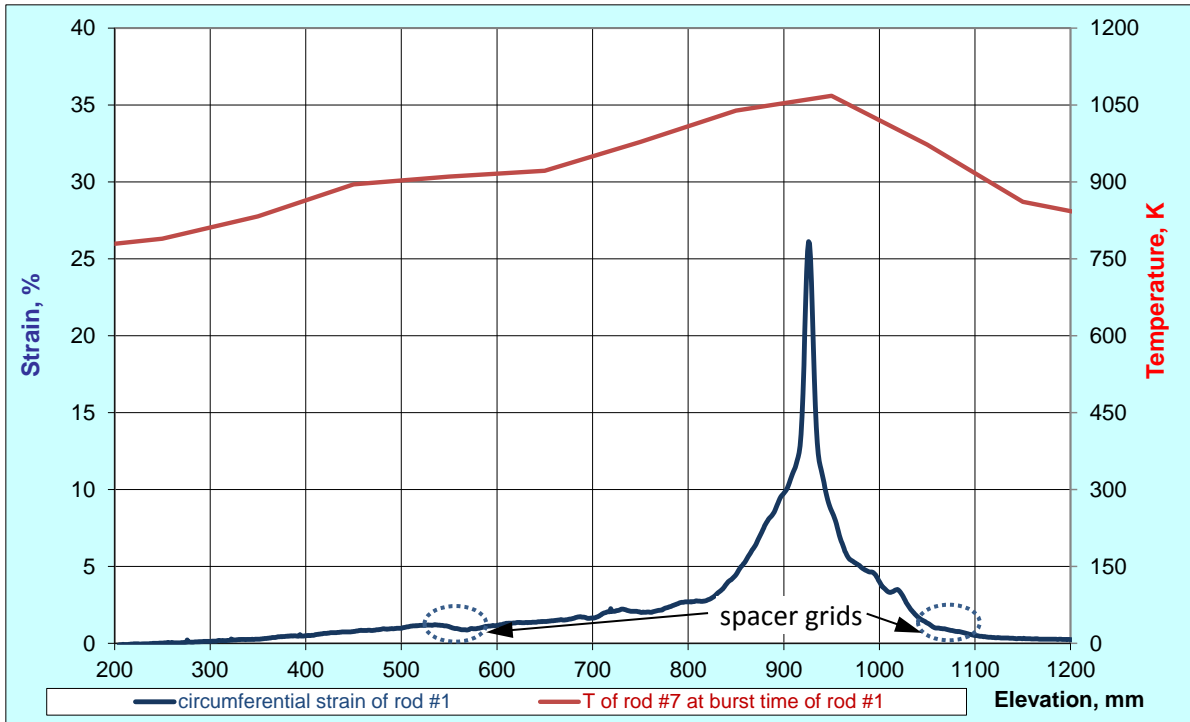


Figure 69 QUENCH-L3, Rod #1; longitudinal changing of circumferential strain (top); azimuthal diameter downwards from burst (bottom).

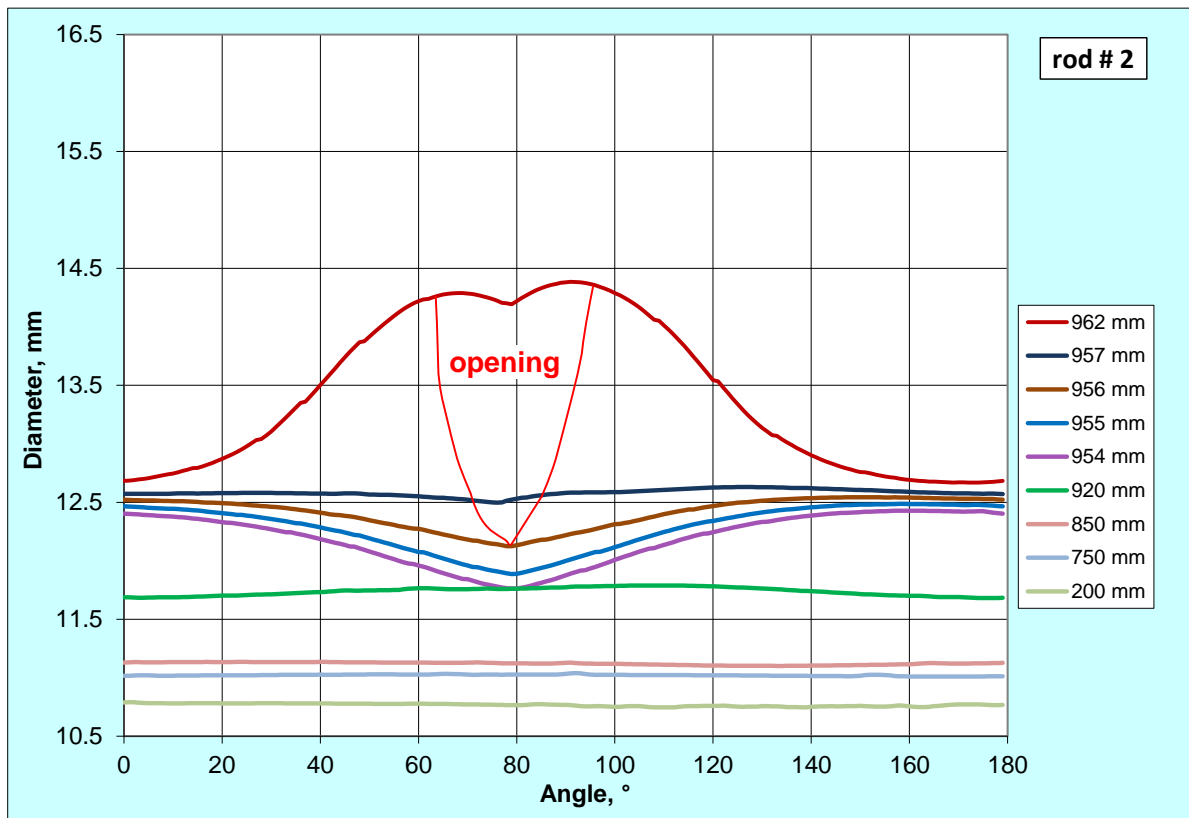
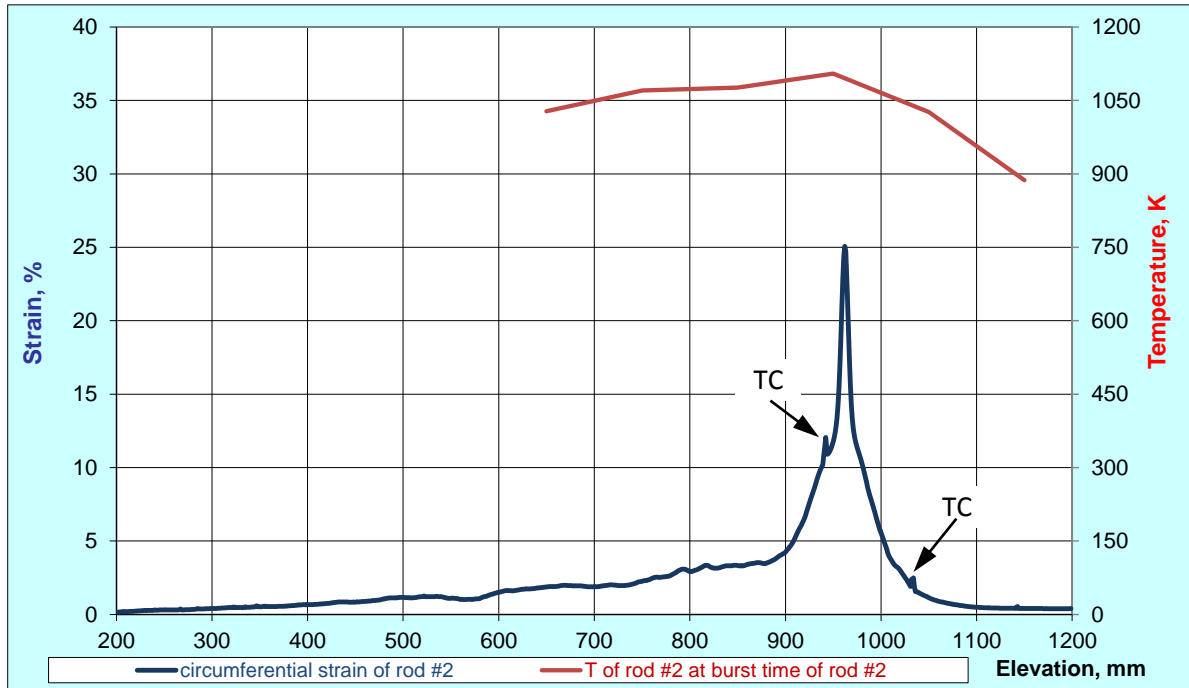


Figure 70 QUENCH-L3, Rod #2; longitudinal changing of circumferential strain (top); azimuthal diameter downwards from burst (bottom).

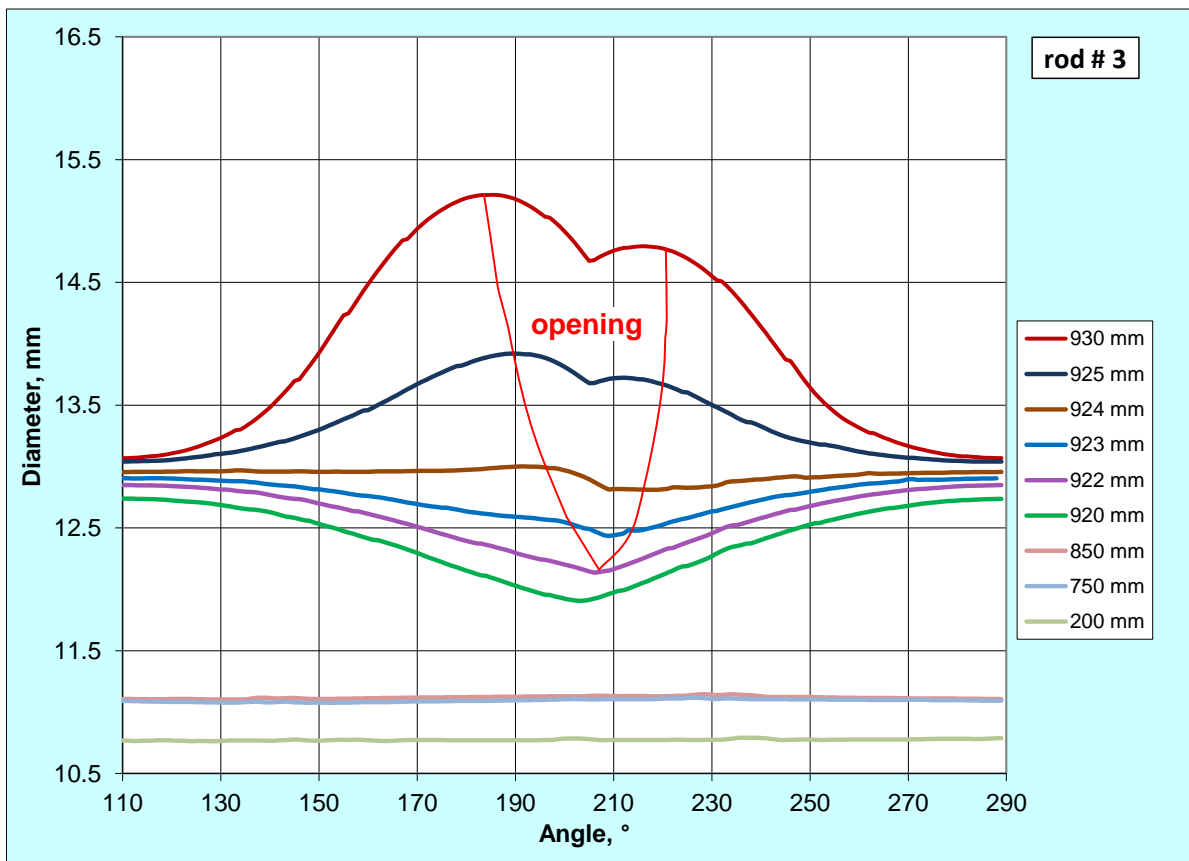
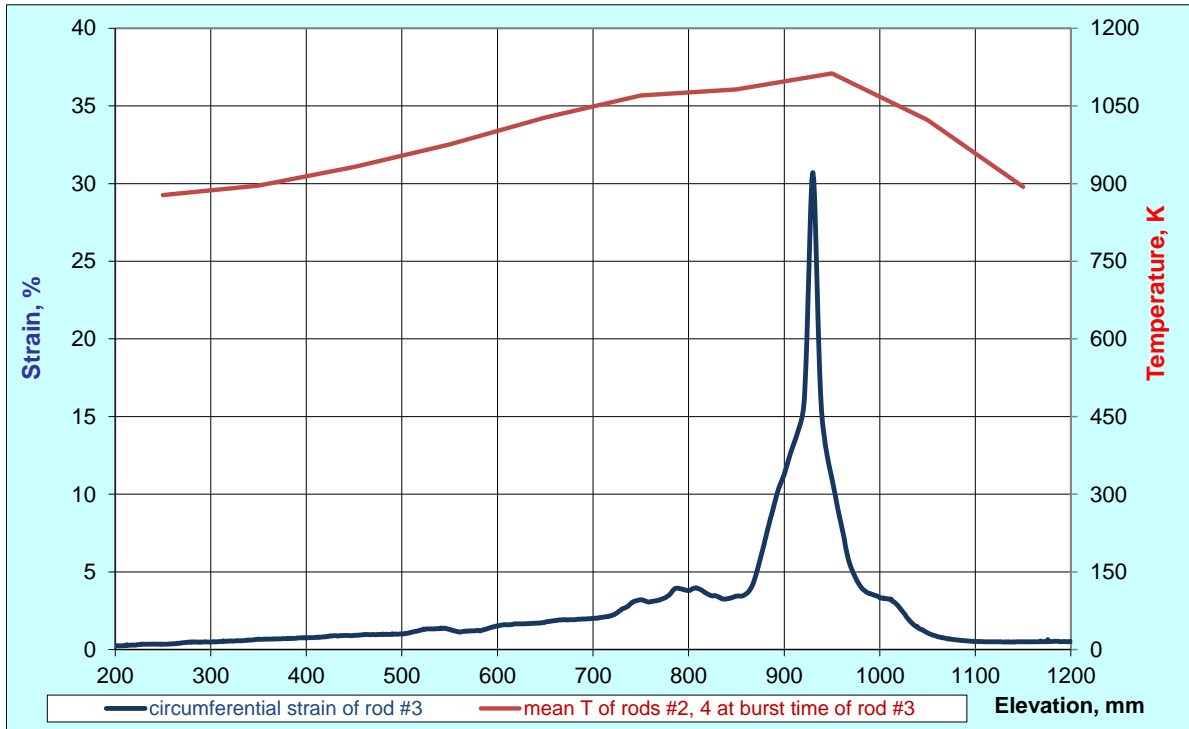


Figure 71 QUENCH-L3, Rod #3; longitudinal changing of circumferential strain (top); azimuthal diameter downwards from burst (bottom).

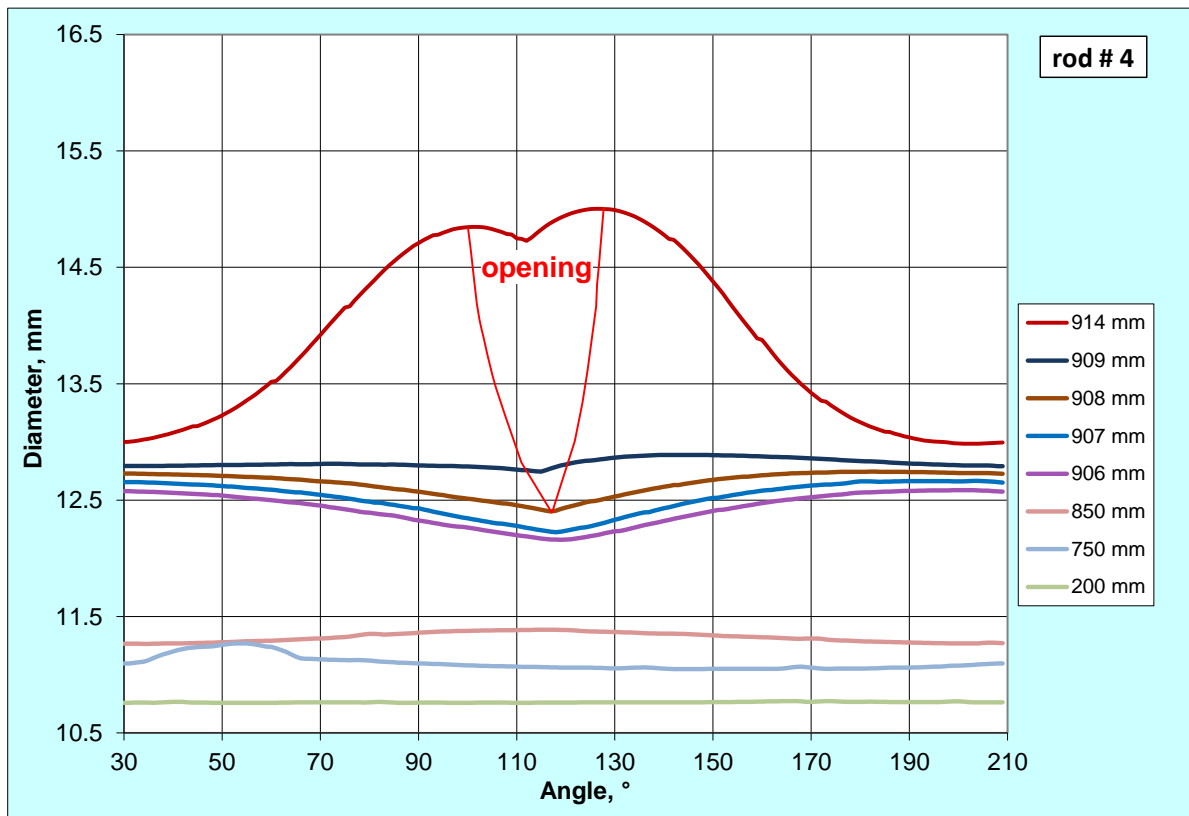
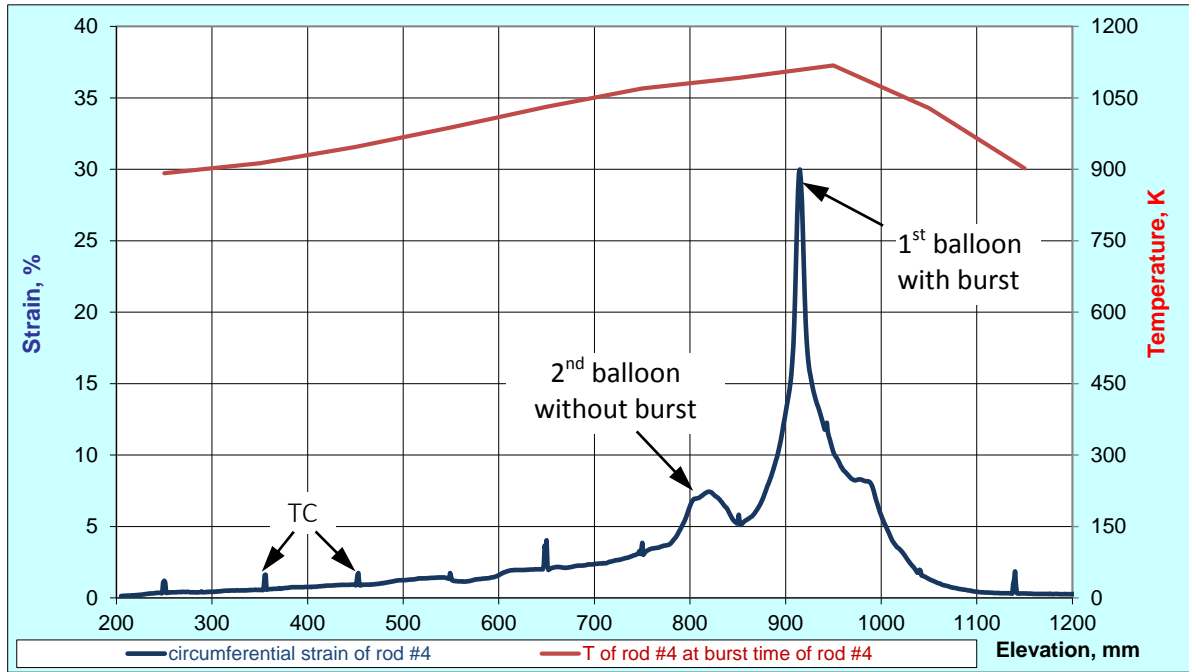


Figure 72 QUENCH-L3, Rod #4; longitudinal changing of circumferential strain (top); azimuthal diameter downwards from burst (bottom). Spikes: thermocouple.

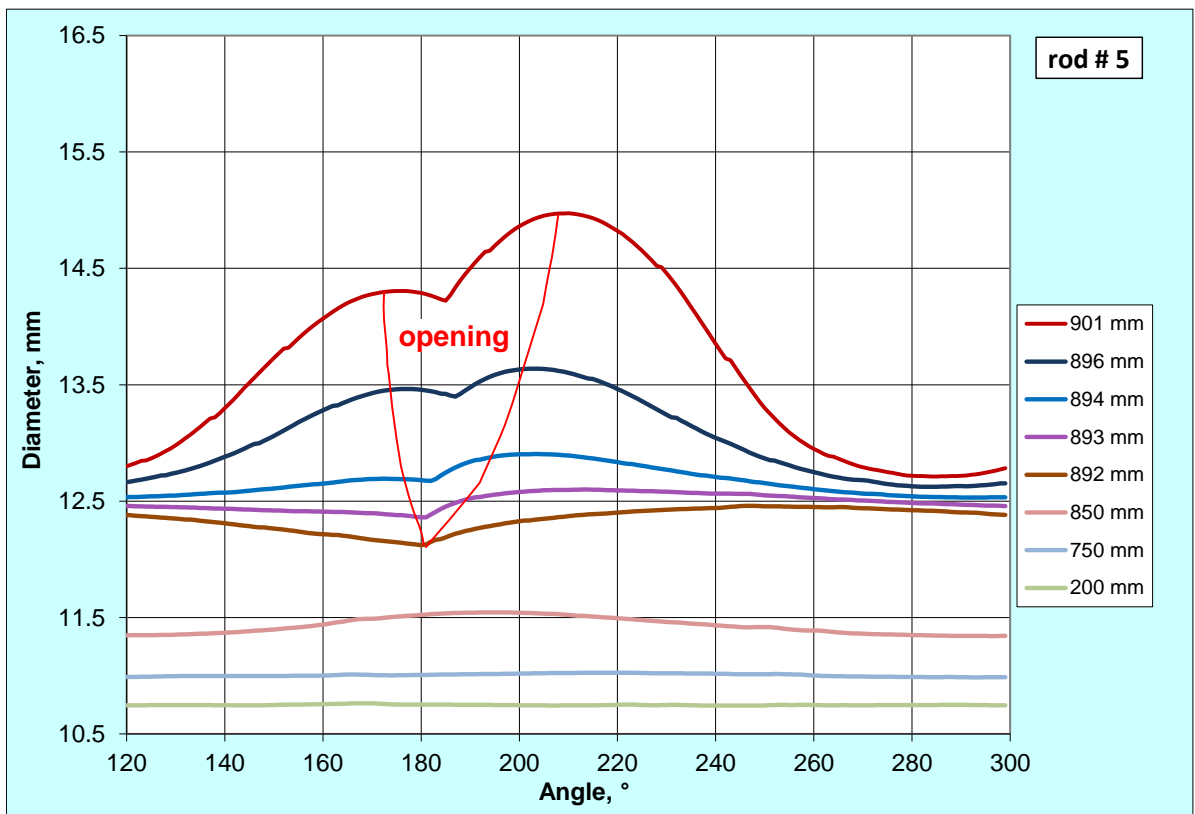
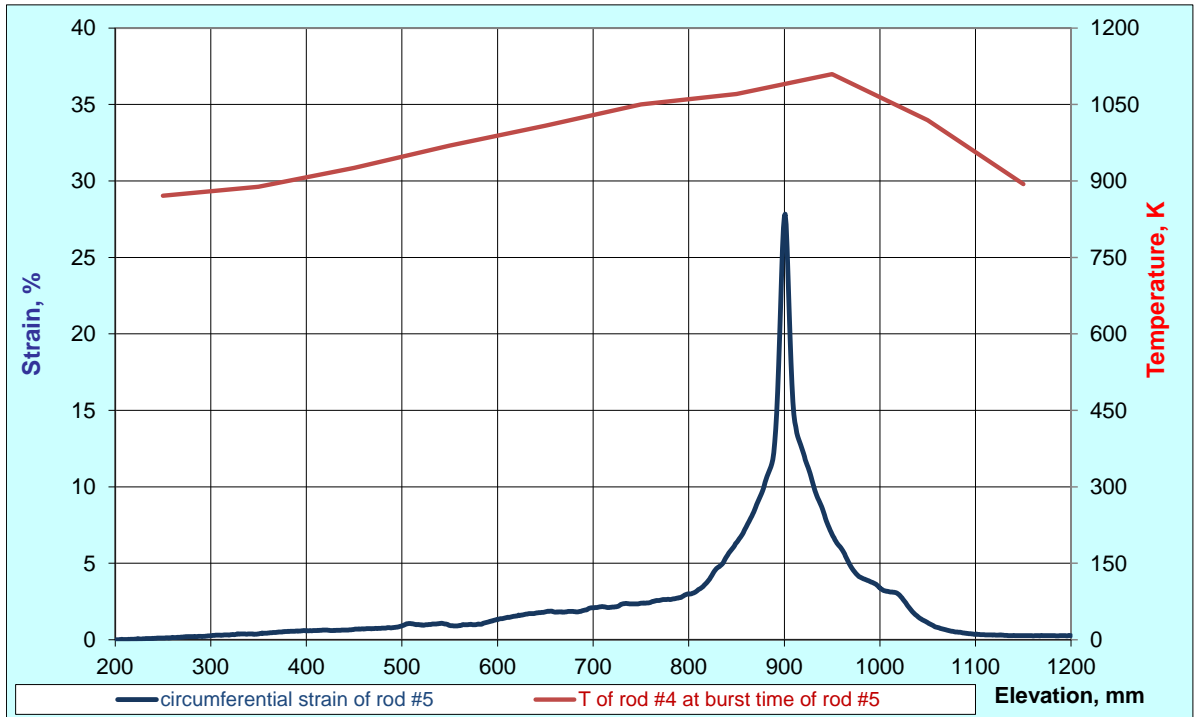


Figure 73 QUENCH-L3 , Rod #5; longitudinal changing of circumferential strain (top); azimuthal diameter downwards from burst (bottom).

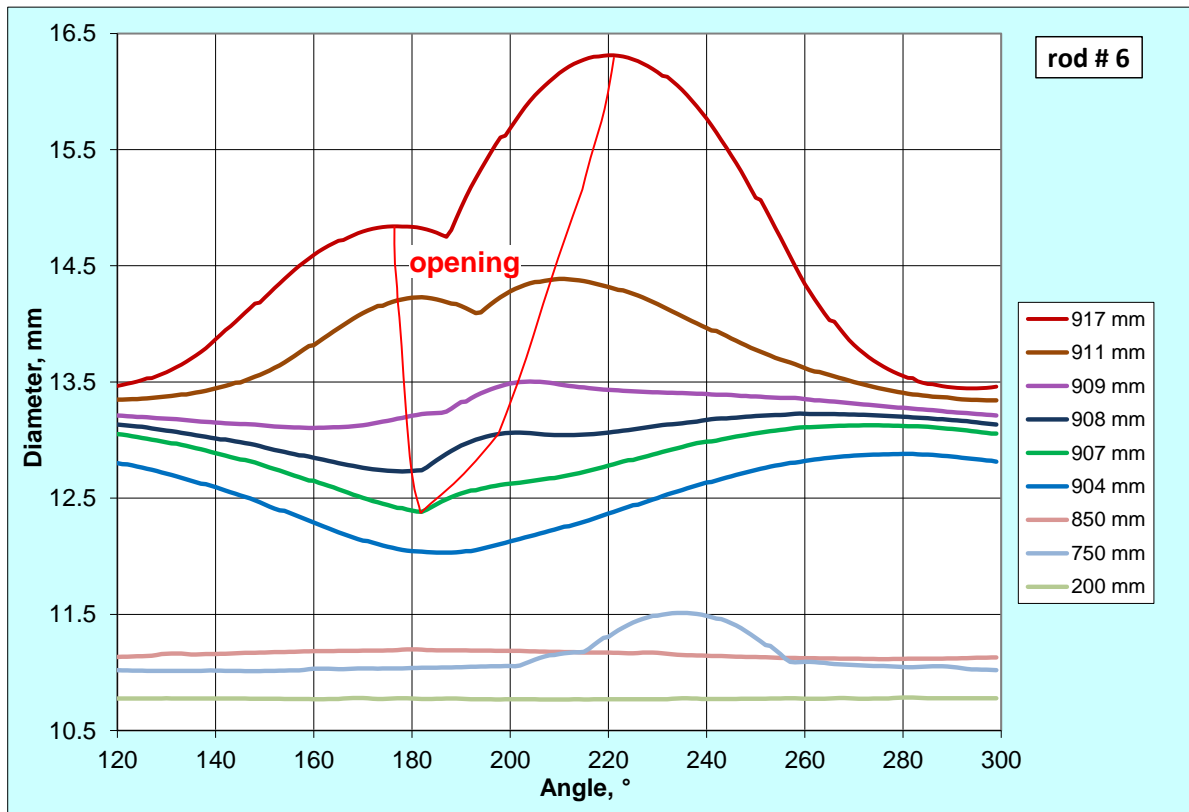
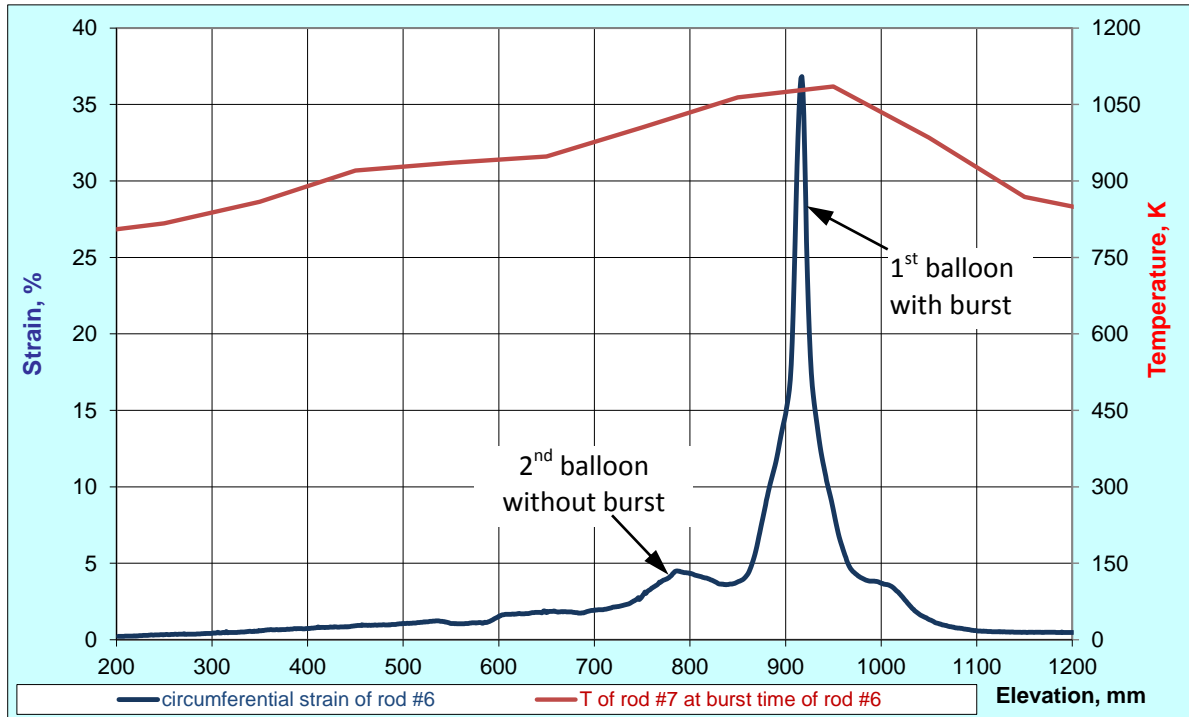


Figure 74 QUENCH-L3, Rod #6; longitudinal changing of circumferential strain (top); azimuthal diameter downwards from burst (bottom).

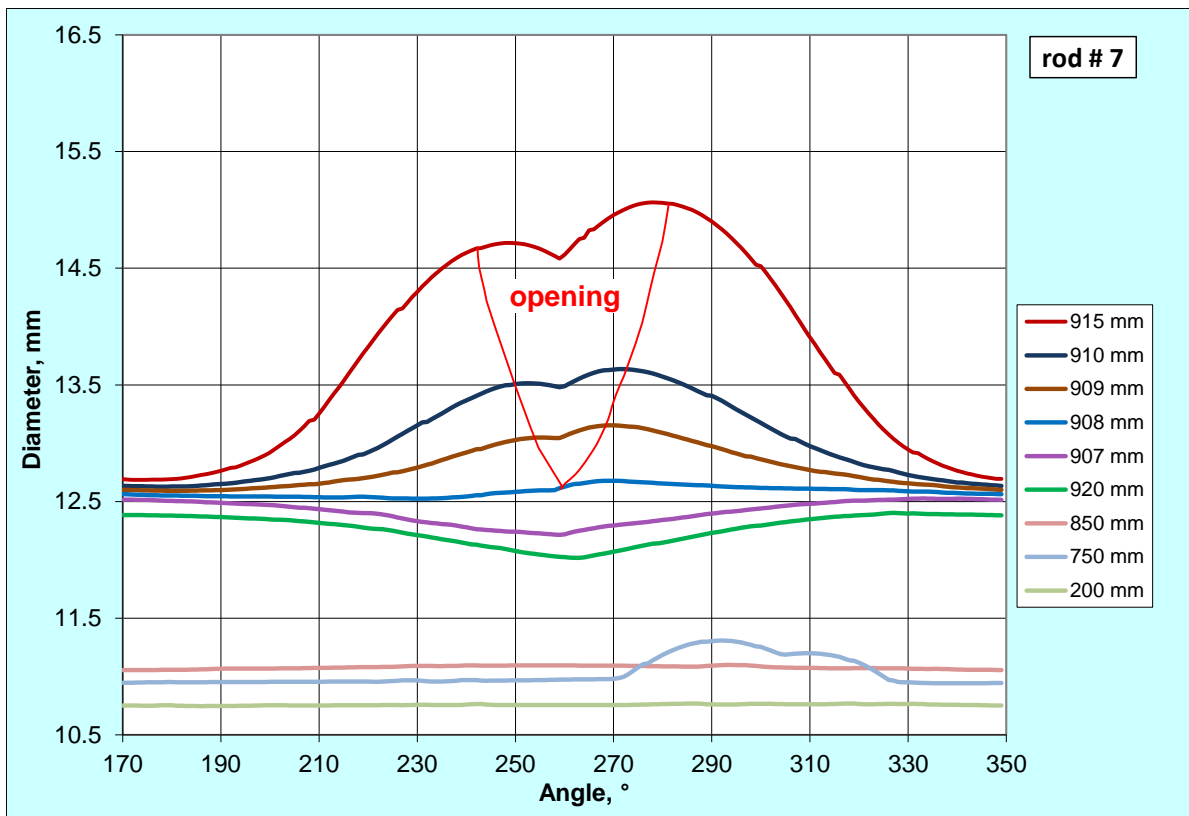
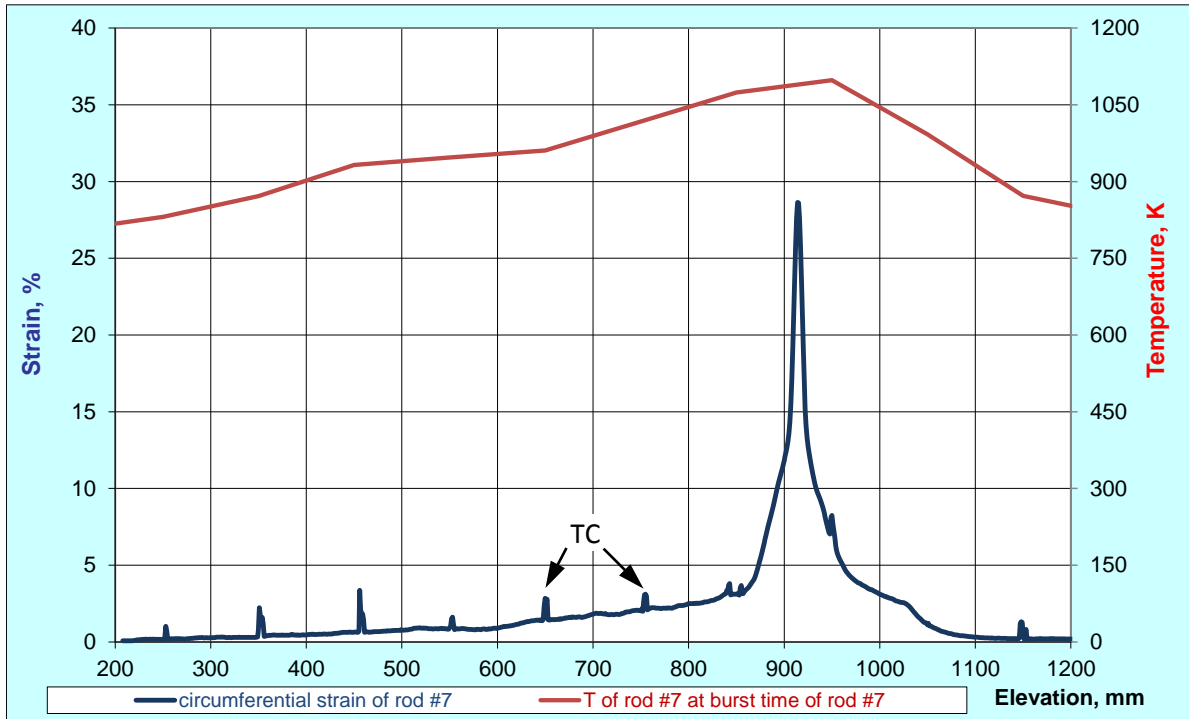


Figure 75 QUENCH-L3, Rod #7; longitudinal changing of circumferential strain (top); azimuthal diameter downwards from burst (bottom). Spikes: thermocouples.

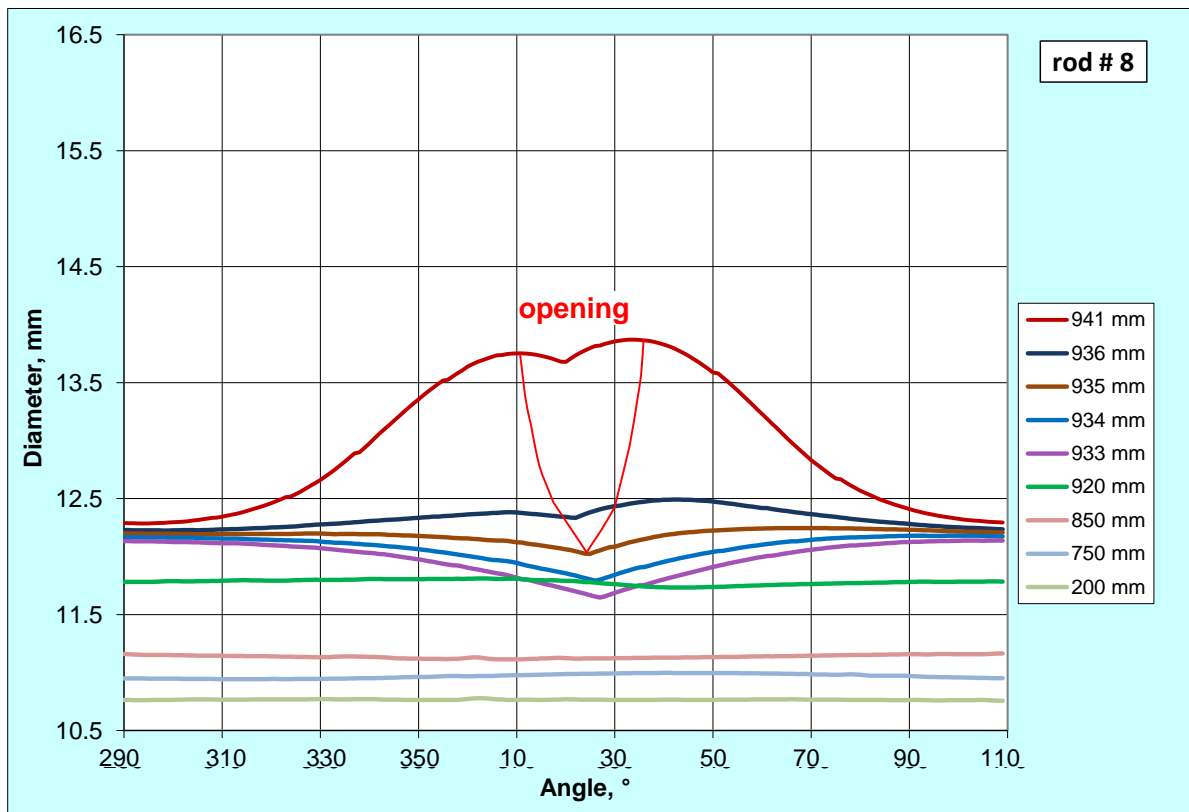
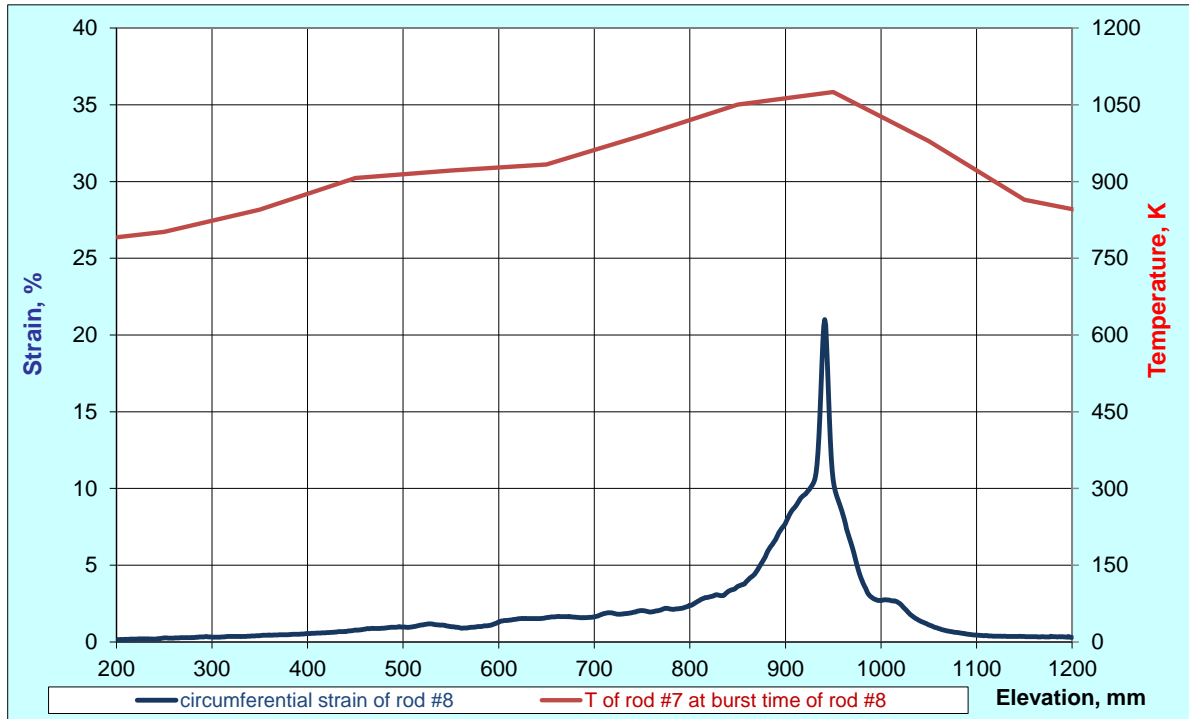


Figure 76 QUENCH-L3, Rod #8; longitudinal changing of circumferential strain (top); azimuthal diameter downwards from burst (bottom).

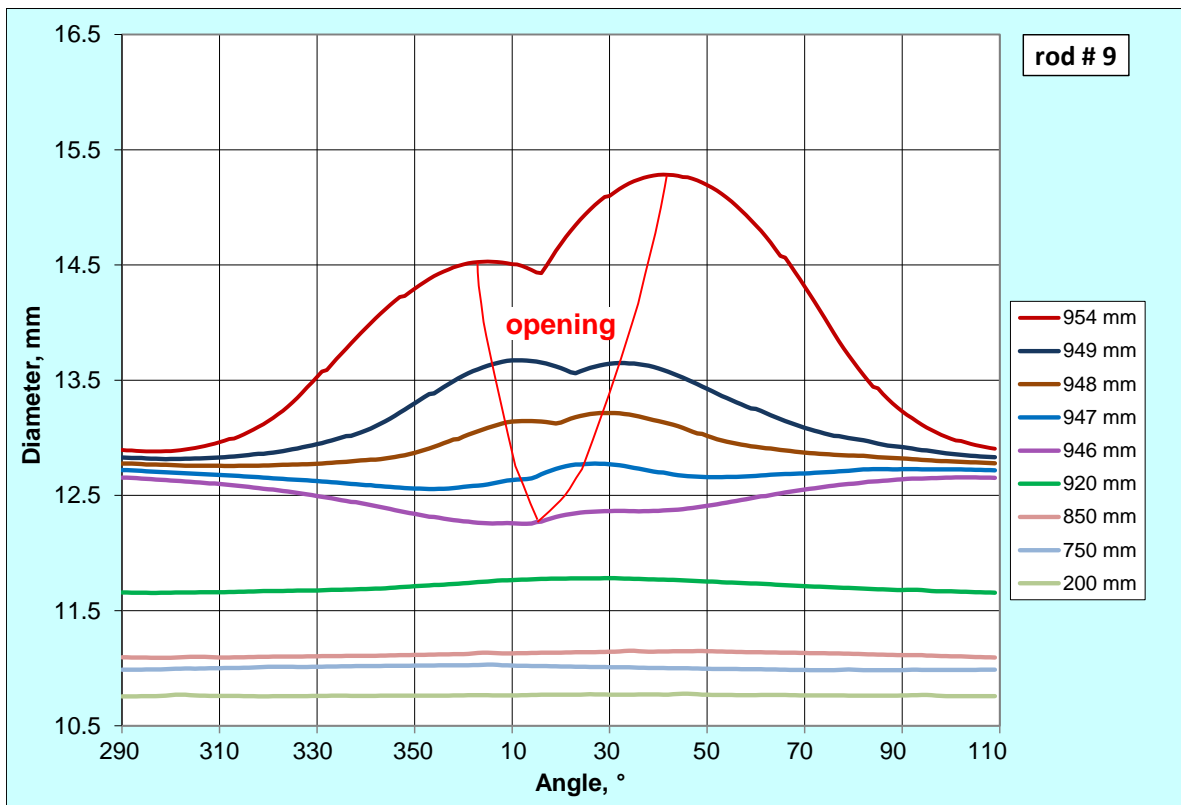
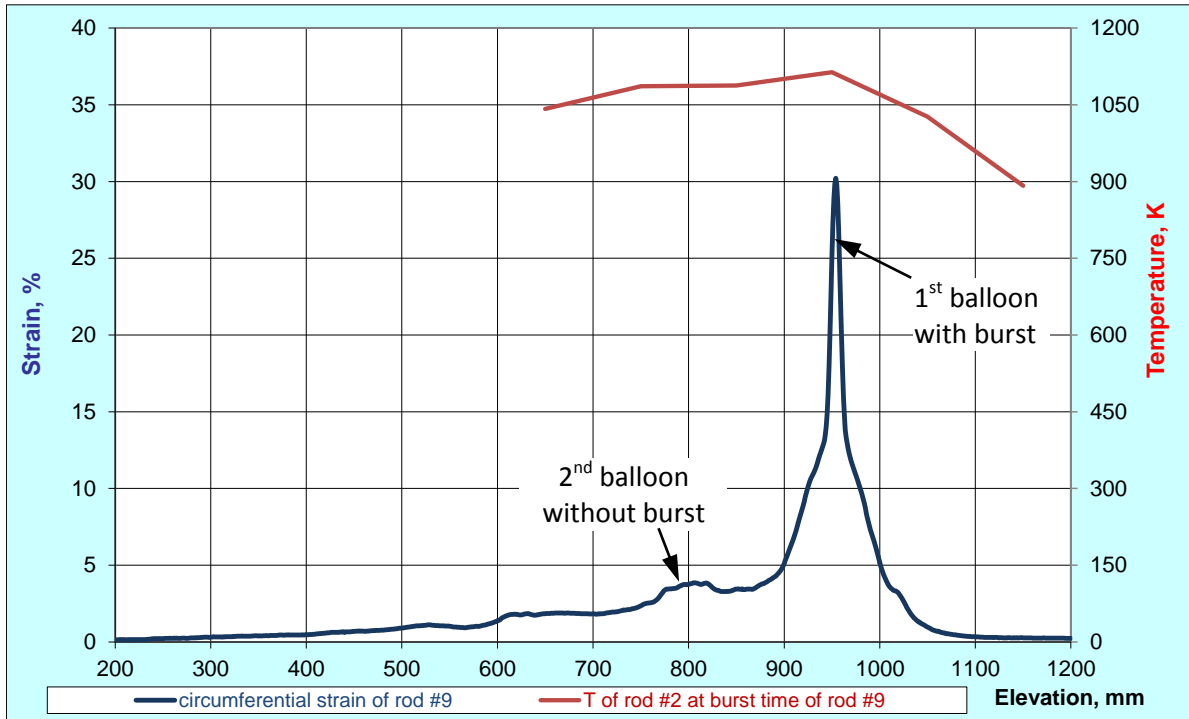


Figure 77 QUENCH-L3, Rod #9; longitudinal changing of circumferential strain (top); azimuthal diameter downwards from burst (bottom).

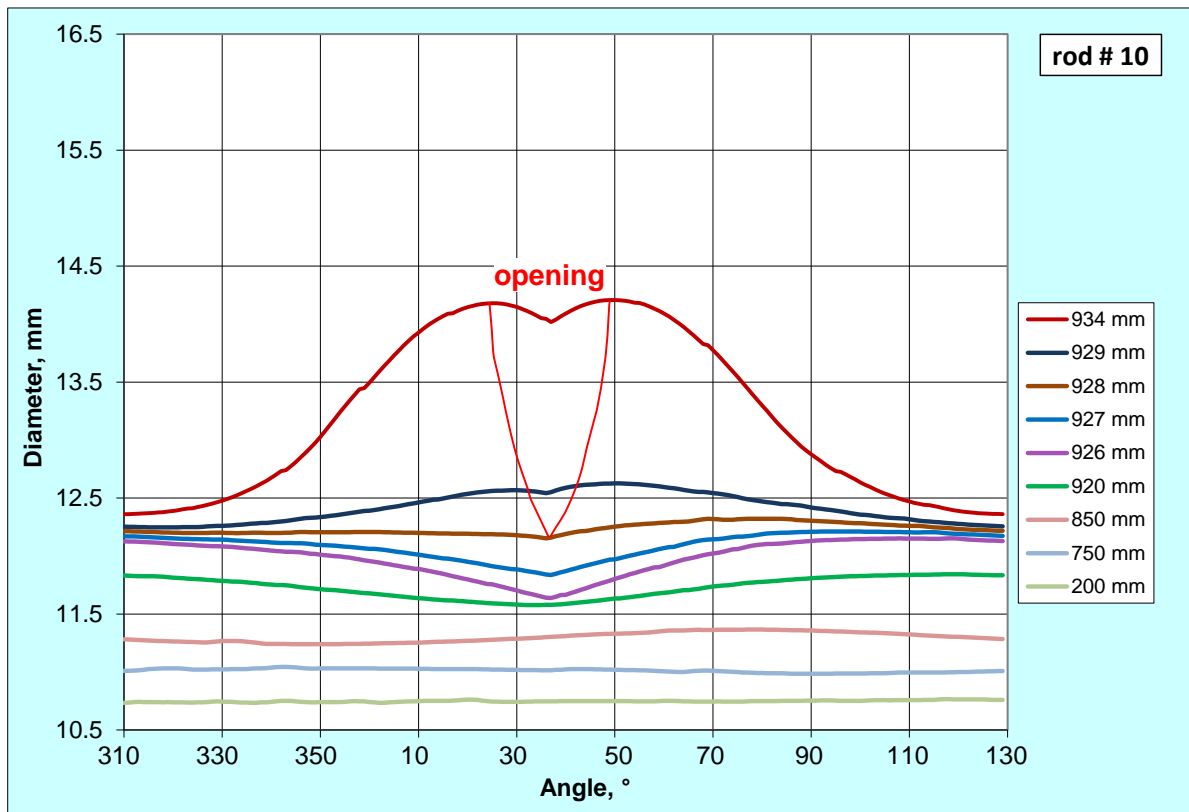
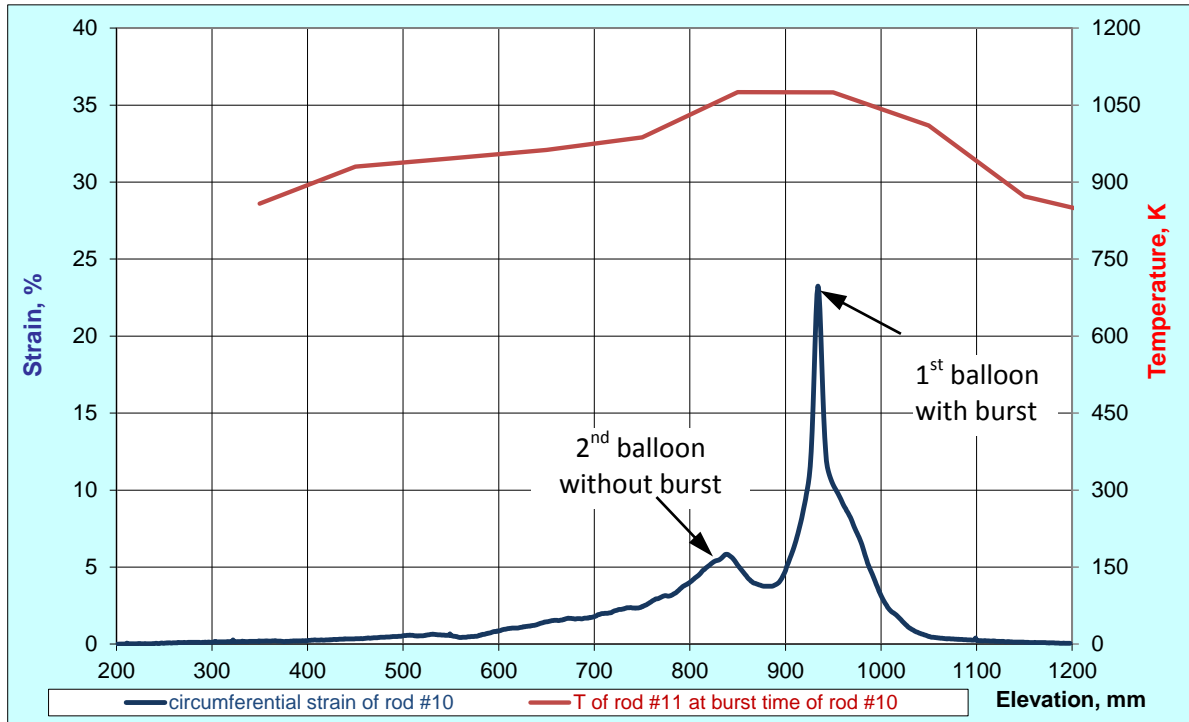


Figure 78 QUENCH-L3, Rod #10; longitudinal changing of circumferential strain (top); azimuthal diameter downwards from burst (bottom).

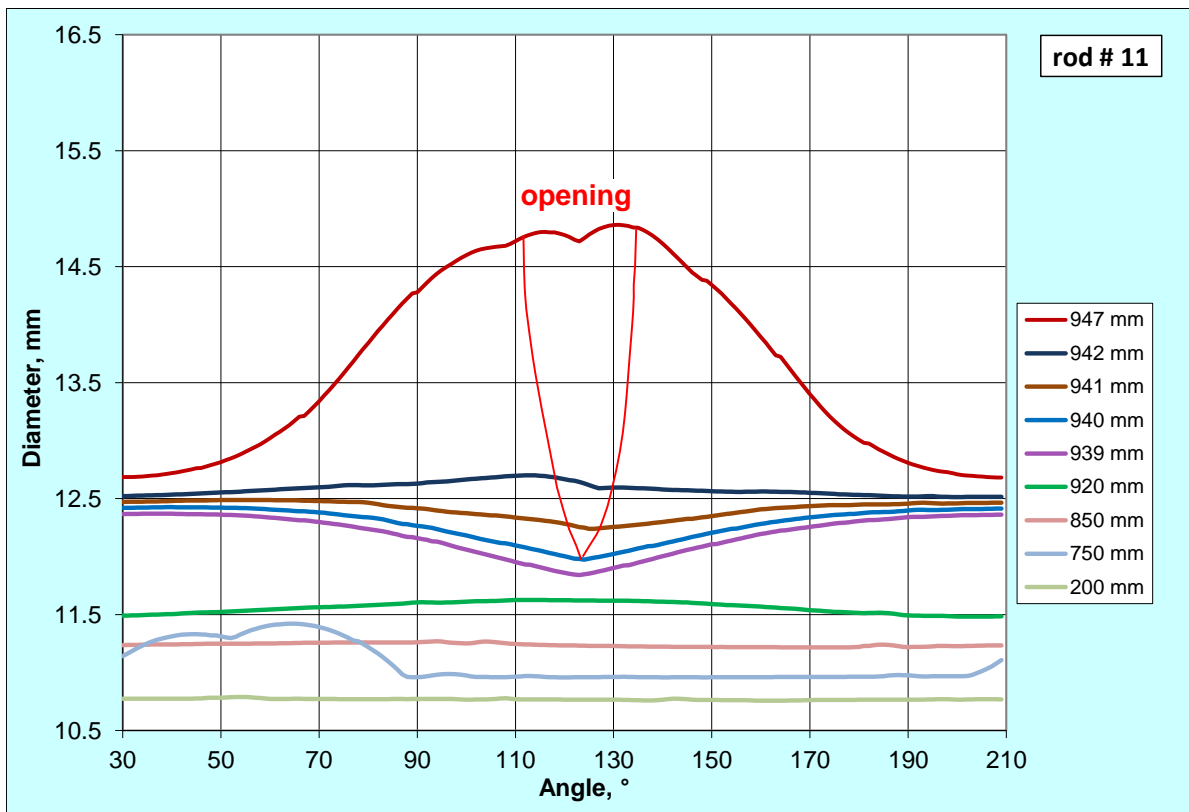
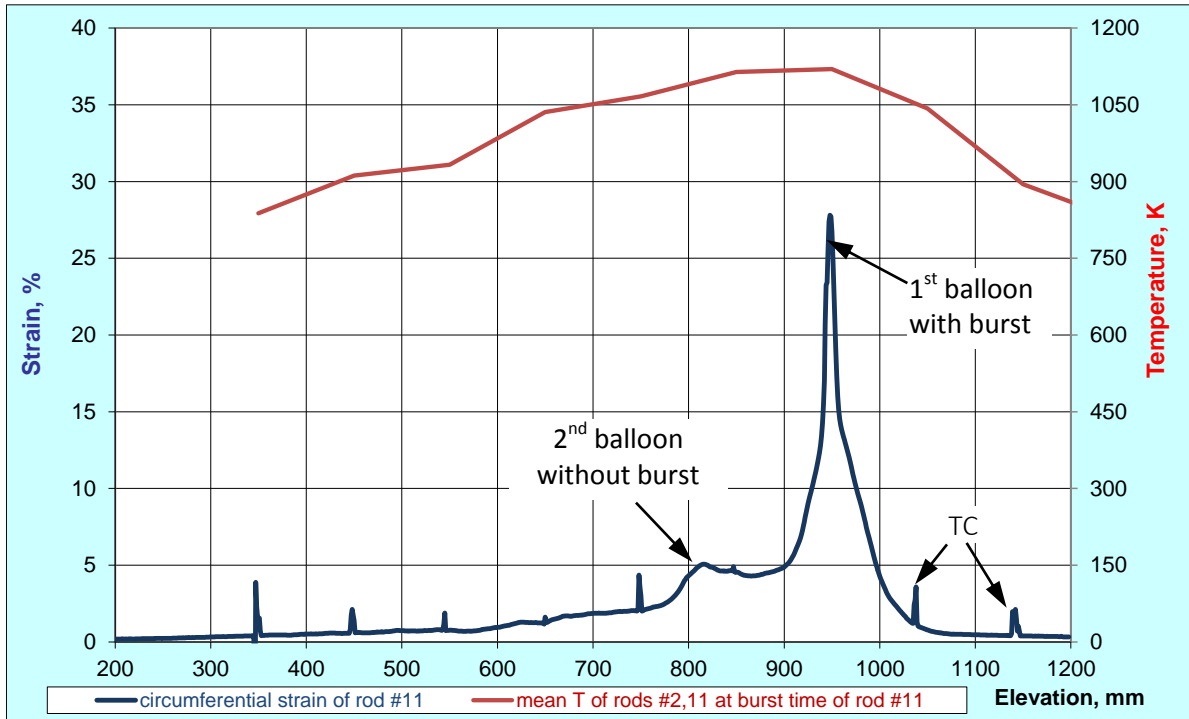


Figure 79 QUENCH-L3, Rod #11; longitudinal changing of circumferential strain (top); azimuthal diameter downwards from burst (bottom). Spikes: thermocouple.

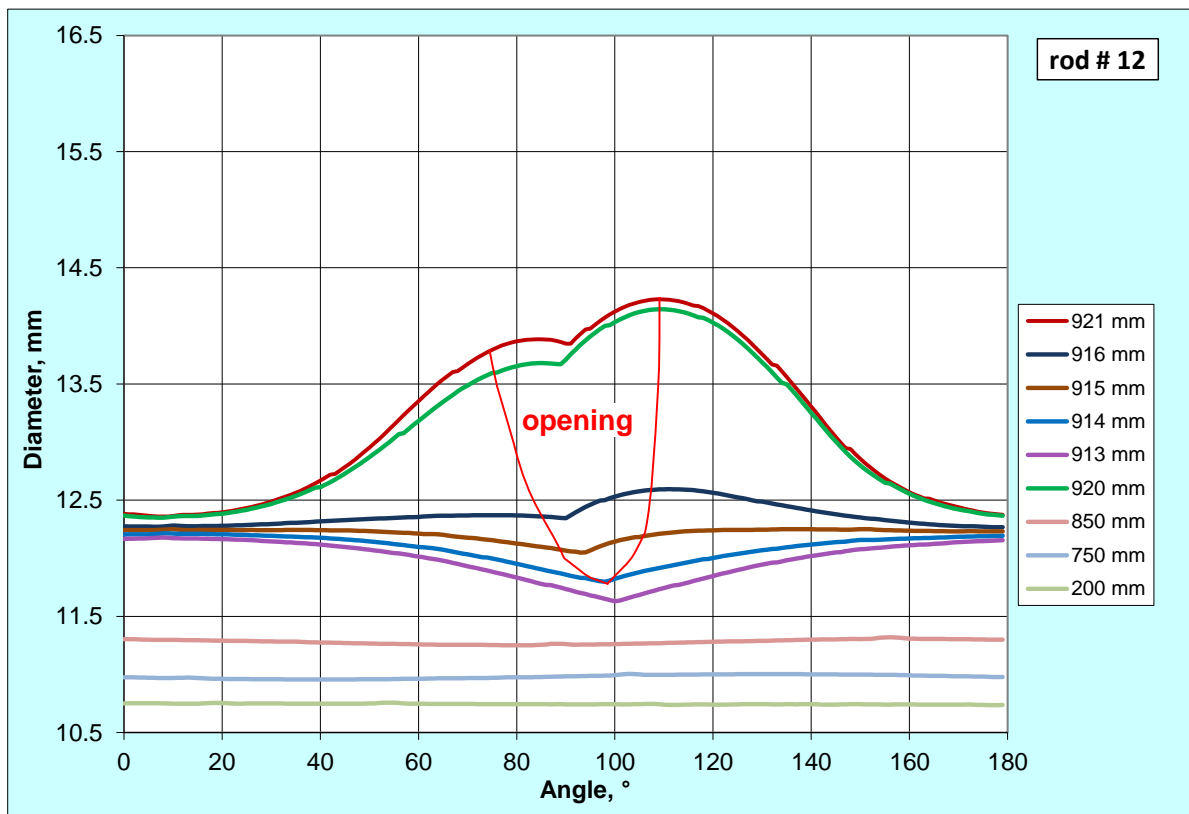
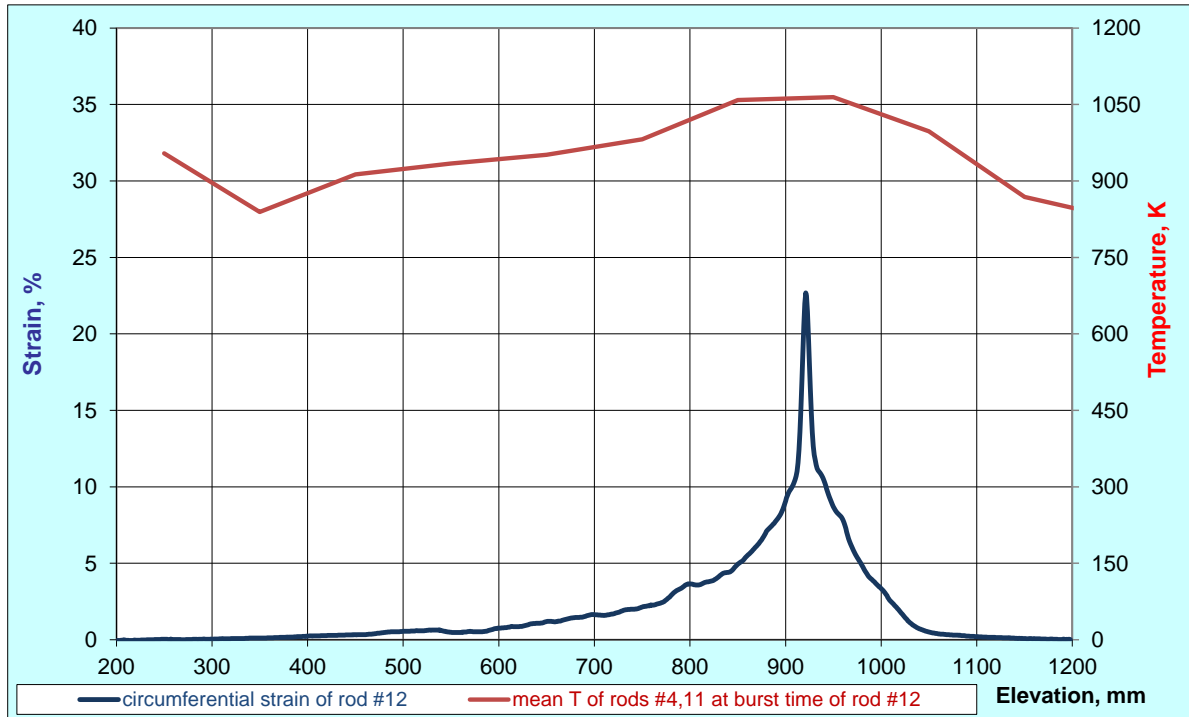


Figure 80 QUENCH-L3, Rod #12; longitudinal changing of circumferential strain (top); azimuthal diameter downwards from burst (bottom).

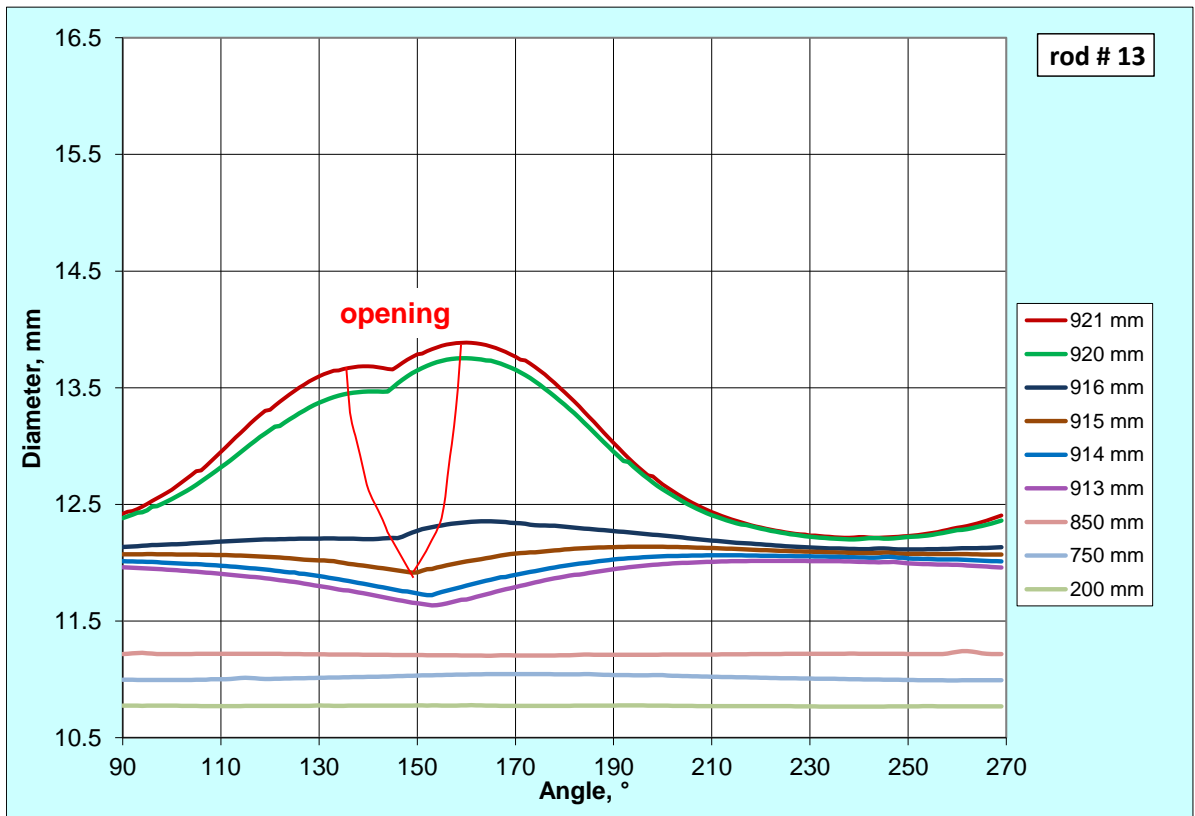
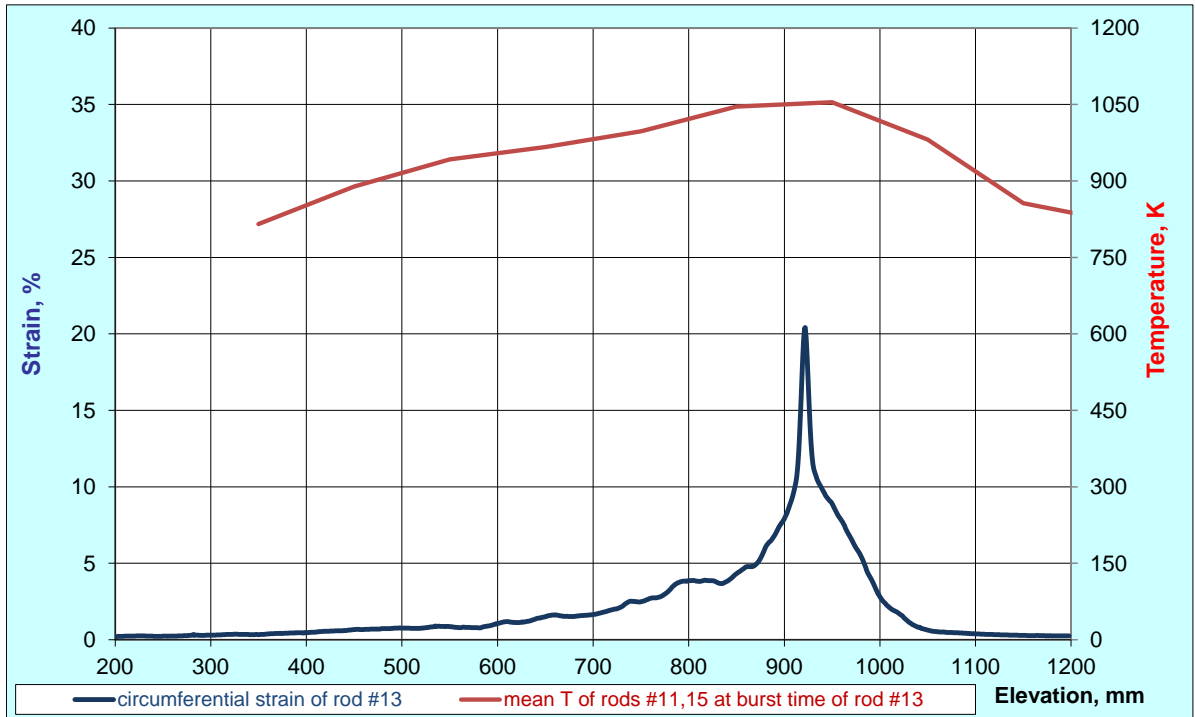


Figure 81 QUENCH-L3, Rod #13; longitudinal changing of circumferential strain (top); azimuthal diameter downwards from burst (bottom).

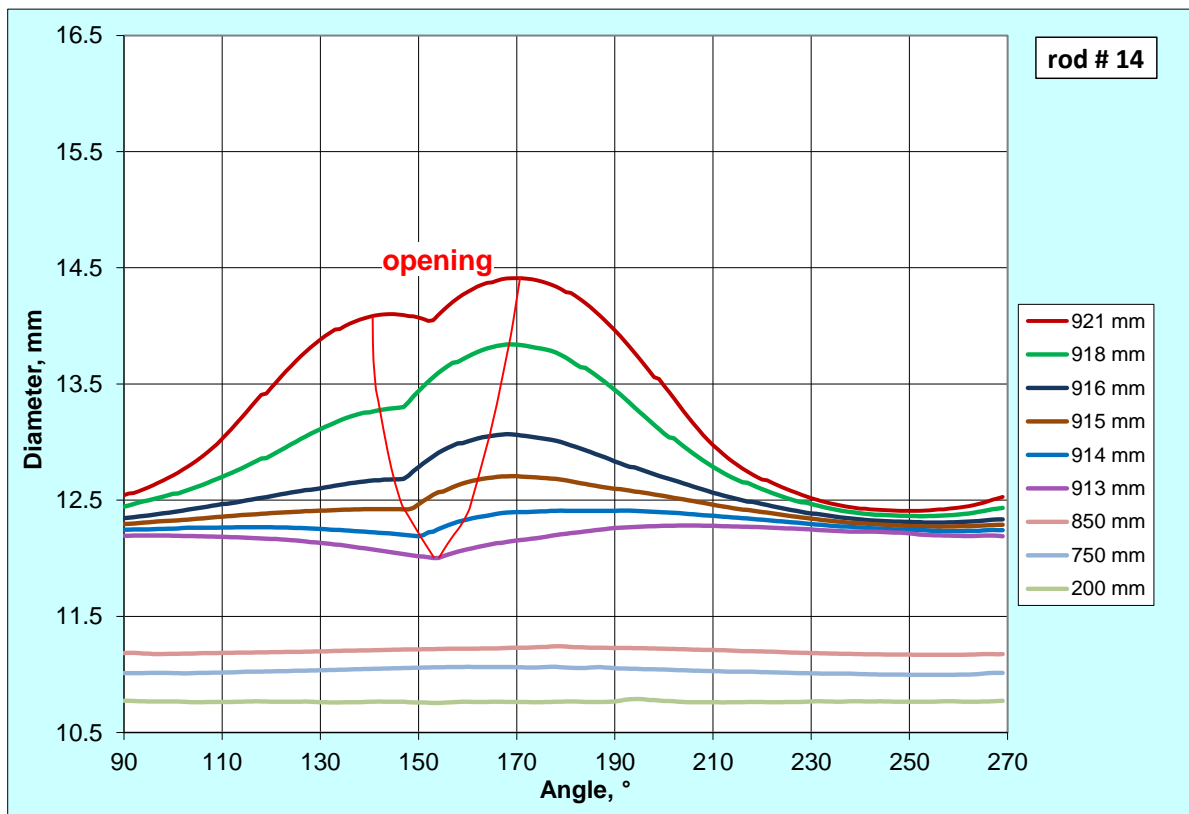
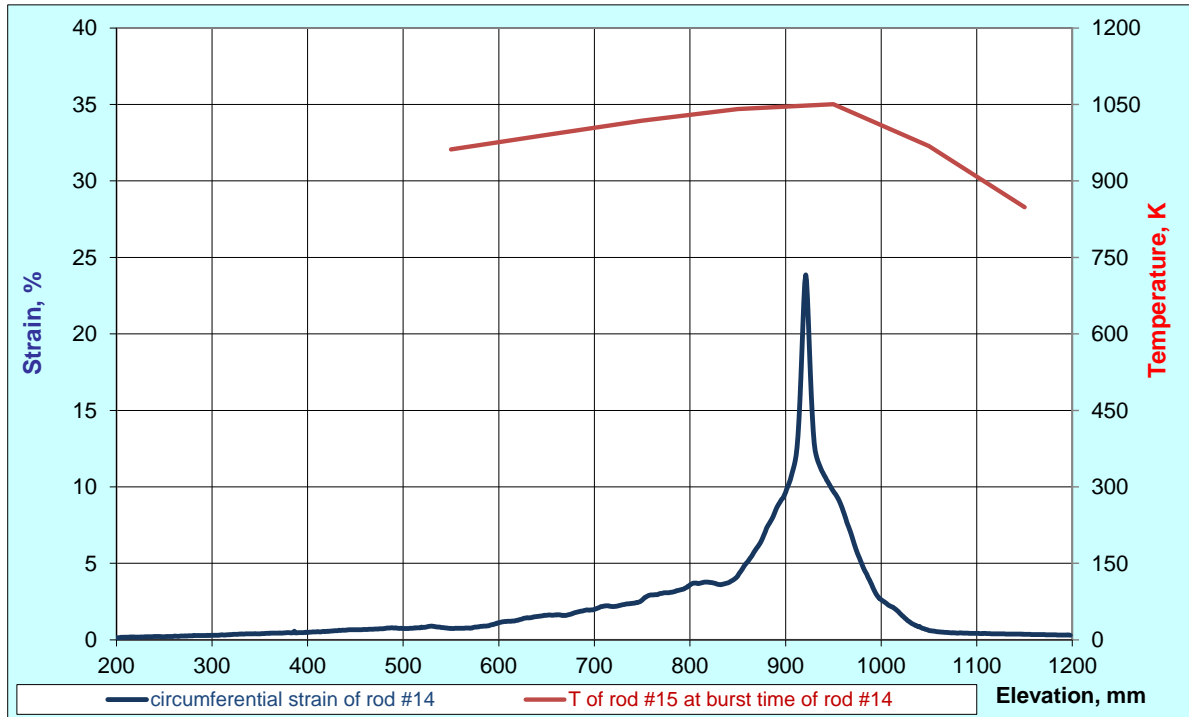


Figure 82 QUENCH-L3, Rod #14; longitudinal changing of circumferential strain (top); azimuthal diameter downwards from burst (bottom).

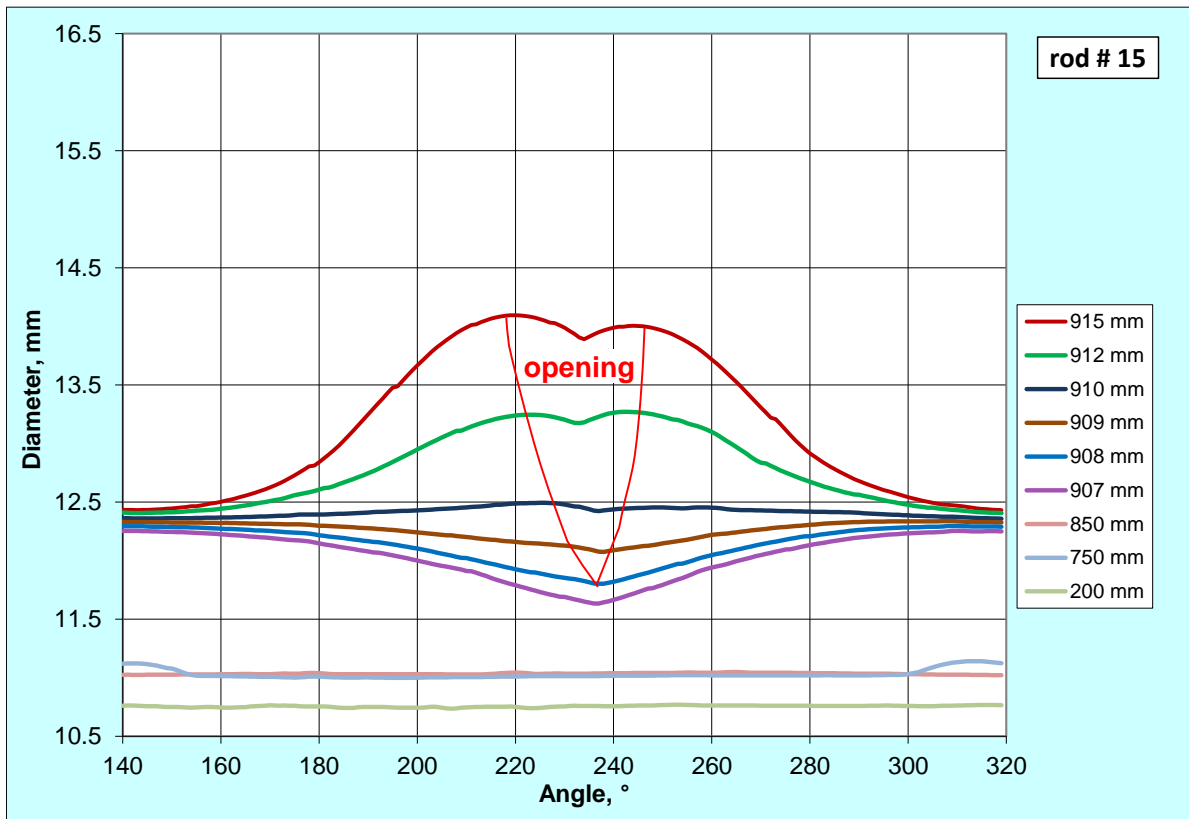
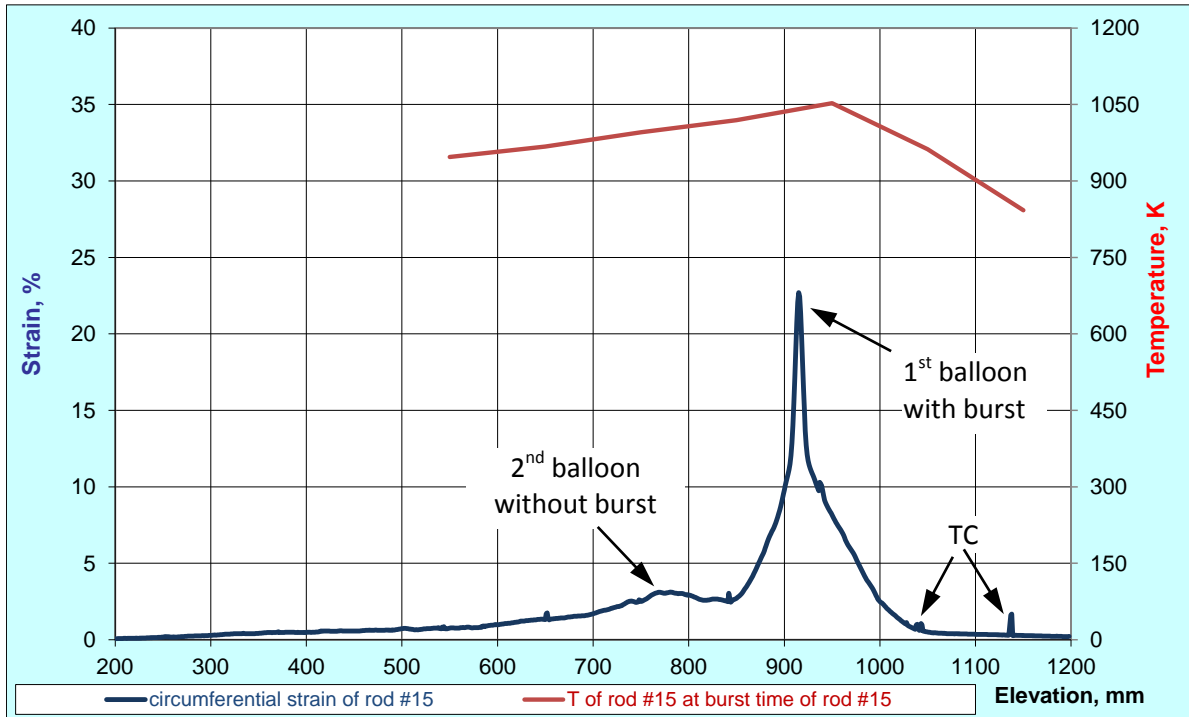


Figure 83 QUENCH-L3, Rod #15; longitudinal changing of circumferential strain (top); azimuthal diameter downwards from burst (bottom). Spikes: thermocouple.

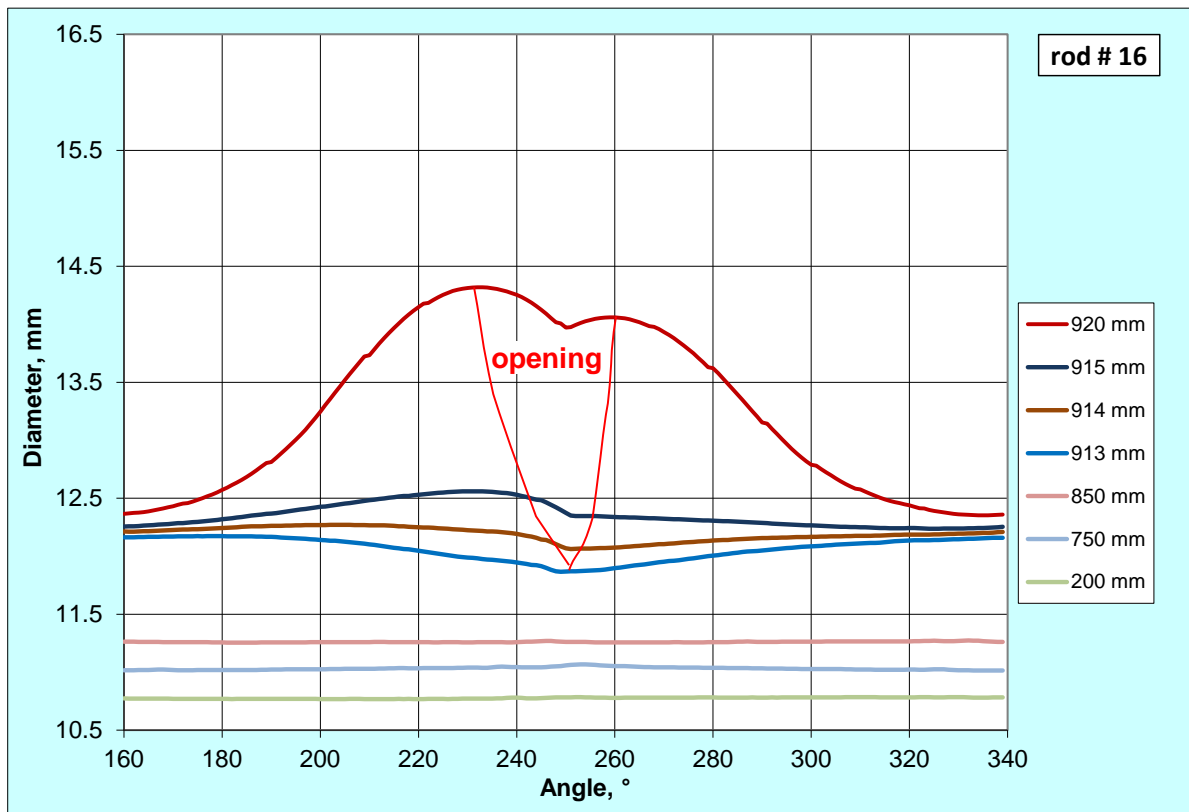
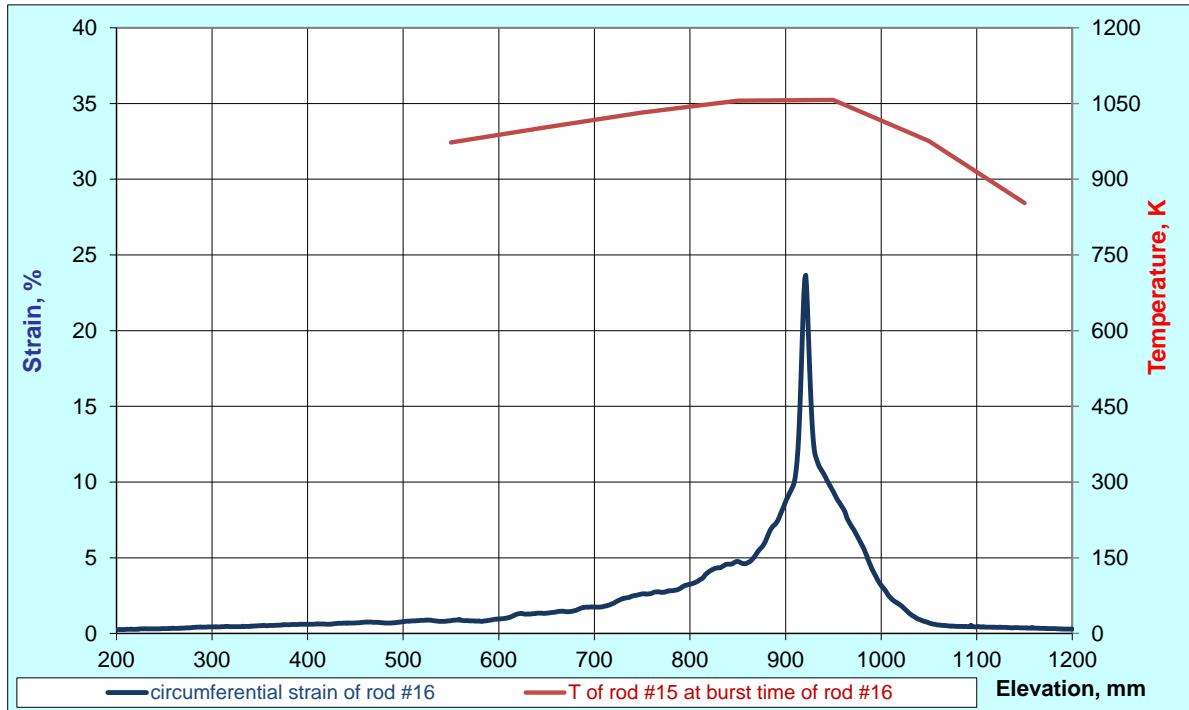


Figure 84 QUENCH-L3, Rod #16; longitudinal changing of circumferential strain (top); azimuthal diameter downwards from burst (bottom).

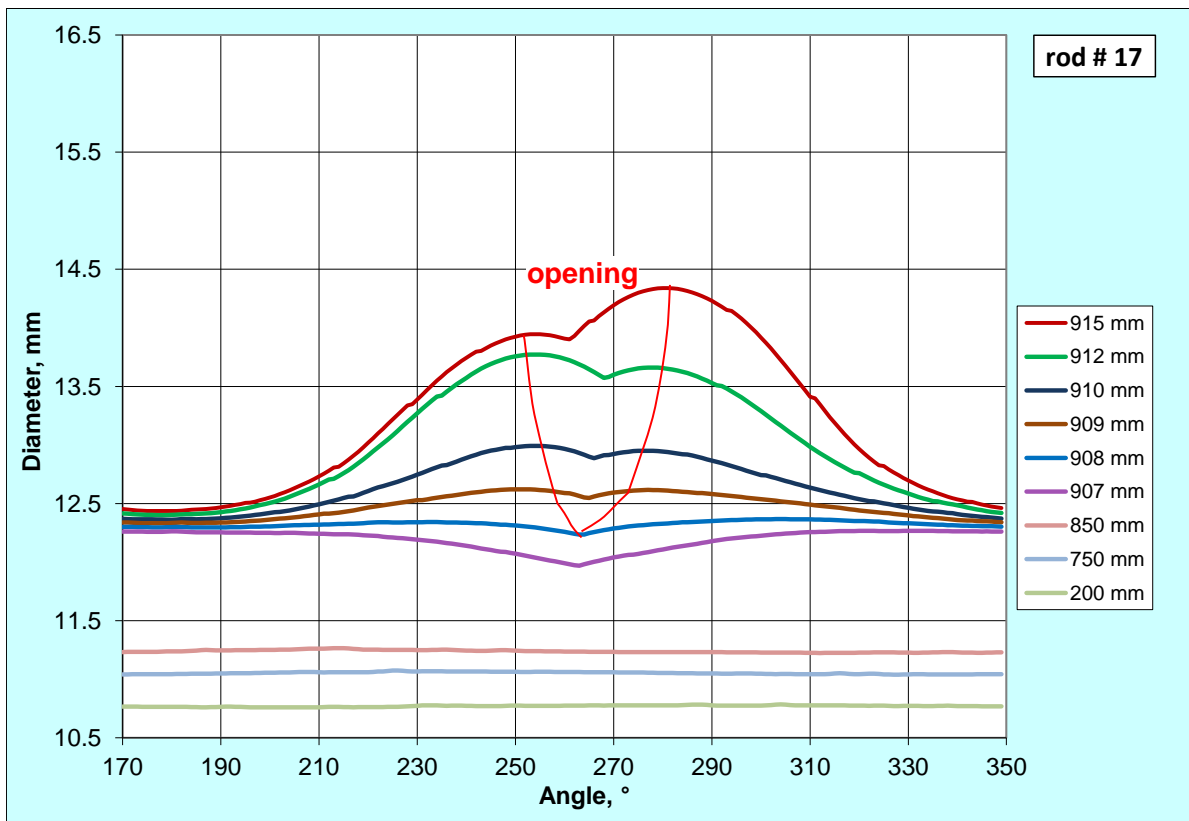
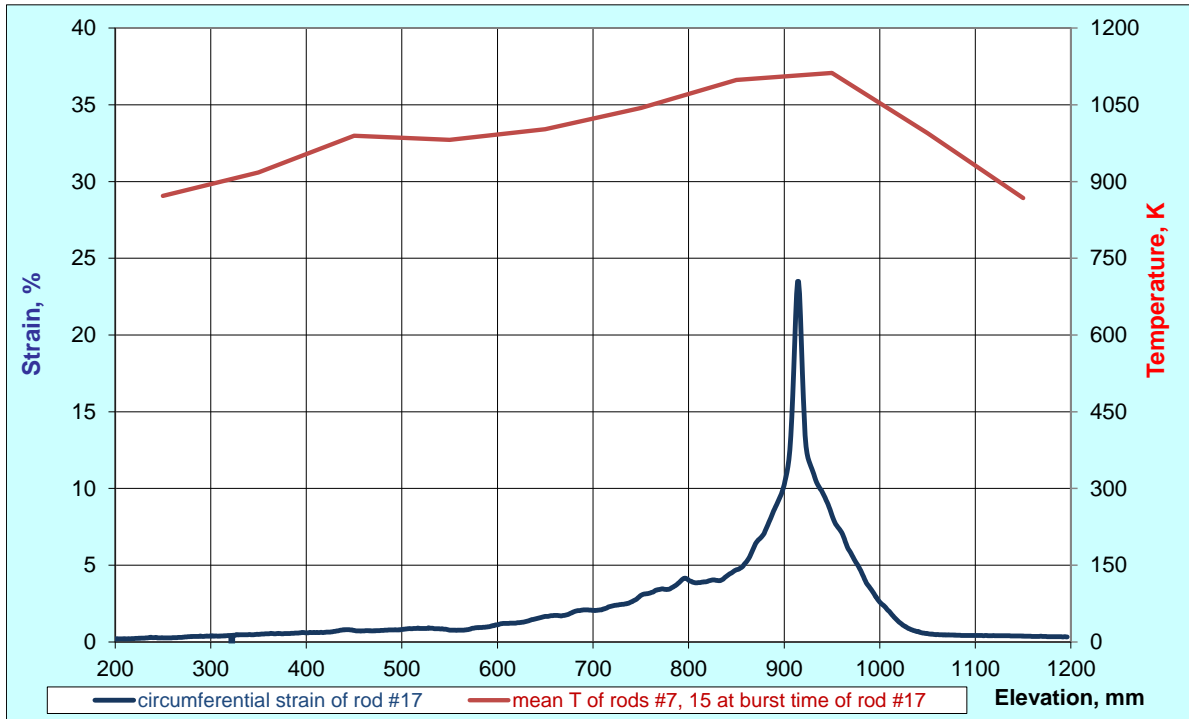


Figure 85 QUENCH-L3, Rod #17; longitudinal changing of circumferential strain (top); azimuthal diameter downwards from burst (bottom).

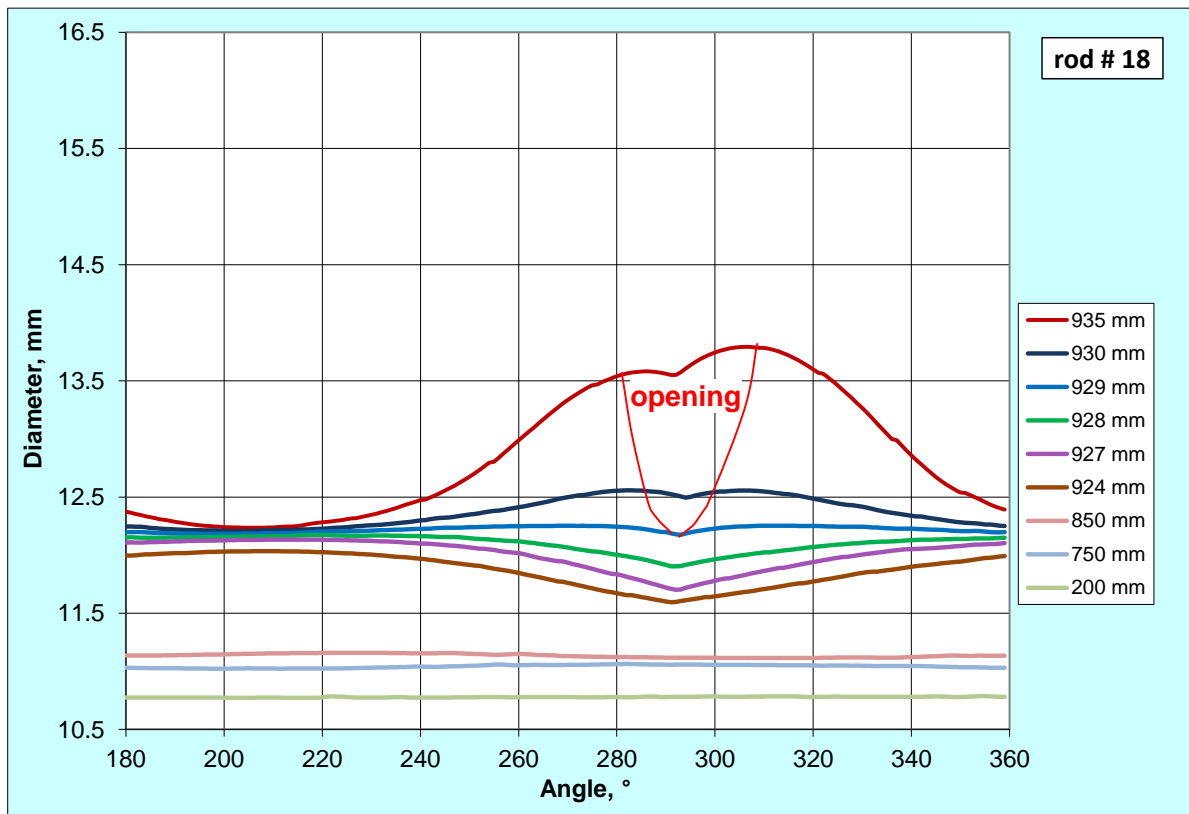
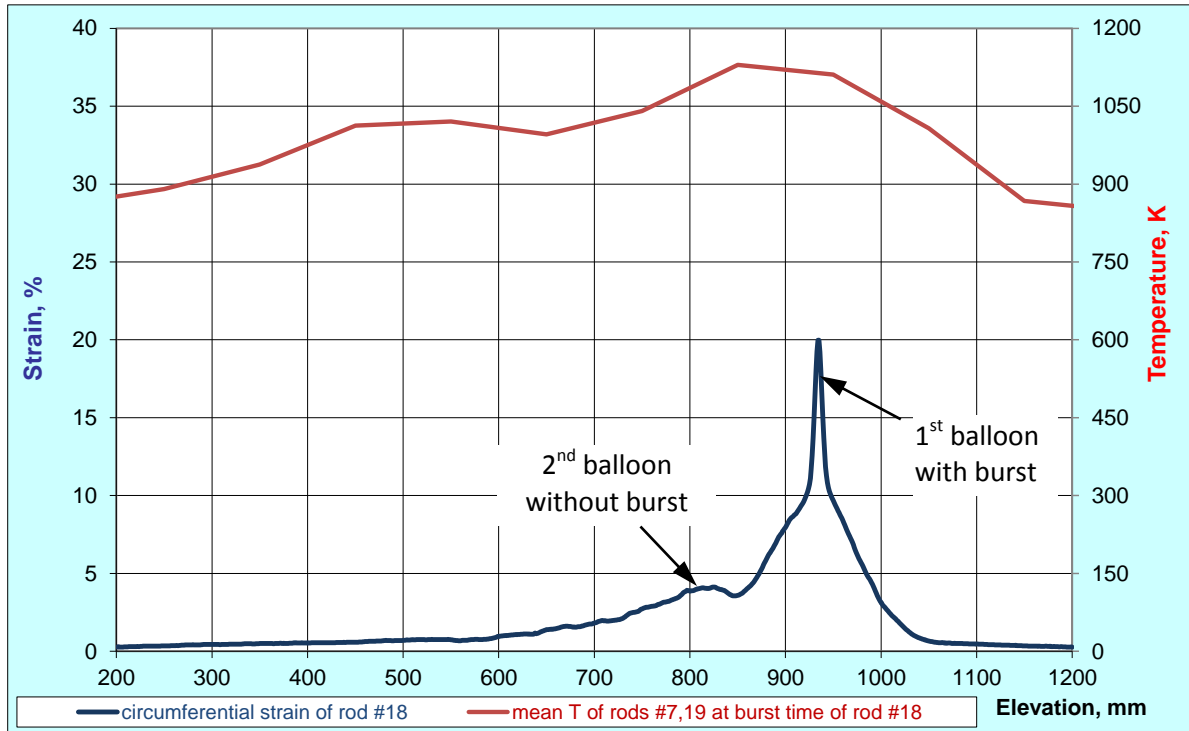


Figure 86 QUENCH-L3, Rod #18; longitudinal changing of circumferential strain (top); azimuthal diameter downwards from burst (bottom).

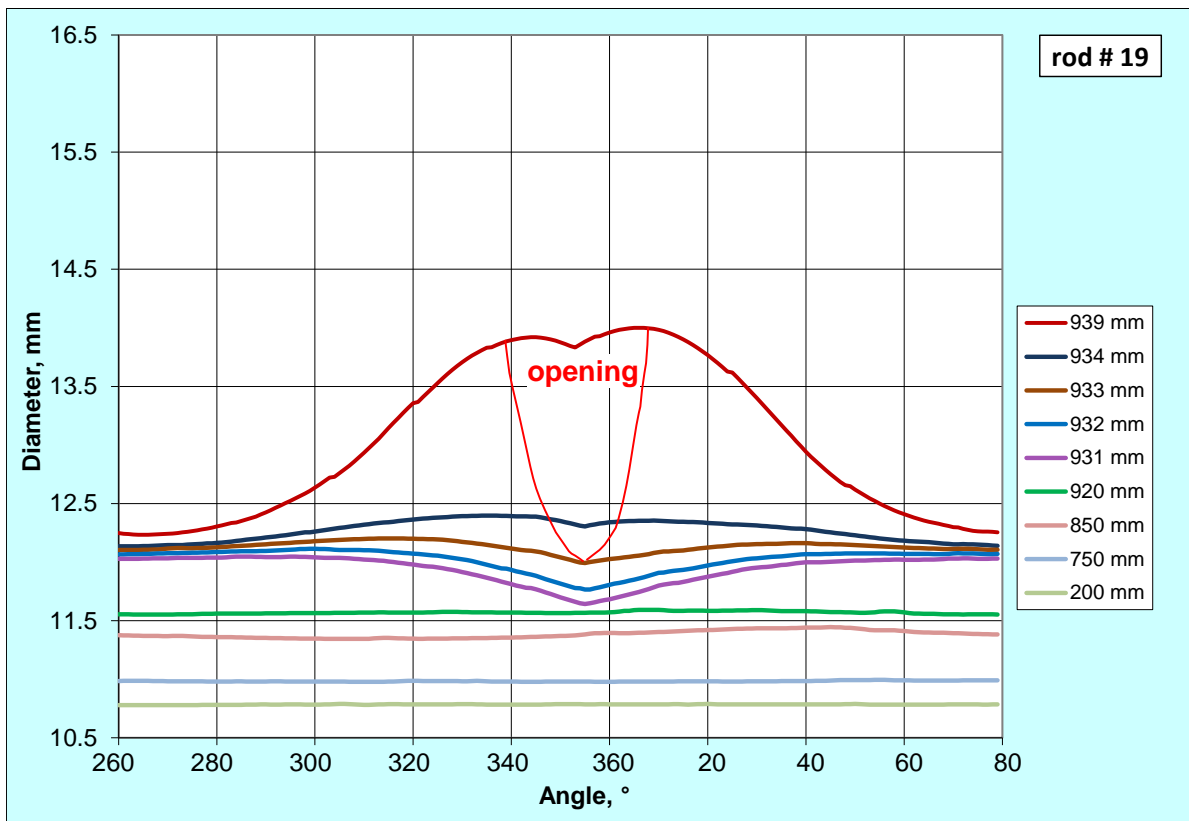
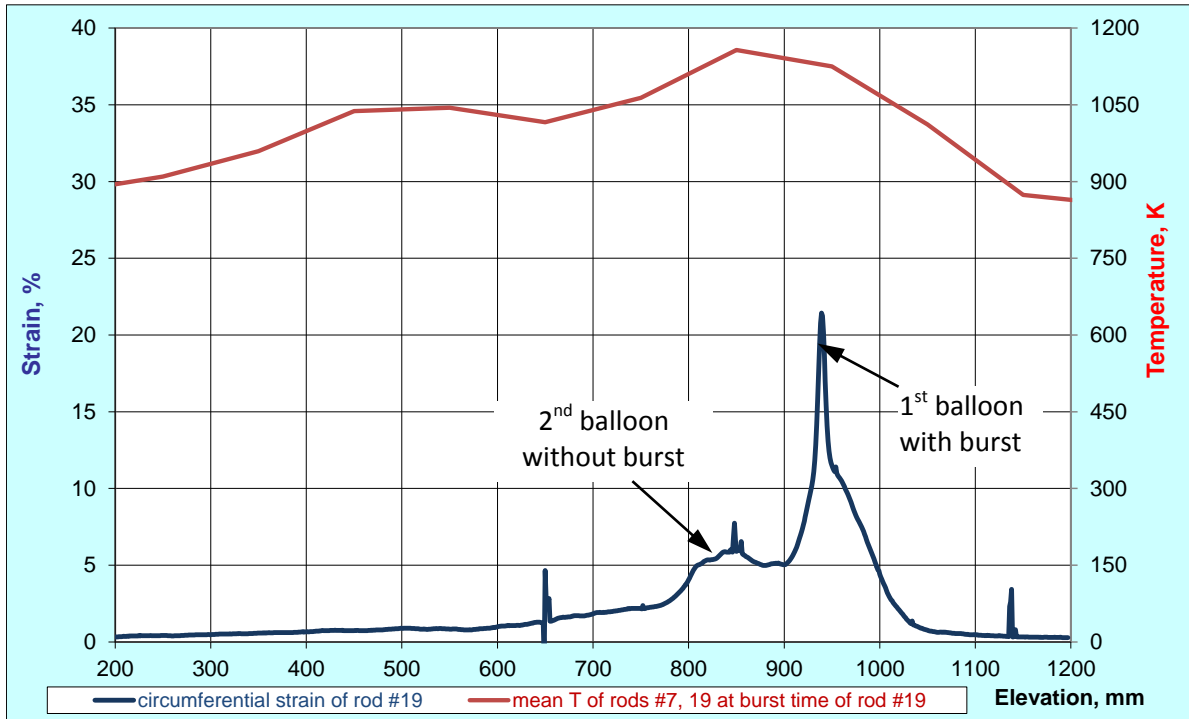


Figure 87 QUENCH-L3, Rod #19; longitudinal changing of circumferential strain (top); azimuthal diameter downwards from burst (bottom). Spikes: thermocouples.

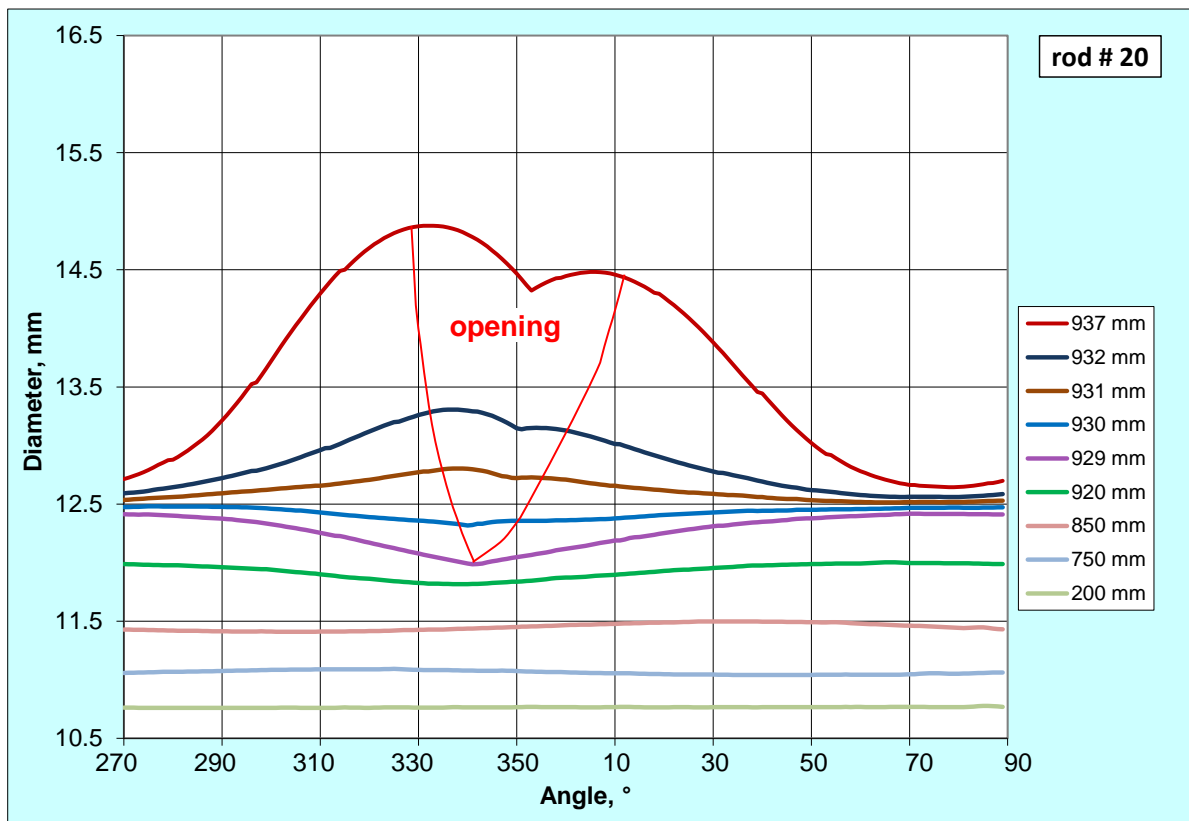
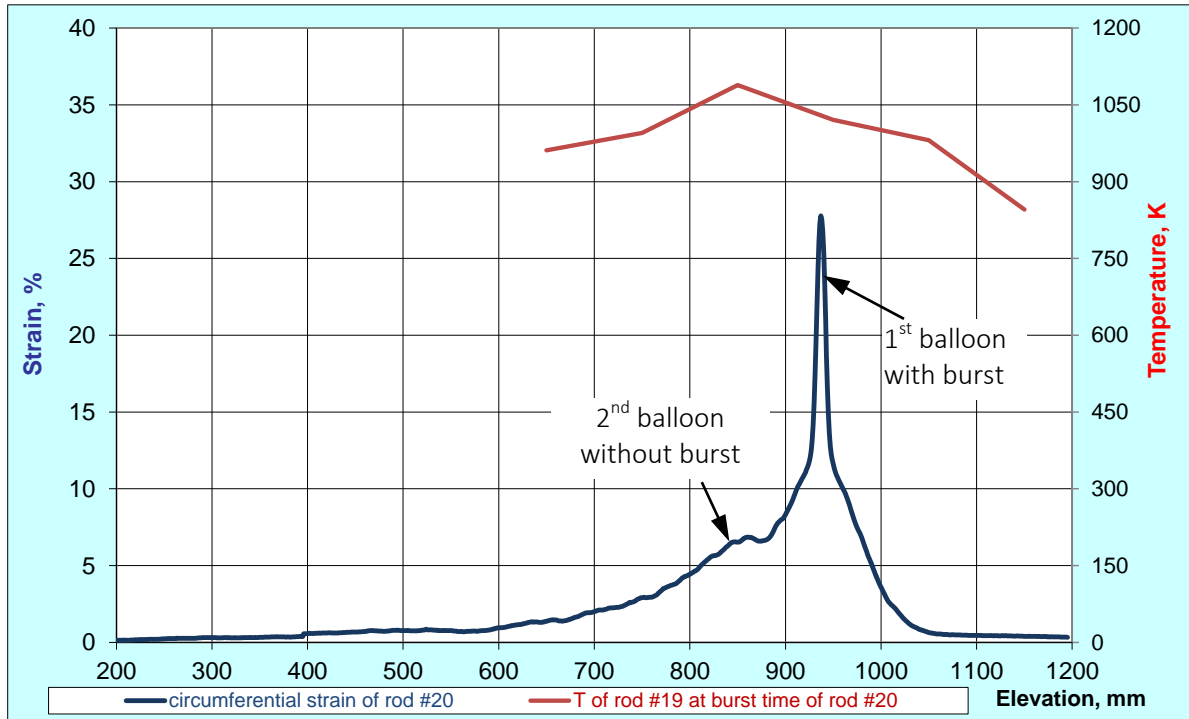


Figure 88 QUENCH-L3, Rod #20; longitudinal changing of circumferential strain (top); azimuthal diameter downwards from burst (bottom).

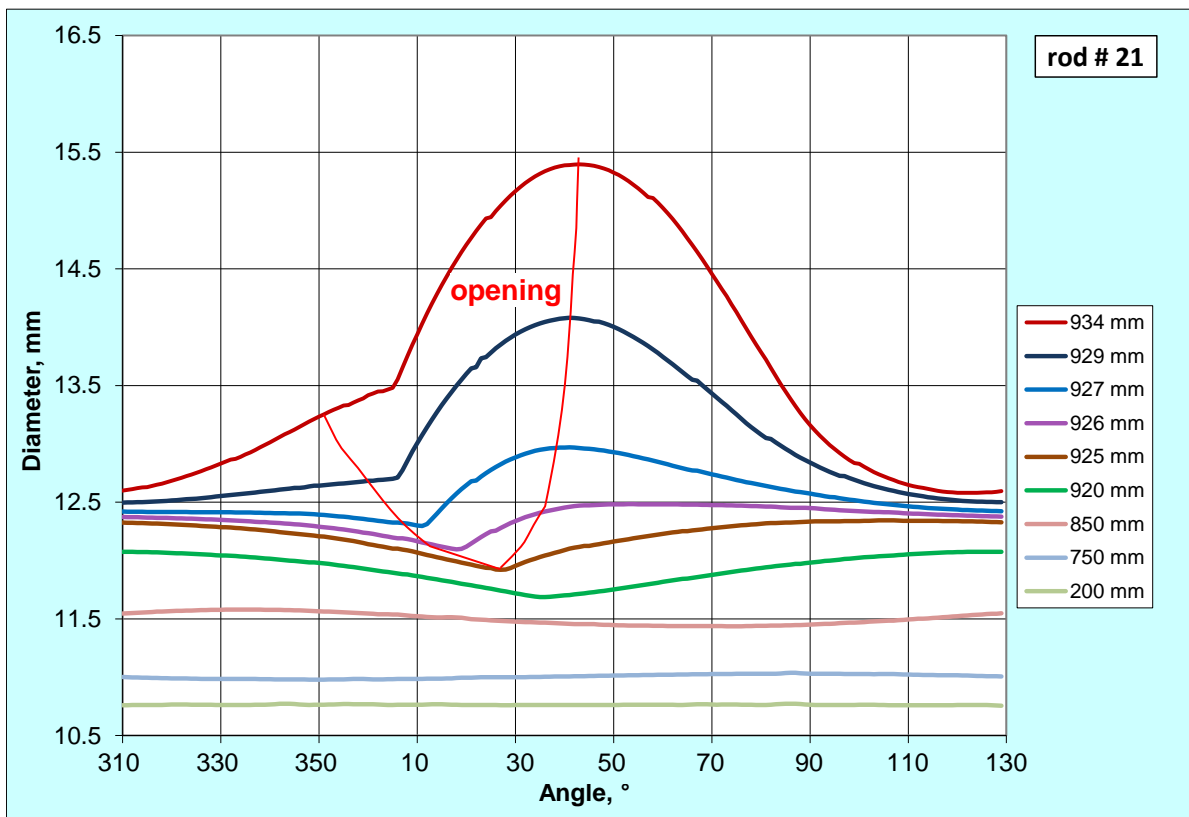
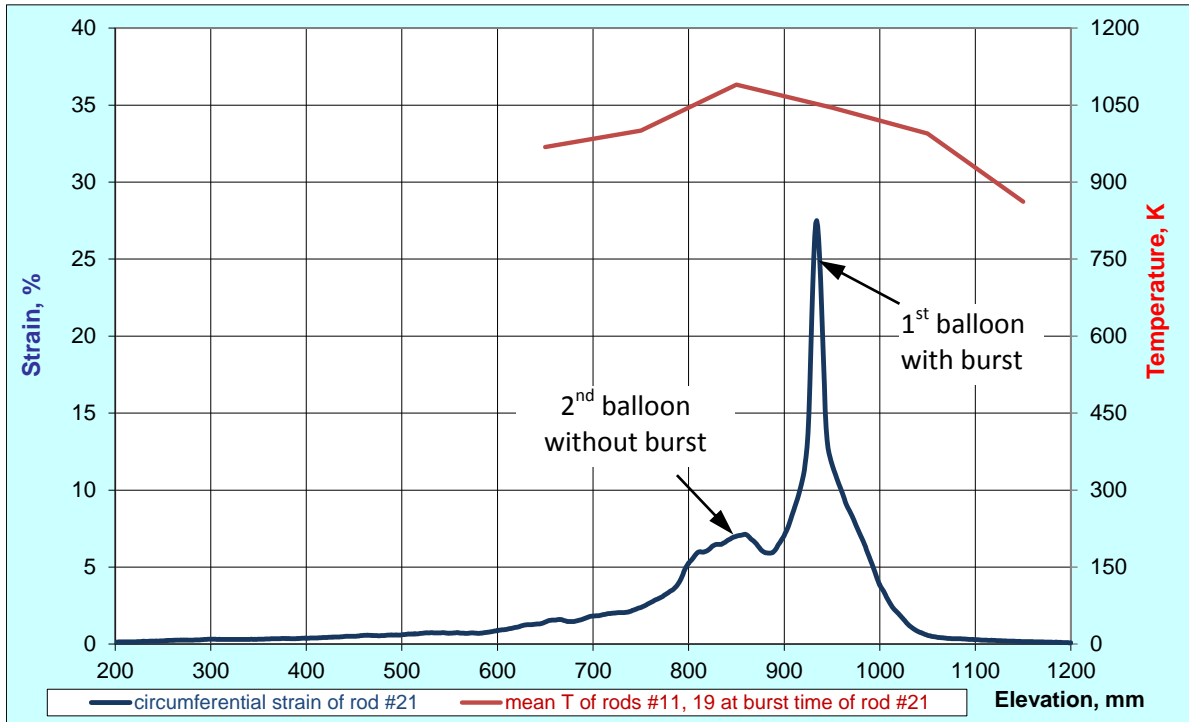


Figure 89 QUENCH-L3, Rod #21; longitudinal changing of circumferential strain (top); azimuthal diameter downwards from burst (bottom).

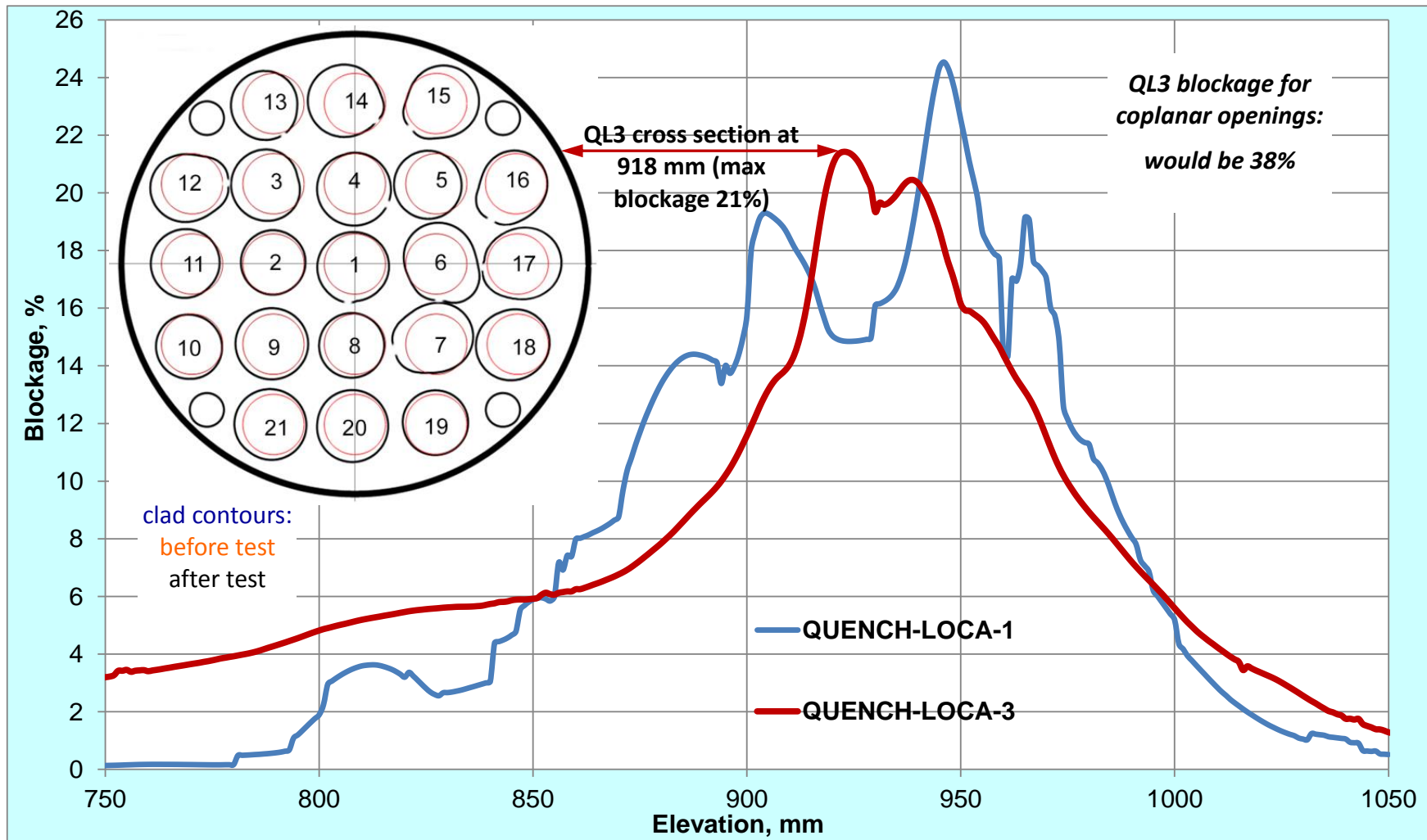


Figure 90 Axial distribution of coolant channel blockage for QUENCH-L1 and -L3 bundles.

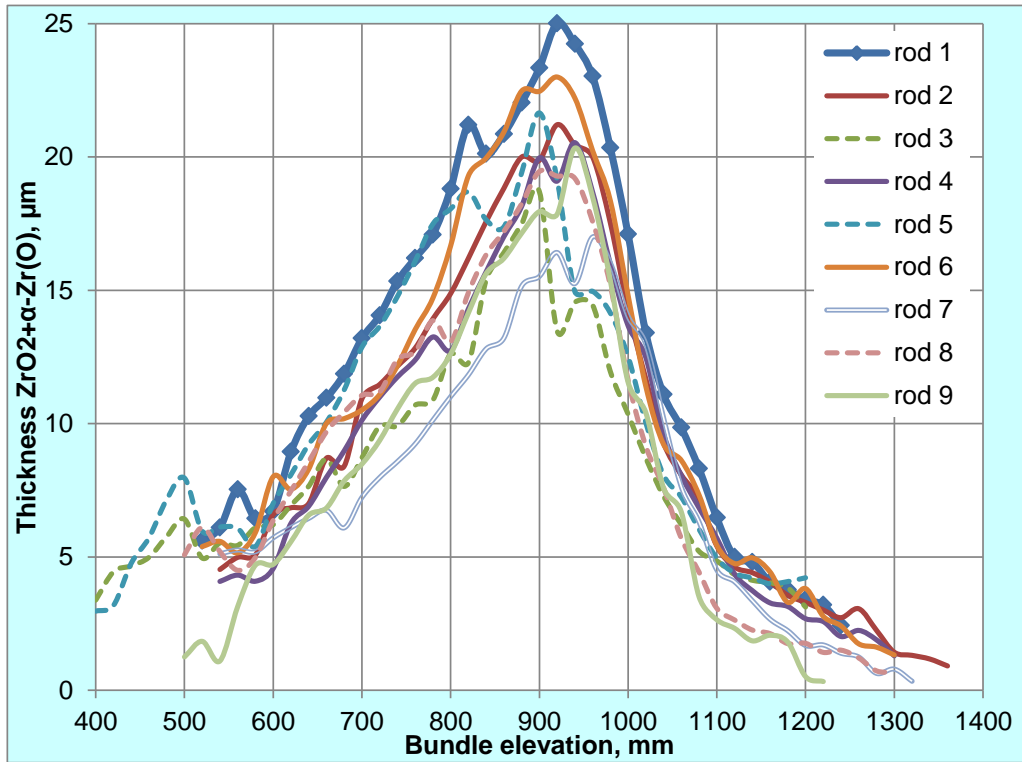


Figure 91 QUENCH-L3: results of eddy-current measurements of axial layer thickness distribution for claddings of inner rods.

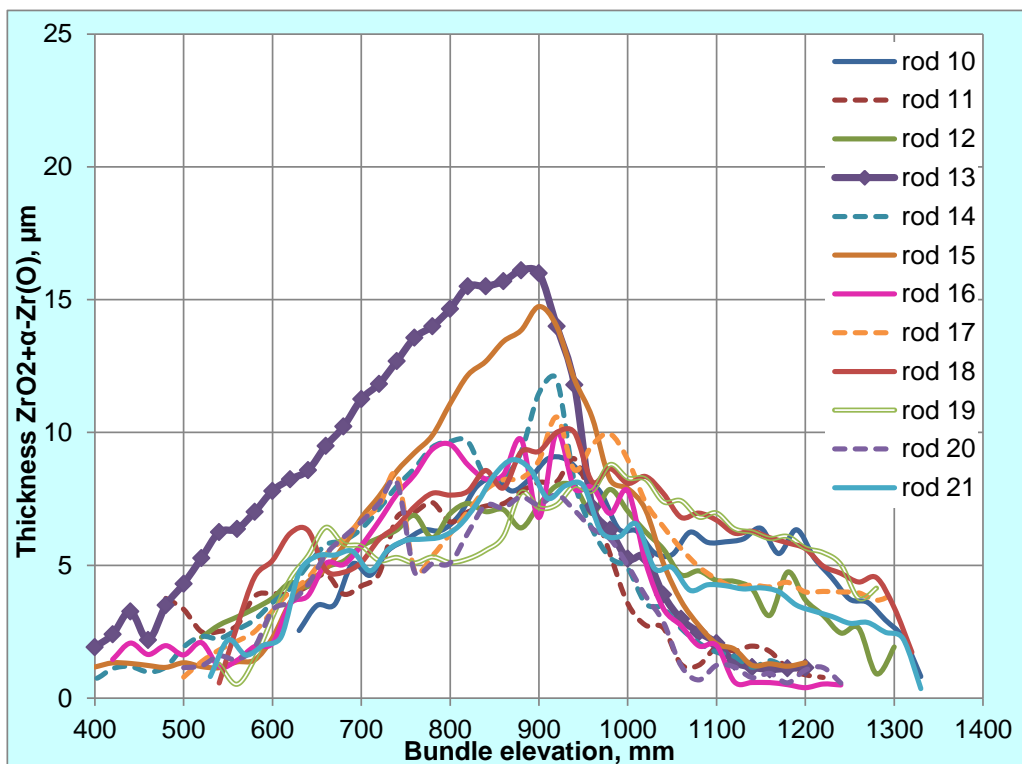
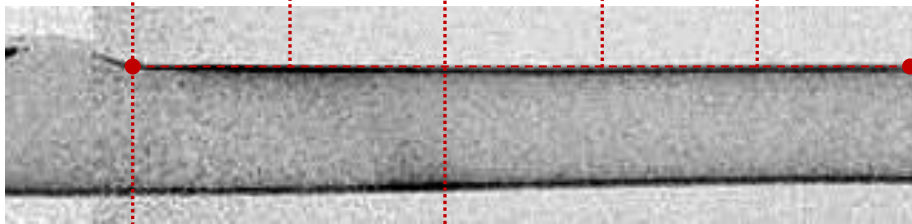
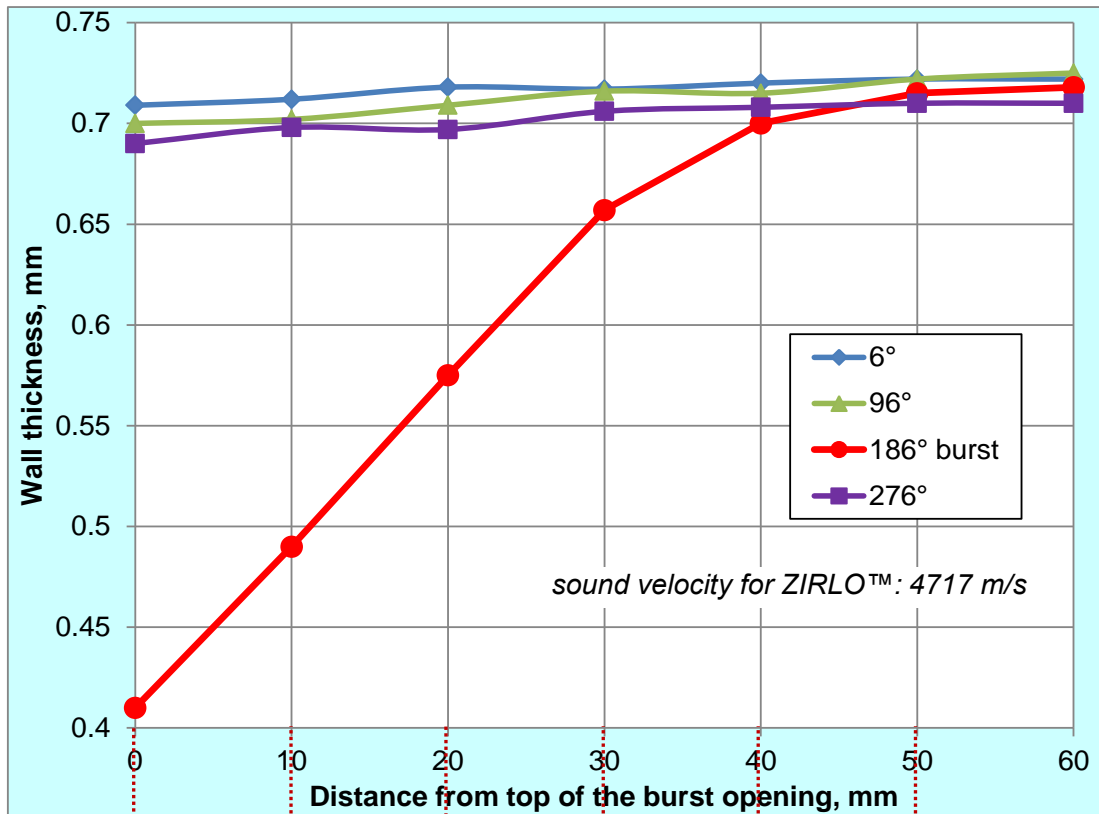


Figure 92 QUENCH-L3: results of eddy-current measurements of axial layer thickness distribution for claddings of outer rods.



neutron radiography above burst opening



neutron tomography above burst opening: localization of hydrided region (blue)

Figure 93 QUENCH-L3; ultrasound measurement of wall thickness for rod #6 with corresponding results of neutron radio- and tomography.

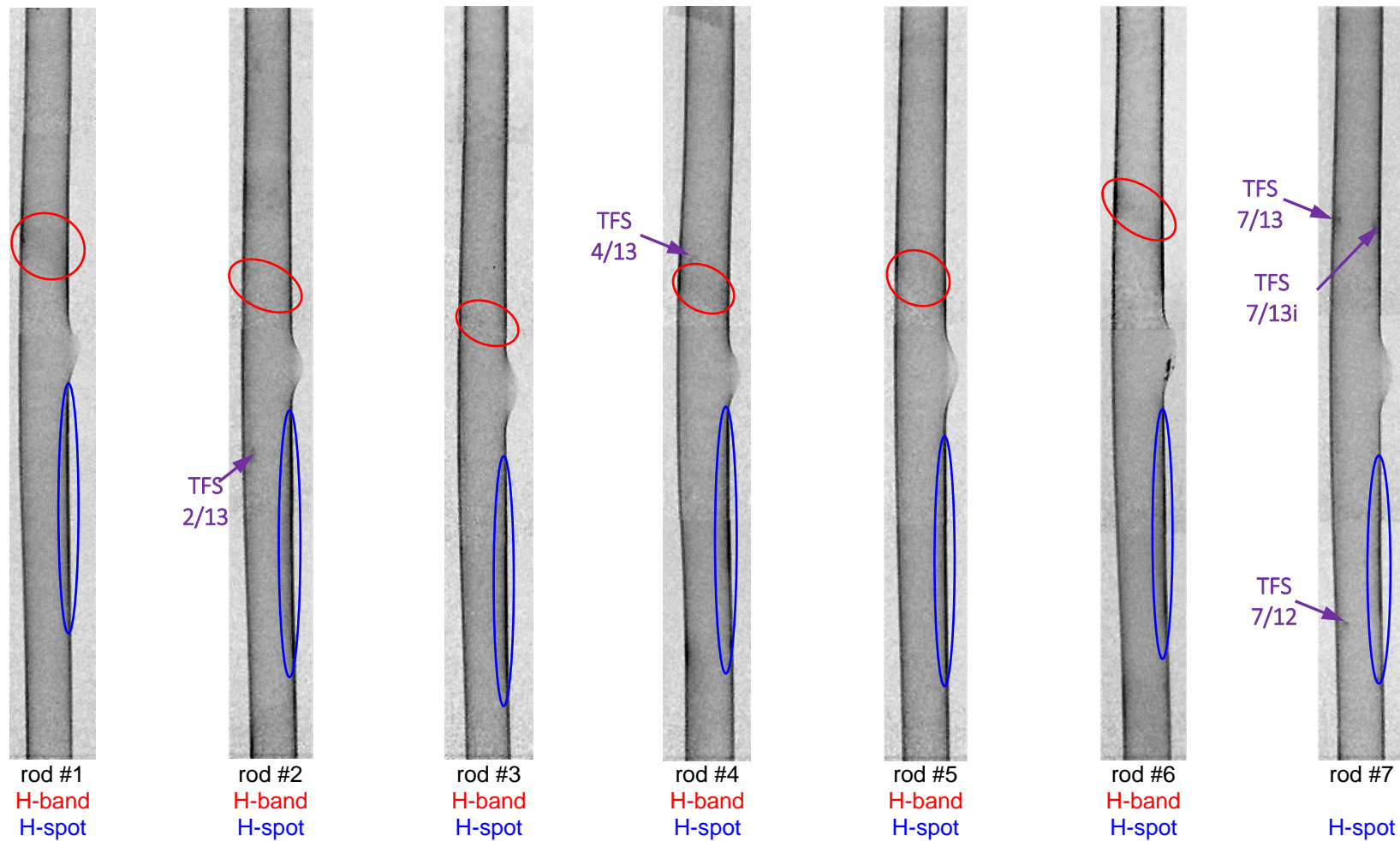


Figure 94 QUENCH-L3; Neutron radiographs of inner rods: hydrogen bands above burst openings and hydrogen spots below burst openings.

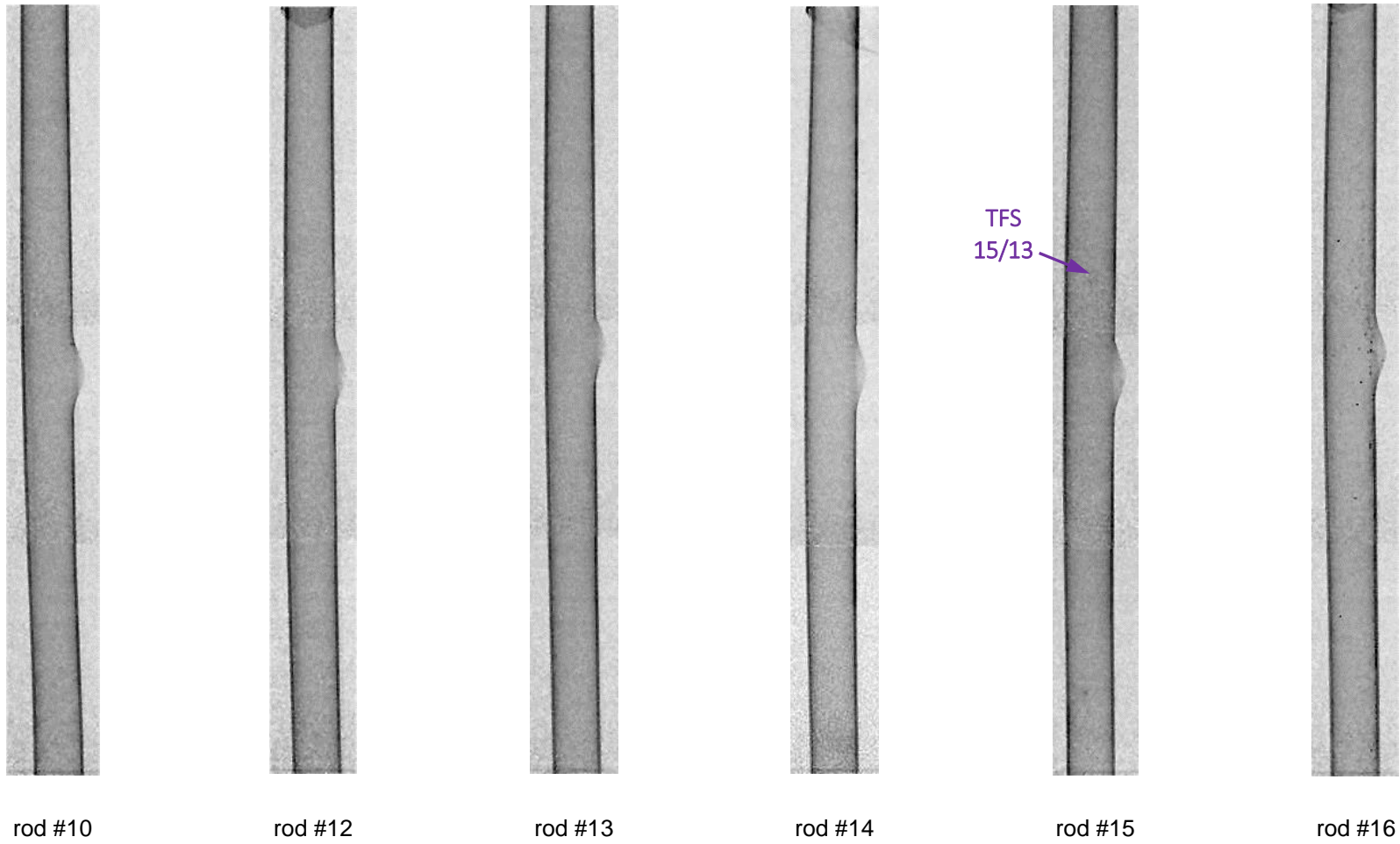


Figure 95 QUENCH-L3; Neutron radiographs of outer rods

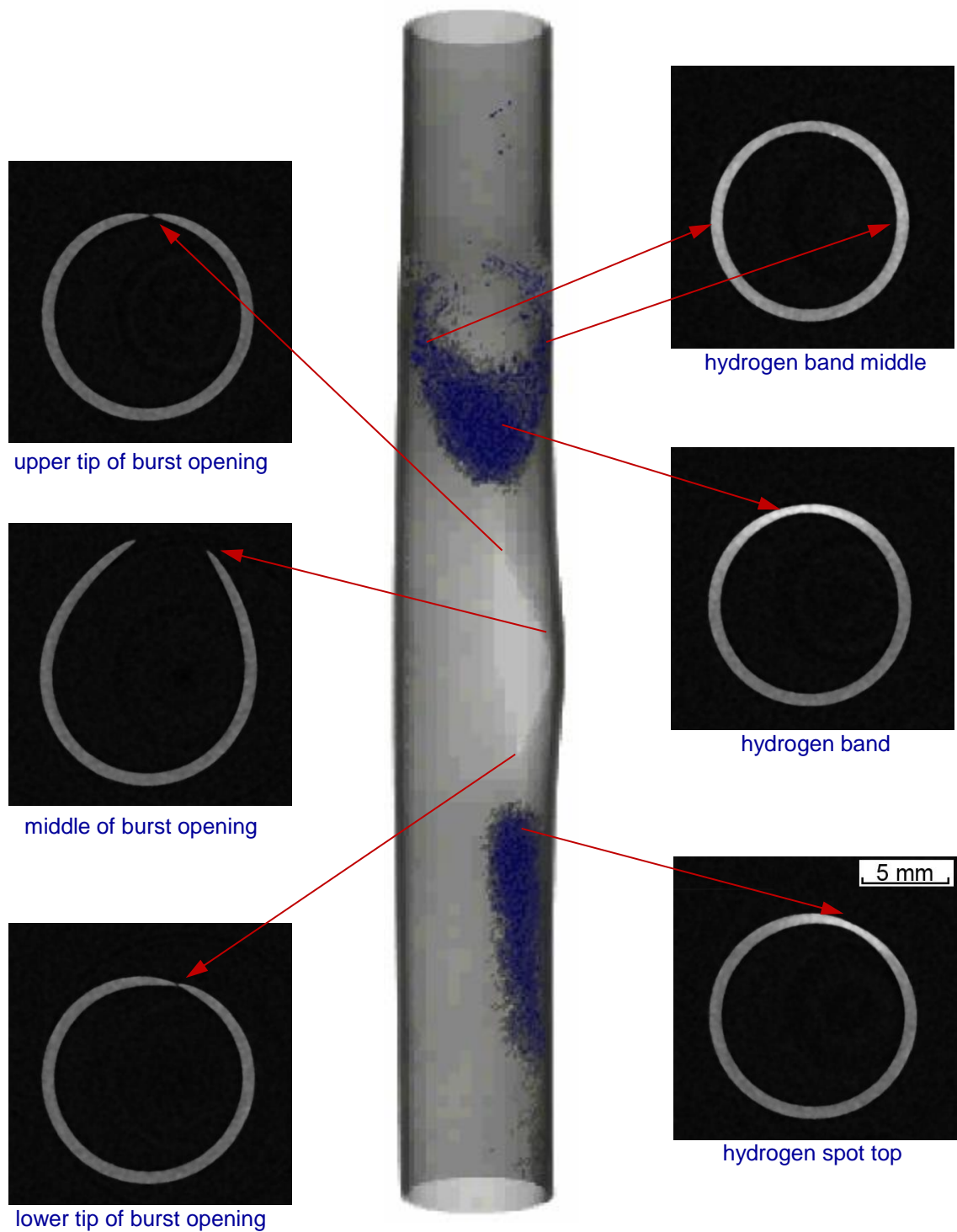


Figure 96 QUENCH-L3; tomography of rod #1: correspondence between long section (view from burst opening) and cross sections (bottom view); left - features of burst opening, right - areas with high hydrogen concentration (light segments).

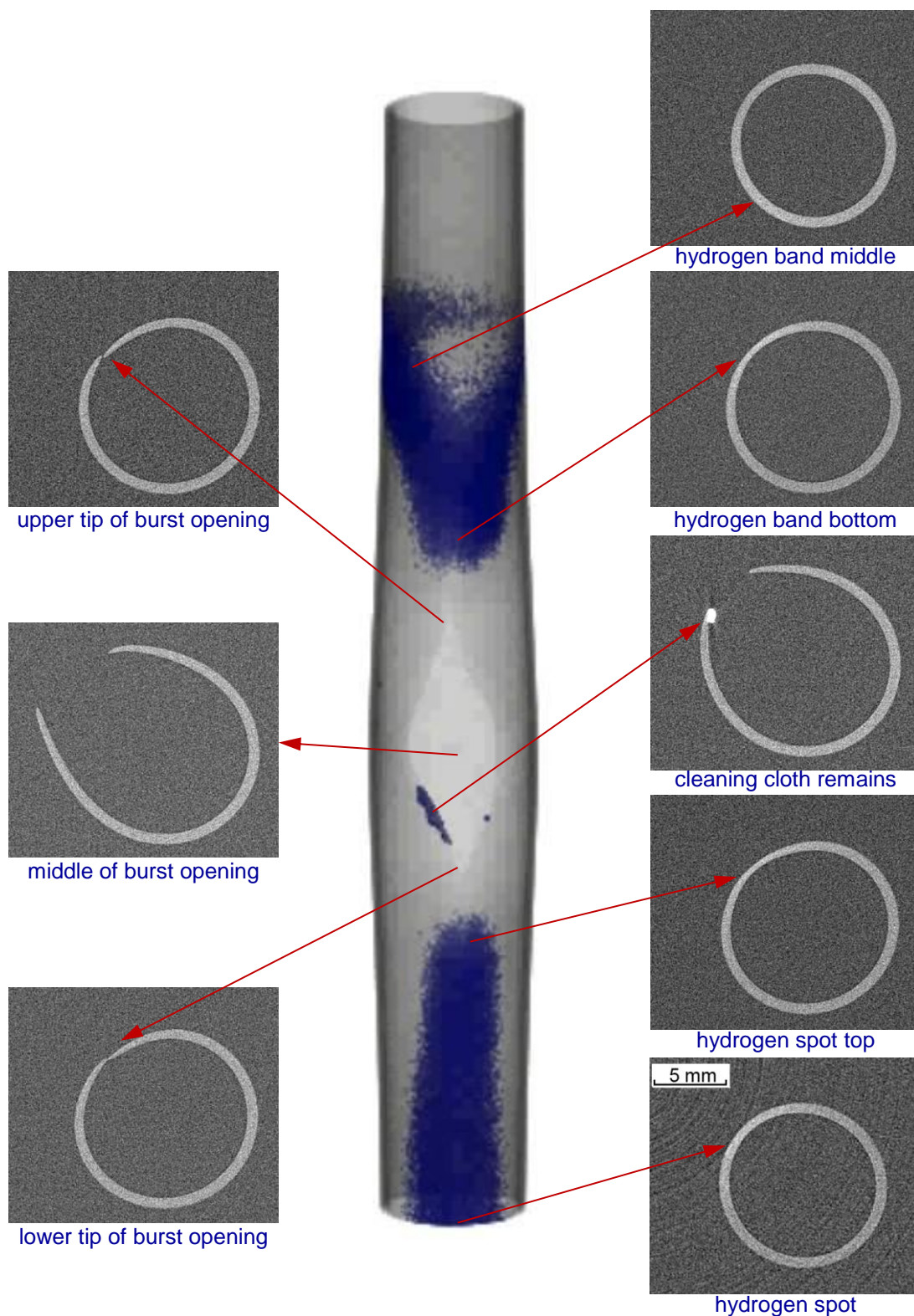


Figure 97 QUENCH-L3; tomography of rod #6: correspondence between long section (view from burst opening) and cross sections (bottom view); left - features of burst opening, right - areas with high hydrogen concentration (light segments).

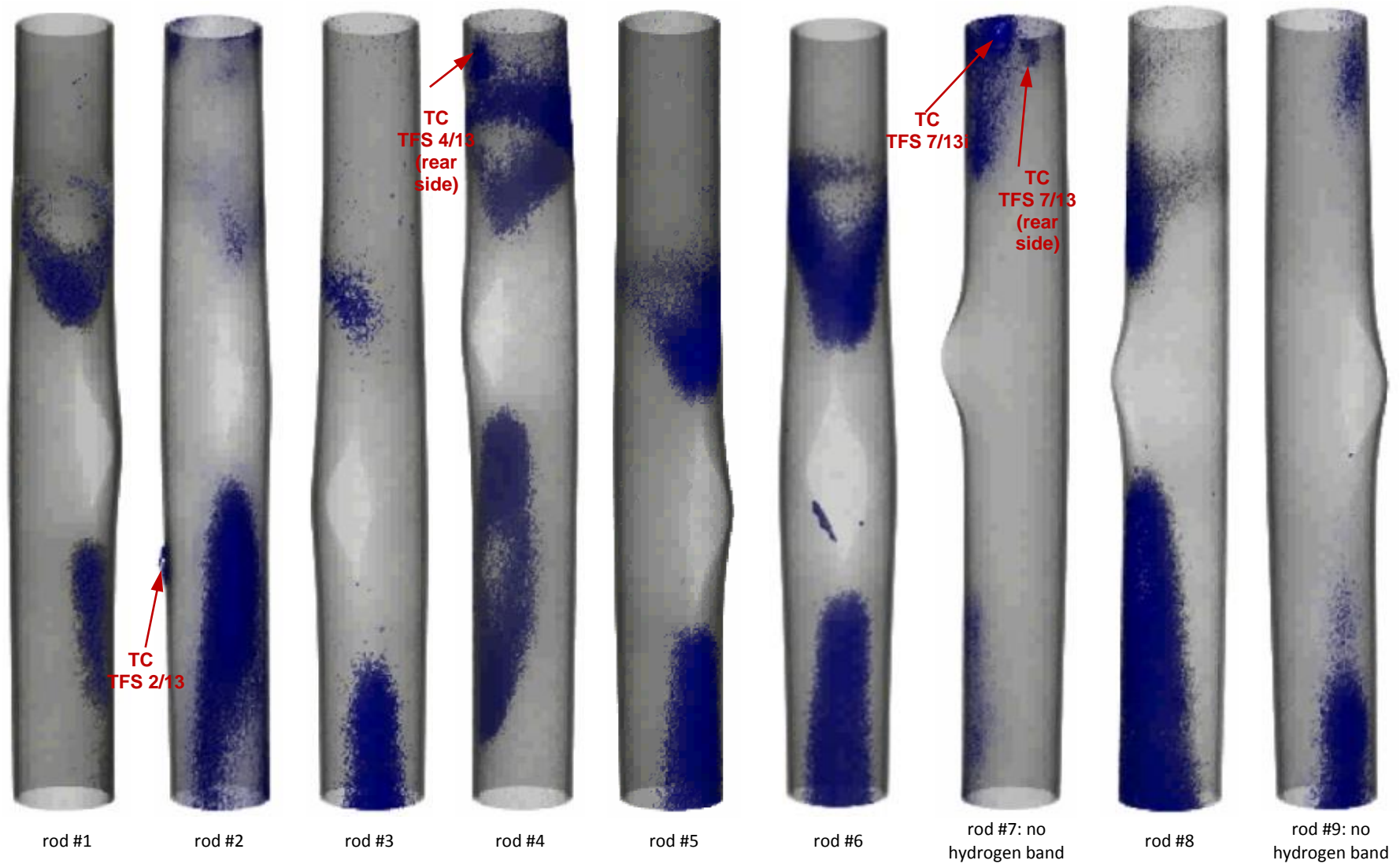


Figure 98 QUENCH-L3; tomography results for inner rods: hydrogen bands above burst opening and hydrogen spots below burst opening.



rod #10: single points (surface effects?)



rod #13: hydrogen spot eventually at contact pellet-cladding



rod #16: (surface effects?)



TC
TFS 19/13

rod #19: (surface effects?)

Figure 99 QUENCH-L3; outer rods: absence of hydrogen bands.

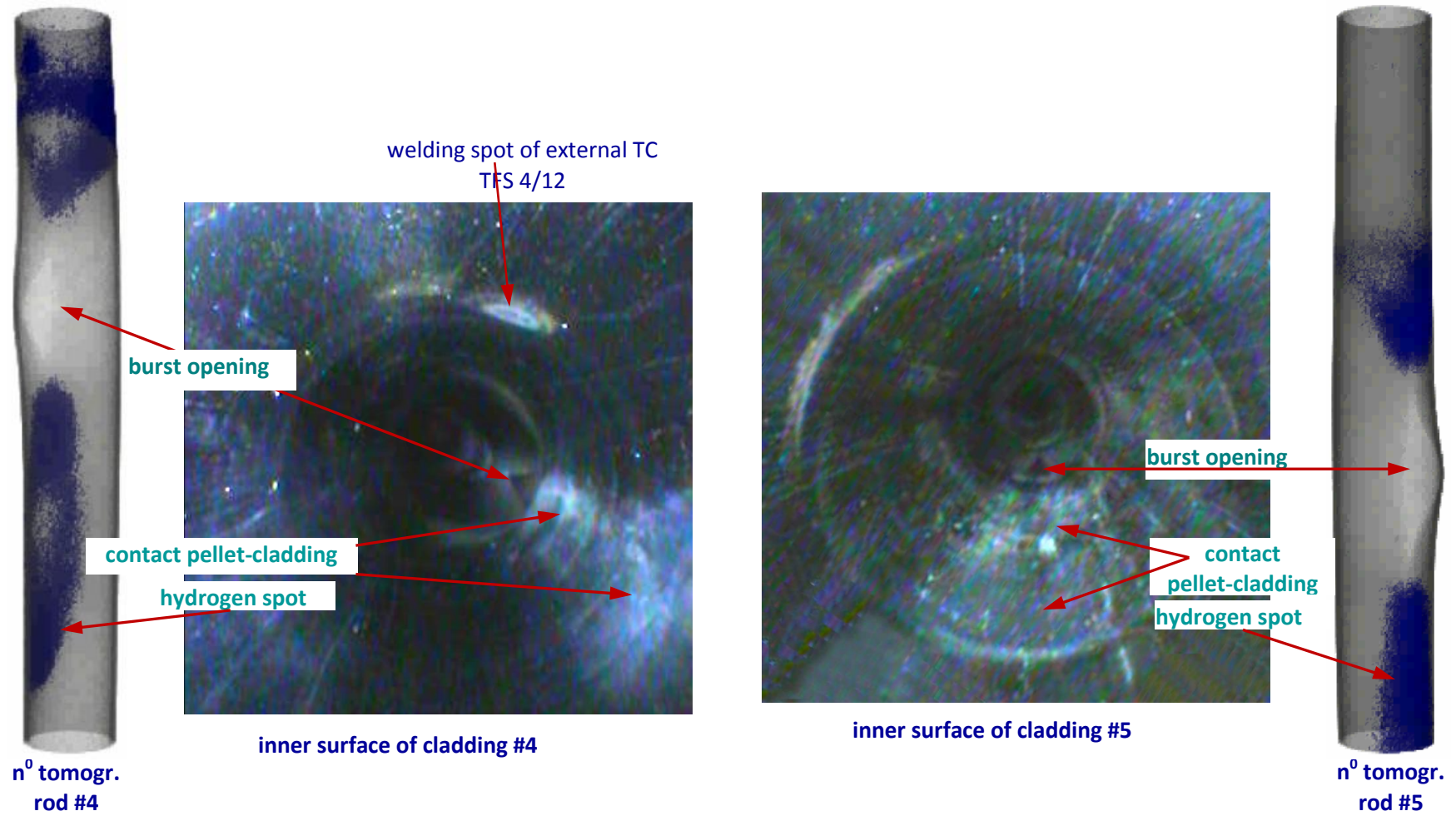


Figure 100 QUENCH-L3; correspondence between videoscope observations and tomography for rods #4 and #5: hydrogen spot at the position of contact between pellet and cladding below burst opening.

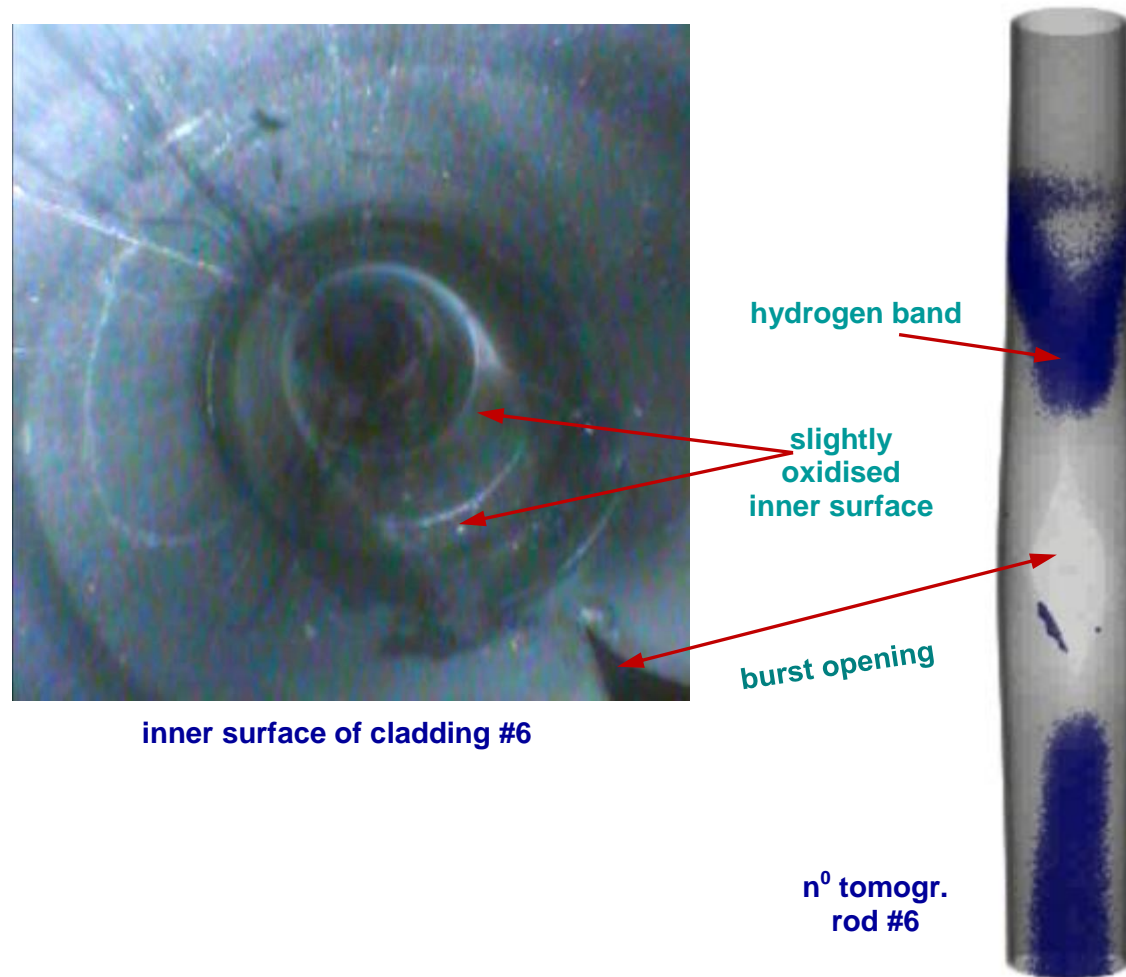


Figure 101 QUENCH-L3; correspondence between videoscope observations and tomography for rod #6: hydrogen band at the position of slightly oxidised inner cladding surface.

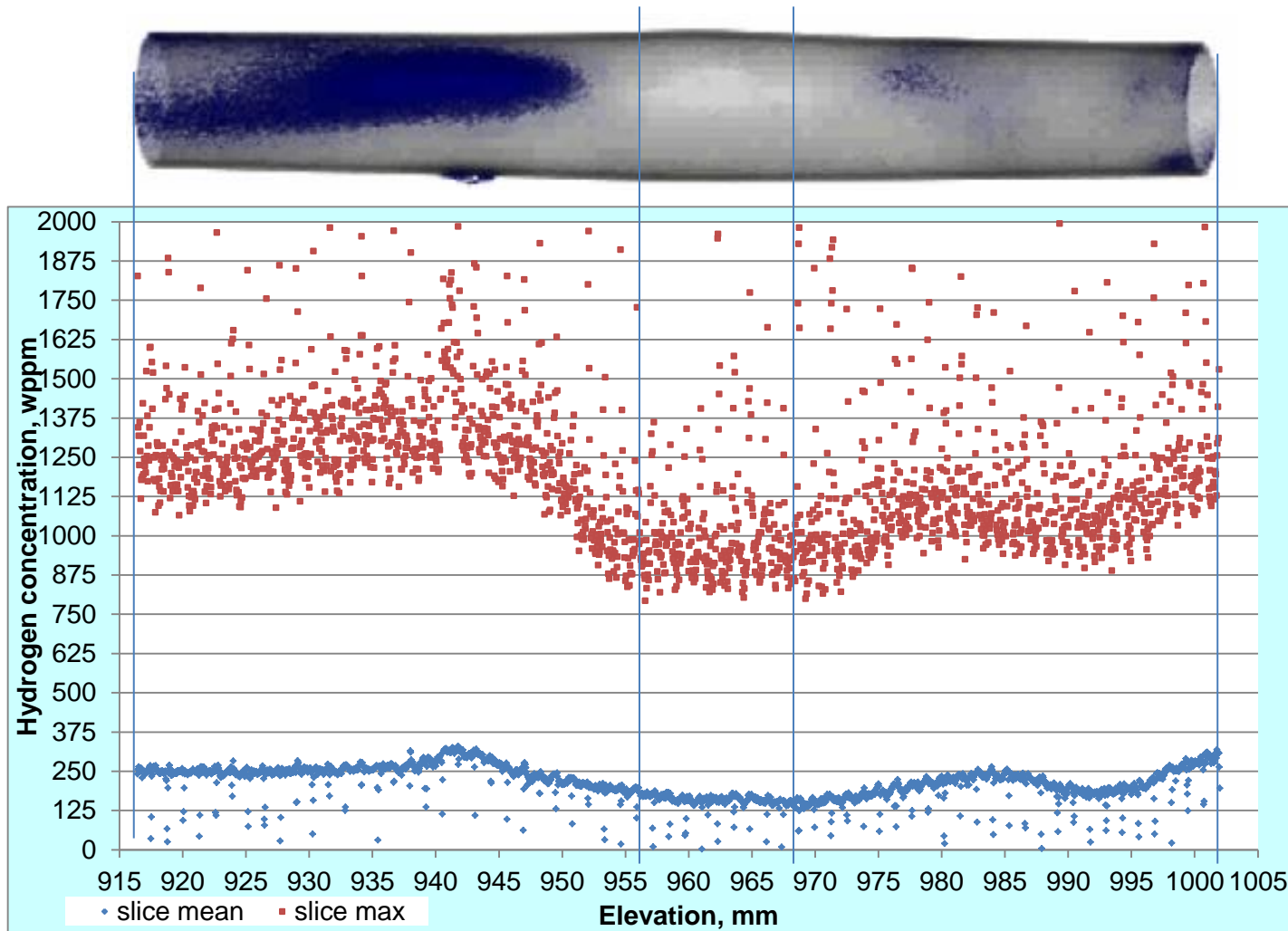


Figure 102 QUENCH-L3; correspondence between reconstruction of tomography image and plots of mean and maximal hydrogen concentrations in rod #2, plots adjusted to edges of burst opening.

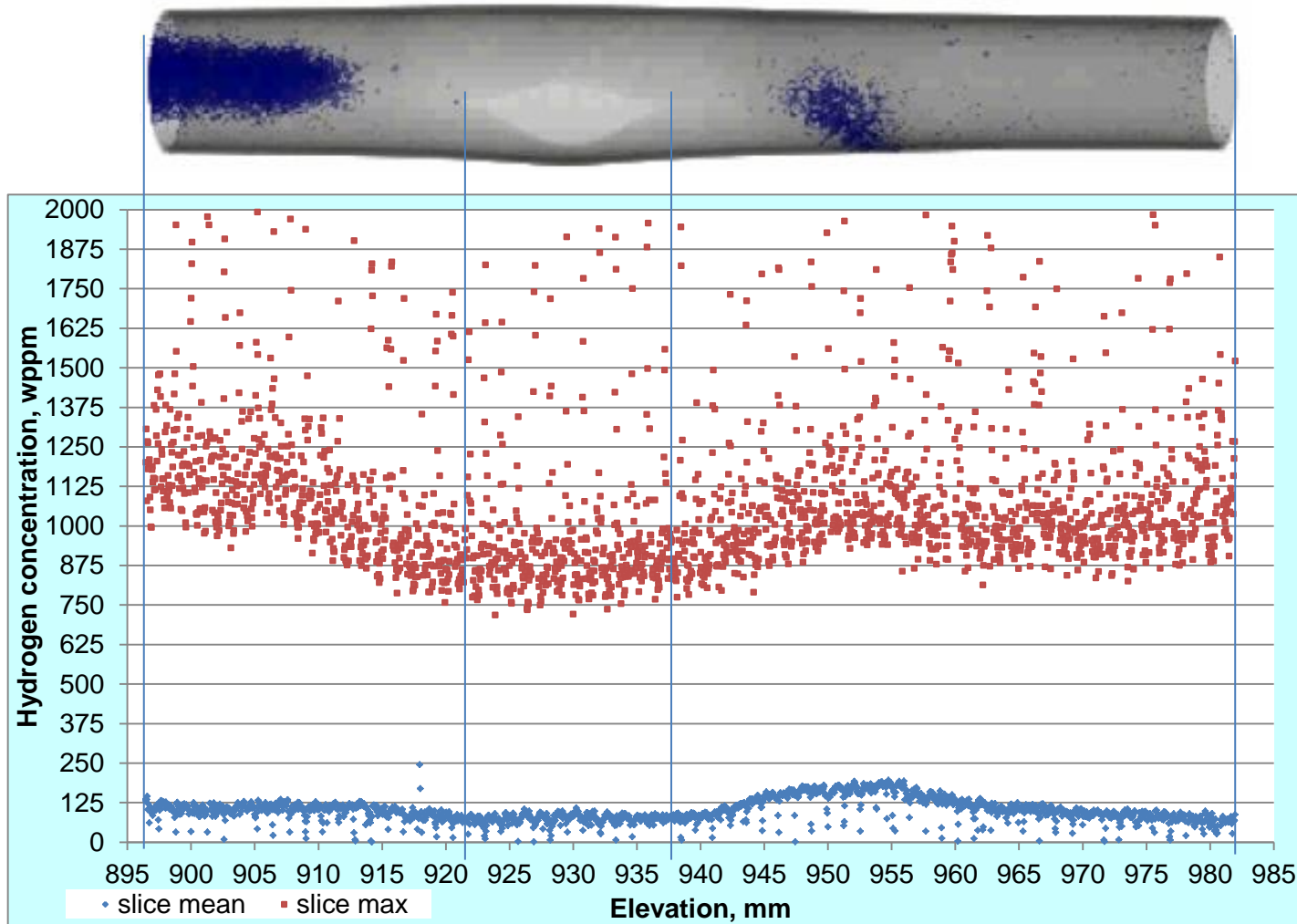


Figure 103 QUENCH-L3; correspondence between reconstruction of tomography image and plots of mean and maximal hydrogen concentrations in rod #3, plots adjusted to edges of burst opening.

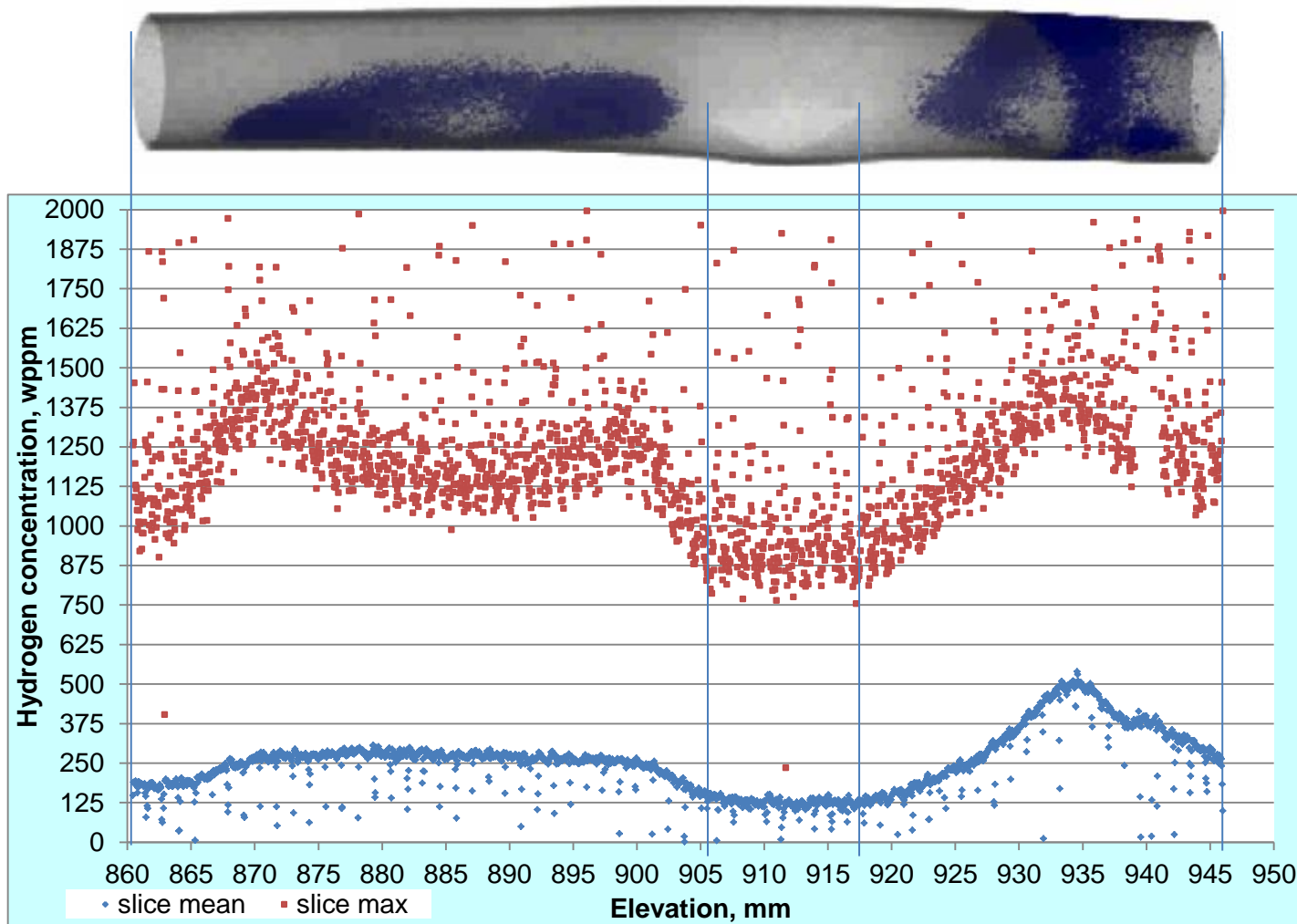


Figure 104 QUENCH-L3; correspondence between reconstruction of tomography image and plots of mean and maximal hydrogen concentrations in rod #4, plots adjusted to edges of burst opening.

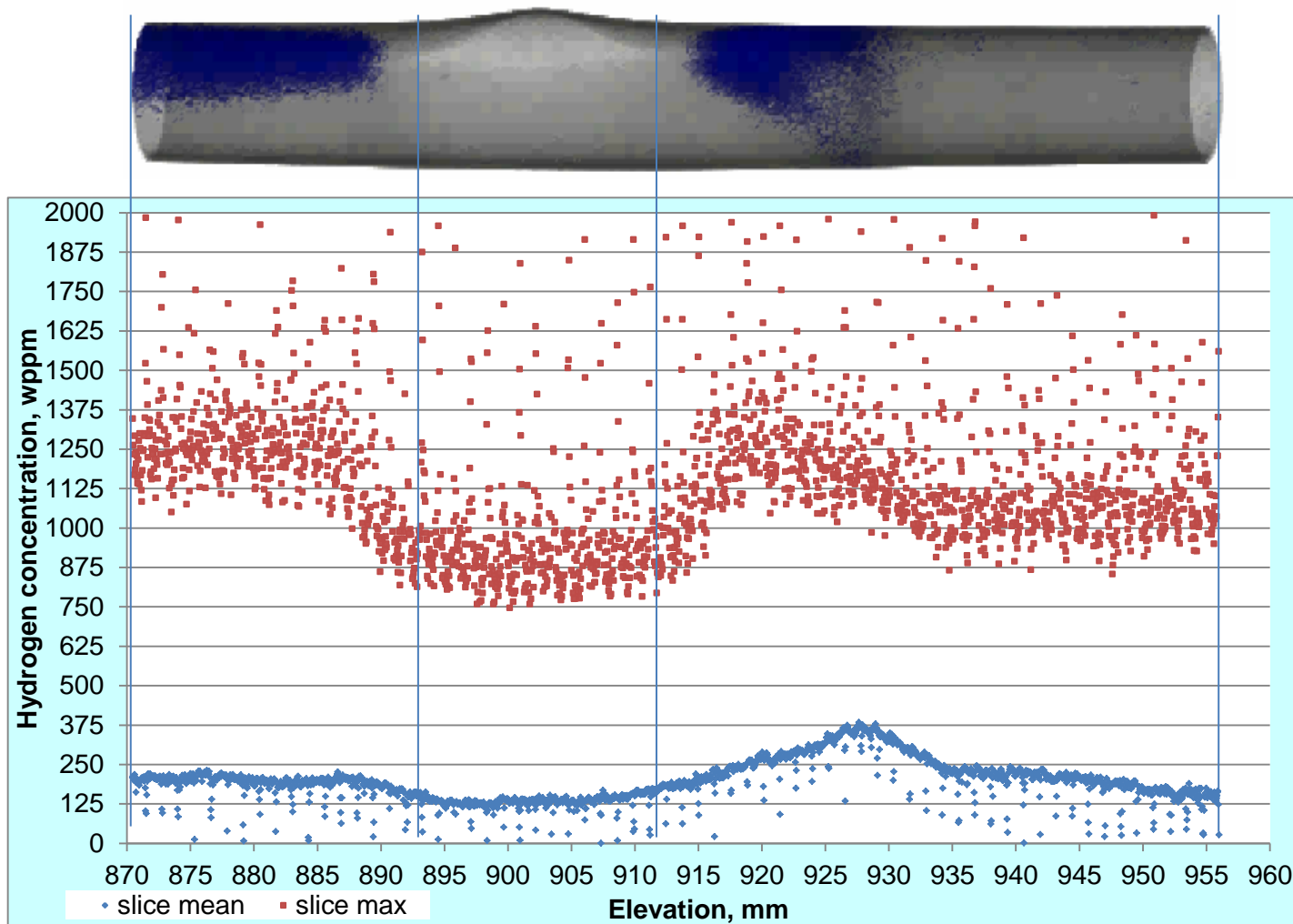


Figure 105 QUENCH-L3; correspondence between reconstruction of tomography image and plots of mean and maximal hydrogen concentrations (calculated for each cross section slice of 40 μm width) in rod #5, plots adjusted to edges of burst opening.

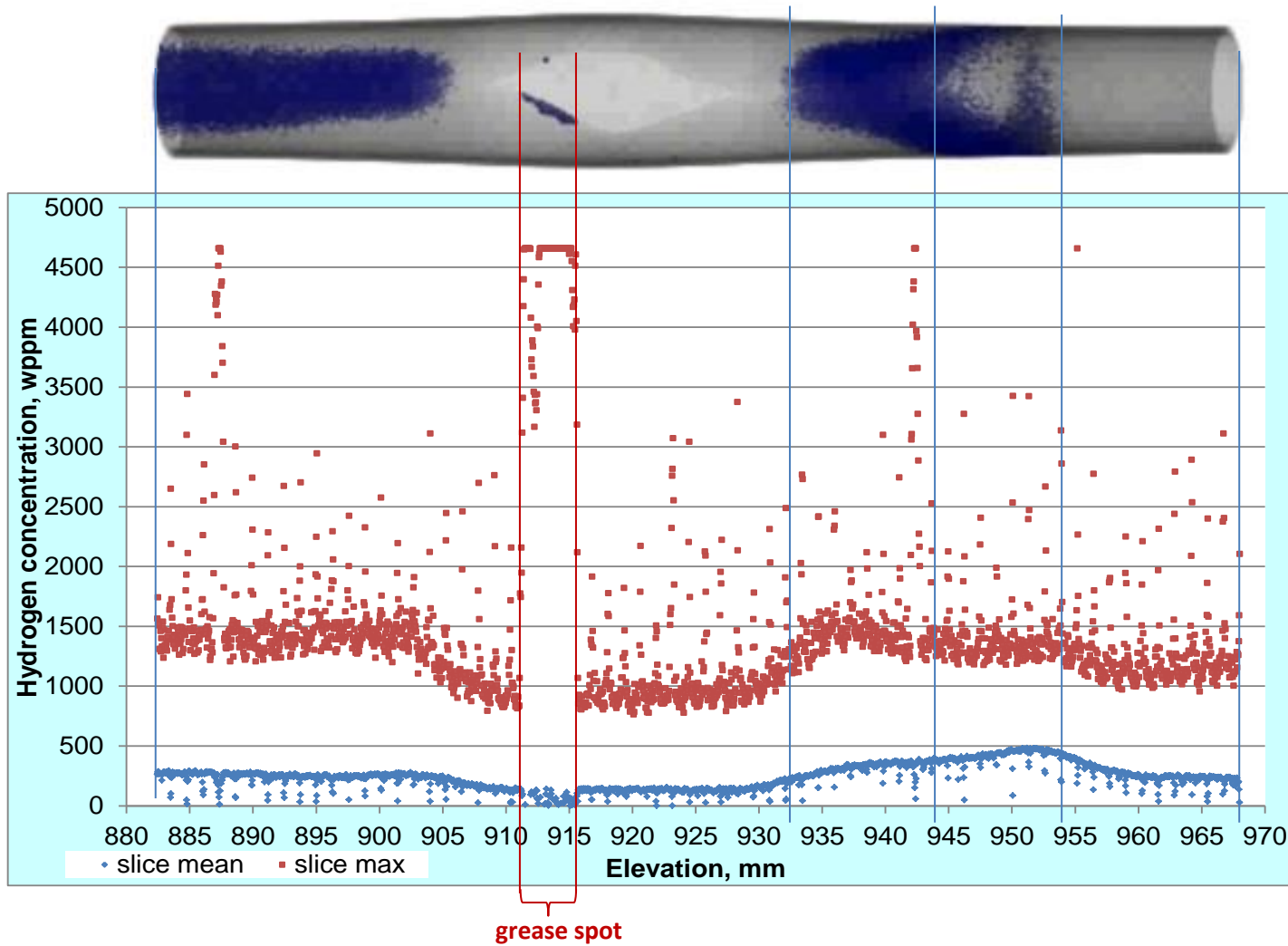
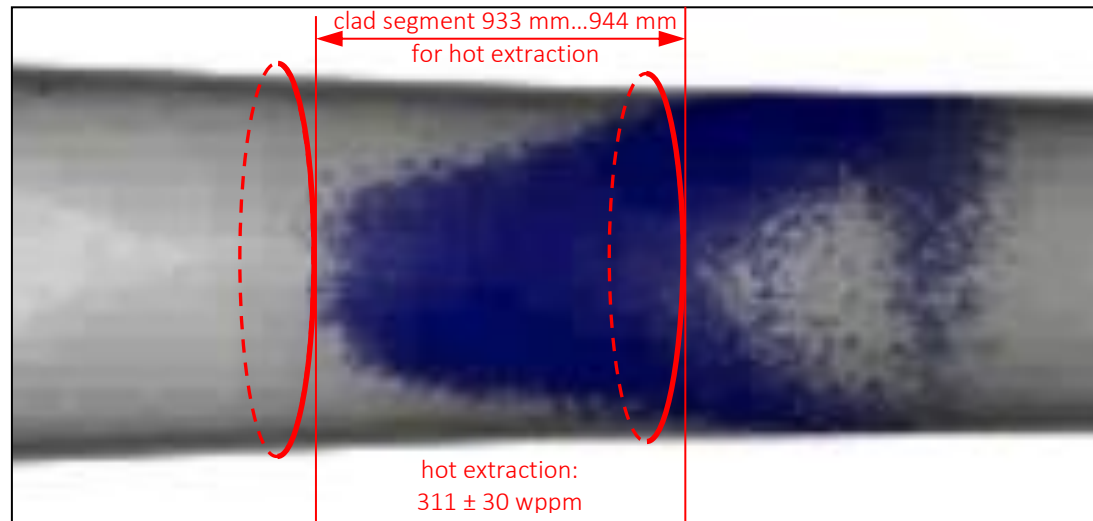
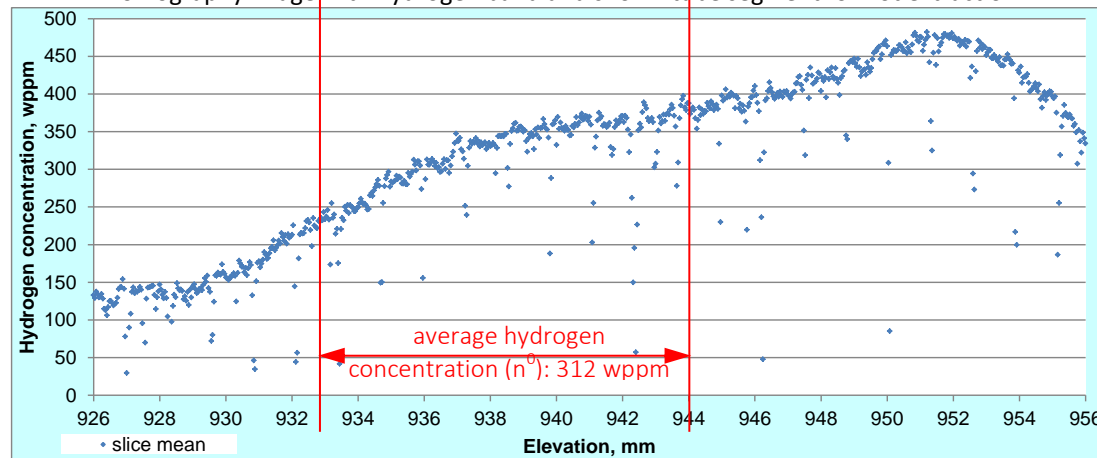


Figure 106 QUENCH-L3; correspondence between reconstruction of tomography image and plots of mean and maximal hydrogen concentrations in rod #6, plots adjusted to position of the grease spot at the burst opening edge.



Tomography image with hydrogen band and shown tube segment for hot extraction



Results of n^0 -tomography analysis: axial distribution of *mean* hydrogen concentrations calculated for each cross section slice with width of 40 μm (thinning of clad wall above burst opening not considered)

Figure 107 QUENCH-L3; Comparison of two methods of hydrogen concentration measurement for rod #6: neutron tomography and hot extraction.

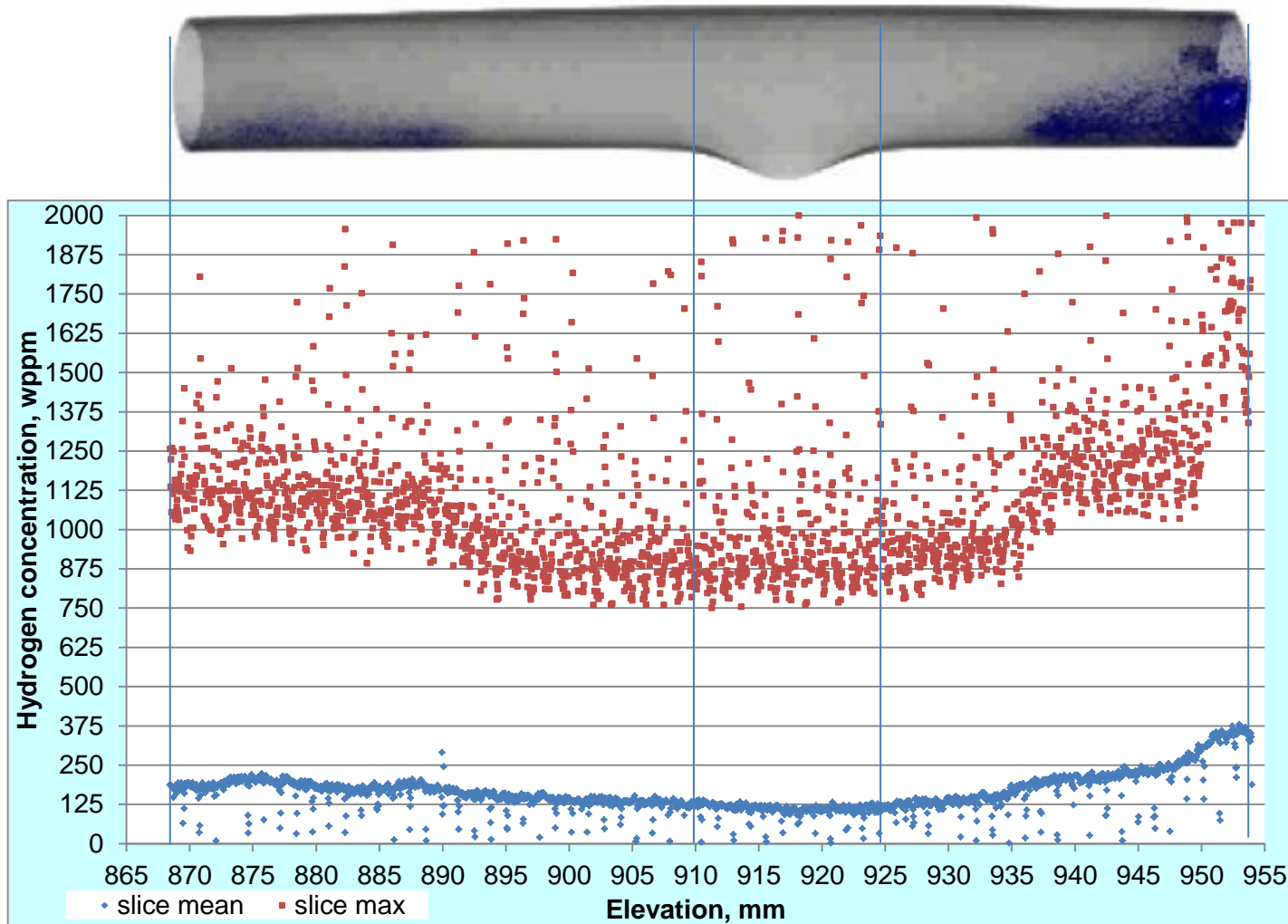


Figure 108 QUENCH-L3; correspondence between reconstruction of tomography image and plots of mean and maximal hydrogen concentrations (calculated for each cross section slice of 40 μm width) in rod #7, plots adjusted to edges of burst opening.

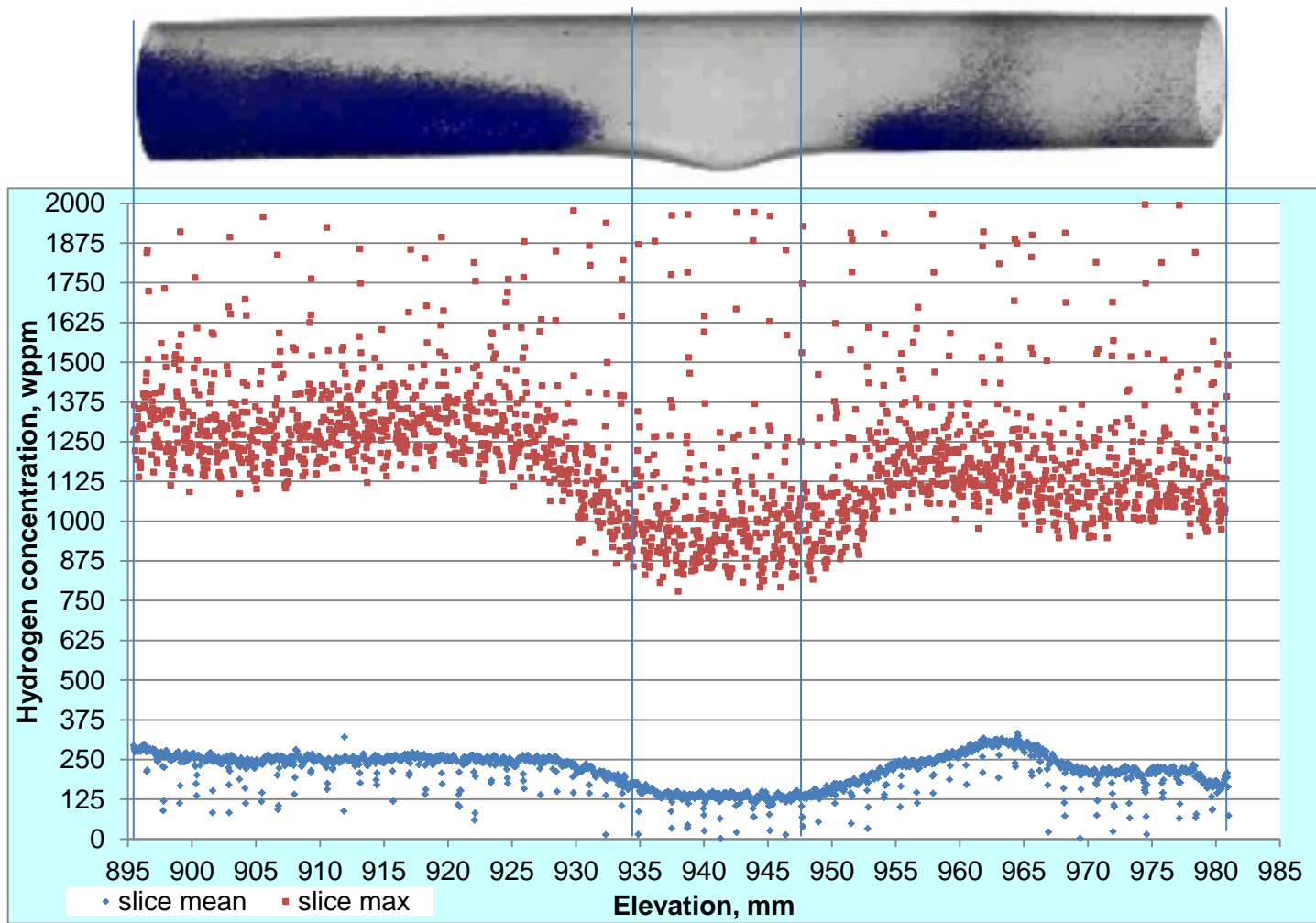


Figure 109 QUENCH-L3; correspondence between reconstruction of tomography image and plots of mean and maximal hydrogen concentrations (calculated for each cross section slice of 40 μm width) in rod #8, plots adjusted to edges of burst opening.

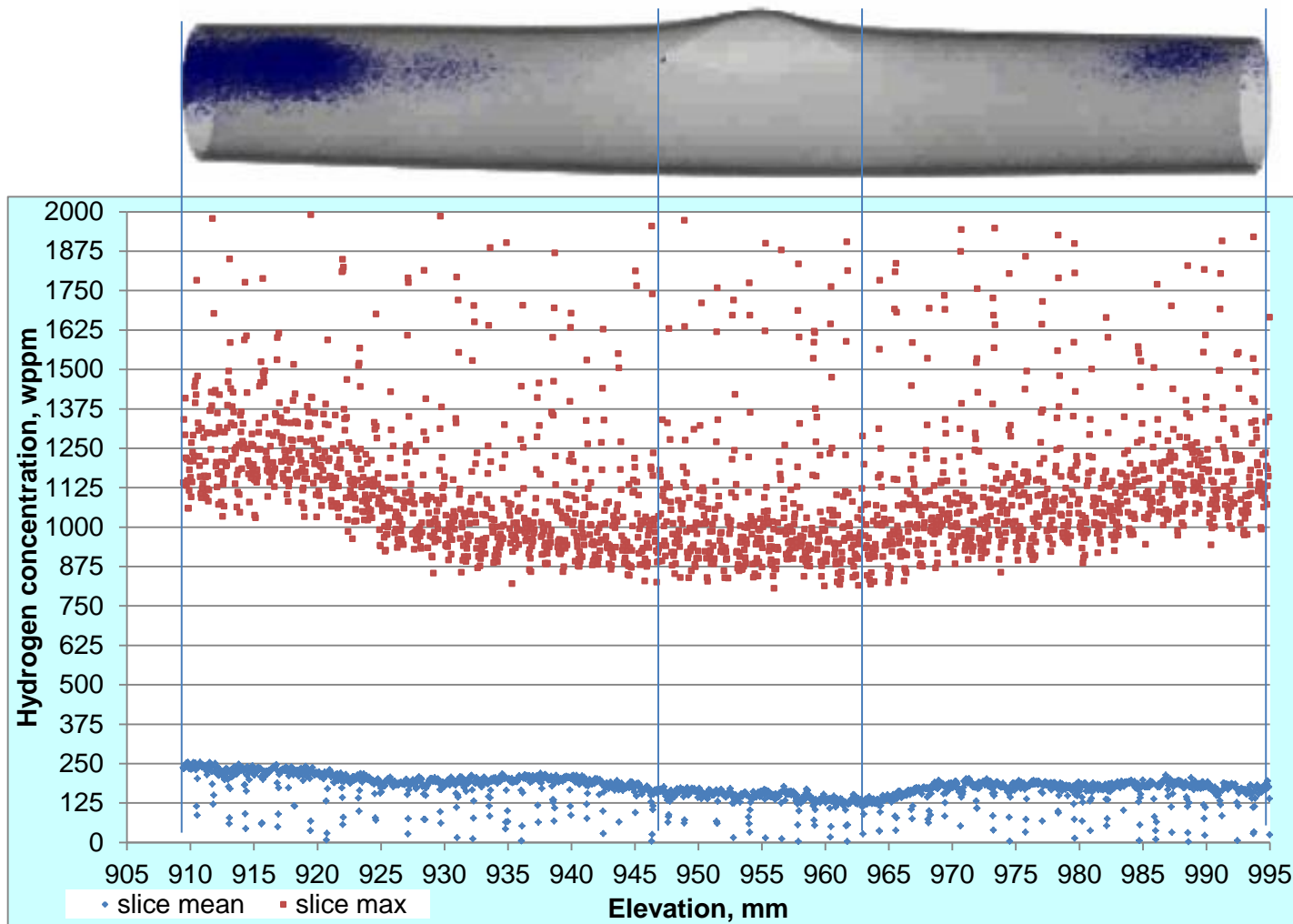


Figure 110 QUENCH-L3; correspondence between reconstruction of tomography image and plots of mean and maximal hydrogen concentrations (calculated for each cross section slice of 40 μm width) in rod #9, plots adjusted to edges of burst opening.

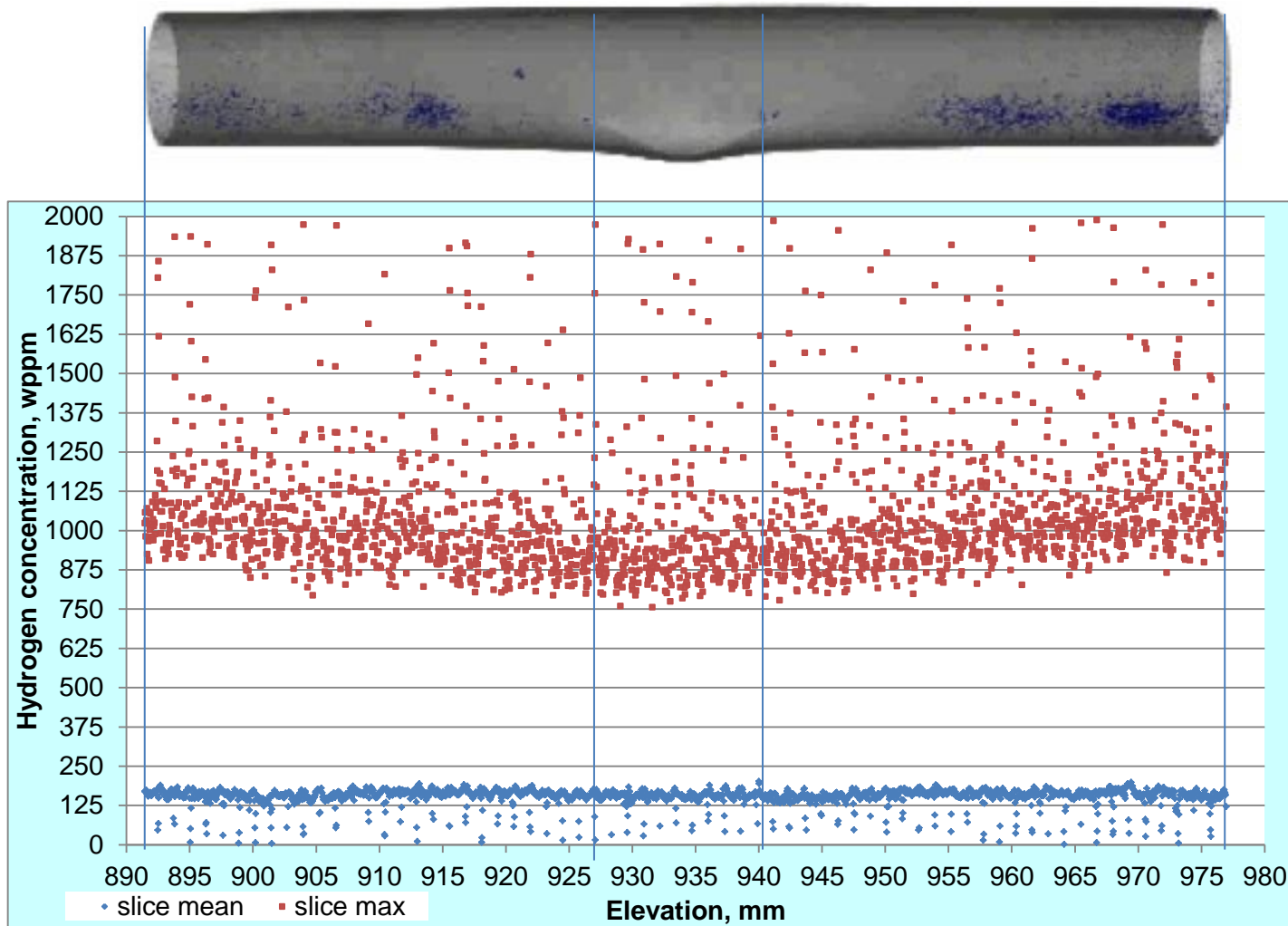


Figure 111 QUENCH-L3; correspondence between reconstruction of tomography image and plots of mean and maximal hydrogen concentrations (calculated for each cross section slice of 40 μm width) in rod #10, plots adjusted to edges of burst opening.

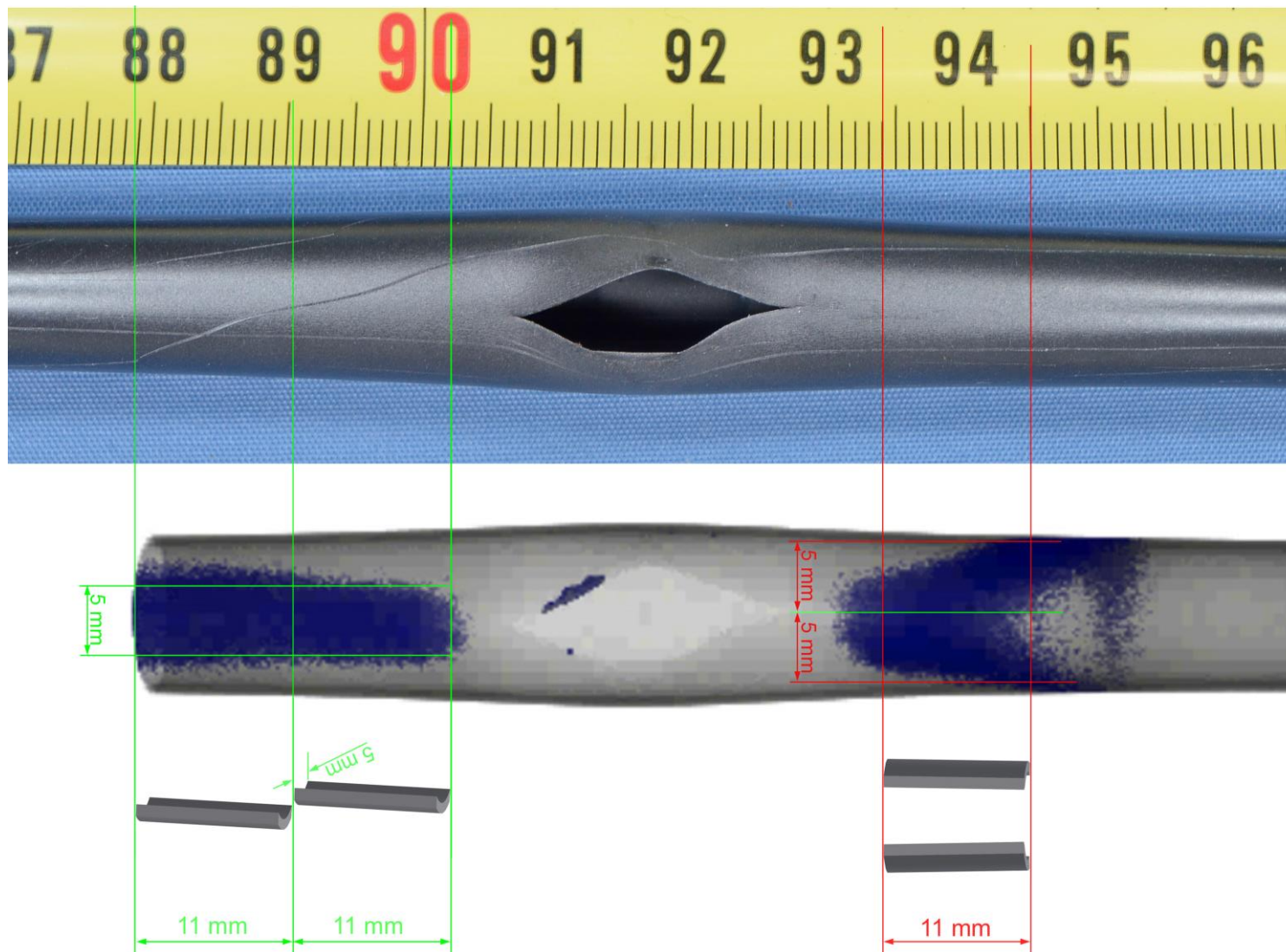


Figure 112 QUENCH-L3; positions of 4 cladding segments of rod #6 for hot extraction.

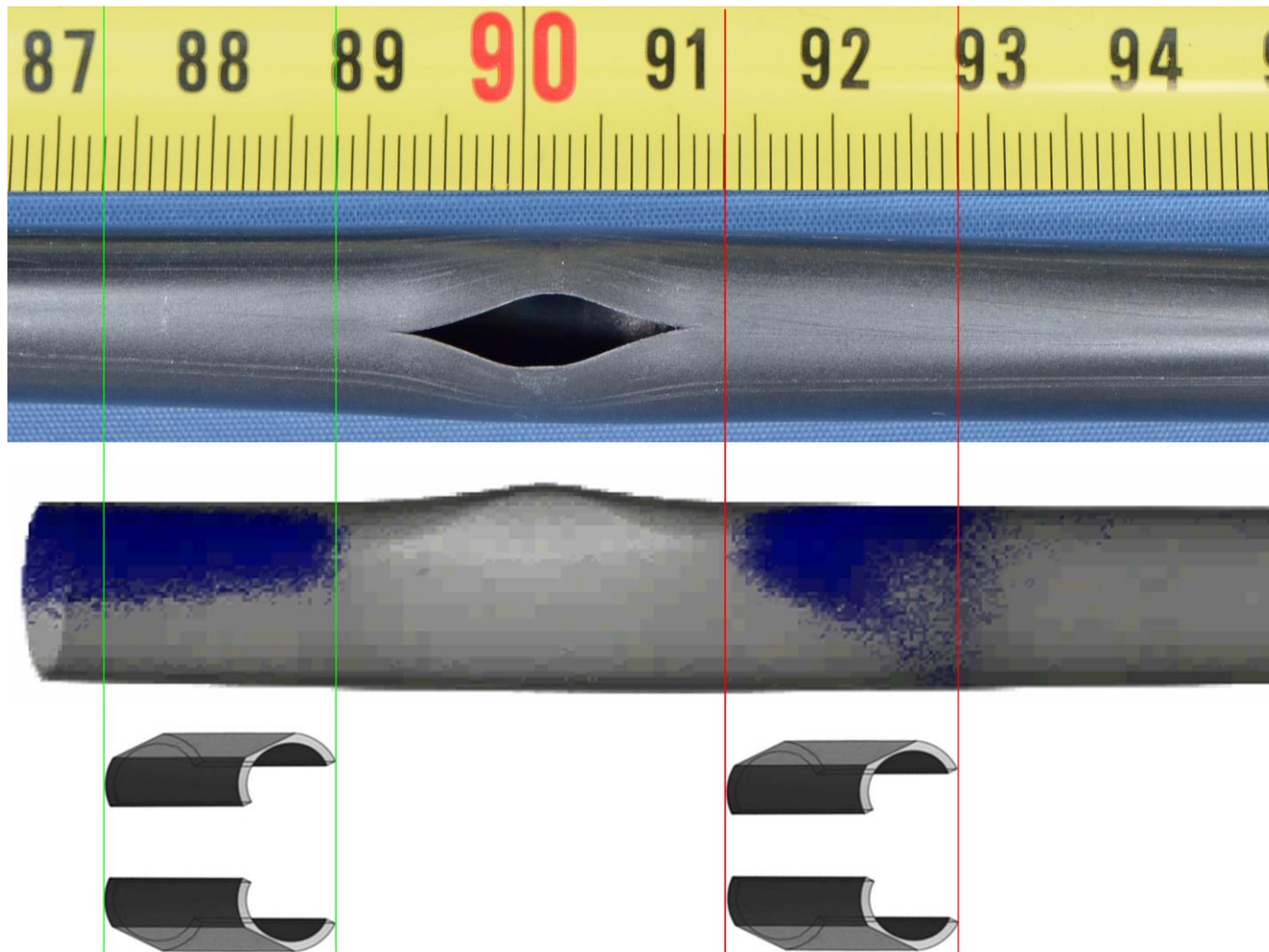


Figure 113 QUENCH-L3; positions of 4 cladding segments of rod #5 for XRD analysis (2 segments at the line of the burst opening and 2 segments at the opposite side).

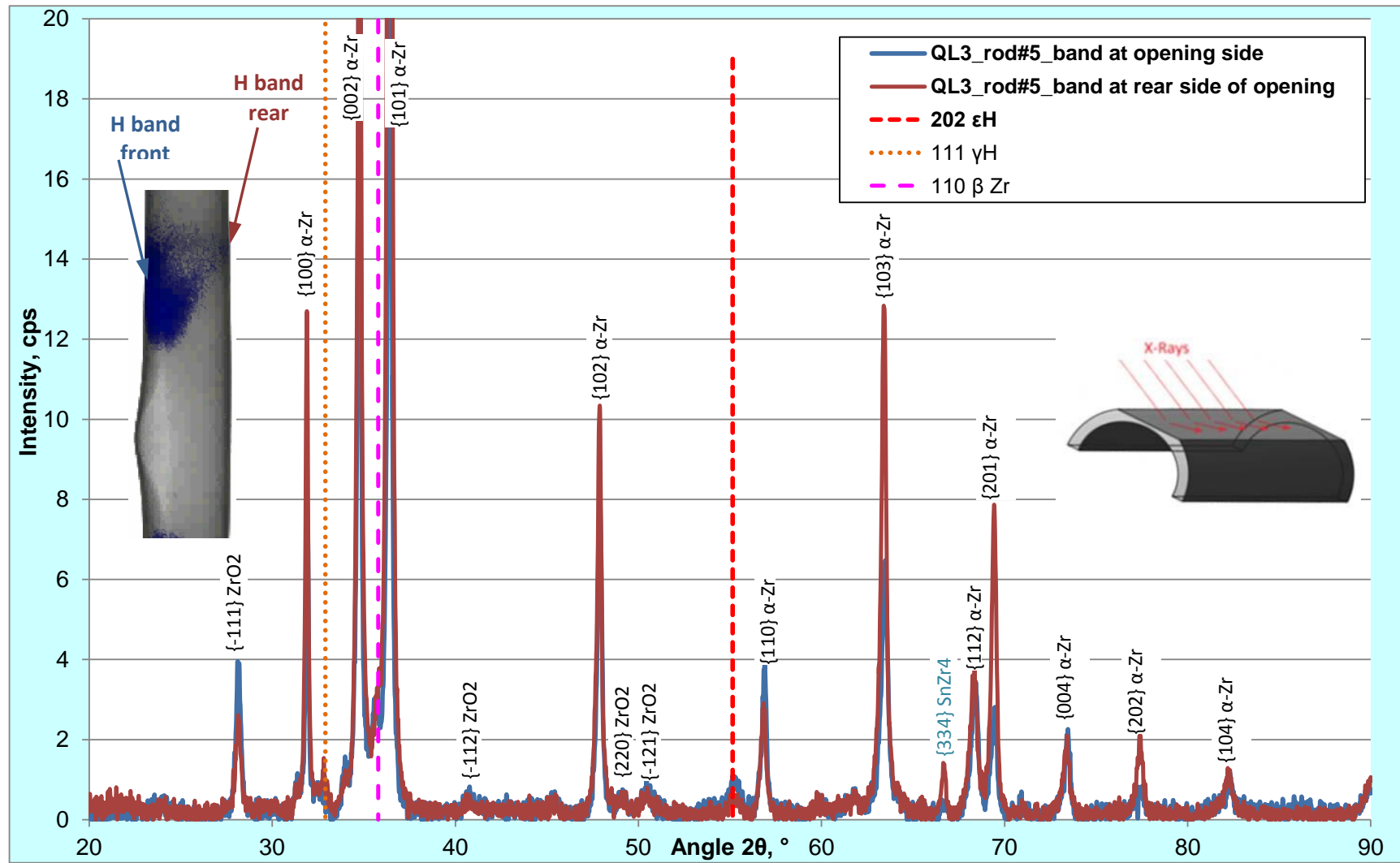


Figure 114 QUENCH-L3; XRD analysis of rod #5 at the elevations of hydrogen band: ϵ -, and γ -hydrides and β -Zr (due to Nb) inside the band at opening front and at opposite side of opening.

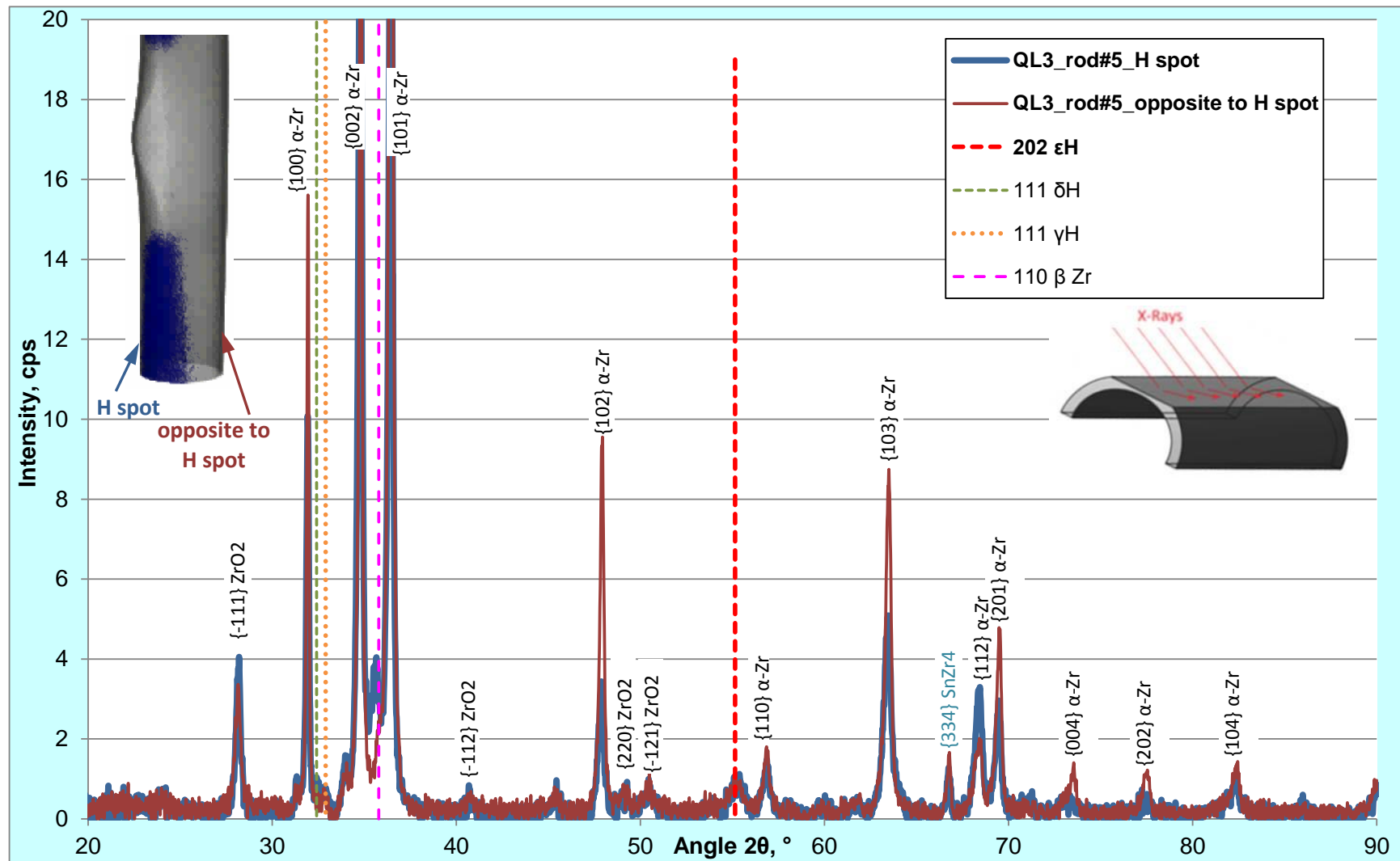


Figure 115 QUENCH-L3; XRD analysis of rod #5 at the elevations of hydrogen spot: ϵ -, δ -, and γ -hydrides and β -Zr (due to Nb) inside the spot and at the cladding side opposite to spot.

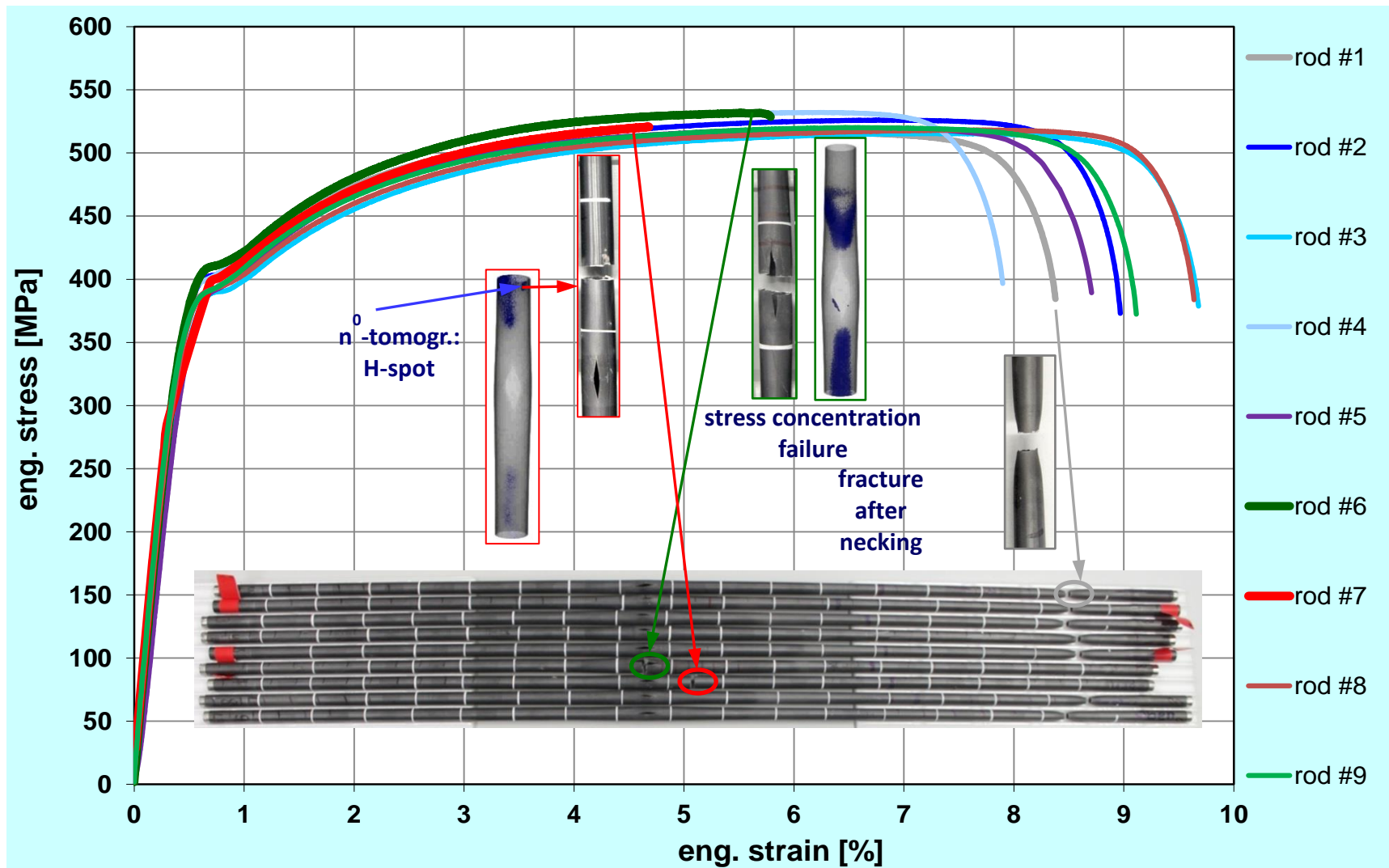


Figure 116 QUENCH-L3; results of tensile tests with claddings of the inner rod group.

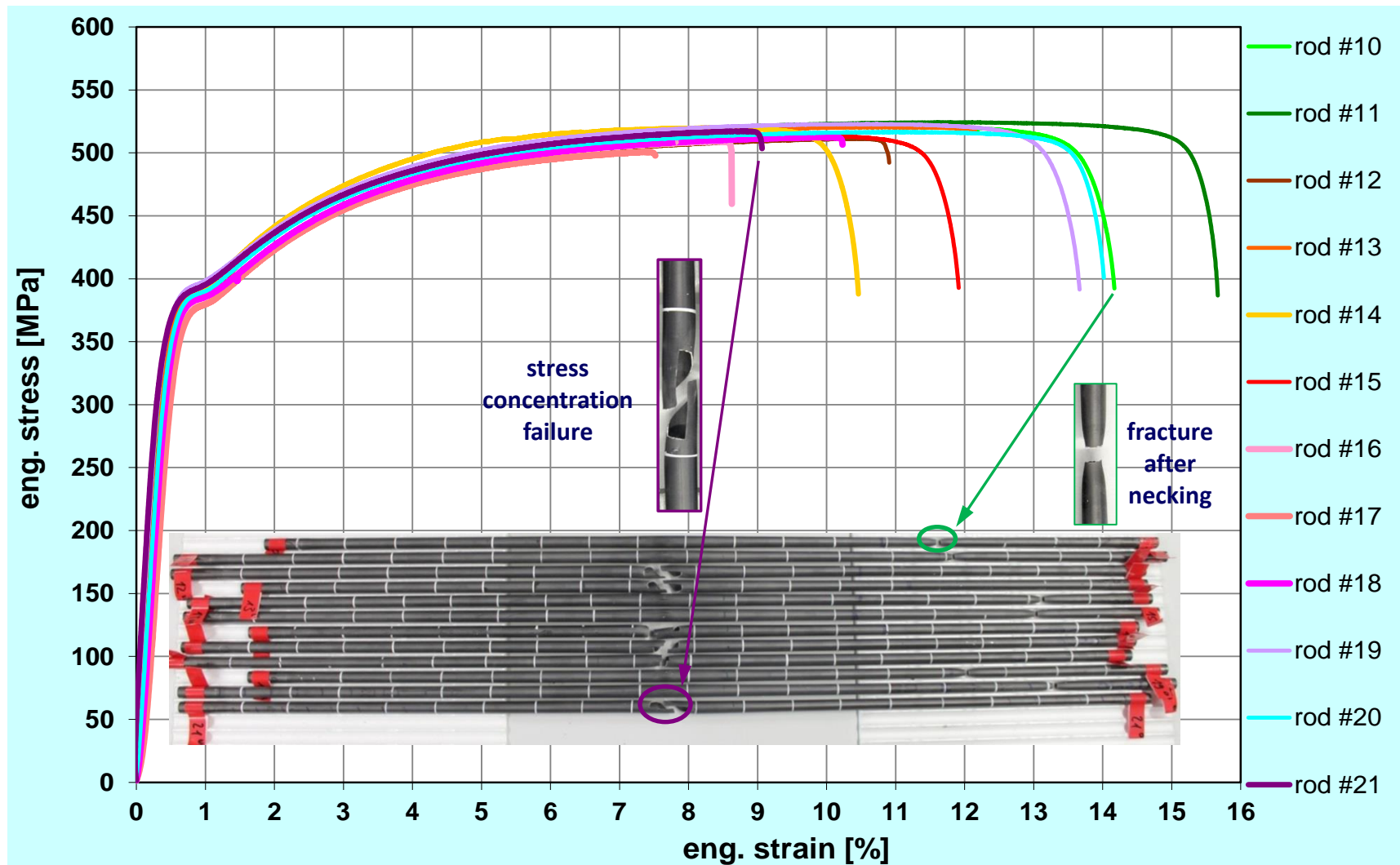



Figure 117 QUENCH-L3; results of tensile tests with claddings of the outer rod group.



The QUENCH-L3 experiment was performed in the framework of the QUENCH-LOCA test series. For the QUENCH-L3 test, as-received ZIRLO™ cladding tubes with an outside diameter of 10.75 mm have been used. Like in all experiments of the QUENCH LOCA series, all 21 electrical heated fuel rod simulators were separately pressurized with krypton to 55 bar. According to a temperature/time scenario typical for a LBLOCA in a German PWR, the test started with a maximal heat-up rate of 8 K/s, continued with a cooling stage lasted 120 s and terminated with 3.3 g/s/rod water flooding. The maximum cladding temperature of about 1350 K was reached at the end of the heat-up stage at elevation 950 mm. The circumferential temperature difference at individual claddings was up to 70 K at burst onset. The maximum thickness of oxide and alpha layers at outer cladding surface was 25 μm. During quenching, following the high-temperature test stages, no fragmentation of claddings was observed indicating that the residual strengths and ductility was sufficient. Some rods have up to three ballooning regions. Due to the low ballooning degree the maximum blockage ratio of the cooling channel was 21%. Cladding wall thinning from 725 to 450 μm due to ballooning was observed at the burst side along 50 mm below and above burst opening. The cladding burst occurred at temperature between 1064 and 1188 K. The average burst opening parameters were: width 3.9, length 14.4 mm. Neutron tomography analyses showed the maximal values of hydrogen concentration (averaged through cladding cross section) between 170 and 500 wppm. Tensile tests at RT revealed the following: seven claddings fractured due to stress concentration at edges of burst opening; thirteen clads failed after necking far away from burst opening. This indicates that the hydrogen enrichments formed at used LOCA scenario had only minor effect on the mechanical cladding failure behavior.